Linear Permanent Magnet Oscillatory Machine and its Control

Teză destinată obţinerii
titlului ştiinţific de doctor inginer
la
Universitatea "Politehnica" din Timişoara
în domeniul INGINERIA MECANICĂ
de către

Ing. Agarliţă Sorin-Cristian

Conducător ştiinţific: prof.univ.dr.ing. Ion Boldea
Referenţi ştiinţifici: prof.univ.dr.ing. Ioan Adrian Viorel
prof.univ.dr.ing. Mircea Radulescu
conf.univ.dr.ing. Lucian Nicolae Tutelea

Ziua susţinerii tezei: 26.06.2009

BUPT

Seriile Teze de doctorat ale UPT sunt:

1. Automatică
2. Chimie
3. Energetică
4. Ingineria Chimică
5. Inginerie Civilă
6. Inginerie Electrică
7. Inginerie Electronică şi Telecomunicaţii
8. Inginerie Industrială
9. Inginerie Mecanică
10. Ştiinţa Calculatoarelor
11. Ştiinţa şi Ingineria Materialelor

Universitatea „Politehnica” din Timişoara a iniţiat seriile de mai sus în scopul diseminării expertizei, cunoştinţelor şi rezultatelor cercetărilor întreprinse în cadrul şcolii doctorale a universităţii. Seriile conţin, potrivit H.B.Ex.S Nr. 14 / 14.07.2006, tezele de doctorat susţinute în universitate începând cu 1 octombrie 2006.

Copyright © Editura Politehnica – Timişoara, 2009

Această publicaţie este supusă prevederilor legii dreptului de autor. Multiplicarea acestei publicaţii, în mod integral sau în parte, traducerea, tipărirea, reutilizarea ilustraţiilor, expunerea, radiodifuzarea, reproducerea pe microfilme sau în orice altă formă este permisă numai cu respectarea prevederilor Legii române a dreptului de autor în vigoare şi permisiunea pentru utilizare obţinută în scris din partea Universităţii „Politehnica” din Timişoara. Toate încălcările acestor drepturi vor fi penalizate potrivit Legii române a drepturilor de autor.

România, 300159 Timişoara, Bd. Republicii 9,
tel. 0256 403823, fax. 0256 403221
e-mail: editura@edipol.upt.ro

BUPT

Preface

This thesis represents an approach to linear interior permanent magnet motors design and control by introducing a novel topology that can be used both in automotive industry and in household devices. The present thesis comprises the motor optimal design realized with two algorithms, three finite element (FEM) analyses, introduces two position estimators based on FEM derived data, and presents open loop and closed loop position control performance of the proposed linear actuator.

Outline of the thesis

The present thesis comprises seven chapters that unfolds as follows.

The first chapter presents a literature survey of the two main applications for which the proposed interior permanent magnet actuator was designed: electromagnetic valves and linear resonance compressors.

In **the second chapter**, the purposed topology of linear machine is introduced. Three types of finite element analysis are presented: electromagnetic, thermal and mechanical.

The third chapter deals with optimal design based on FE (Finite Element) analysis. Two algorithms are introduced, in terms of theory, and utilized in the optimal design process: Grid Search and a modified Hooke-Jeeves algorithm.

In **the fourth chapter** open loop control is treated. The actuator's dynamic model that utilizes FEM derived data is described. Open loop simulations (U/f, I/f) validated with experiments and two estimators are presented.

The fifth chapter deals with closed loop position control with and without sensor. Two combined PI and SM controllers part of a cascaded architecture designed to control the actuator are introduced. Experiments are presented.

The sixth chapter deals with the experimental platform, by describing its main components both hardware and software.

The seventh chapter concentrates the conclusion and the original contributions of the present thesis.

Acknowledgement

I would like to express my gratitude to my supervisor, Prof. Ion Boldea, from University Politehnica of Timisoara, Faculty of Electrical Engineering, whose guidance, support and constructive means of working with Ph.D. students made this work possible. Also, Prof. Fabrizio Marignetti from University of Cassino, Frosinone, Italy deserves my deeply-felt thanks, for all the support and attention offered.

I wish to thank to Assoc. Prof. Lucian Tutelea whose patience, willing and valuable ideas helped me to achieve this work. Also Dr. Sever Scridon and Emil Lazarescu from BEE Speed Automatizari deserve many thanks.

Finally, I'm forever indebted to my family for their unbounded patience and endless support offered when it was most needed.

Timisoara, April 15th, 2009
Sorin-Cristian AGARLIŢĂ

Agarliţă, Sorin-Cristian

Linear Permanent Magnet Oscillatory Machine and its Control

Teze de doctorat ale UPT, Seria 6, Nr. 15, Editura Politehnica, 2009, 220 pagini, 237 figuri, 4 tabele.

ISSN: 1842-7022

ISBN: 978-973-625-910-4

Keywords: LPMOM, Finite Element Analysis, Direct Search Algorithms, Hooke-Jeeves, Sliding Mode Control, Cascaded Arhitecture Control

Objectives of the thesis:

- to introduce a novel linear permanent magnet oscillatory machine;
- to develop electromagnetic, thermal and mechanical finite element analysis;
- to implement a optimal design program based on FEM derived data;
- to implement an open-loop control of the purposed linear machine;
- to introduce FEM based position estimators for sensorless closed loop control purposes;
- to implement a sensorless position closed loop control of the purposed linear machine.

BUPT

Table of Contents

Chapter 1 Linear interior PM actuators and their applications 13

1.1 Automotive Electrical Systems Trends 13

1.2 Internal Combustion Engine Basics 20

1.3 Variable Valve Timing 22

1.4 Electromechanical Valves 25

1.5 Rotary Electromechanical Valve Actuators – Literature Survey 27

1.6 Linear electromagnetic valve actuator – Literature Survey 34

1.7 Linear resonance compressors 56

Summary 59

Chapter 2 Finite Element Analysis of the proposed configuration 63

2.1 Finite Element Analysis – An Introduction 63

2.2 Electromagnetic FEA 65

2.2.1 Theoretical background 65

2.2.2 Electromagnetic FEA – The Software 66

2.2.3 The proposed Configuration 67

2.2.4 The operating principle 68

2.2.5 Electromagnetic FEA results and experimental validation 70

2.2.6 FEMM derived core loss Model 78

2.3 Thermal FEA 83

2.3.1 Theoretical background 83

2.3.2 Thermal FEA – The Software 84

2.3.3 Thermal FEA results 85

2.4 Mechanical FEA 92

2.4.1 Theoretical background 92

2.4.2 Mechanical FEA – The Software 93

2.4.3 Mechanical FEA results 94

Summary 97

Chapter 3 Finite Element Optimal Design of the proposed configuration 99

3.1 Direct versus Indirect Search optimization algorithms 99

3.2 The grid search optimization algorithm 102

3.3 Hooke-Jeeves optimization algorithm 105

3.3.1 Theoretical background 105

3.3.2 Modified Hooke Jeeves optimization algorithm 109

BUPT

Summary 119

Chapter 4 Open loop Control - Simulation and experimental results 121

4.1 Introduction – Open Loop Control Systems 121

4.2 Open-loop U/f dynamic control – simulation and experimental validation 122

4.3 Open-loop I/f dynamic control – simulation and experimental validation 129

4.4 Position estimation using FEM derived dependencies 131

4.4.1 A FEM derived position estimation 131

4.4.2 Position estimation validation when performing U/f open loop control 136

4.4.3 Position estimation validation when performing I/f open loop control 138

Summary 154

Chapter 5 Closed loop position sensorless control 157

5.1 Closed Loop Control Systems –An introduction 157

5.1.1 PID Close loop control system 157

5.1.2 Sliding Mode Control 160

5.1.3 Cascade arhitecture – basic considerations 162

5.2 Combined sliding mode and PI controller closed loop performance with position measured 163

5.2.1 The controller 163

5.2.2 Experimentally obtained results 167

5.3 Combined sliding mode and PI controller sensorless closed loop control 172

5.3.1 Fixed amplitude and frequency sinusoidal prescribed position performance 172

5.3.2 Step amplitude change at constant frequency of prescribed position 189

5.3.3 Step amplitude and step frequency change of the prescribed position 191

5.3.4 Closed loop position sensorless control performance analysis 194

Summary 196

Chapter 6 The Experimental test platform 199

6.1 The hardware platform components 199

6.1.1 The Linear Interior PM Actuator 200

BUPT

6.1.2 The DSpace platform 203
6.1.3 The high speed analogue sensor laser 205
6.1.4 The single phase inverter 206
6.1.5 The bi-directional load cell 209
6.2 The Software 210
Summary 215

Chapter 7 Conclusion and Contributions 217
7.1 Conclusion 217
7.2 Original contributions 218

Author's papers related to the Ph.D. thesis

Author's CV

Chapter 1 - Linear interior PM actuators and their applications

We will present in this chapter the two main applications for which our proposed interior permanent magnet actuator was designed: electromagnetic valves actuation and linear resonance compressors. A review of several solutions for achieving Variable Valve Timing (VVT) operation of internal combustion engines (ICEs) with linear and rotary actuators is presented. Different topologies of linear motors designed for linear compressors will be analyzed. Let us start first with a short exposure of today's automotive electrical systems trends.

1.1 Automotive Electrical Systems Trends

In the past several years there is a revolution in the design of electrical system in automotive. This is the result of increasingly sophisticated engine and body controls, as well as the introduction of new, electrically controlled functions of the car.

The main electrical bus of the future will be 42 V, and it will be buffered by a 36 V battery. Due to the fact that many devices and electronic control units require voltages different from 42, conversion from the 42 V bus to these other voltages will be necessary. Electromechanical engine valves will demand both conversion and sophisticated control at different power levels. [1]

The direction in automotive industry is to replace mechanical actuators by electrical, improving electrical system efficiency, finding alternatives to the present 14 Vdc system, and improving safety and comfort by introducing new functions that are best controlled electrically. Packing flexibility is the main motivation of the electrifying process of the car.

Mechanically driven devices, such as power steering, water pumps and air conditioning, are located on the front of the engine and driven by the "front-end accessory drive" (FEAD). The flexibility feature needed by automotive designers can be provided by eliminating the FEAD. The average electrical load will increase as Figure 1.1 tries to anticipate for a high-end car.

BUPT

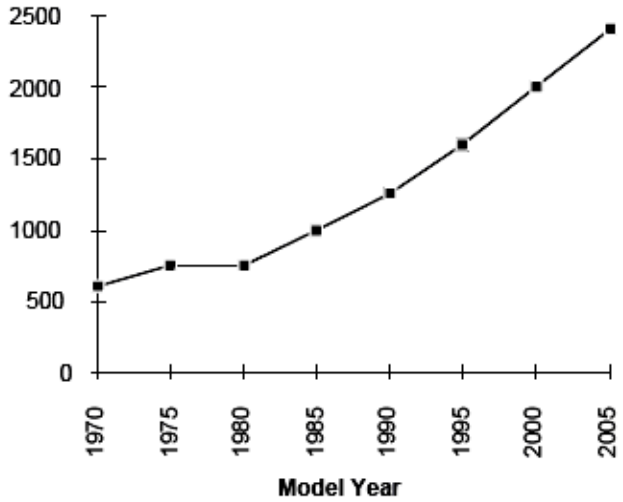

Figure 1.1 Historical and anticipated average electrical load in a high end automobile

In the US and Europe programs are being developed in order to redesign the electrical systems.

The new requirements being placed on the electrical system, and revised criteria for cost, efficiency, packaging and expandability are providing the first opportunity for a radical redesign of the automotive electrical system since the change from 6V to 12V in the early 50's [1]. One of the most important enabling technologies available to this redesign process is power electronics.

In [1] Professor J. Kassakian (Laboratory for Electromagnetic and Electronic Systems - The Massachusetts Institute of Technology) describe the automobile's present electrical system and the system developments that are expected to create a very large and diverse market for power electronic controls, systems and devices.

Due to the concern of increasing fuel economy, reducing emissions and providing a greater degree of safety an increase in electrical load have resulted. By rethinking the design of some of the main engine components such as the engine cooling fan, the water pump, the oil pump, the automatic transmission clutch system, and the engine valve train future efficiency and functional improvements can be provide. A major obstacle is the cost of the controlling power electronics. As production is initiated and volumes increase, costs should decrease. However, the primary challenge for power electronics will remain cost, and reducing cost is the only way to increase the penetration of power electronics in the car [2]. Figure 1.2 illustrates the typical load dump transient at 8000 rpm. The initial spike is caused by the alternator voltage and the following longer transient is produced by the decay of the alternator field.

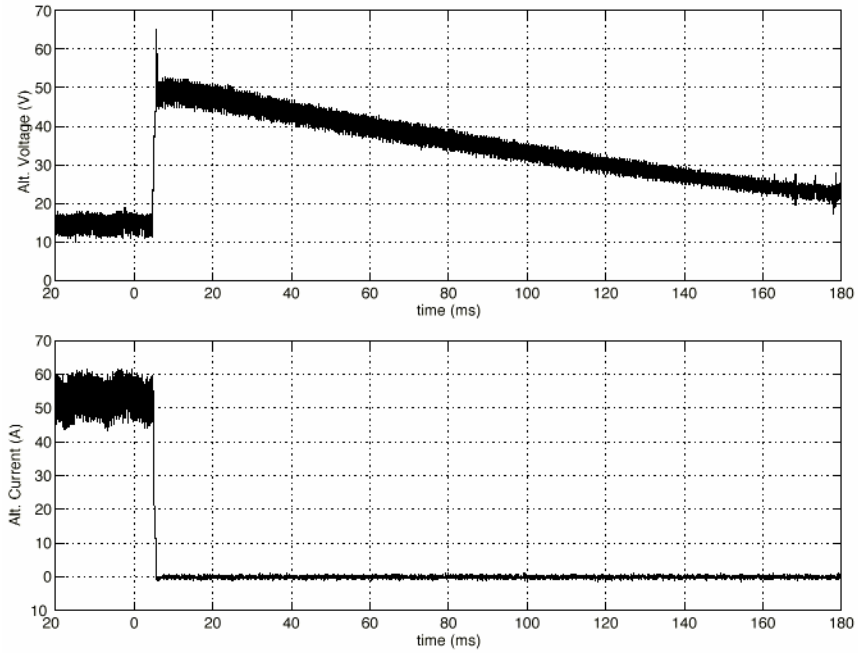

Figure 1.2 Typical load dump transient

In [2] the main electrical problems in automotive are presented. A key concern is the electrical environment in today's cars. The maximum under hood ambient temperature is specified by different manufacturers to be between 125^0C and 150^0C, depending on under hood packaging philosophy, while the minimum operating ambient is -40^0C. The environmental factors affecting automotive electronics can be found in [3], and Table 1 shows ambient temperatures for various vehicle locations [2].

Table 1 - High temperature extremes in automobiles by location [2, 4]

Vehicle Location	Maximum Temperature (^{0}C)
Exterior	85
Chassis	
- isolated	85
- near heat source	121
- drive train high temp location	177
Interior	
- floor	85
- rear deck	104
- instrument panel	85
- instrument panel top	177
Trunk	85
Under hood	
- Near radiator support structure	100
- Intake manifold	121
- Near alternator	131
- Exhaust manifold	649
- Dash panel (normal)	121
- Dash panel (extreme)	141

The most demanding specification results from a phenomenon known as a "load dump transient", that occurs when a fully loaded alternator has its load disconnected. This may occur when the battery is being charged at its maximum rate and a terminal connector suddenly comes loose. In this case the alternator field current cannot be instantly reduced, so the alternator's voltage behind reactance, which can exceed sometimes 100 V, appears at its terminals. The car's entire electrical system is has to face this transient. Some mitigation of the transient is provided by avalanche diodes in modern cars, but a maximum system voltage of 40–60 V is still assumed for design purposes.

Currently the electrical system has a 12 V lead-acid battery for energy storage and power capability, thus creating a network with a nominal voltage of 14.4 V when the engine is on. A conceptual diagram of the system is shown in Figure 1.3 [5].

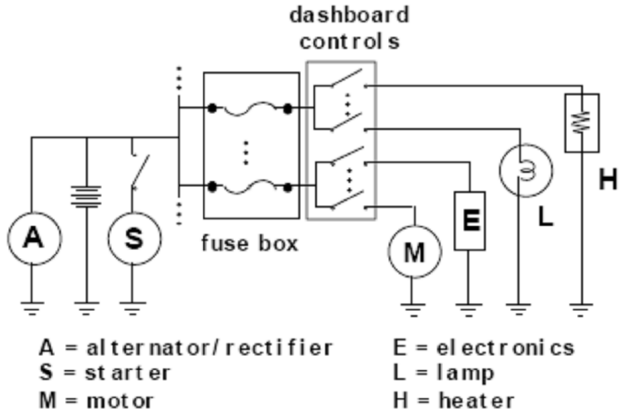

Figure 1.3 Diagram of conventional 14V automotive electrical network

Generating 42V

There can be found in literature several designs for automotive alternators that provide increases in peak and average power output. An alternator design that uses a conventional Lundell machine and incorporates a switched mode rectifier along with a special load-matching control technique is presented in [6]. This design allows higher levels of output power and efficiency to be achieved as compared to conventional designs. Knowing the fact that the electromechanical engine valves have a large speed dependent power requirement, this design is ideal for supplying anticipated new loads.

Figure 1.4 illustrates a simple electrical model for the conventional Lundell alternator system.

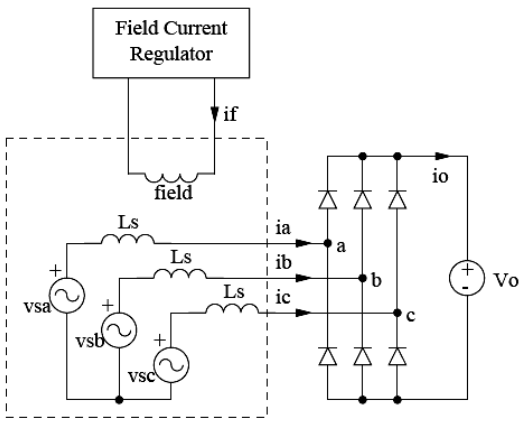

Figure 1.4 Simple Lundell alternator model

It is known that a conventional Lundell alternator cannot achieve the maximum power possible, for speeds above idle, because the fixed output voltage is not matched to the alternator characteristic at these speeds. The new design and control approach introduced in [6] allows the maximum load-matched power to be attained at all speeds. By utilizing both field control and a simple switched mode rectifier one can achieve substantially higher power and performance than conventional systems, particularly at speeds above idle. High power is achieved by utilizing the switched-mode rectifier as a second control handle to properly match the constant-voltage load to the alternator.

The switched mode rectifier (Figure 1.5) permits the machine voltage, and hence its power, to increase with speed while maintaining a constant 42 V dc output.

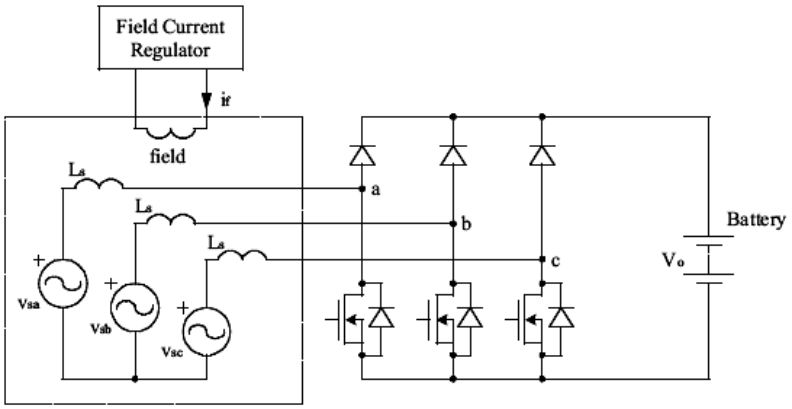

Figure 1.5 A conventional Lundell alternator modified by the addition of a switched-mode rectifier.

Integrated Starter/Generator

Conventional „idle-stop" systems help to save fuel by automatically shutting down the engine when the driver brings the vehicle to a halt (at traffic lights, for example) and automatically restarting the engine when the driver subsequently wishes to pull away.

This technology helps by reducing emissions, increasing fuel economy and reducing acoustic noise, especially in urban areas.

The torque required to start the engine is considerable and this should be done in about 50 ms in order to provide a smooth driving experience where the driver is unaware of any delay when starting from a stop. A number of vehicles incorporating an integrated starter/generator (ISG) have been demonstrated. The long-term vision is that this ISG be mounted directly on the crankshaft of the engine

and replace the flywheel. Toyota has reported vehicle production incorporation idle-stop technology. Figure 1.6 shows an ISA comprising a switched reluctance motor.

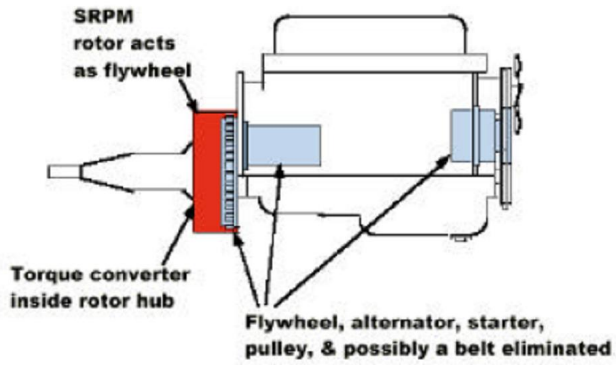

Figure 1.6 ISA consisting of a switched reluctance PM motor integrated with the transmission

Electric Active Suspension

The active suspension systems uses electrical actuators to maintain the car on a level trajectory as the wheels undergo uneven vertical motion due, e.g., to a rough road. Figure 1.7 shows a schematic of an electric active suspension system using a linear permanent magnet motor as the actuator. Alternatives using rotary actuators have also been proposed.

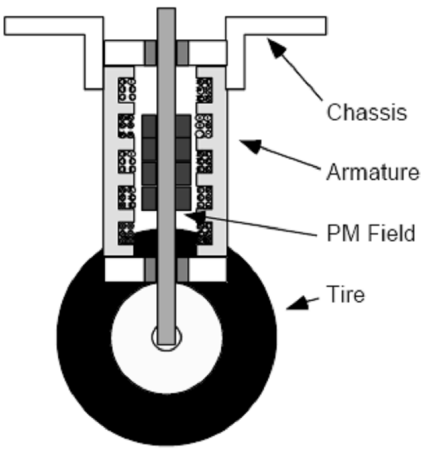

Figure 1.7 Active suspension using linear motor

Another technology that needs the 42V power net is Variable Valve Timing (VVT) which uses electromechanical devices to actuate the engine valves.

One of the main applications of the linear motor presented in this thesis is VVT. The next section of the chapter will concern with aspects related to Internal Combustion Engines and their valve actuating problems.

1.2 Internal Combustion Engine Basics

The internal combustion engine is a heat engine in which the burning of a fuel occurs in a limited space called a combustion chamber. This exothermic reaction of a fuel with an oxidizer creates gases of high temperature and pressure, which are permitted to expand. The defining feature of an internal combustion engine is that useful work is performed by the expanding hot gases acting directly to cause movement, for example by acting on pistons, rotors, or even by pressing on and moving the entire engine itself (Figure 1.8)

If cylinder heads are the heart of an engine, then the camshaft and valve train have to be the brains of the operation. Timing the opening, closing, lift, and duration of each valve event is central to increasing power and torque.

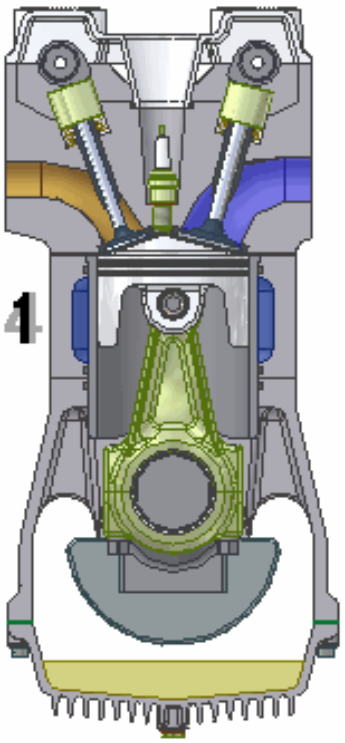

Figure 1.8 ICE chamber cross-section

A valve train consists of valves and a mechanism which opens and closes them. The opening and closing system is called a camshaft. The camshaft uses lobes (cams) that push against the valves to open them as the camshaft rotates. The system uses springs to return the valves to their closed position. This is a critical job, and can have a great impact on an engine's performance at different speeds. One of the key part of any camshaft is the shape of the cams. As the camshaft spins, the cams open and close the intake and exhaust valves in time with the motion of the piston. Thereby there is a direct relationship between the shape of the cam lobes and the way the engine performs in different speed ranges.

When the piston starts its intake stroke and the intake valve opens, the air/fuel mixture in the intake runner starts to accelerate into the cylinder. When the piston reaches the bottom of its stroke, the mixture is moving at a pretty high speed. If you were to slam the intake valve shut, all of that air/fuel mixture would come to a halt and will not enter the cylinder. By leaving the intake valve open a little longer, the momentum of the fast-moving air/fuel mixture continues to force air and fuel into the cylinder as the compression stroke is started by the piston. In this case, the faster the engine goes, the faster the air/fuel mixture flows and the longer we would want the intake valve to stay open. We would also want the valve to open wider at higher speeds. Also affecting the cams performance is lift, the duration, overlap and timing.

Next we will explain three key parameters that affects engine's performance: lift, duration and overlap.

Lift

Lift refers to maximum valve lift. This is how much the valve is "lifted" off its seat at the cam lobe's highest point. The intake and exhaust valves need to be open to let air/fuel in and exhaust out of the cylinders. Generally, opening the valves quicker and further will increase engine output. Increasing valve lift, without increasing duration, can yield more power without much change to the nature of the power curve. However, an increase in valve lift almost always is accompanied by an increase in duration. This is because ramps are limited in their shape which is directly related to the type of lifters being used, such as flat or roller. Figure 1.9 illustrates a typical camshaft .

Figure 1.9 ICE camshaft

Duration

Duration is the angle in crankshaft degrees that the valve stays off its seat during the lifting cycle of the cam lobe. Increasing duration keeps the valve open longer, and can increase high-rpm power. Doing so increases the RPM range that the engine produces power. By increasing duration without a change in lobe separation angle will result in increased valve overlap.

Overlap

Overlap is the angle in crankshaft degrees that both the intake and exhaust valves are open. This occurs at the end of the exhaust stroke and the beginning of the intake stroke. Increasing lift duration and/or decreasing lobe separation increases overlap. At high engine speeds, overlap allows the rush of exhaust gasses out the exhaust valve to help pull the fresh air/fuel mixture into the cylinder through the intake valve. Increased engine speed enhances the effect. Therefore increasing overlap, increases top-end power and reduces low-speed power and idle quality.

Any given camshaft will be perfect only at one engine speed. At every other engine speed, the engine won't perform to its full potential. A fixed camshaft is, therefore, always a compromise.

1.3 Variable Valve Timing

A major problem in conventional combustion engines is that choice of traditional camshaft control of valves. The clasical solution which uses a camshaft is satisfactory in overcoming parameter changes in the system, but is not sufficiently efficient in terms of the production of pollutant exhaust, and is also improvable in terms of overall motor efficiency.

There are a couple of ways by which car manufacturer's vary the valve timing. The most well known system is the VTEC which is used on some of the Honda engines. Other systems which some of you might not have heard of are:

VarioCam/VarioCam Plus which is used on some of the Porsche engines

- **MIVEC** (Mitsubishi Innovative Valve timing and lift Electronic Control) which is used on the Mitsubishi engines
- **VVT-i** (Variable Valve Timing with Intelligence) and now VVTL-i (Variable Valve Timing and Lift with Intelligence) which is being used on the current Toyota and some Lexus engines,
- **VVL** (Variable Valve Lift) which is used on the Nissan engines and also featured in the 350Z is the **CVTCS** (Continuously Variable Valve Timing System)

• **VANOS** (Variable Onckenwellen Steuerung) which is used in the BMW engines and also the Double VANOS system on the new 3 Series and they are many more similar systems used by manufacturers such as Ford, Lamborghini and even Ferrari [7].

The engine is basically an air pump and, as such, the most effective way to increase horsepower and/or efficiency is to increase an engine's ability to process air. There are a number of ways to do this that range from altering the exhaust system to upgrading the fuel system to installing a less-restrictive air filter. Due to the fact that the engine's valves play a major role in how air gets in and out of the combustion chamber, it makes sense to focus on them when looking to increase horsepower and efficiency [7].

Honda, Toyota and BMW and quite a number of other manufacturer's have increased their research in this field over the past recent years. By using advanced systems to alter the opening and closing of engine valves, they have created more powerful and clean burning engines that require less fuel and are relatively small in displacement.

Until recently, a manufacturer used one or more camshafts (plus some pushrods, lifters and rocker arms) to open and close an engine's valves. The camshaft/camshafts was turned by a timing chain that connected to the crankshaft. As engine rpm's rose and fell, the crankshaft and camshaft would turn faster or slower to keep valve timing relatively close to what was needed for engine operation.

The dynamics of airflow through a combustion chamber change radically between 2,000 rpm and 6,000 rpm. Despite the manufacturer's best efforts, there was just no way to maximize valve timing for high and low rpm with a simple crankshaft-driven valve train. Instead, engineers had to develop a "compromise" system that would allow an engine to start and run when pulling out of the driveway but also allow for strong acceleration and highway cruising at 120+ kmph. Because of the "compromise" nature of standard valve train systems, when engines weren't in their "good performance zone" they wasted fuel and worked with poor performance.

Variable valve timing has changed all that. By developing a way to change valve timing between high and low rpm's, car manufactures can now tune valve operation for optimum performance and efficiency throughout the entire speed range.

Honda was the first car manufacture to introduce what it called VTEC in its Acura-badged performance models like the Integra GS-R and NSX. VTEC stands for Variable Valve Timing and Lift Electronic Control. The system uses two sets of camshaft profiles - one for low and mid-range rpm and one for high rpm operation. An electronic switch shifts between the two profiles at a specific rpm to increase

BUPT

peak horsepower and improve torque. While this system does not offer continuously variable valve timing, it can make the most of high rpm operation while still providing solid drivability at lower rpm levels. Honda is already working on a three-step VTEC system that will further improve performance and efficiency across the engine rpm range.

The camshaft in a pushrod engine is often driven by gears or a short chain. Gear-drives are generally less prone to breakage than belt drives, which are often found in overhead cam engines.

Instead of using an on/off system that VTEC employs, Toyota decided to develop a continuously variable system that would maximize valve timing throughout the rpm range. Dubbed VVTi for Variable Valve Timing with intelligence, Toyota uses a hydraulic rather than mechanical system to change the intake cam's phasing. The main difference from VTEC is that VVTi maintains the same cam profile and alters only when the valves open and close in relation to engine speed. Also, this system works only on the intake valve while VTEC has two settings for the intake and the exhaust valves, which makes for a more dramatic gain in peak power than VVTi can claim.

The camshafts on some Ferrari engines are cut with a three-dimensional profile that varies along the length of the cam lobe. At one end of the cam lobe is the least aggressive cam profile, and at the other end is the most aggressive. The shape of the cam smoothly blends these two profiles together. A mechanism can slide the whole camshaft laterally so that the valve engages different parts of the cam. The shaft still spins just like a regular camshaft, but by gradually sliding the camshaft laterally as the engine speed and load increase, the valve timing can be optimized.

Several other manufacturers, including Ford, Lamborghini and Porsche have jumped on the cam phasing bandwagon because it is a relatively cheap method of increasing horsepower, torque and efficiency. BMW has also used a cam phasing system, called VANOS (Variable Onckenwellen Steuerung) for several years. Like the other manufacturers, this system only affected the intake cams. But, as of 1999, BMW is offering its Double VANOS system on the new 3 Series. As you might have guessed, Double VANOS manipulates both the intake and exhaust camshafts to provide efficient operation at all rpm's. This helps the new 328i, equipped with a 2.8-liter inline six, develop 193 peak horsepower and 206 pound-feet of torque. More impressive than the peak numbers, however, is the broad range of useable power that goes along with this system.

Several engine manufacturers are experimenting with systems that would allow infinite variability in valve timing. For example, imagine that each valve had a solenoid on it that could open and close the valve using computer control rather

than relying on a camshaft. With this type of system, you would get maximum engine performance at every RPM.

To conclude, the major advantages of VVT are:

- fuel savings of 20% or higher due to the fact that the intake process at part load can be controlled, eliminating this way the need of intake throttle valve and the related pumping losses;
- the maximum load will increase with 10% and up to 50% at low speed torque, generating a more flat torque characteristic that leads to better driveability of the vehicle;
- pollutant emission reduction, especially in NO production; the possibility of achieving high internal exhaust gas recirculation (EGR) rate, through both retarding or advancing exhaust valve closing, significantly reduces the cylinder peak temperature, resulting in NO reduction up to 90%;
- increased burn rate;
- improved combustion stability at low speed;
- reduced energy consumption. [8]

1.4 Electromechanical Valves

The valves are classically controlled mechanically through linkages to the crankshaft. A camshaft is connected through a chain or belt (the timing chain) to the crank. The cams then act on pushrods, rocker arms or the valve stems themselves to cause the valves to open and close in synchronism with the position of the piston in the respective cylinder. Valve timing affects fuel economy, dynamic performance, and emissions, but since the cam design is fixed, these attributes can be optimized at only a single engine speed and load condition.

If all the valves were controlled by an electrical actuator instead of a mechanical camshaft, each valve could be controlled independently for timing, profile and lift. This would make possible not only performance optimized with respect to fuel economy, dynamics and emissions at every speed and load condition, but would also permit the deactivation of cylinders to improve fuel economy at cruise, and potentially reduce starting torque requirements. The former is achieved by closing all valves in a cylinder, and the latter by opening all valves in the engine. It is even conceivable that the engine could be "statically" started, that is, started without turning it over with a starter motor.

BUPT

The concept is to employ direct fuel injection (DFI) to inject a small amount of fuel into the appropriate cylinder (determined by piston position) with its valves closed, then fire the cylinder to begin engine motion. Figure 1.10 shows a popular design concept for an electromechanical valve. It can be viewed as a resonant spring-mass system which oscillates between open and closed, being held at each state by the upper or lower electromagnet [2].

Ideally no energy is lost in the transition, and because the magnetic circuit has no gap in the open or closed position, the required holding force can be obtained with very little MMF, i.e., magnet current. In reality the situation is more complicated because of thermally induced dimensional variability and the work required to overcome gas pressure on opening the exhaust valves. What is evident, however, is that whatever electromechanical mechanism is used, it will be controlled by power electronics according to a very complex algorithm involving inputs of engine speed, load, exhaust gas conditions, temperature and injection dynamics.

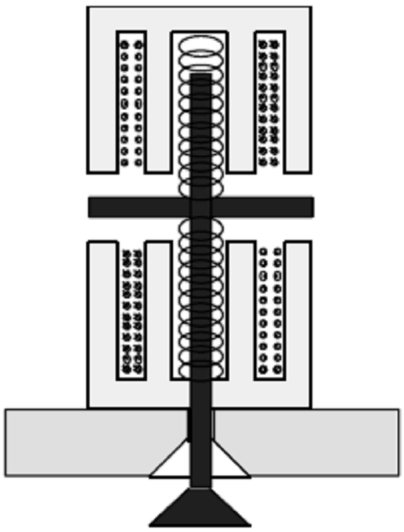

Figure 1.10 Typical electromechanical valve actuator

1.5 Rotary Electromechanical Valve Actuators – Literature Survey

The technologies used to actuate the valves use rotary or linear motors. When using rotary motors the motion has to be transformed using various systems like: rod -crank, pinion-rack and screw-nut. This type of solutions is called indirect drive actuation. When we produce the linear motion without any mechanical transformation we talk about direct drive actuation topologies.

An interesting indirect drive that uses an electromechanical valve drive (EMVD) incorporating a nonlinear mechanical transformer can be found in [9].

The special shaped disk cam acts as a Nonlinear Mechanical Transformer (NTF) to transform the rotary motion into linear motion. Also its shape allows for small holding and driving currents, and small seating velocity (velocity at which the valve engages its seat).

An IC engine valve's kinematics profiles (such as valve position versus time, valve speed versus time, and so on) are of fixed shape and are timed relative to the engine crankshaft position. From a control systems perspective, we say the engine valves are not controllable. If instead, we could independently control the duration, phase and lift of the valves, a marked improvement in emissions, efficiency, maximum power, and fuel economy would be seen [10]. The engine's mechanical design, although simple, compromises the efficiency and maximum power of the engine [9].

The kinematics variables for a conventional IC engine valve, are shown in Figure 1.11.

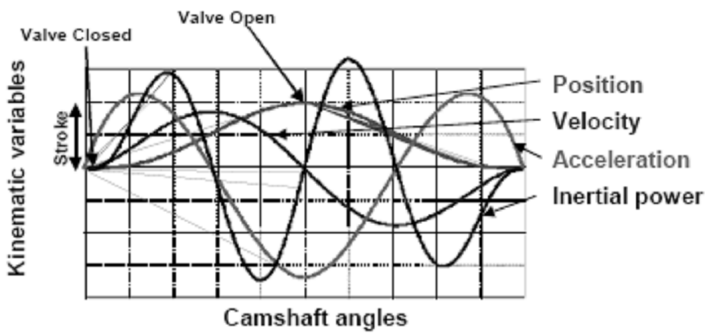

Figure 1.11 Conventional Valve Train Profiles

The valve stroke is defined as the displacement of the valve from fully-open to fully-closed positions. Valve transition time is defined as the time taken for the valve to go from one end of its stroke to the other. The inertial power profile shown in Figure 1.11 is obtained as the product of inertial force and valve velocity, and has an instantaneous peak value on the order of 2–3kW for each valve in a typical engine. The average power losses associated with driving the engine valves is approximately 3kW for 16 valves in a 2:0L, 4 cylinder engine at 6000rpm engine speed and wide open throttle.

Although the valve inertial power is very large, it is also regenerative – after an initial input of inertial power, this inertial power is regenerated continuously. The system use springs to store the initial required energy and then the energy is transferred cyclically to the engine valve and cam. In order to be a competitive technology, any variable valve actuation system must use this large inertial power in an economical way [11].

One of the main problems is the seating velocity of the valve, which has to be small (less than 3 cm/s at 600 rpm engine speed, and less than 30 cm/s at 6000 rpm engine speed) to assure a soft landing of the valve to prevent excessive wear of engine valves and acoustical noise.

Most electromagnetically-driven VVT systems utilize one of the main characteristics of conventional IC valve profiles – the regenerative inertial power. The core of these actuators is the valve-spring system, where an engine valve is coupled to two springs as shown in Figure 1.12. The equilibrium position for this mass-spring system is in the middle of the valve stroke. Such a system has an inherent natural frequency (ω_n), mass (m), effective spring constant (k), and damping ratio (ξ). Assuming there was no damping, an initial displacement of the valve in the direction of either spring would result in sustained oscillations of the valve at the system's natural frequency $\omega n = \sqrt{\frac{k}{m}}$.

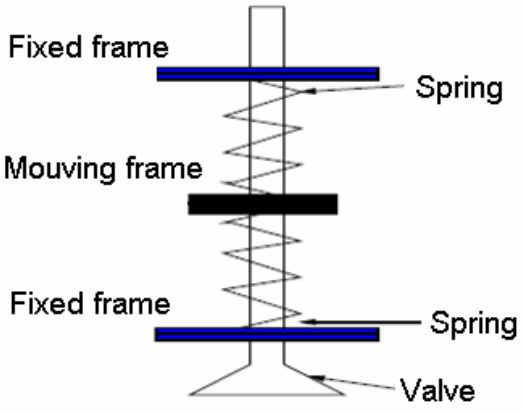

Figure 1.12 Valve-spring system

In frictionless case the electromechanical actuator for the valve-spring system only has to be able to hold the valve at either end of its stroke. In reality, due to gas forces in the engine, especially on the exhaust valves, additional work is required to reject the gas force disturbance.

Figure 1.13 shows a normal-force actuated valve-spring system [11]. Each electromagnet exerts a unidirectional normal force, and thus, the system employs two normal force actuators. The force exerted by these actuators is proportional to the square of the current input, but decreases as a function of the air gap between the actuator and the armature. Hence, these actuators have a nonuniform force constant. For a fixed level of current, the solenoids exert large forces when the valve is at their end of the stroke, but small forces when the valve is at the far end of the stroke.

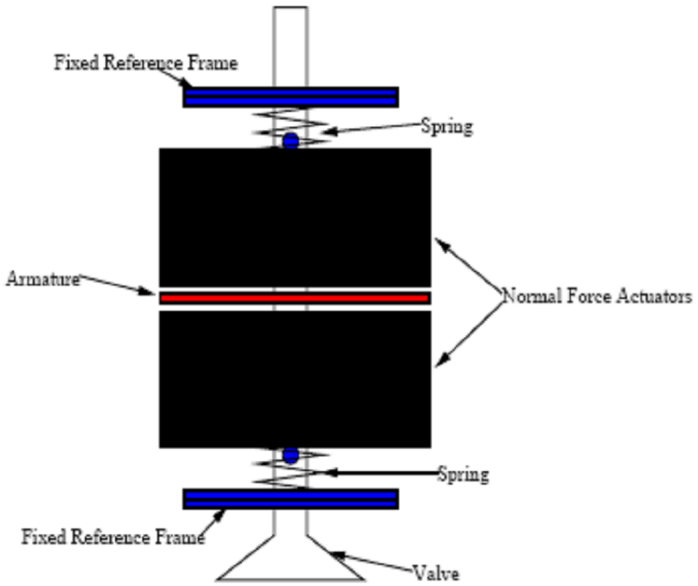

Figure 1.13 Normal force actuated valve spring system

In [9] Professor John Kassakian proposes an EMVD incorporating a nonlinear mechanical transformer. This EMVD comprises an electric motor that is coupled to a valve spring system with a nonlinear mechanical transformer (NTF). Figure 1.14 shows a schematic of this EMVD and Figure 1.15 shows a desirable nonlinear mechanical transformer characteristic between the z and μ domains.

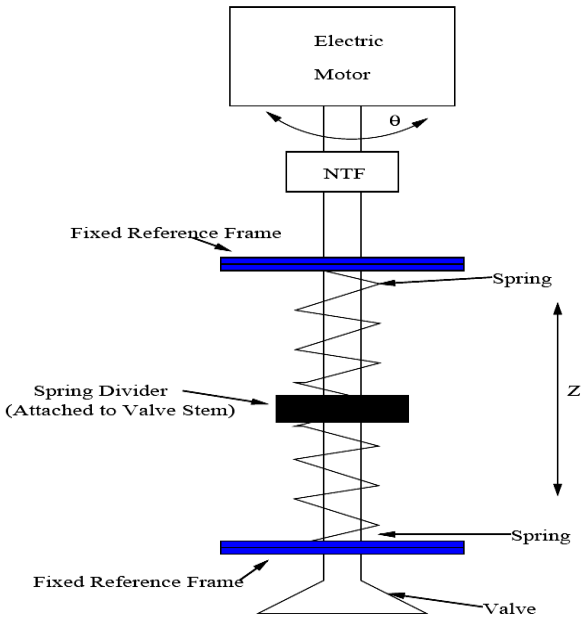

Figure 1.14 Proposed Electromagnetic Magnetic Valve Drive [9]

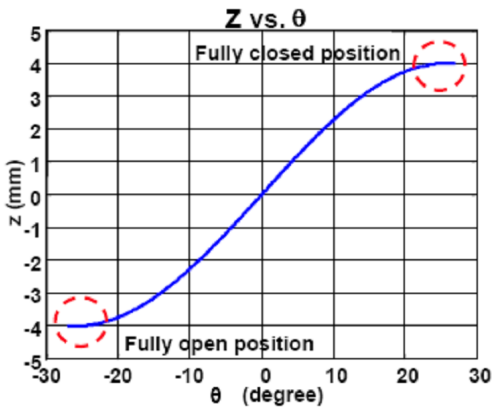

Figure 1.15 Characteristic of the Nonlinear Transformer

In the proposed EMVD, the electric motor acts as a uniform force constant actuator, giving an excellent control handle over valve position in the z domain. Using well-known active control techniques, small seating velocities, small position and velocity errors, and smooth kinematics variables can be achieved. In addition, the characteristic of the NTF can be designed such that the holding and driving currents in the system are reduced.

At either end of the stroke, the slope of the NTF characteristic is very small. Thus, the reflected motor inertia in the z domain is very large, creating inherently smooth valve kinematics profiles, since the valve is slowed down by the large effective inertia when it is opened and closed. Moreover, the large spring force at the ends of the stroke when reflected to the θ domain is small, allowing the use of small motor currents to hold the valve open or closed. In effect, the NTF enables the use of small holding and driving currents when actuating the valve. In addition, because the gas force on the exhaust valve is largest at the opening end of the exhaust stroke, the reflected gas force in the θ domain is also small.

The dynamic characteristics of the proposed EMVD change along the valve stroke. At the ends of the stroke, the effective inertia in the z domain is large, while at the midpoint of the stroke, this effective inertia is small. Thus, in the z domain, the effective system gain of the valve-spring system decreases at the ends of the stroke and increases at the midpoint of the stroke.

The experimental apparatus is shown in Figure 1.16.

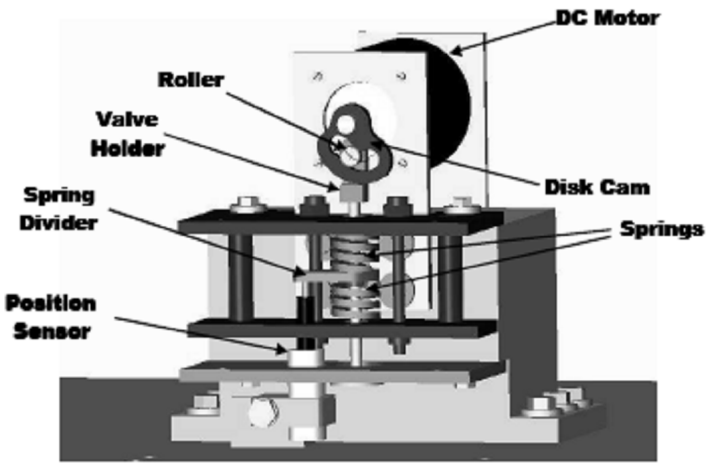

Figure 1.16 A cross section of the experimental apparatus

The block diagram of the feedback-controlled EMVD apparatus is shown in Figure 1.17. The reference input is the desired valve position, and the system output is the actual valve position. The difference between the two is passed into a controller which provides an appropriate current input to a motor drive. This motor drive supplies the desired current to the motor.

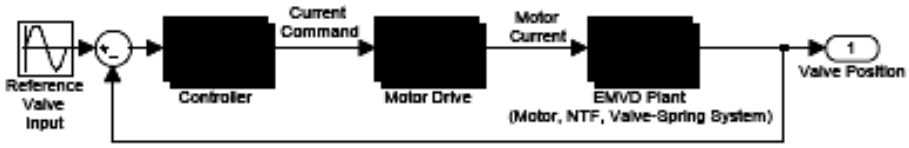

Figure 1.17 The EMVD as a Feedback Control System

A controller that is modeled in MATLAB's Simulink software on the PC and implemented on the dSPACE board, provides a control input to the motor drive circuit via a DAC channel. This control input is calculated using the measured displacement and the displacement command function. A current-control input was selected for feedback controlled EMVD system. Hysteresis current control keeps the actual motor current within a certain hysteresis band of the desired motor current by switching on opposite pairs (a high-side MOSFET on one side of the bridge and a lowside MOSFET on the other side of the bridge) of MOSFETs in the bridge. This control method features a simple control loop, fast response time and well-defined ripple current.

The author needed a motor with low inductance (100uH) and low resistance (1Ω) in order to make it easier to meet the slew rate requirement on the motor drive. The motor was also chosen because it is able to respond with enough torque up to frequencies of 150Hz.

1.6 Linear electromagnetic valve actuator – Literature Survey

The vast majority of the systems used to provide VVT comprise a linear motor. We can find in literature polarized linear actuators and unpolarized linear actuators. In the case of polarized actuators the PMs flux can be added in series or in parallel with the flux created by the coils. In a series polarized actuator the flux of the coils crosses the magnet so the possibility of demagnetization is present. However, the presence of PMs leads to a relatively linear force variation for small air-gaps, allowing for a good control of the landing of the moving part. Also the PMs flux can be used to optimize the overall power consumption [12, 13]. We find in literature single-step actuators, where the pole pitch equals the actuator total stroke, and multi–step actuators. One can find in [14] a brief examination of several electromagnetic actuators and an evaluation of their viability for the specified application.

Next we will examine some of the topologies found in literature in order to see how they produce the needed mechanical force, what are the rated powers, how they manage the mechanical energy produced, and how their control looks like.

In a conventional linear valve actuator the moving part is attracted by the two electromagnets. The stroke is relatively high, about 8 mm. The fast motion is obtained by the two springs. The neutral position is in the middle, and the two electromagnets mainly operate by holding the moving part at the two ends of the stroke. Because the forces they produce are proportional to the inverse square value of the airgap for a given current, the control of the landing is difficult. Moreover maintaining the low and high position needs permanent electric consumption. To solve these problems, polarised actuators can be used [15, 16].

By adding the flux of permanent magnet to the flux created by the coils, it is possible to obtain permanent attraction forces and linear behavior for small airgap. In the actuator shown in Figure 1.18 the flux created by the magnets is in series with the flux created by the coils [16].

It owns many advantages:

- at the high and low position, the permanent magnet flux creates an attraction force which can maintain the moving part without current consumption
- the force variation is relatively linear for small airgap, allowing a best control of the landing of the moving part.

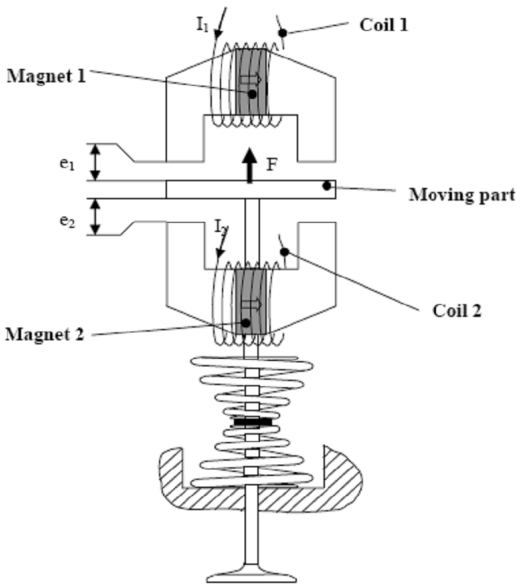

Figure 1.18 Polarized valve actuator. The magnet flux is in series with the flux coil

For the coil the magnet thickness is an additional airgap and must be as reduced as possible. The magnet must create an important induction, but it can be submitted to high inversed magnetic field created by the coil. For such a configuration, Rare Earth magnets are well adapted.

The expression of the force developed by the polarized system show that the polarized actuator has a linear response as a function of the current I, and consequently can be more easily controlled, Figure 1.19.

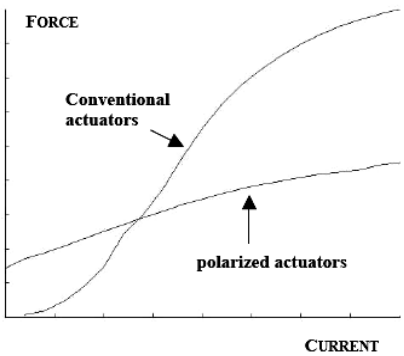

Figure 1.19 Comparison between non polarized and series polarized actuator: the force measurement as function of the current for a given airgap.

Another linear actuator solution for valve actuation is presented in Figure 1.20. [17]

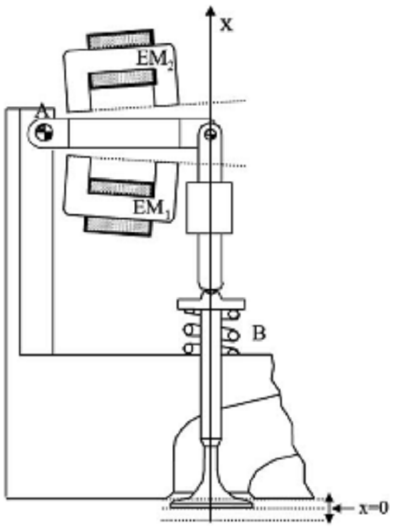

Figure 1.20 Valve sketch

In [17] a control system architecture is presented. It is shown that a position tracking controller is needed: a key point is the design of the reference trajectory to be tracked. Actuator physical limitations strongly influence the feasible trajectory when low valve seating velocity is required, thus affecting valve transition time. Owing to the same limitations, valve electromagnets have to be energized for a significant part of the trajectory, thus allowing valve position reconstruction starting from electrical measurements only. A method for position reconstruction is presented, which makes use of auxiliary coils to reconstruct electromagnets fluxes; it is shown via sensitivity analysis that the functional characteristics of position reconstruction and its accuracy are compatible with the required applications. The trajectory design is then addressed as an optimization problem that explicitly considers the tradeoff between fast dynamic performance and system robustness.

In Figure 1.20 is presented the considered actuator (variable reluctance) which is composed of a mobile mechanical part (valve, levers), a spring B counteracted by a torsion bar A, two mechanical stops and two electromagnets, each developing a unidirectional force needed to move the valve along the vertical axis x. Electromagnet EM2 is used to close the valve and electromagnet EM1 to open it. Torsion bar A delivers a force in the negative direction, and spring B gives force in the opposite direction. The spring/torsion bar system is preloaded to an

amount such that when no other forces are present, the valve is in the center of its stroke.

The mathematical model of the system is:

$$\ddot{x} = \frac{1}{M}\left(-kx - b\dot{x} - \frac{1}{2}\frac{\partial R_1}{\partial x}\Phi_1^2 - \frac{1}{2}\frac{\partial R_2}{\partial x}\Phi_2^2\right) \tag{1.1}$$

$$\dot{\varphi}_1 = \frac{1}{N}(v_1 - r_1 i_1) \rightarrow Ni_1 = R_1(x)\varphi_1 + F_1(\varphi_1) \tag{1.2}$$

$$\dot{\varphi}_2 = \frac{1}{N}(v_2 - r_2 i_2) \rightarrow Ni_2 = R_2(x)\varphi_2 + F_2(\varphi_2) \tag{1.3}$$

Where: x – the valve position, M – valve mass, k – spring constant, b – friction coefficient, $R_{1,2}$ – the reluctance functions, $\varphi_{1,2}$ – the two electromagnet's fluxes, $Ni_{1,2}$ – the magnetomotive force (MMF), $F_{1,2}$ - MMF drop in the iron portion of the magnetic flux path (Figure 1.20), $v_{1,2}$ – two electromagnet's voltages, $r_{1,2}$ – the coil's resistances, $i_{1,2}$ – currents through coils.

The magnetomotive force in iron is illustrated in Figure 1.21.

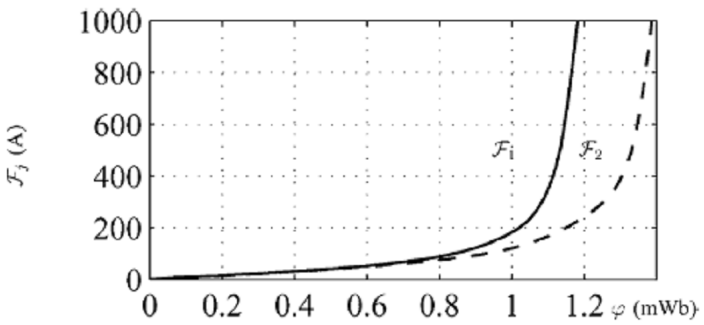

Figure 1.21 Magnetomotive force in iron

The simplified mathematical model of the variable reluctance actuator is obtained under the following hypotheses:

- magnetic hysteresis and Focault currents are negligible. This is reasonable, since laminated electromagnets with low magnetic hysteresis characteristics are used.

- the magnetic circuits of the two electromagnets are decoupled. Although they share a common flux path in the lever, the assumption is justified since the two electromagnets will be alternatively operated during normal operating mode.

The goal of the control system is to move the valve from the fully closed to the fully open position (and vice-versa) avoiding noisy and wearing hits against the hard mechanical stops. Since the positions of the mechanical stops are uncertain, this "soft-landing" behavior can only be achieved by controlling the speed of the valve when it is approaching the mechanical stops. In this case a position tracking control along a reference trajectory is needed, which has to be suitably designed. Closed-loop position control is, therefore, needed when approaching the landing position, but when the valve is in the central part of the transition (high air gap with respect to both magnets) closed-loop control is not necessary. Forces supplied by the magnets in these control positions are not significant due to small values of reluctance variation. Very high currents should be imposed to increase these forces, leading to magnetic saturation [17].

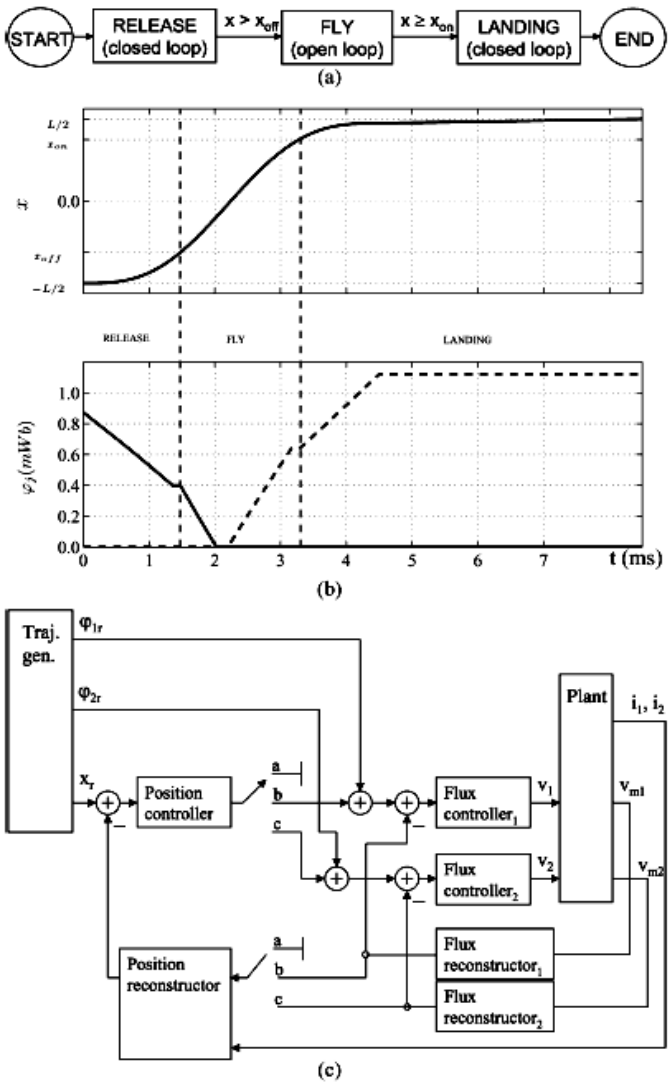

Figure 1.22 (a) Valve transition diagram during valve motion (closing). (b) Closing trajectory: position and flux trajectories, with the related control states. (c) Control scheme.

Referring to Figure 1.22, the control first enters RELEASE state. When in this state, closed loop position control is needed to prevent unpredictable valve movement due to instability. EM1 is the active actuator [switches at position "b" in Figure 1.22 (c)]. When the valve distance from the releasing magnet is greater than a fixed threshold xoff (central region of the transition), control enters FLY state where open-loop position control is applied [switches at position "a" in Figure 1.22

(c)]. The releasing magnet EM1 is switched off, while the catching magnet EM2 will be switched on at time defined by the reference trajectory design. From time T1 up to the exit from the FLY state (x>xon), closed-loop flux control on the catching magnet is used, in order to guarantee that the system enters LANDING state with a proper flux level. Here closed loop position control is activated [switches at position "c" in Figure 1.22 (c)] on the magnet EM2 until the mechanical stop is reached [17].

The flux and position measurements during the RELEASE and the LANDING states are needed in the controller.

In [18] it is presented an extremum seeking controller designed to reduce the magnitude of valve impacts. Based on a measure of the sound intensity at impact, the controller tunes a nonlinear feedback to achieve impact velocities of less than 0.1 m/s while maintaining transition times of less than 4.0 ms. The control strategy is implemented with an eddy current sensor, to measure the valve position, and a microphone. The valve actuator is presented in Figure 1.23.

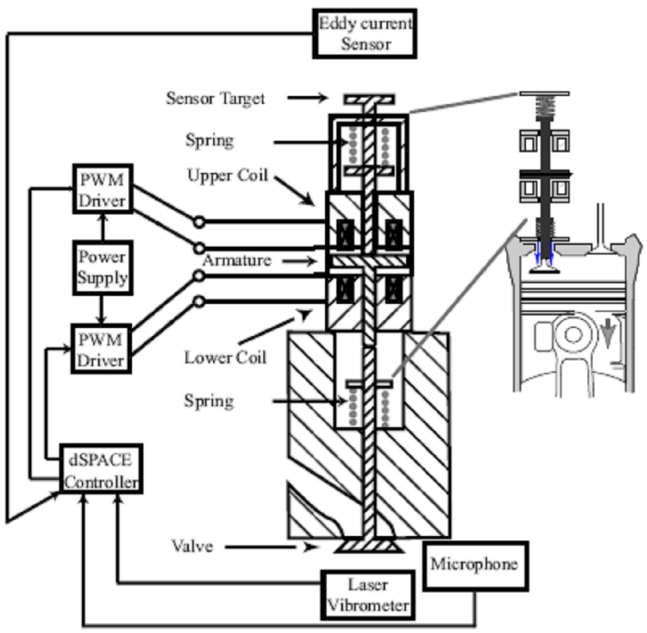

Figure 1.23 Electromechanical valve actuator and experimental setup [18]

Valve motion is controlled via the voltage applied to the upper and lower magnetic coils as follows. Initially the armature is held against the upper magnetic coil causing the valve to rest in the closed position, creating an imbalance in the net spring force acting on the armature. When the voltage applied to the upper magnetic coil is reduced to zero, the potential energy in the springs drives the

armature across the gap. A catching voltage is then applied to the lower magnetic coil to capture and hold the armature, thus opening the valve. The reverse process is used to close the valve.

Minimizing wear and noise, while allowing for operation at high engine speeds, requires that: - the impact velocity between the armature and magnetic coil be less than 0.1 m/s. (in the case of multiple impacts, the impact velocity is taken to be the largest one), and - the transition time, from when the valve is 98% open/closed to 98% closed/open, be less than 4.0 ms. Achieving these requirements is referred to as "soft landing".

The seeking controller adjusts a nonlinear feedback from cycle to cycle to reduce the impact velocity. A small microphone obtains a measure of the sound intensity which the controller then minimizes. The reduced sound intensity results in decreased impact velocities. The advantage of the extremum seeking controller is that it does not require a model of the system dynamics and its computational load is minimal.

The controller is implemented as follows: The displacement of the armature is determined by the eddy current sensor which detects changes in a magnetic field, generated by the sensor, caused by the motion of the sensor target attached to the rear of the armature. Based on the encoded nonlinear feedback and the measured displacement the dSpace processing board regulates the duty cycle of the PWM amplifiers to control the armature motion during a valve closing/opening event. The switching frequency of the PWM amplifiers is sufficiently fast that they assume that the active voltage applied to the actuator is the duty cycle command multiplied by the supply voltage (180 V). At the end of each valve closing/opening event a microphone is used to obtain a measure of the sound intensity of the impact. The extremum seeking controller then uses this measurement to tune the nonlinear feedback before the next valve closing/opening event to reduce the impact velocity. The experimental results are obtained using the laser vibrometer, which is capable of measuring both the position and velocity very accurately. The measurements obtained from the laser vibrometer are only used to determine the effectiveness of the controller and are not used in the feedback.

Next we will consider some feedback issues. At the beginning of the armature travel the magnetic force generated by the catching coil has very little influence on the armature. During this period it is undesirable to apply large voltage inputs to the system to control the armature motion. Doing so would not only increase power consumption, but large currents generated early in the transition may result in high impact velocities. A more practical solution is to let the potential energy stored in the springs do the work of moving the armature across the gap. However, if voltage is not applied until the armature is near the catching coil, it is difficult to generate the necessary current to capture the armature due to the back-

BUPT

EMF which becomes significant near the magnetic coil. Both of these phenomena are captured in the system model. The magnetic force is inversely proportional to the square of the distance. Thus, at large distances the magnetic force is much less than the spring force and has little influence on the armature motion [18].

Small voltages should be applied while the armature is far from the magnetic coil and large voltages when the armature is near the magnetic coil. This methodology is the opposite of linear feedback, where the input is proportional to the error, Figure 1.24.

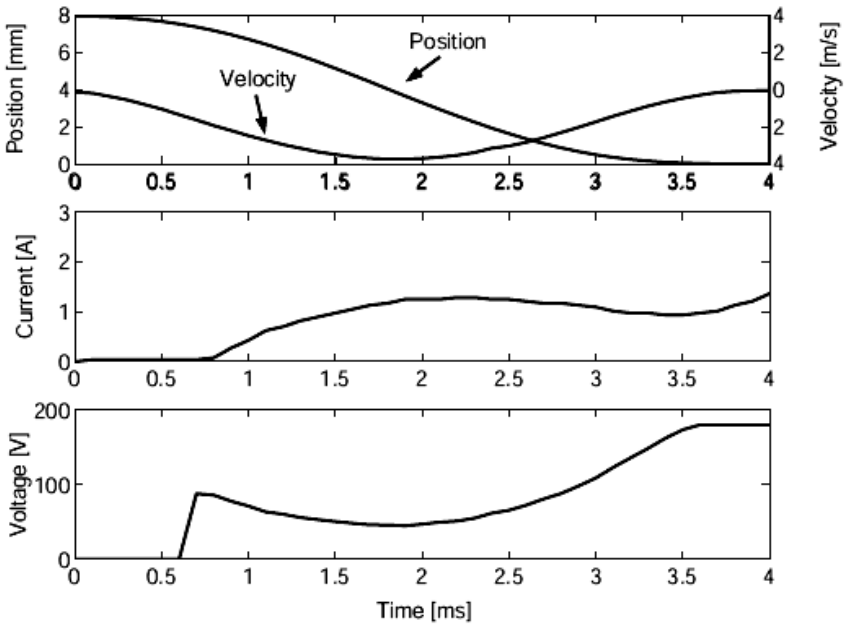

Figure 1.24 Experimental results using nonlinear controller

We can see from Figure 1.24 that the feedback is only applied after the first millimeter of travel to ensure that the armature has been released before control is applied.

The temperature, humidity, and other environmental factors in the laboratory in which these experiments were conducted were not tightly controlled and are largely influenced by the outside weather. These unknown factors appear to have a small influence on the performance of the system.

For the prototype solenoid valve actuator in Figure 1.25 a lumped parameter that uses FEA results is reported in [19]. In the article is developed a finite-element analysis (FEA) model to describe transient and static operation of gas-exchange valves. The FEA model is validated by experimental testing on an actual automotive

BUPT

prototype valve. They show that a nonlinear lumped-parameter model that uses FEA results also closely matches experimental data. The lumped-parameter model is suitable for optimization of design and can be readily used for closed-loop simulation. The authors present a simplified lumped-parameter model to facilitate controller design. Finally, they compare a dynamic open-loop simulation with experimental results.

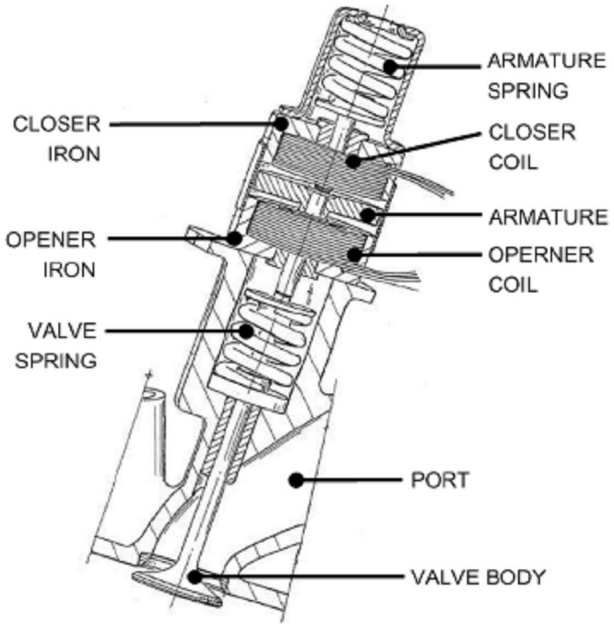

Figure 1.25 Schematic of prototype solenoid valve actuator

Active control is required to prevent excessive valve seating velocity, premature wear and acoustic emissions [20], [21]. Solenoid valve control is also a challenge due to nonlinear effects such as magnetic saturation and system uncertainties including large disturbance forces from combustion pressure and parameter variation due to temperature change and component wear.

This linear actuator is characterized by a short stroke, small air gap, and flat pole and armature geometries. The flat-face, short-stroke properties allow for faster response at larger air gaps in addition to stronger holding forces due to increased flux density.

Other configurations such as conical pole/armature interfaces produce greater fringing, resulting in a more linear force-position relationship but sacrifice force density. The electromagnets are only required for "catching" the armature at either end of the stroke as well as overcoming friction and pressure forces. The

mechanical system of the actuator can be considered as a mass-spring oscillator with an undamped natural frequency of approximately 150-200 Hz. For the steady-state force, constant current was input to the coil. To avoid overheating the coil, excitation levels were limited to 40 A. The static force results are plotted in Figure 1.26 as lines of constant magnetomotive force (MMF). This nonlinear force response is indicative of the flat pole face armature actuator type. Experimental results beyond 4 mm are not included due to load cell resolution at low loads.

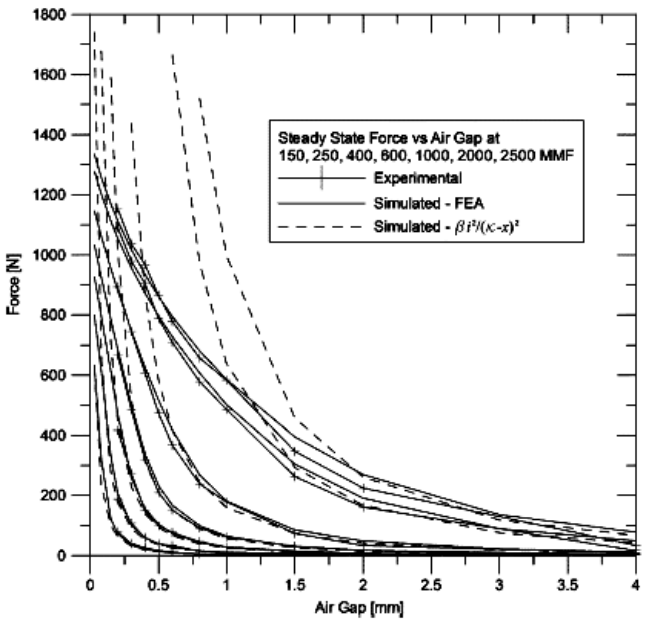

Figure 1.26 Experimental and simulated force versus air gap for various excitations.

In the dynamic simulation shown in Figure 1.27 no closed-loop control is implemented and the armature is simply released from the closer magnet and caught with the opener using a constant current command.

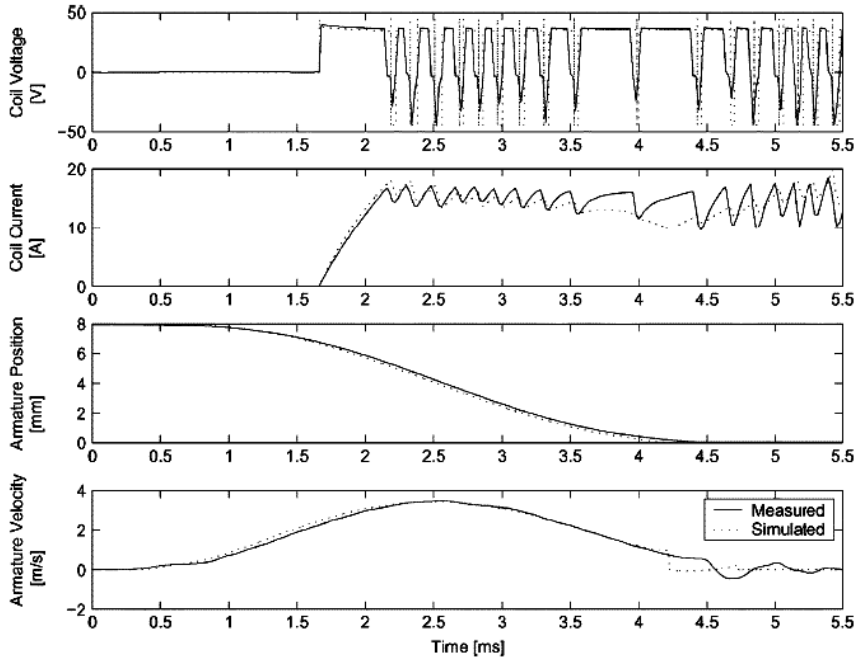

Figure 1.27 Dynamic simulation and experimental results of a opener magnet

In [22] we find a parallely polarized actuator solution. The parallel polarization seems to be an attractive solution, because the flux driven by the coils does not cross the magnet as in series polarized actuators [23]. This idea has been developed in several actuators. The one presented in Figure 1.28 has been designed by General Motors [24]. The moving part, the plunger, has two stable positions, when one of the two airgaps is null. The motion between theses two stable positions is driven by the 2 springs that try bring back in the center position.

The obtained force variation is shown on Figure 1.29. The two springs give a restoring force, which is linear as function of the displacement from the centrer position. The magnetic force without current is symmetrical. For low airgap, the magnetic attraction force is higher than the spring force to obtain a stable position without any current. If the mobile part is in A position, the current in the coil A is used to reduce the force exerted in this airgap to start the movement to B. When the moving part arrives near the B position, the current in coil B is driven in such a way to make the landing of the moving part as soft as possible.

For low values of the aigap, the curve of the force as a function of the distance and of the current is relatively linear. It makes the control easier in comparison with non polarized actuators.

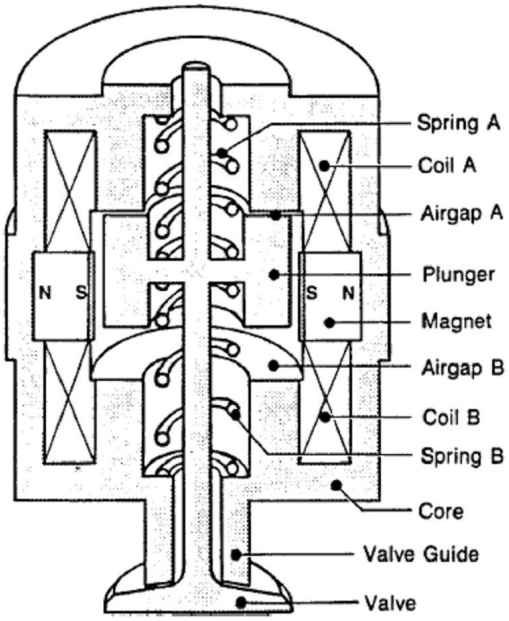

Figure 1.28 Coaxial valve actuator

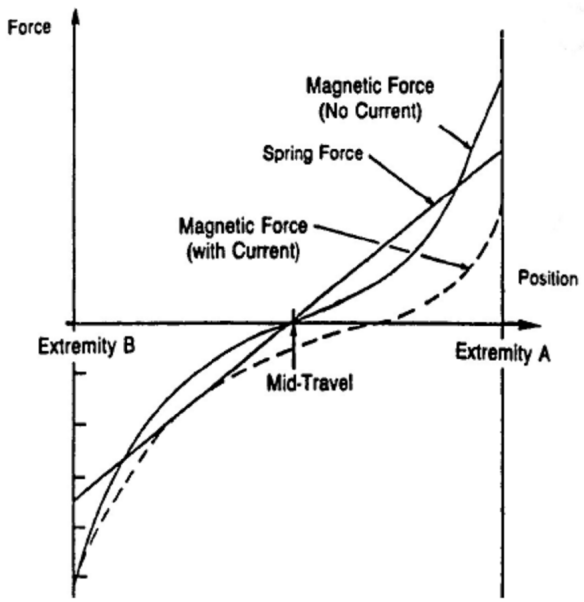

Figure 1.29 Force variation for a parallel polarization actuator

Another interesting model is presented in [25] where the proposed model allows setting up an optimum configuration of the magnetic circuit from the point of view of the power consumption. In fact, even minor variations in the geometrical configuration can result in significant variations in the numerical value of the power consumption, affecting the global vehicle power requirement.

The mechanical subsystem (Figure 1.30) - consisting of two springs, the valve, the valve stem, armatures and bolts, has been modeled following a scheme with lumped parameters.

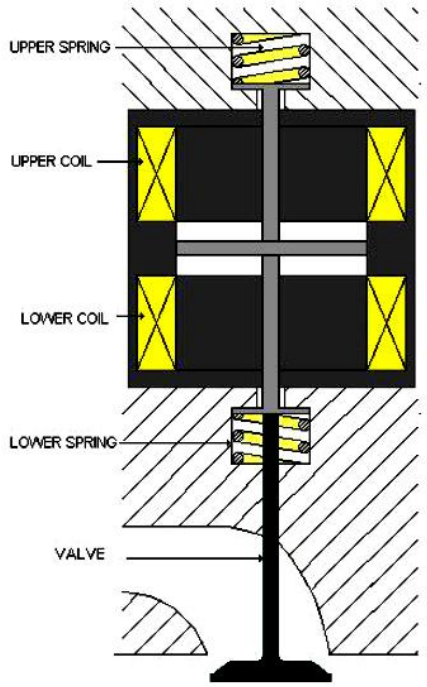

Figure 1.30 Mechanical subsystem [25]

The magnetic subsystem has been accurately modeled and simulated by means of software for the 2D FEM analysis applied to electromagnetism, developed by the Authors on purpose and previously validated. The numerical evaluation of mechanical forces due to the electromagnetic interaction can be evaluated using the Virtual Works Method (VWM) or the Maxwell Stress Tensor Method (MSTM). In the MSTM the numerical value of the electromagnetic force depends only on the flux density in the path where the Maxwell tensor is evaluated, producing large local errors. For this reason the electromagnetic force acting on the valve has been estimated using the VWM. From the value of the magnetic energy, the mechanical

BUPT

force as a function of valve position has been calculated leading to the fact that the model can be used as an alternative to steadystate experimental tests.

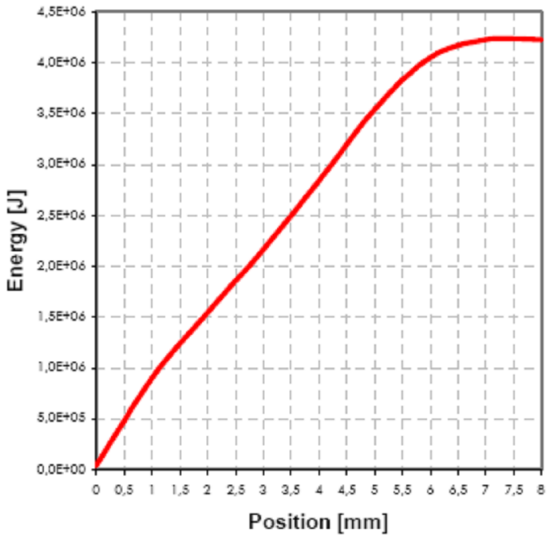

Figure 1.31 Magnetic energy vs position

The magnetic energy (Figure 1.31) has been evaluated by means of the FEM. Thanks to the symmetry of the EV, just ¼ of the structure has been analyzed. A section of the lower coil is on the left; a quarter of the armature stem is on the right; the armature stroke is represented with a number of intermediate positions.

By means of the FEM software the magnetic field has been calculated for different positions of the mobile part, keeping the coil current constant; the results have been interpolated.

Reference curves for the valve lift, velocity and acceleration have been fixed, keeping the most important dynamical aspects into account. For instance, the variation of acceleration must be limited, to avoid excessive inertial stresses, and the valve landing must not be sharp, to avoid fatigue stresses that can lead to mechanical fractures. Limit values have been drawn from the literature. The curves of the current in the upper and lower coils and of the resulting valve lift are shown in Figure 1.32. When the holding current in the upper coil goes to zero, the valve starts to open under the action of the spring. At a certain point it is catched by the lower coil, in which a current started to flow. The latter then reaches the holding value. The process is repeated in a similar way but in opposite sense for the valve closing.

BUPT

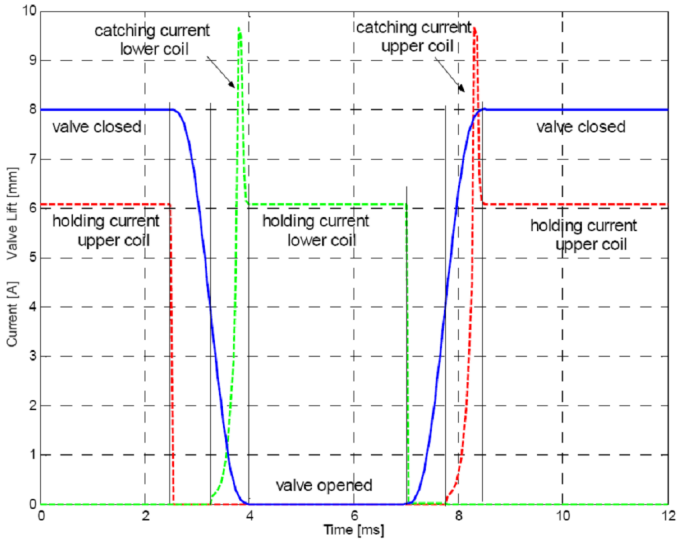

Figure 1.32 Valve lift, upper and lower coil currents vs time at 5000 rpm witk k = 75 N/mm

In [25] an analytical model has been defined, by means of a simple and robust algorithm, allowing an accurate evaluation of power consumption as a function of the geometrical configuration and some physical parameters of the system and for whatever control strategy applied to the system. Some analyses have been performed for fixed coils, varying the armature geometry to minimize the power consumption.

New types of linear actuators for a latching electromechanical valve, using permanent magnets, are proposed in [26].

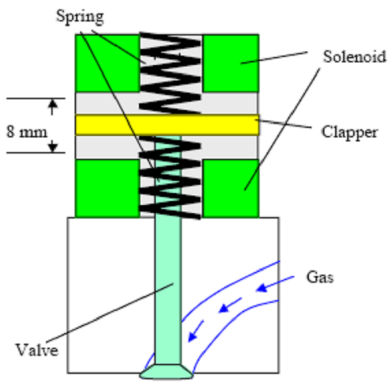

Figure 1.33 Double solenoid actuator

Those actuators overcome some of the problems that are characteristic of conventional double solenoid actuators. In order to characterize the performance of the proposed system, dynamic simulations using finite-element analyses have been made. The results show that the dynamic response of the valve system may make this design suitable for application in an internal combustion engine.

The main operating principle of proposed actuators is similar to the double solenoid type (Figure 1.33) in that the moving clapper is actuated by the net potential energy in compressed springs. However, to address the problems associated with the solenoid actuator, permanent magnets are utilized in the proposed actuators to aid in valve latching.

Valve-Control 1 has one permanent magnet for latching the clapper and Valve-Control 2 has two permanent magnets. Figure 1.34 and Figure 1.35 show the schematic diagram of Valve-Control 1 and Valve-Control 2 respectively.

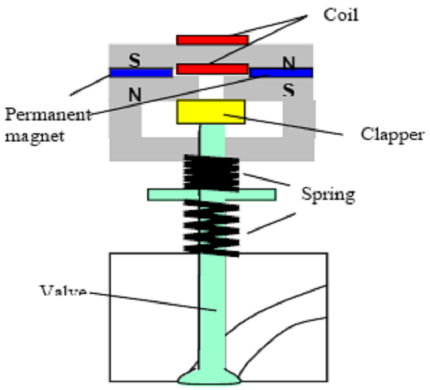

Figure 1.34 Valve control 1

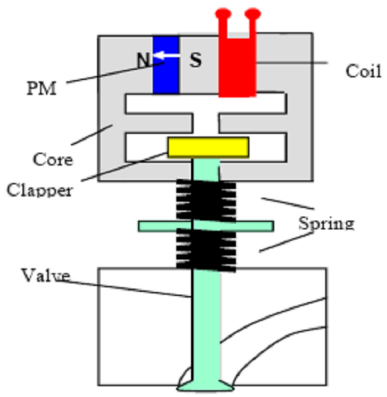

Figure 1.35 Valve control 2

These actuators are composed of permanent magnets, one electromagnetic coil, a laminated steel core and clapper, two springs and the valve body. The armature and the valve are one continuous body. As the armature moves up and down, the engine valve closes and opens. The total travel distance of clapper is 8mm. Valve-Control 1 and Valve-Control 2 have similar operating principles. At start, the permanent magnets hold the armature at the upper position, i.e. the valve is closed, because the magnetic force exceeds the spring force. To open the valve, the coil is energized. As the flux of permanent magnet is partially cancelled, the spring force exceeds the magnetic force. The armature is thus released, the valve starts opening, and is it accelerated by the stored energy in the springs. After the neutral stroke position, the coil is reverse energized, and the permanent magnet and electromagnet catch the armature at the bottom. The motion from the lower end to the upper end is the inverse operation of the steps above.

Another interesting configuration is presented in paper [27].

Similar functioning principle (use of a passive rail and permanent magnet excitation) is presented in [28] and [29]. The rail is passive and therefore the linear motor will be based on the variable reluctance principle. The cylindrical mover features two different radii for creating the teeth. The geometry is displayed in Figure 1.36. The permanent magnets are placed alternately so as to generate a switching flux.

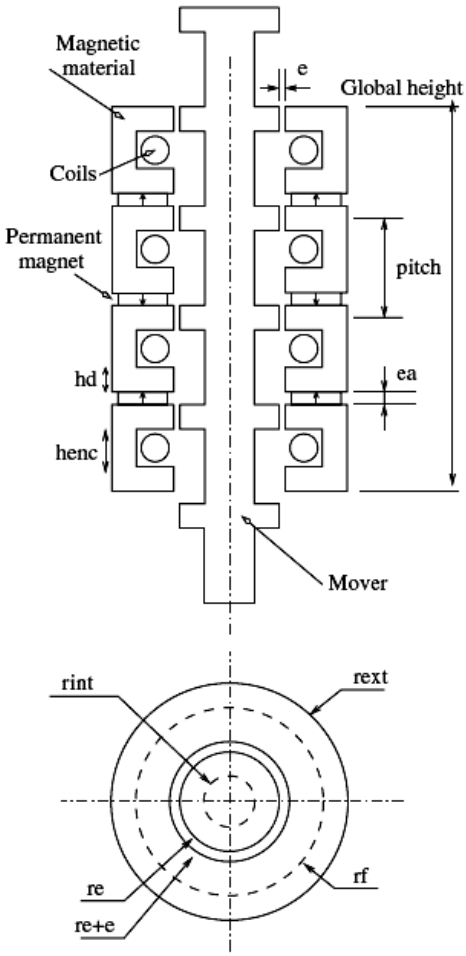

Figure 1.36 Geometry of the proposed actuator [27]

Mover displacement is limited to the pitch given that the strength is pitch-periodic. The same authors as in [27] introduce in [30] a hybrid direct drive illustrated in Figure 1.37.

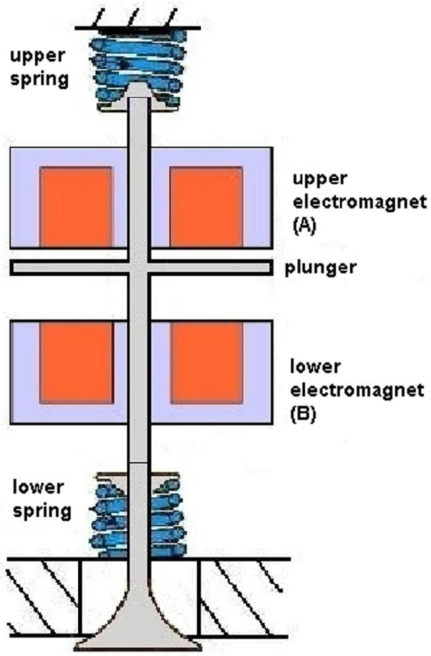

Figure 1.37 Geometry of the actuator [30]

The electromagnets are fixed, and the plunger attached to the rod, which pushes on the valve, moves between the two extreme positions. Depending on the plunger position, the springs are more or less compressed, and the neutral position is in the middle of the air gap. This structure is called unpolarised because there is no permanent magnet. Some features of this solution are: - the permanent position of the plunger is in the middle of the air gap without power supply, - in order to start, a little period of oscillation of the plunger is necessary: the springs start resonating thanks to the electromagnets, and the plunger is then stuck to the desired electromagnet. The oscillations are indispensable because of the small force of the electromagnet when the plunger is in the middle of the air gap. A drawback of the topology is that in order to stop the plunger in an extreme position, it is necessary to supply the electromagnet corresponding, in order to create a force opposing to the spring's force. When the supply is turned off, the springs push on the plunger and move the rod, and then the valve.

There are other several drawbacks with this structure. The start, with the resonance of the springs, the system needs a specific command.. As another drawback is that this solution is too noisy, because of the impact velocity, which is too important and hard to control.

The profile of the currents injected in the upper and lower coils is given by Figure 1.38.

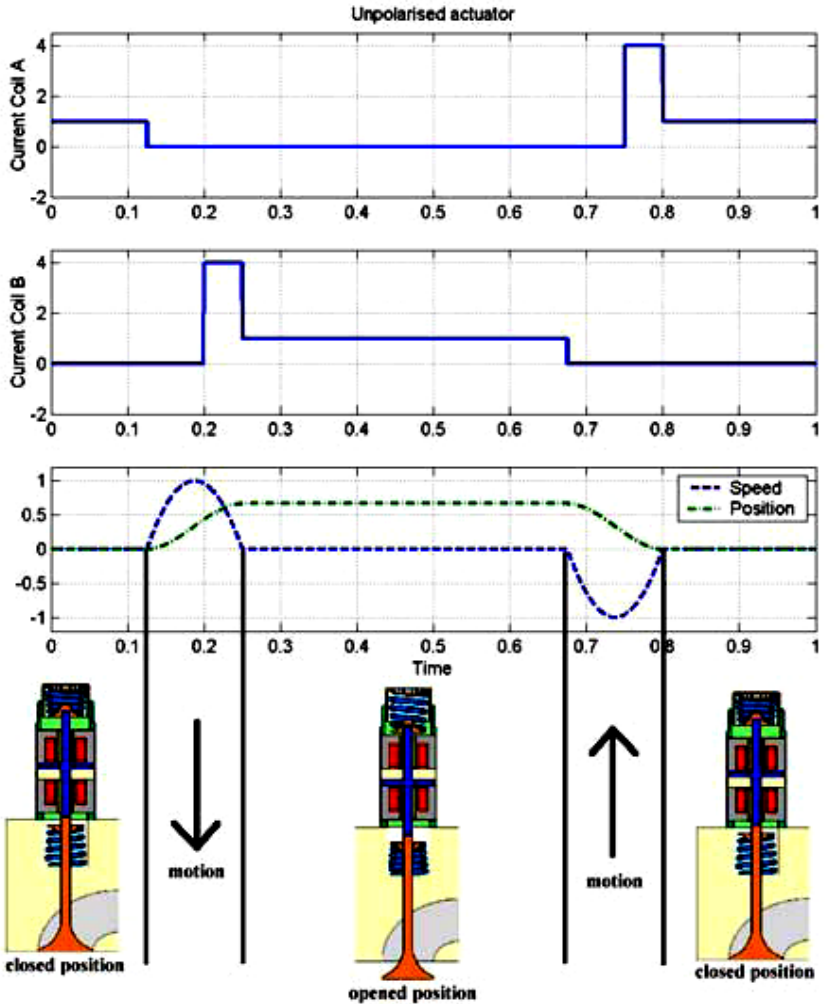

Figure 1.38 Profiles of the currents in the coils, position and speed profiles for the unpolarised actuator

Due to those elementary drawbacks that the actuator must satisfy another structure is described in this paper [30]. The structure is the same as the basic one, but with two permanent magnets (Figure 1.39, [31] and [32]).

The addition of PMs leads to new command strategies. The PMs help to lock the plunger in the extreme position only with the force of the magnets. The plunger is then released by negative current injection in the coil, in order to opposite its flux

to the magnets one, and to decrease the resultant magnetic force. The potential energy stored in the springs moves the plunger. The main advantage of this strategy is that there is no current consumption in locked position, as no current is injected to oppose to the springs force.

The main drawback of the addition of the magnets is that they add an air gap, which reduces the magnetic force developed by the coils. On the other hand, this new air gap decreases the global inductance, so the current variation in the coils may be faster for the control.

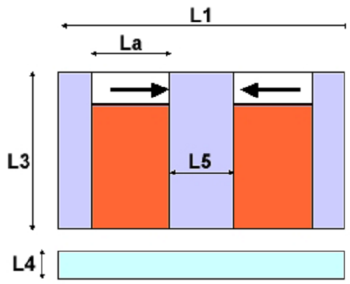

Figure 1.39 Polarized actuator

The profile of the currents injected in the upper and lower coils is illustrated by Figure 1.40.

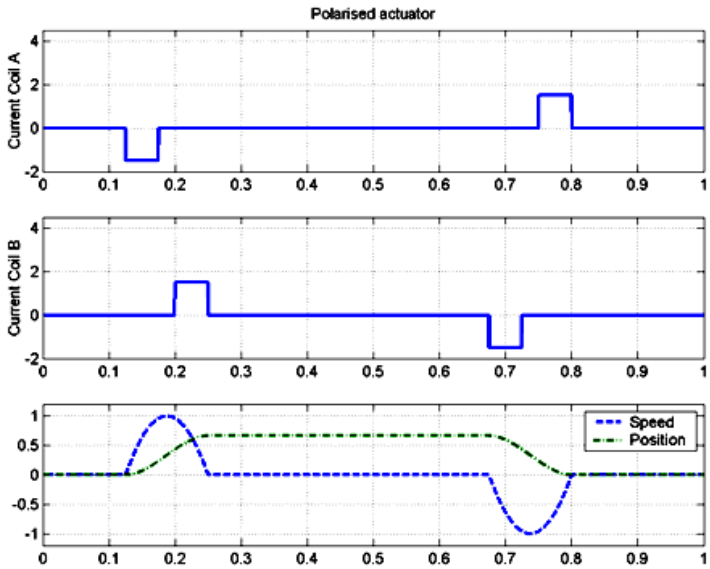

Figure 1.40 Profiles for the polarized actuator

1.7 Linear resonance compressors

In this section will be presented another major application of the proposed linear interior permanent magnet actuator: the linear resonance compressors.

Free-pistons compressors use a linear motor to move a reciprocating piston back and forth in its cylinder. This type of compressors avoids the use of crankshafts, connecting rods and bearings, but has a major drawback, the necessity to provide a long stroke sliding seal between the piston and the cylinder [33].

The main advantage of such a compressor is the possibility to connect directly the moving part of the motor with the compressor's piston. Some principles of such motor-compressor are presented in [34]. As mentioned above the lack of any mechanical transformer leads to an increased efficiency of the drive, while dimensions and costs are decreased.

This type of compressor with oscillating motor is topical for small compressors (up to 1kW) utilized in household refrigerating devices. LG Electronics, Electrolux and Embraco manufacture these type of refrigerators today.

Diaphragm compressors use a simple flexible membrane instead of an intake element. In this case, only the membrane and the compressor box come in touch with the pumped gas, thereby it is best suited for applications where toxic and explosive gases need to be pumped. The membrane has to be reliable in order to support the strain of pumped gases. Also it must resist to high temperature values.

Various topologies of such linear compressors or oscillating motor-compressors are available in literature.

In [35] a tubular oscillating permanent magnet actuator modeling and analysis are performed. An improved analytical model is proposed for a single-phase tubular Linear Oscillatory Actuator (LOA) that has PMs on its mover. The magnets are displaced in a quasi-Halbach pattern. By using an axially magnetized magnet as a flux return path for the adjacent radially magnetized magnets, the mover back-iron can be removed, reducing this way the moving mass and therefore the spring stiffness, without excessively compromising the overall performance.

In [36] oscillating synchronous motors are presented for compressor drives. Two types of oscillating synchronous motors are distinguish for this application: the excited motor (that uses PMs) and pulsating current motors.

In Figure 1.41 an oscillating linear synchronous excited motor in a drive of double-sided piston compressor is shown.

Variants of this type of motors with PMs are presented. The magnets can be placed in the motor's stator (see Figure 1.42) as well as in the mover (Figure 1.43), without changing the principle the motor's performance.

BUPT

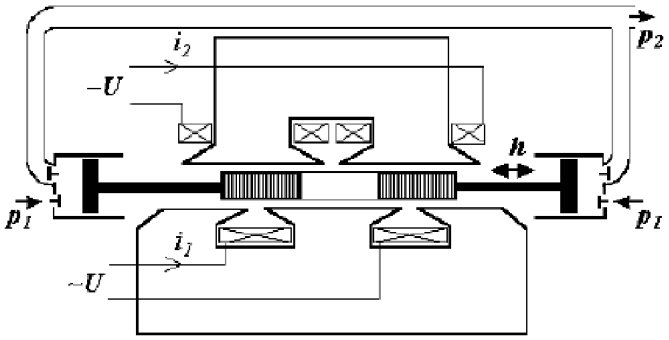

Figure 1.41 Oscillating linear synchronous excited motor

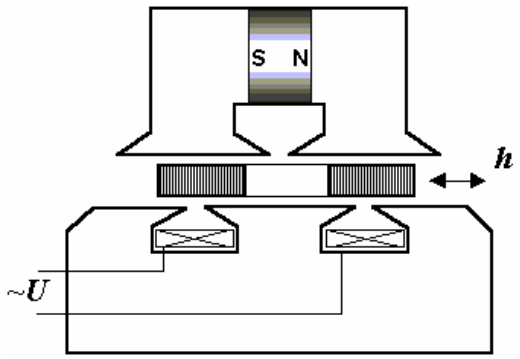

Figure 1.42 Oscillating synchronous excited motor with PMs in the stator

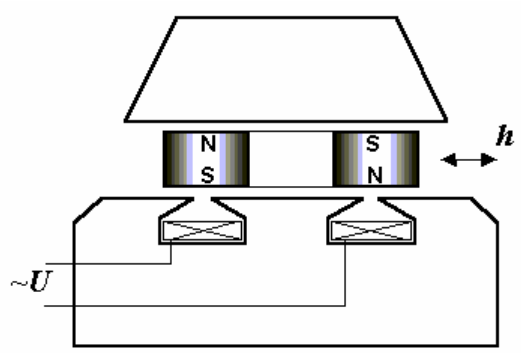

Figure 1.43 Oscillating synchronous excited motor with PMs in the rotor

In Figure 1.44 is illustrated the simplest asymmetric pulsating current motor in a single side compressor drive. The presence of the mechanical spring is mandatory and well known.

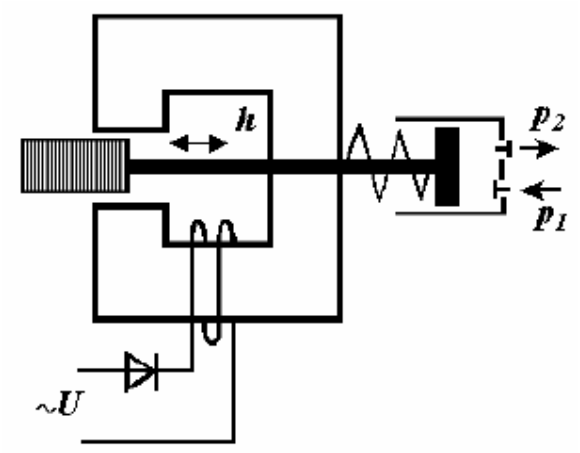

Figure 1.44 Asymmetric oscillating synchronous pulsating current motor

A symmetric pulsating current motor topology is shown in Figure 1.45.

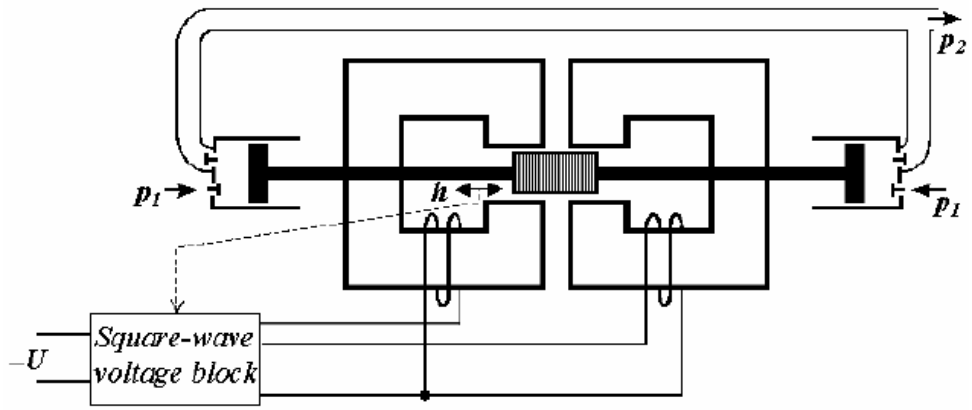

Figure 1.45 Symmetric oscillating synchronous pulsating current motor

These types of motors are generally driven by a variable pulse width voltage waveform both in amplitude and frequency.

BUPT

SUMMARY

In this chapter an overview of the main applications of our purposed actuator have been presented. Automotive Electrification trends have been introduced in order to include the purposed actuator in the process. In what concerns the actuator's automotive application, a literature survey was presented both rotary and linear based actuators. Topologies of linear resonance compressors have been introduced. Fuel savings, maximum engine load increase, pollutant emissions reduction are benefits that provide a great potential of the electromagnetic valves actuators in future cars development. In addition, cost reduction in household refrigerating devices using linear motors is an important issue that manufactures will not neglect.

CHAPTER 1 REFERENCES

[1] Kassakian, J.G., „Automotive electrical systems - the power electronics market of the future", Record of Applied Power Electronics Conference and Exposition, 2000. APEC 2000. Fifteenth Annual IEEE, Vol. 1, pages: 3-9, New Orleans, LA, USA

[2] Kassakian, J.G., „The Role of Power Electronics in Future 42 V Automotive Electrical Systems", EPE Journal, Vol. 13, Part 4, pages 38-42, 2003, Germany.

[3] SAE Electronic Systems Committee, "Recommended Environmental Practices for Electronic Equipment Design," SAE Recommended Practice SAE J1211, November, 1978.

[4] A. Graf, D. Vogel, J. Gantioler, and F. Klotz, "Intelligent Power Semiconductors for Future Automotive Electrical Systems," Elektronik im Kraftfahrzeug, Munich, June 3-4, 1997

[5] Emilian Ceuca, „The 42 Volt power net arhitecture standards", ACTA Journal, Vol. 2, 2001, Alba Iulia, Romania

[6] D. J. Perreault and V. Caliskan, "A New Design for Automotive Alternators," SAE Paper 2000-01-C084, IEEE-SAE International Conference on Transportation Electronics (Convergence), Dearborn, MI, USA, October, 2000.

[7] Streetracersonline – „Camshafts and Valve Train Basics", Article by Abdul Rehman, July 2004, UK - http://www.streetracersonline.com/articles/camshafts/

[8] Marcello Montanari, Fabio Ronchi, Carlo Rossi, IEEE, and Alberto Tonielli - "Control of a camless engine electromechanical actuator: Position

Reconstruction and Dynamic Performance Analysis" , IEEE Transactions on Industrial Electronics, Vol. 51, No. 2, APRIL 2004

[9] W. S. Changz, T. A. Parlikarz, M. D. Seemanz, D. J. Perreaulty, J. G. Kassakian, and T. A. Keimy - "A new electromagnetic valve actuator", Power Electronics in Transportation, 2002

[10] T. Ahmad, and M. A. Theobald, "A Survey of Variable-Valve-Actuation Technology," *SAE Technical Paper Series*, Paper 891674, 1989.

[11] W. S. Chang, T. A. Parlikar, J. G. Kassakian, and T. A. Keim, "An Electromechanical Valve Drive Incorporating a Nonlinear Mechanical Transformer," in *SAE World Congress*, Detroit, MI, March 2003.

[12] E. Sedda, C. Fageon, J.P. Yonnet, „Permanent magnet actuators for electromagnetic automotive applications ", LDIA 2003, 8-10 September 2003, Birmingram, UK

[13] S. Guerin, E. Sedda, C. Faegon, J.P. Yonnet, C. Chillet, „An original configuration of linear actuator with parallel polarization", LDIA 2003, 8-10 September 2003, Birmingram,UK

[14] C. Bernez, X. Mininger, H. Ben Ahmed, M. Gabsi, M. Lecrivain, E. Gimet, E.Sedda, "High-acceleration linear drives: Application to electromagnetic valves", International Journal of Electrical Engineering in Transportation, vol. 1, no. 1, 2005, pp. 27-40

[15] S. Guerin, E. Sedda, P. Yonnet, C. Chillet, "An original configuration of linear actuator with parallel polarizarion", Proceedings of the 4th International Symposium on LDIA2003, pp. 557-559

[16] Jean-Paul Yonne, Christophe Fageon, Christophe Baldi, „Linear or Rocking Actuators for Camless Systems?", International Journal of Electrical Engineering in Transportation, vol. 1, No. 2, 2005

[17] M. Montanari, F. Ronchi, C. Rossi, A. Tonielli, "Control of a camless engine electromechanical actuator: Position Reconstruction and Dynamic Performance Analysis", IEEE TIE vol. 51, no. 2, April 2004, pp 299-311.

[18] PETERSON Katherine S, STEFANOPOULOU Anna G, „Extremum seeking control for soft landing of an electromechanical valve actuator", Automatica Journal, Vol. 40, no. 6, pp. 1063-1069, 2005, USA

[19] Ryan R. Chladny, Charles Robert Koch and Alan F. Lynch, "Modeling Automotive Gas-Exchange Solenoid Valve Actuators", IEEE Transaction on Magnetics, Vol. 41, No. 3, pp. 1155-1162, March 2005

[20] Y. Wang, "Camless engine valvetrain: Enabling technology and control techniques," Ph.D. thesis, Univ. California, Santa Barbara, 2001.

[21] J. Savage and J. Matterazzo, "Application of design of experiments to determine the leading contributors to engine valvetrain noise," presented at the SAE 1993 World Congr., Paper 930884.

[22] S. Guerin, E. Sedda, C. Fageon, J.-P. Yonnet, and C. Chillet, An Original Configuration of Linear Actuator with Parallel Polarization, Proceedings of the Fourth International Symposium Linear Drives for Industry, Birmingham, September 2003 (University of Sheffield, Sheffield, UK, 2004), pp. 557–559.

[23] E. Sedda, C. Fageon, and J.-P. Yonnet, Permanent Magnet Actuators for Electromagnetic Valve in Automotive Applications, Proceedings of the Fourth International Symposium Linear Drives for Industry, Birmingham, September 2003 (University of Sheffield, Sheffield, UK, 2004), pp. 545–548.

[24] B. Lequesne, "Fast acting, long stroke solenoids with two springs", IEEE Trans on Indus Appl, vol 26, n°5, sept-oct 1990, p 848-856

[25] "Dynamic Analysis of Electromechanical Valve Actuators by means of FEM Techniques", Ch. Boccaletti, P. Di Felice, E. Santini, ICEM 2004

[26] Kim, J., Lieu, D. K., 2005, "Designs for New, Quick-Response, Latching Electromagnetic Valve," Proceeding of International Electric Machines and Drives Conference 2005, pp. 1773~1779, 2005.

[27] C. Bernez, M. Gabsi, H. Ben Ahmed, M. Lecrivain and E. Gimet - "High-acceleration linear Drives: Dimensioning and Constraints relative to electromagnetic Valves" - Laboratoire SATIE - ENS Cachan, 61, av. du Prsident Wilson, 94235 Cachan Cedex, France

[28] I. Boldea and S. Nasar, *Linear motion electromagnetic devices*, Taylor and Francis, Eds. G & B Science Pub, 2001.

[29] O. Roubicek and M. S. Pejsek, "Oscillatory synchronous linear motor with permanent-magnet excitation," *IEE*, vol. 127, January 1980.

[30] C. Bernez, X. Mininger, H. Ben Ahmed, M. Gabsi, M. Lecrivain, E. Gimet, E.Sedda - "High-acceleration linear drives: Application to electromagnetic valves", SATIE (UMR 8029 CNRS) - ENS Cachan – France - PSA Peugeot Citroën – France

[31] H. Ben Ahmed, M. Gabsi, M. Lécrivain, C. Fageon, E. Sedda: "Actionneur électromécanique de commande de soupape pour moteur à combustion interne", *Brevet Français,* déposé le 18 Février 2003 sous le n° 0301948, déposant PSA.

[32] M. Lécrivain, M. Gabsi, H. Ben Ahmed, E. Sedda, C. Fageon: "Actionneur électromécanique de commande de soupape pour moteur à combustion interne et moteur à combustion interne muni d'un tel actionneur", *Brevet Français*, déposé le 15 janvier 2004 sous le N° 04 50092, déposant groupe PSA.

[33] Ch. Lawrenson, V. Popham, R. Burr. *Linear resonance compressor driven by a variable gap-reluctance linear motor*. Proc. 16th International

BUPT

Compressor Engineering Conference at Purdue, USA, paper C23-1 (6 p.), July 2002.

[34] Kudarauskas S., Guseinoviene E., Simanyniene L.: *Analysis of the oscillating synchronous pulsating current motor and the piston compressor drive*. Proc. of International XIII Symposium on icromachines and Servodrives, Krasiczyn, Poland, September 2002, pp. 177-184.

[35] Chen, X. Zhu, Z.Q. Howe, D. *„Modeling and Analysis of a Tubular Oscillating Permanent Magnet Actuator*", Industry Applications Society Annual Meeting, 2008, IAS'08, October 2008, pp. 1-8.

[36] Guseinoviene, E. Kudarauskas, S. Senulis, A. Simanyniene, L. Vaupsas, J, „Oscillating synchronous pulsating current motor-compressor supplied from DC source", Prace-Institute Elektrotechniki, Poland 2004, Vol. 220, pages 7-16.

BUPT

Chapter 2 - Finite Element Analysis of the proposed configuration

2.1 Finite Element Analysis – An Introduction

When not too many computers where available yet, the design of electrical machines was realized in the classical way using one-dimensional models. Some electro magnetic parts of the machine were considered to form a homogenous element in a magnetic circuit approach. This type of models allows the calculation of specific stationary operating points of the machine. The use of Laplace transformations made possible the analysis of the machine when performing dynamic operation. The development of numerical methods for electrical machines started with the finite difference method which was followed and further overtaken from the finite element method [1].

The first numerical models of electrical machines, electromagnetic fields considering imposed current sources could be simulated by applying first order triangular elements [2]. Further developments of the finite element method lead via the definition of external circuits to problem formulations with imposed voltage sources, which where more accurate models with respect to the realistic machine that is operated by a voltage. Today's developments are directed to all aspects of coupled fields. There are the thermal/magnetic problems or structure dynamic field problems coupled to the electromagnetic field; e.g. acoustic noise in transformers and rotating machines excited by electromagnetic forces. Parallel with the developments of the finite element method first attempts to numerically optimize the finite element models where made. Optimizations of realistic machine models where first performed in the late 80s and early 90s.

The development of electromagnetic devices such as electrical machines, transformers, heating devices and other kinds of actuators face engineers with several problems. The design of an optimized geometry and the prediction of the operational behavior a more precise knowledge of the dependencies of the field quantities inside the magnetic circuit was needed. Electrical machines need to be optimized in several manners. The torque produced and force behavior needs to be determined and losses estimated. The physical correlations like the Maxwell equations are well known for many years, but the analytical calculation methods

force a lot of neglect and simplifications. Correction factors have emerged determined by practical experience to consider different effects. The Finite-Element Method (FEM) is today state-of-the-art for the calculation of electromagnetic, structural-dynamical, and thermal. With the improvements of the performance of personal computers and workstations the models have become three-dimensional with the number of elements increasing. The bandwidth of possible applications is advancing steadily and research projects are opening up new perspectives for the development of electrical machines [3].

Static and transient finite-element calculations of the electro-magnetic field enable the designers to optimize electrical devices. Furthermore, the Finite-Element method allows for the development and optimization of new devices without the necessity of extensive prototyping, which is a more economical approach.

The finite element method (FEM) has proved its ability in analyzing and designing electromagnetic devices, and it is now an important tool in the electrical machine design process. Using the FEM, the machine geometry is brought to an optimum, and the machine steady-state characteristics are computed. In the case of a conventional machine, as the induction machine for instance, there are design algorithms, based on many experimental results, which allow obtaining quite a good machine design without using FEM.

2.2 Electromagnetic FEA

2.2.1 Theoretical background

The Finite Element Method (FEM) is based on Maxwell's equations. Every electromagnetic phenomenon can be associated to the seven basic equations, the four Maxwell equations (2.1), (2.2), (2.3), (2.4) and equations of the materials (2.5). The equations are listed in their differential form and integral form.

$$\nabla xE = -\frac{\partial B}{\partial t} \; ; \; \oint_C Edr = -\frac{d\phi}{dt} \tag{2.1}$$

$$\nabla B = 0 \; ; \; \oint_S BdS = 0 \tag{2.2}$$

$$\nabla D = \rho \; ; \; \oint_S DdS = Q \tag{2.3}$$

$$B = \mu H \; ; \; D = \varepsilon E \; ; \; J = J_0 + J_C = J_0 + \sigma E \tag{2.4}$$

E, D, B, H – electric and magnetic field vectors, J – the space charge density, Φ – the magnetic flux, I – the conducted current, Q – the charge, C respresents the contour integral, S – the surface integral

Together with the material equations they form the complete set of equations describing the fields completely. The seven equations describe the behavior of the electromagnetic field in every point of a field domain. The conducting current density can be distinguished by a material/field dependent part $\mathbf{J}_c$ and by an impressed and given value $\mathbf{J}_0$. We need to assume that the physical properties of the material's (permittivity ε, permeability μ, conductivity σ) do not vary with time and are piecewise homogenous.

In order to solve the Maxwell's equations, the differential form of them and the mathematical functions, the potentials, satisfying the Maxwell equations, have to be used. The choice of a potential takes into account the type of field problem. Various potential formulations are possible for the different field types. Their appropriate definition ensures the accurate transition of the field problem between continuous and discrete space. The use of these field quantities leads to a reduction of the number of differential equations [1].

2.2.2 Electromagnetic FEA – The Software

The software used to realize electromagnetic Finite Element Analysis on the proposed topology is FEMM, which stands for Finite Element Method Magnetics [4].

The program is a suite of programs which helps solving low frequency electromagnetic problems on two-dimensional planar and axisymmetric domains. The program addresses linear and nonlinear magnetostatic problems, linear and nonlinear time harmonic magnetic problems, and linear electrostatic problems.

The program has three parts:

- **Interactive shell** - a Multiple Document Interface pre-processor and a post-processor that contains a CAD-like interface for laying out the geometry of the problem to be solved and for defining material properties and boundary conditions;
- **triangle.exe** which splits the solution region into a large number of triangles, a vital part of the finite element process (Jonathan Shewchuk - Carnegie-Mellon University web page);
- **Solvers** – takes a set of data files that describe problem and solves the relevant Maxwell's equations to obtain values for the desired field throughout the solution domain.

A very important feature that integrates the FEMM software is the LUA scripting language (The name means 'moon' in Portuguese) [5], which is integrated into the interactive shell. The program can both build and analyze a geometry and evaluate the post-processing results, simplifying the creation of various topologies. All edit boxes in the user interface are parsed by Lua, this way allowing equations or mathematical expressions to be entered into any edit box instead of a numerical value.

Lua can be described as a "multi-paradigm" language, providing a small set of general features that can be extended to fit different problem types, rather than providing a more complex and rigid specification to match a single paradigm. Lua does not contain explicit support for inheritance, but allows it to be implemented relatively easily with metatables. Lua also allows programmers to implement namespaces, classes, and other related features using its single table implementation. First-class functions allow the employment of many powerful techniques from functional programming; and full lexical scoping allows fine-grained information hiding to enforce the principle of least privilege [6].

Lua is a dynamically-typed language because types are attached to values instead of variables. Lua uses eight basic types: nil, Boolean, number, string, table, function, user data, and thread. Numbers are double-precision oating-point numbers, corresponding to the type double in C, but it is easy to compile Lua using float or long instead. Because strings are implemented as arrays of bytes with an explicit size, they can contain arbitrary binary data, including embedded zeros.

Tables are associative arrays, which can be indexed by any value (except nil) and can hold any value. Functions are either Lua functions or C functions written according to a protocol for interfacing with the Lua virtual machine.

In this chapter electromagnetic, thermal and mechanical FE analysis results made on the proposed valve actuator topology will be presented.

2.2.3 The proposed Configuration

The cross section of the proposed actuator is illustrated in Figure 2.1

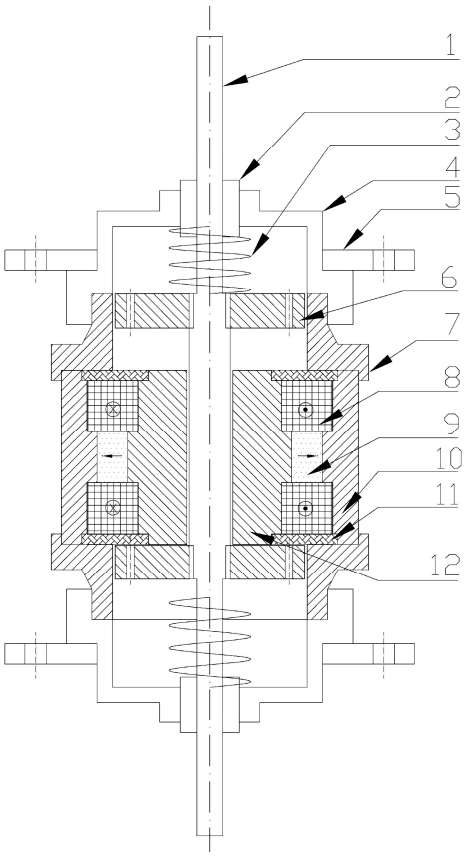

Figure 2.1 The proposed actuator topology – cross section view

Where:

- 1 – actuator's shaft, made of stainless steel;
- 2 – linear bearings, made of bronze;

- 3 – spring;
- 4 – actuator's cover, made of aluminum;
- 5 – actuator's mounting ring made of aluminum;
- 6 – actuator's moving plates, made of stainless steel / Atomet EM1;
- 7 – actuator's intermediate stator made of Atomet EM1;
- 8 – actuator's coils;
- 9 – permanent magnets;
- 10 – actuator's external stator;
- 11 – ring resin;
- 12 – actuator's internal stator.

The shaft (1) and the moving plates (6) are mechanically coupled by using an internal thread (M8) on the mover and an external one on the shaft. The mover plate has 6 holes in order for the air to flow as it's moving from one extreme to another. All pieces will be mechanically fixed by the aid of two actuator mount rings (5).

We choose to manufacture 2 types of plates, one type is made of stainless steel and the other is made of Atomet EM1. For the first tests we utilized the stainless steel plates because they are more rigid with respect to mechanical stress than the Atomet Em1 ones. This option has also proved useful when we performed open loop experiments due to the damping effect caused by core losses in the material. However, this will be discussed in the following chapters.

2.2.4 The operating principle

As seen in the first chapter various linear topologies can be found in literature, but in order to be a competitive solution for achieving VVT they have to satisfy several key issues:

- zero holding current;
- the presence of springs to store the potential energy needed to move the valve between the extreme positions;
- fast transition time, no more than 3.5 ms, enough for 6 krpm engine speed;
- low seating velocity, no more than 0.3 m/s @ 6krpm;
- no more than 3kW, same as that of a conventional valve drive with 8 intake and 8 exhaust valves;
- maximum valve speed – 3.5 m/s;
- high valve acceleration – up to 5000 m/s^2;
- volume of the package – no more than 1 dm^3;

- fast force variation in order to overcame the pressures inside the cylinder;
- up to 600N of developed thrust [7];
- low electrical constant in order to facilitate fast current response at different positions;

The working principle of proposed actuator is described below.

The valve it's held in one of the two extreme positions due to the force created by the magnets acting on one plate and relaxing the spring near it. The opposite spring, being compressed, on the other extreme, push against the mover plate to detach the valve and position it in the middle of the stoke. The spring force should be therefore smaller than the PMs developed force. By injecting a corresponding current into the two twin coils connected in series, the PMs flux is "destroyed", the moving part is released an begins to travel to the other end using the energy stored in the spring. It will not arrive at the other end only due to this energy, therefore a catching current (voltage) has to be injected (applied) having a corresponding direction (polarity).

It should be noticed that the flux produced by the coils, although in series with the PMs flux, don't cross it, so there is no possibility of demagnetization.

The magnets are radially magnetized and are placed on the outer circumference of the internal stator reducing this way the eddy current losses.

The valve, which can be attached to the shaft, will move between the two ends with energy stored in the springs, which leads to an overall power economy.

Due to the fact that the two twin coils are connected in series a single phase inverter is needed to control the valve, Figure 2.2.

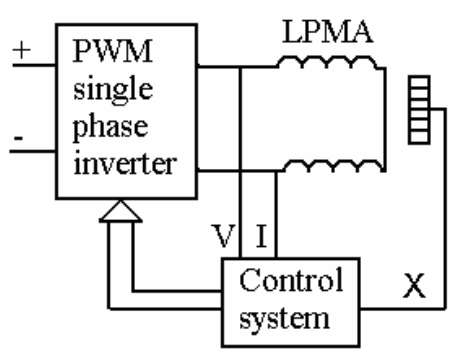

Figure 2.2 Basic control scheme

2.2.5 Electromagnetic FEA results and experimental validation

The actuator's geometrical dimensions were obtained after performing an optimal design using two searching algorithms: the grid search optimization technique and the Hooke-Jeeves optimization algorithm. However, these aspects will be discuss later in this chapter.

The electromagnetic Finite Element Analysis (FEA) is performed using FEMM freeware software [4]. The package is composed of an interactive shell encompassing graphical pre- and post-processing; a mesh generator; and various solvers.

The steps followed during a FEA performed with FEMM are:

- **Physical problem description** (Problem Type, Length Units, Frequency, Depth, Solver Precision and Minimum Angle)
- **The geometrical model design** – the geometry can be realized using the CAD-like features of the software or by importing it as a DXF file.
- **Boundary definition establishment** – the user has to define an adequate number of boundary conditions to guarantee a unique solution.
- **Material assignment** – each geometrical closed region has assigned properties specified in a dialog box that have to do with the material that block is composed of, as well as some attributes about how the material is put together;
- **Boundary conditions assignment**
- **Mesh generation**
- **FEM solver execution**
- **Results extraction and analysis**

Our configuration is an axi-symmetrical one and therefore we only need half of a cross section view to analyze, Figure 2.3.

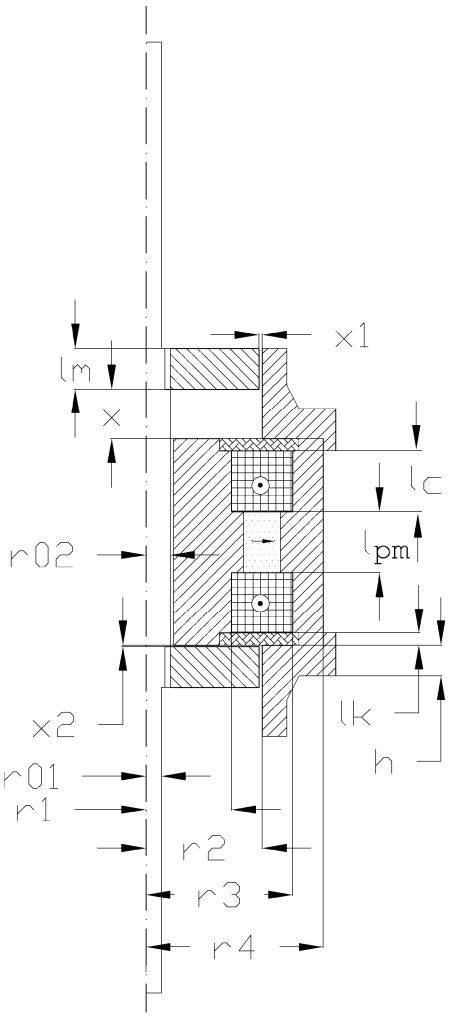

Figure 2.3 Geometry of the proposed configuration

Each dimension emerged from an optimization process, and their numerical values are:

- r_{01} = 5 mm – shaft small radius;
- r_{02} = 8 mm – shaft big radius;
- r_1 = 14 mm – interior stator average radius;
- r_2 = 19 mm – mover plate external radius;
- r_3 = 24 mm – coils outer radius;
- r_4 = 29 mm – external stator outer radius;
- x = 8 mm – valve displacement;

- x_1 = 0.5 mm – air gap 1;
- x_2 = 0.2 mm – air gap 2;
- l_m = 6.68 mm – mover length;
- l_c = 12 mm – copper slot length;
- l_{pm} = 8 mm – pm length;
- l_k = 2 mm;
- h= 5 mm.

The finite element analyzed geometry is illustrated in Figure 2.4.

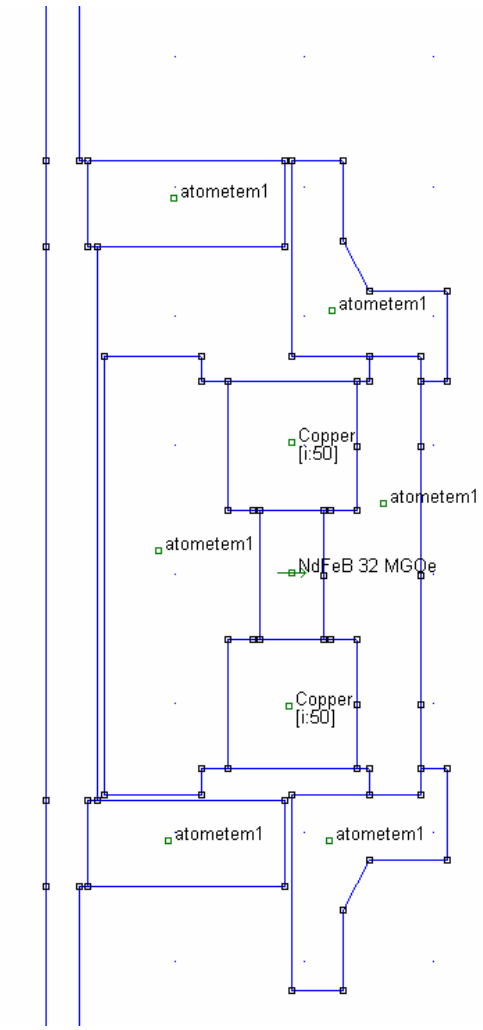

Figure 2.4 FEMM analyzed geometry

The only boundary condition needed is a Dirichlet boundary. In this type of boundary condition, the value of potential *A* is explicitly defined on the boundary, in our case *A* = 0 along it to keep magnetic flux from crossing.

The magnetic part is made of Atomet-EM1, which is a resin based composite material produced by QMP (Quebec Metal Powders). The ATOMET EM1 process flow starts with a high purity iron powder, which is essential for good magnetic properties, then the iron powder is combined with a resin-binder system providing a highly compressible product with high densities and strengths after curing. The iron powder and lubricant mixture is first pressed and then cured at 200°C in air for half minute. This results in a low-cost, high-performance material directly applicable to powder metal fabrication techniques and soft magnetic components. The main characteristics of the SMC used are illustrated in Figure 2.5 and Figure 2.6 [8].

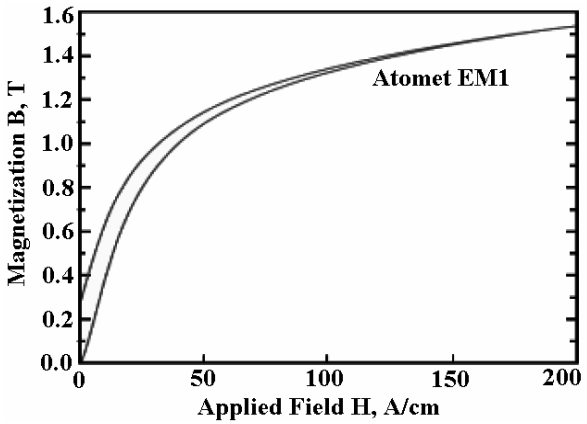

Figure 2.5 B-H characteristic of Atomet EM1

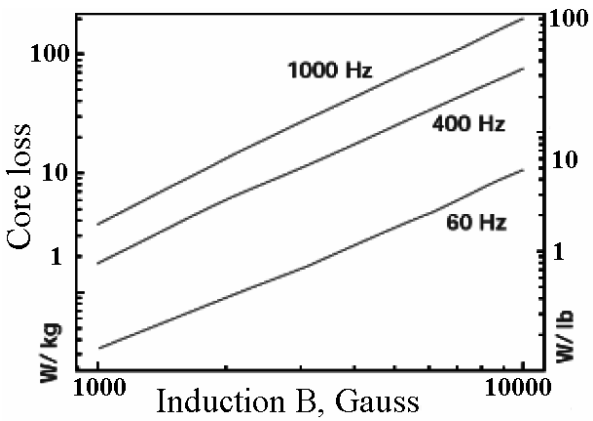

Figure 2.6 Core loss vs. induction for Atomet EM1

The flux lines created by PMs for three different positions of the mover are illustrated in Figure 2.7. It should be noticed how the flux lines concentrates into the lower reluctance path.

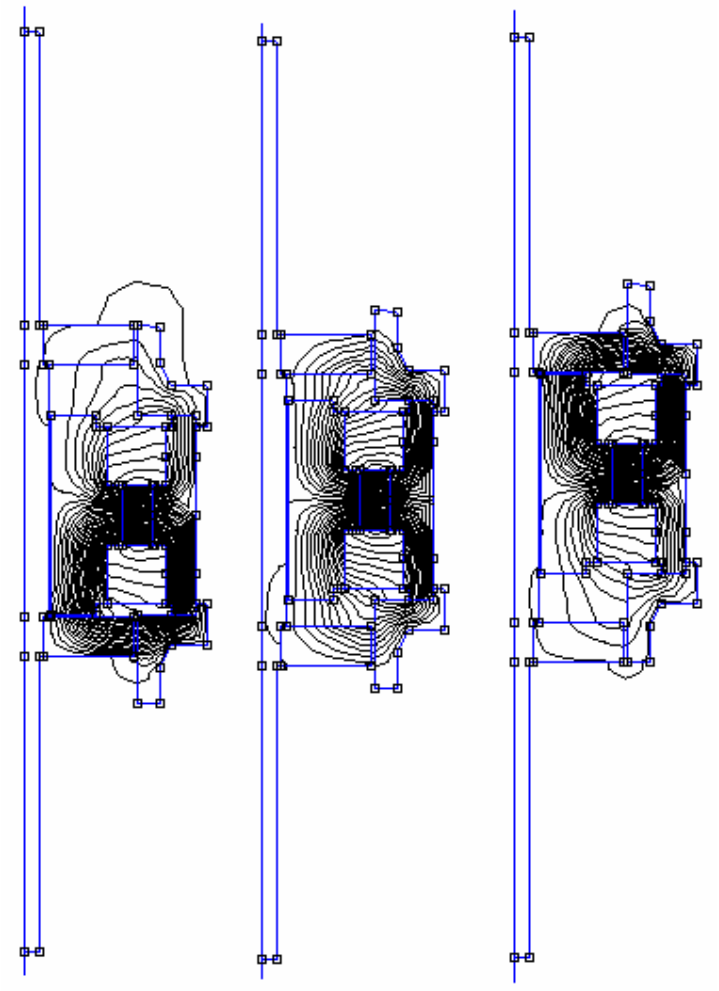

a) b) c)

Figure 2.7 Flux lines produced by PMs: a) up mover position, d) center mover position, c) down mover position

The flux density distribution in the actuator is illustrated in Figure 2.8. As can be seen in order to obtain the force needed (around 600 N) the average flux density in the interior stator should be around 1.3 T. There are areas, near edges,

where the material is saturated. The current in the coils is 25A and the valve is open.

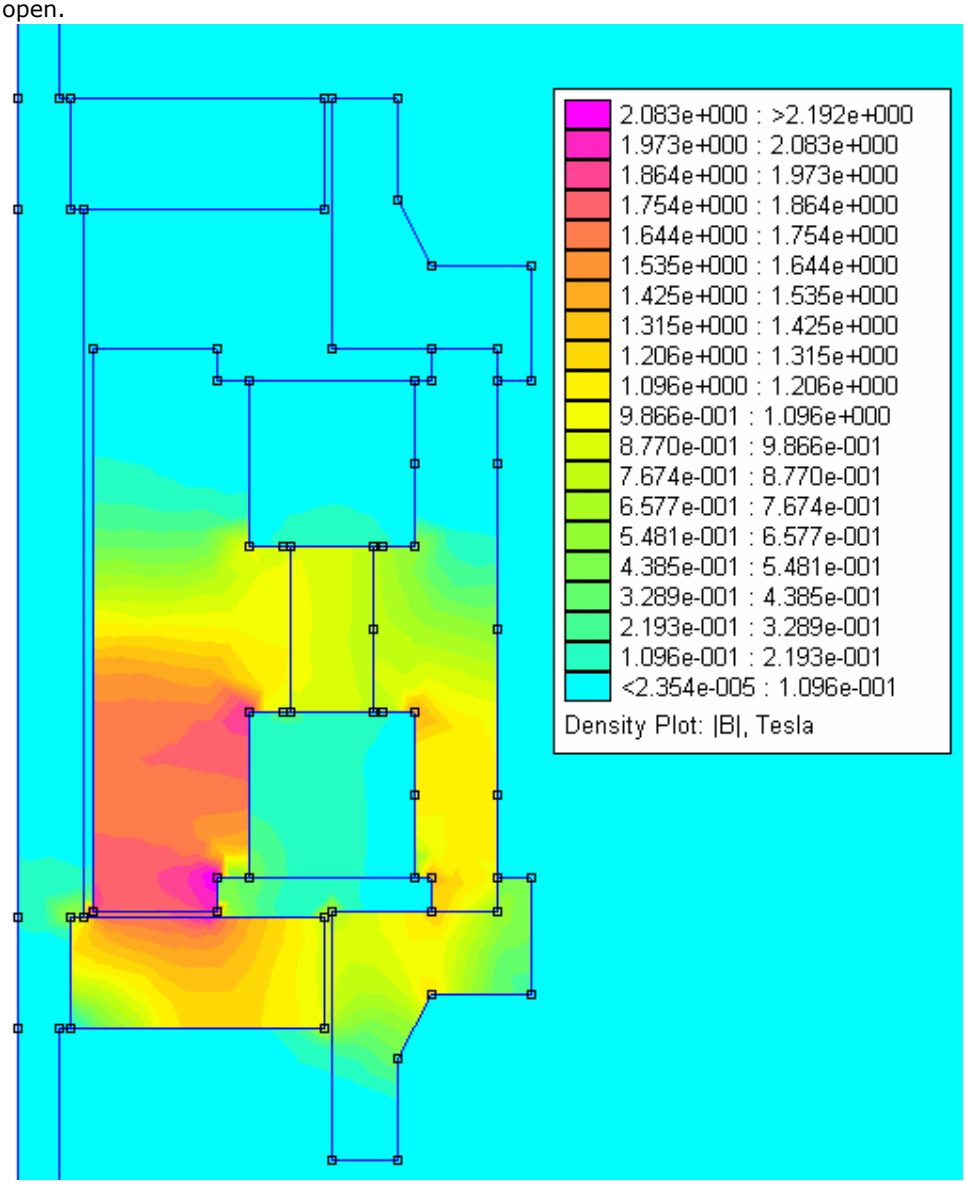

Figure 2.8 Flux density distribution, I=25A, valve open

Next we present some dependencies fetched from FEA that help to characterize the actuator.

The force has been calculated by FEMM using the Weighted Stress Tensor Volume Integral. This volume integral simplifies the computation of forces, as compared to evaluating forces via the stress tensor line integral of differentiation of coenergy. Results are more accurate with finer meshing around the region upon which the force is to be computed. One limitation of the Weighted Stress Tensor integral is that the regions upon which the force is being computed must be entirely surrounded by air and/or abutting a boundary, otherwise results may be deduced from differentiation of coenergy.

The Weighted Stress Tensor block is a volume integral version of Maxwell's stress tensor that automatically selects a collection of paths for the integration that yield quite good force results. This approach is similar to the weighted stress tensor approach described in [9], [10].

Figure 2.9 presents force variation with position for various injected currents (I = 0, 5, 10, 15, 20, 25 A). The lines represent the FEMM derived forces and the dots represent the measured force. The force was measured using a bi-directional load cell.

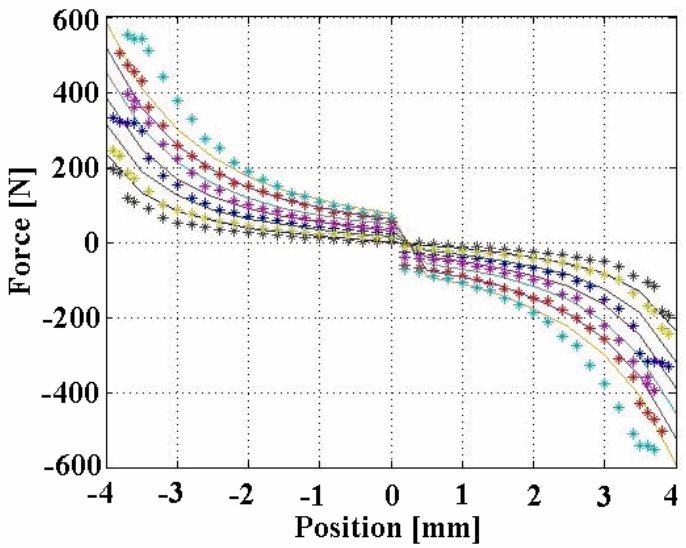

Figure 2.9 Force [N] vs. position [mm] for 6 current values – FEMM derived (–) and measured (*)

One can see that the actuator is able to develop the desired force. Because this variation is a bijection we will use it later in Chapter 4 to estimate the actuator force in the Matlab/Simulink dynamic model.

The total flux in the machine is considered to cross along the external stator of the actuator and comprise the flux of the coils and PMs. The total flux variation

BUPT

with current for different displacements is presented in Figure 2.10. This dependency being also a bijective function will be used in the dynamic model.

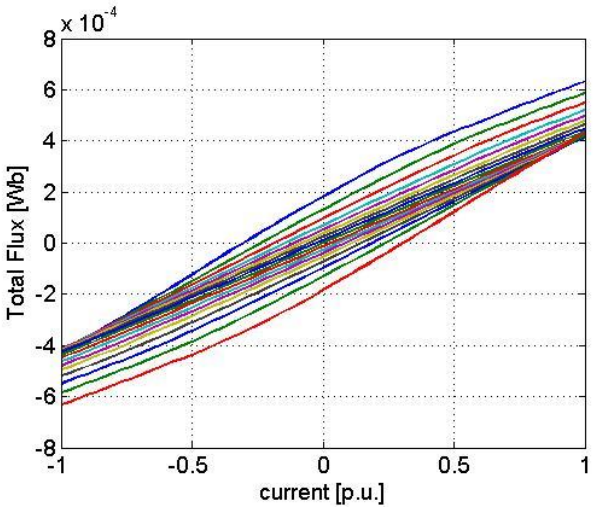

Figure 2.10 Total flux [Wb] / Current [p.u.] / position

Transient inductance variation with current and position is illustrated in Figure 2.11.

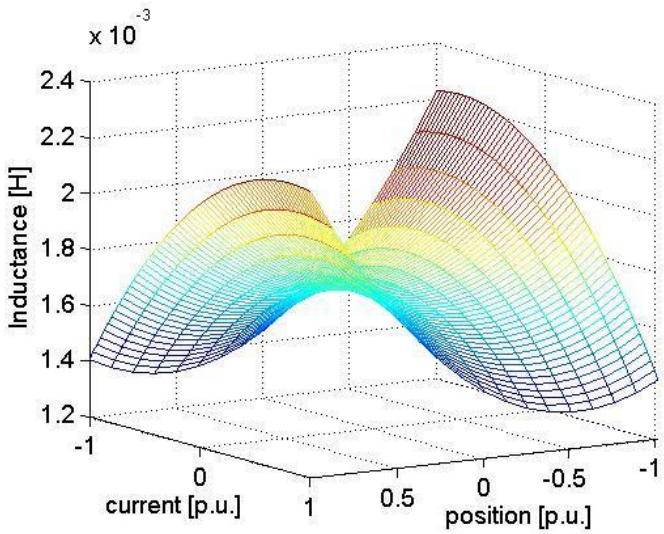

Figure 2.11 Transient inductance [H] / Current [p.u.] / position [p.u.]

The cogging force developed by the actuator is shown in Figure 2.12. The force is zero in the middle of the stroke, which is also a mechanically stable point, where the forces of the springs that push against each other cancel themselves and the cogging force is 0 N.

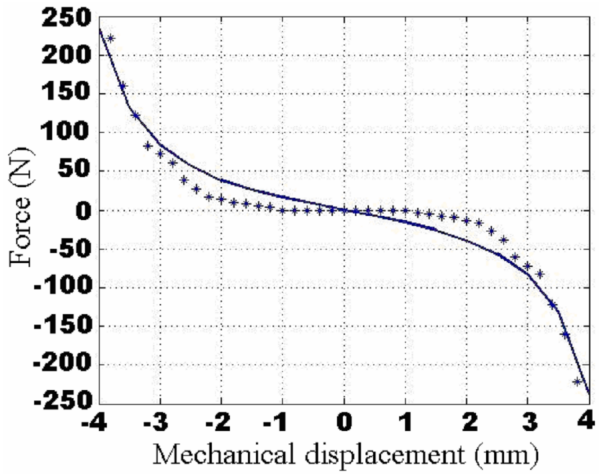

Figure 2.12 Cogging force – FEMM derived (–) and measured (*) [11]

2.2.6 FEMM derived core loss Model

We introduce in [12] a numerical model in order to evaluate the potential losses in the actuator. We choose to split each part of the motor core made of Atomet-Em1 in regions. For each region we fetched from FEMM the average flux density variation for 8 mm displacement of the mover and a sinusoidal current injection (50 x 2 turns and 30 (A) peak current value).We considered that for a full stroke displacement the current has a sinusoidal variation, in such a way that the full stroke corresponds to a semi-period of the current, with means that the amplitude is reached at the middle stroke position. Having all these values we have determined the maximum flux density variation as the mover goes between the two extreme positions. The actuator's regions used to calculate the core loss are illustrated in Figure 2.13.

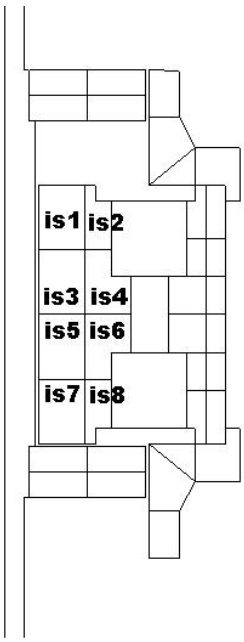

Figure 2.13 Interior stator core loss model regions

The variation of the flux density in the interior stator for the 8 regions considered, is shown in Figure 2.14.

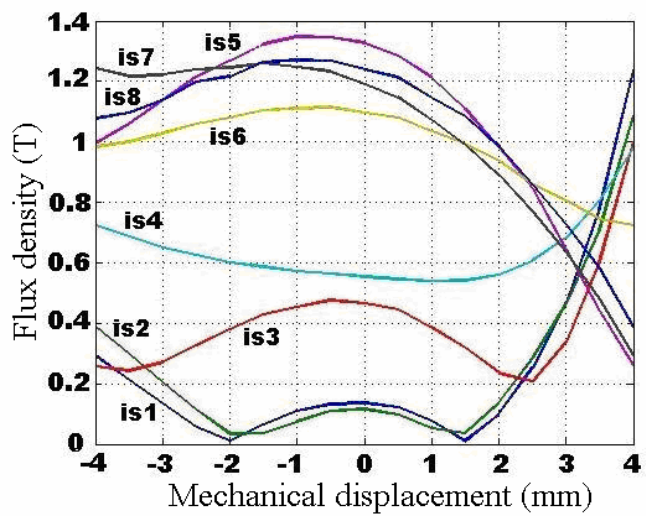

Figure 2.14 Interior stator flux density variation for mover's full displacement

Knowing the specific core losses in Atomet-EM1 (Figure 2.15), at 100 (Hz) frequency and 1 (T), and using formula (2.5) we can calculate the core losses [13, 14].

$$P_{core} \approx \rho_{A-EM1} \cdot vol \cdot p_{100Hz,1T} \cdot \frac{f}{100} \cdot B_{\max}^2 \tag{2.5}$$

where:

- P_{core} – core losses in the block;
- ρ_{A-EM1} = 7100 (Kg/m3) – Atomet-EM1 density;
- vol – volume of the corresponding block;
- $p_{100Hz,1T}$ = 20 (W/Kg) – Atomet-EM1 specific core losses for 100 (Hz) frequency and 1(T) flux density;
- f – actual frequency;
- B_{max} – maximum flux density variation in a certain block.

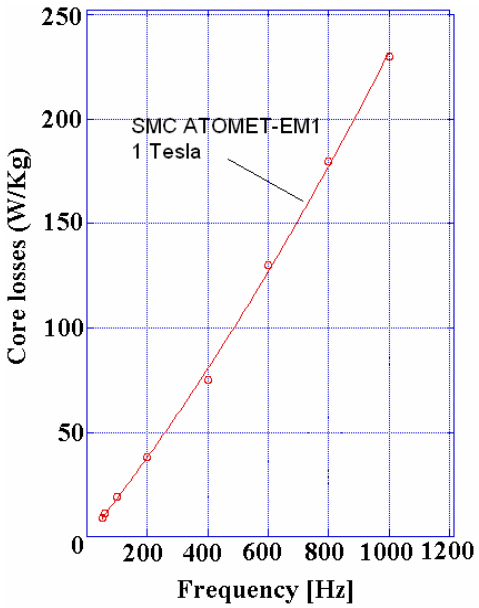

Figure 2.15 Core losses for the SMC material Atomet-EM1[15]

Figure 2.16 shows the core losses in all 6 parts of the motor made of Atomet Em-1: um, dm – up mover, down mover; is, es – interior stator, exterior stator; ius, ids – intermediate up stator, intermediate down stator.

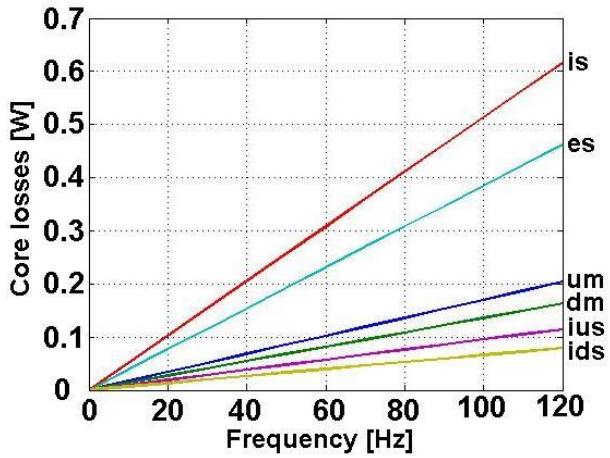

Figure 2.16 Core losses versus current frequency for each part of the motor for Ipeak = 30 (A), 2Nc = 100 (Ampere-turns)

As can be seen in Fig. 2.16, the maximum flux density variation (the maximum core losses) is in the inner stator, the one took as an example to illustrate how the losses were calculated.

Next, we will illustrate the total core losses variation with frequency for different values of the sinusoidal current amplitude in the Atomet-EM1 made parts of the actuator, Figure 2.17.

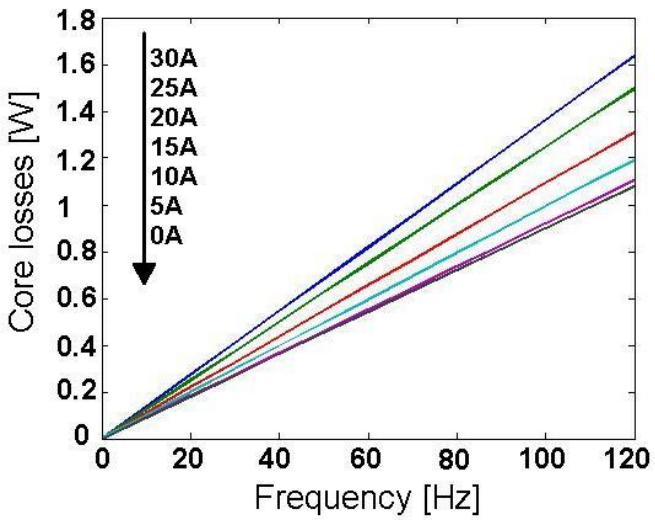

Figure 2.17 Core losses versus current frequency for all motor's Atomet-EM1 made parts

For 120 (Hz) sinusoidal current frequency, a maximum of 30 (A) amplitude and for a full displacement of the mover, the eddy current losses in the magnets, if they were made of one piece, obtained from FE analysis are around 30 (W). In the manufactured actuator, to reduce drastically these losses, the PM is made of ten parallelepipedic magnet parts, placed on the inner stator circumference. The losses in the actuator magnets are then times smaller (3 (W)). The copper losses remain the most important source of heat and are around 115 (W) for both coils for 21 (A) RMS sinusoidal current value, as the total core losses are less than 4.5 (W).

BUPT

2.3 Thermal FEA

2.3.1 Theoretical background

Heat transfer is involved in several physical processes, and it can be the limiting parameter for many of them, thereby a thermal FEA is very important. Heat transfer often appears together with, or because of, other physical phenomena, making a coupled FEA analysis more realistic in describing thermal processes.

The modeling of heat transfer effects has become ever more important in the design of products in many areas including the electronics, automotive, and medical industries. The combination of experimental data along with theoretical analyses through computer models has proven to be an effective way to understand thermal problems and to decrease production costs.

Heat transfer is defined as the displacement of energy caused by a difference in temperature.

There are three mechanisms that characterize the heat transfer process:

Conduction – the heat flux is proportional to the temperature gradient and takes place through different mechanisms in different media:

- in a gas through collisions of the molecules;
- in a fluid through oscillations of each molecule in a limited space formed by its nearest neighbors;
- in metals by electrons carrying heat or in other solids by molecular motion.

Convection - takes place through the net displacement of a fluid, which translates the heat content in a fluid through the fluid's own velocity. The term convection is also used for the heat dissipation from a solid surface to a fluid, where the heat transfer coefficient and the temperature difference across a fictive film describe the flux.

Radiation - takes place through the transport of photons, which solid surfaces can absorb or reflect [16].

In out thermal FEA we consider two heat transfer mechanisms: conduction and convection. Next we will introduce some basic formulas to understand the entities involved.

Fourie's Law describes the **conduction** heat transfer:

$$q = -k \cdot \nabla T \tag{2.6}$$

Where:

- q – heat flux [W/m^2] ;
- T – temperature [K];
- k – thermal conductivity [W/mK];

Heat transfer due to **free convection** is described by Newton's Law of Cooling:

$$q = h \cdot A \cdot \Delta T \tag{2.7}$$

Where:

- h – convection heat-transfer coefficient [W/m^{2}K]
- A – exposed area [m^2];
- ΔT – temperature variation [K];

2.3.2 Thermal FEA – The Software

The software used to solve actuator's heat flow problems is FEMM. We have already discussed the main features of the software in Section 2.2.2.

The heat flow part of the software deals with steady-state heat conduction problems. As the author explains, heat flow problems are represented by a temperature gradient, *G* (analogous to the field intensity, *E* for electrostatic problems), and heat flux density, *F* (analogous to electric flux density, *D*, for electrostatic problems).

The heat flux density is governed by Gauss' Law, which says that the heat flux out of any closed volume is equal to the heat generation within the volume. Analogous to the electrostatic problem, this law is represented in differential form as:

$$\nabla F = q \tag{2.8}$$

where *q* represents volume heat generation.

The relation between temperature gradient and heat flux density is expressed by the formula below:

$$F = k \cdot G \tag{2.9}$$

where *k* is the thermal conductivity.

Because the thermal conductivity can be a function of temperature, FEMM software allows for the variation of conductivity as an arbitrary function of temperature. If we need to establish the temperature, *T*, rather than the heat flux density or temperature gradient, we can use Equation (2.10), which relates the temperature to the temperature gradient, *G*:

$$G = -\nabla T \tag{2.10}$$

Substituting the above equation into Gauss' Law and applying the constitutive relationship yields the second order partial differential equation (2.11):

$$-\nabla \cdot (k \cdot \nabla T) = q \tag{2.11}$$

After defining the geometry, introducing the materials properties, heat sources and boundary conditions the software is able to solve (2.11) for temperature T.

2.3.3 Thermal FEA results

Under most operating conditions, the dominant loss is due to the resistance in the stator windings. As we use a composite material for the magnetic parts we can expect low values of the power losses in those parts and in consequence low heat sources.

Knowing all possible losses that may appear in the actuator gives us the possibility to calculate the amount of heat every actuator part can produce and therefore introduce the thermal problem via FEA.

After establishing the geometry of the actuator, we must assign each block a material. The magnetic parts of the actuator are made of **Atomet-EM1**. We must know for this material the following parameters:

- Thermal conductivity (isotropic) – k = 20 W/m K;
- Density – ρ = 7200 kg/m^3;
- Heat capacity – C_p = 506 J/Kg K.

The coils are made of **Copper**, which has the following parameters:

- Thermal conductivity (isotropic) – k = 400 W/m K;
- Density – ρ = 8700 kg/m^3;
- Heat capacity – C_p = 385 J/Kg K.

The magnets are made of **NdFeB**, which has the following parameters:

- Thermal conductivity (isotropic) – k = 10 W/m K;
- Density – ρ = 7500 kg/m^3;
- Heat capacity – C_p = 402 J/Kg K.

The shaft is made of **Stainless Stee**l, which has the following parameters:

- Thermal conductivity (isotropic) – k = 44.5 W/m K;
- Density – ρ = 7850 kg/m^3;
- Heat capacity – C_p = 475 J/Kg K.

The **air** surrounding the actuator has the following parameters:

- Thermal conductivity (isotropic) – k = 0.024 W/m K;
- Density – ρ = 1.2 kg/m^3;
- Heat capacity – C_p = 1012 J/Kg K.

Although the air thermal conductivity depends on air temperature, as one can see in Figure 2.18, we consider here a rather constant value because the temperature gradient is relatively low.

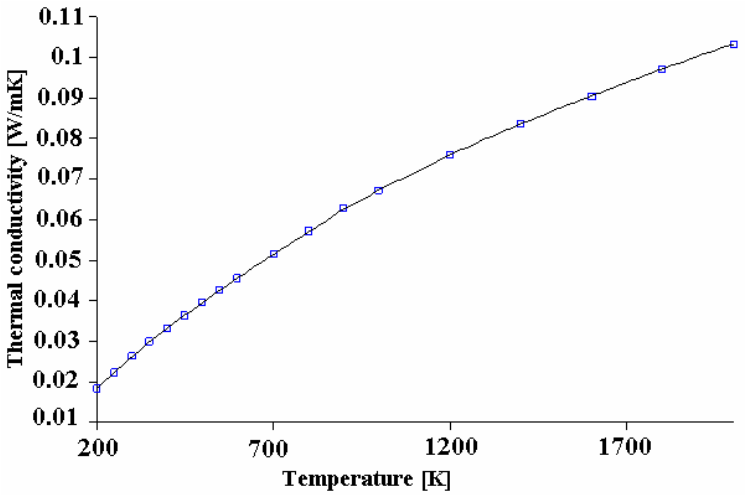

Figure 2.18 Thermal conductivity variation with temerature for air

The boundary conditions play an important role in obtaining an accurate thermal solution. The boundaries that are in contact with air must be defined as convection boundaries, with an adequate heat transfer coefficient.

The heat transfer coefficient used to calculate the heat transfer between the outer surfaces of the actuator parts and the surrounding medium must be grater than 100 (W/m^2K), which leads to the conclusion that the actuator must be cooled with a forced air flow or with water in order to overcome a threshold temperature.

The threshold temperature is established mainly by electrical parameters constraints.

For many fluids, a change in temperature determines density changes. This phenomenon is of particular interest when modeling free-convection problems where density differences drive the fluid flow, but we will not treat this case due the different cooling solution adopted.

The heat capacity of each material introduced in the thermal model can be observed in Figure 2.19.

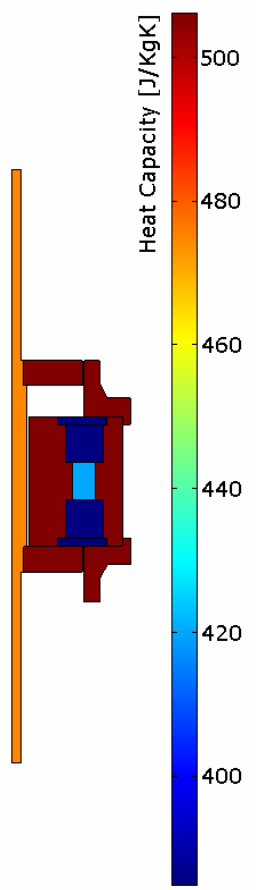

Figure 2.19 Heat capacity distribution along actuator's cross section

As one can see from Figure 2.19, Atomet-EM1, having a high specific heat capacity, will change it's temperature slower than Copper for a given heat energy generated within the actuator. The Copper however has a high thermal conductivity, so it's ability to conduct heat is greater than Atomet-EM1.

Figure 2.20 illustrates the temperature change rate along the actuator's cross section area.

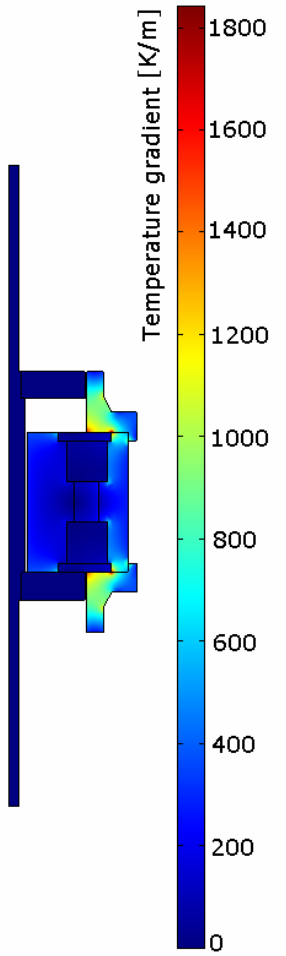

Figure 2.20 Cross-section temperature gradient

The highest values of the temperature gradient are within the intermediate stator, which acts as a heat exchanger.

In Figure 2.21 we can see the temperature distribution and in Figure 2.22 the temperature evolution in all the parts of the actuator.

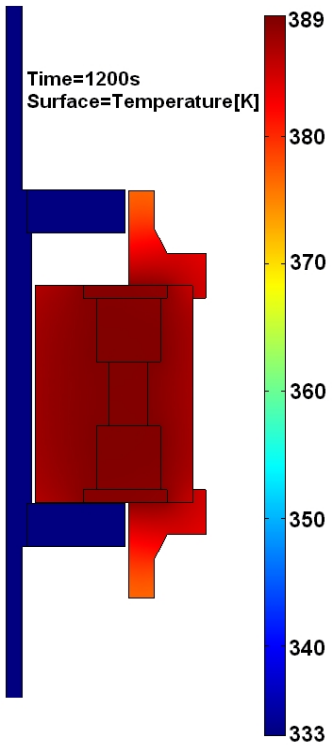

Figure 2.21 Temperature distribution over the actuator's cross section

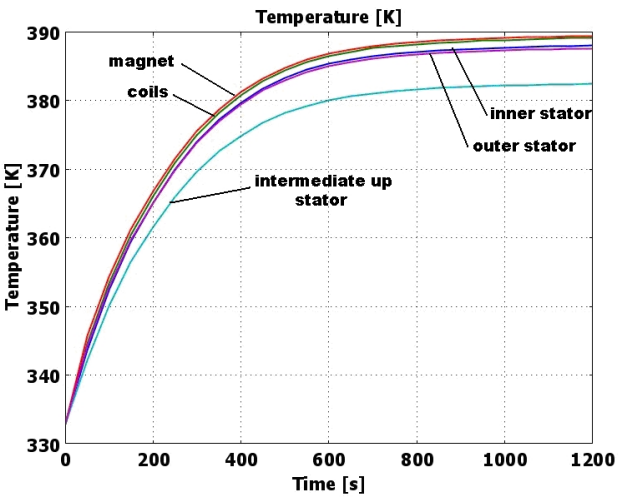

Figure 2.22 Temperature evolution for maximum current fed

To predict the performance of any electromechanical devices, in the design stage, a coupled simulation is recommended due to the dependency of the material characteristics on temperature. The coupled simulation is then characterized by a non-linear system of partial differential and algebraic equations, which can be solved by applying finite element methods and adaptive relaxation techniques.

At these temperatures, the resistance of the copper wire is increased with 50%.

The material properties of permanent magnets are also temperature dependent. The point of irreversible demagnetisation of the magnets is reached much earlier and all magnetic materials lose their properties beyond the Curie temperature [17].

The working temperature of the magnets used is 150 (^{0}C) and the PMs Curie temperature is 310 (^{0}C). The magnets used to build the prototype are NdFeB ($Br_{20(oC)}$=1.29 (T), $Hc_{20(oC)}$=979000 (A/m)), which have α_{Br}= -0.001/degree, α_{Hc}= -0.005/degree as the temperature coefficients for remanence and coercive force [18]. The cogging force obtained using the electromagnetical FEM analysis is about 120 (N) at 120 (^{0}C) working temperature ($Br_{120(oC)}$=1.16 (T), $Hc_{120(oC)}$=489500 (A/m)) which means that the force has decreased 2 times. This means that the actuator will not be able to hold the valve in one of the two extreme positions only with the force of the magnets. In this case Sm_2 Co_7 magnets must be used ($Br_{20(oC)}$ = 1.14 (T), $Hc_{20(oC)}$ = 851506 (A/m)). SmCo magnet is a high performance, low temperature coefficient, permanent magnet made of samarium and cobalt and other rare-earth elements. Its biggest advantage is its high working temperature. This magnets have the temperature coefficients around the following values α_{Br}= -0.0005/degree, α_{Hc}= -0.0022/degree, the working temperature of 250 (^{0}C) and the Curie temperature at 750 (^{0}C) [19].

The formulas used to calculate the remanence and the coercive force are presented below [10]:

$$B_r(T) = B_{r(T0)}[1 + \alpha_{Br}(- _0)] \quad (2.12)$$

$$H_c(T) = H_{c(T0)}[1 + \alpha_{Hc}(- _0)] \quad (2.13)$$

where:

- $B_{r(T0)}$ – PM remanence at T_0 temperature;
- $H_{c(T0)}$ – PM coercive force at T_0 temperature;
- α_{Br} – temperature coefficient for remanence;
- α_{Hc} – temperature coefficient for coercive force;
- T, T_0 – current / initial temperature.

Now, using (2.12) and (2.13), recalculating B_r and H_c for Sm_2 Co_7 at 120 (^{0}C), ($Br_{120(oC)}$ = 1.083 (T), $Hc_{120(oC)}$ = 664174 (A/m)) we obtain around 200 (N)

BUPT

cogging force, which allows the actuator to function correctly even at high temperatures.

The demagnetization characteristic of PMs is shown in Figure 2.23.

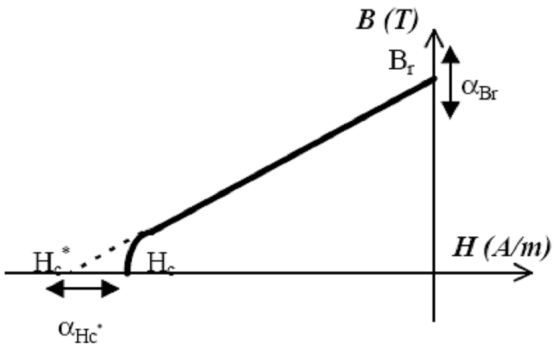

Figure 2.23 Demagnetization characteristic of permanent magnet material

We choose to study the worst case in which the heat transfer coefficient was choose 100 (W/m^2K), but this coefficient can reach grater values depending on the solution adopted, providing this way a better heat extraction and lower electrical parameters variation.

2.4 Mechanical FEA

2.4.1 Theoretical background

The actuator can be modeled as an axial symmetric topology. This type of topology mode uses cylindrical coordinates r, φ (phi), and z. It assumes that the displacement v in the φ direction together with the stress and strains components are zero. Loads are independent of φ, and this application mode allows loads only in the r and z directions, [20].

Figure 2.24 illustrates how to draw the geometry only in the half plane $r \geq 0$ and recover the original 3D solid by rotating the 2D geometry about the z axis.

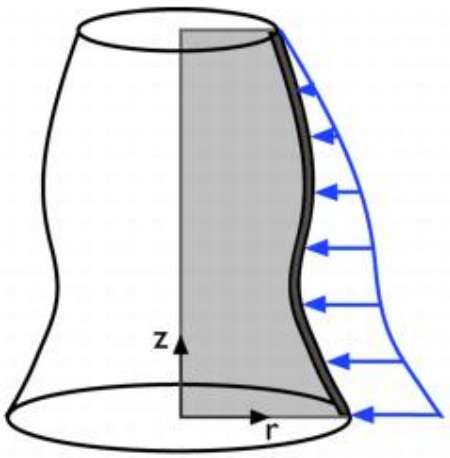

Figure 2.24 2D geometry extracted from a 3D solid

The equilibrium equations in axial symmetry are expressed in Equations (2.14), and the strain-displacement relationships for small displacements are given in Equations (2.15).

$$\begin{aligned} &\frac{\partial \sigma_r}{\partial r} + \frac{\partial \tau_{rz}}{\partial z} + \frac{\sigma_r - \bar{\sigma}}{r} + F_r = 0 \\ &\frac{\partial \tau_{rz}}{\partial r} + \frac{\partial \sigma_z}{\partial z} + \frac{\tau_{rz}}{r} + F_z = 0 \end{aligned} \tag{2.14}$$

BUPT

$$\varepsilon_r = \frac{\partial u}{\partial r},\ \varepsilon_{\phi} = \frac{u}{r},\ \varepsilon_z = \frac{\partial w}{\partial z} \text{ and } \gamma_{rz} = \frac{\partial u}{\partial z} + \frac{\partial w}{\partial r} \tag{2.15}$$

where:

- σ_r, σ_z, σ_θ, τ_{rz} – Cauchy stress in global coordinate system;
- F_r and F_z – body (volume) and edge point loads in global r and z direction;
- ε_r, ε_ϕ, ε_z – Strain in global coordinate system;
- u, w – the deformation components of r and z;

2.4.2 Mechanical FEA – The Software

We used Comsol Multiphysics to analyze the mechanical properties of the proposed PM linear actuator.

The Structural Mechanics Module is a package that extends the COMSOL Multiphysics™ modeling environment with customized user interfaces and functionality optimized for structural analysis. It provides a library of prewritten ready-to-run models that make it quicker and easier to analyze discipline-specific problems.

The module can perform static, eigenfrequency, time-dependent, quasi-static transient, parametric, linear buckling, and frequency response analysis. One can use both linear and nonlinear material models such as elasto-plastic models and include large deformation effects in an analysis. The materials can be isotropic, orthotropic, or fully anisotropic. User can define loads, constraints, and material models in a local, user-defined, or global coordinate system.

All application modes in this module are fully multiphysics enabled, making it possible to couple to any other physics application mode in COMSOL Multiphysics or the other modules.

In order to obtain the loads on each part of the actuator we calculate them first with the Azimuthal Induction Currents Module and paste them as inputs to the Axial-Symmetry Stress-Strain Module.

Depending on the Implementation property selected, COMSOL Multiphysics formulates the Axial-Symmetry application mode using either the equilibrium equations (see Equation (2.14) and (2.15)) or the principle of virtual work, which state that the sum of virtual work from internal strains is equal to work from external loads.

2.4.3 Mechanical FEA results

The mechanical properties of dielectromagnetics materials are dependent on the density and heat treatment temperature, similar to any other powdered metal part. ATOMET EM-1 iron-resin material exhibits the highest cured strength values, up to 130 MPa at a density of about 7.20 g/cm³.

The mechanical FE analysis presented in this paper is a static analysis. We chose to investigate the case in which the mover has to support the maximum force developed by the actuator as the valve pushes against the exhaust pressure in the cylinder. The simulation does not take into account the force of the springs because this will decrease anyway the maximum force that can appear in the mover. A common use of FE mechanical analysis is for the determination of stresses and displacements in mechanical objects and systems.

The material used for the magnetic core parts is Atomet-EM1, which supports very high compacting pressures. The problem with this material, in terms of strength is the Transverse Rupture Strength (TRS), which is around 130 MPa at a curing temperature of 200 Celsius degrees, Figure 2.25.

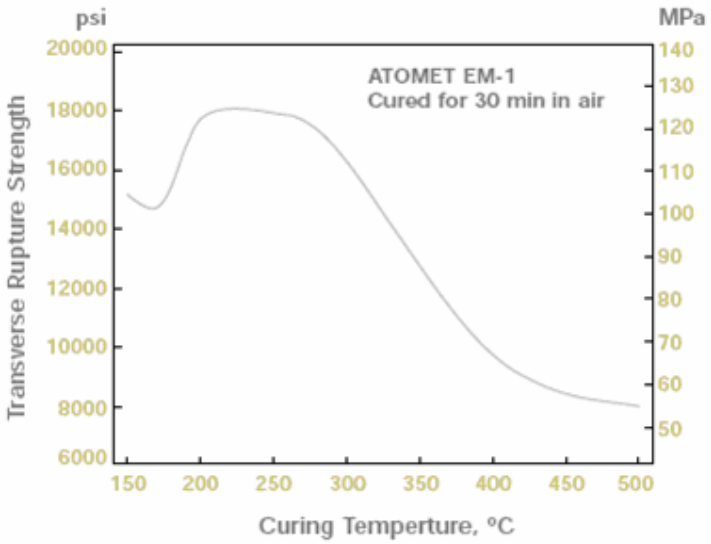

Figure 2.25 Strength versus curing temperature for Atomet-EM1 material

TRS stress however does not appear in the parts of the actuator made of Atomet-EM1. It generally appears in beams supported near the ends, with the load applied midway.

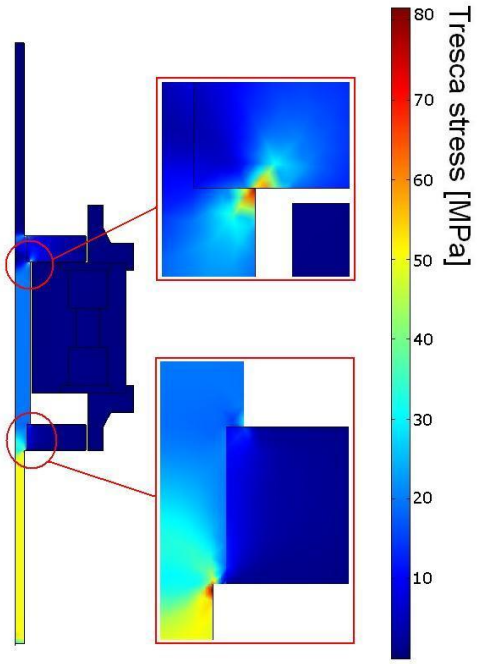

Figure 2.26 Tresca stress in the actuator parts

Figure 2.26 illustrates the maximum shear stress in the actuator parts when the shaft experiences the maximum force and pushes against the pressures in the cylinder. As we can see the maximum value, 80MPa, is reached mainly in the shaft, made of stainless steel, which has the shear strength around 186 MPa. In the region where the shaft and the up plate made of Atomet-EM1 are mechanically fixed we have a 70MPa shear stress value, while the sharing strength for this material is 80MPa.

Figure 2.27 illustrates the normal stress within the actuator. The negative values correspond to the compression stress and the positive values to the tensile stress. The compressive strength for Atomet-EM1 is around 140 MPa and for stainless steel is 440 MPa.

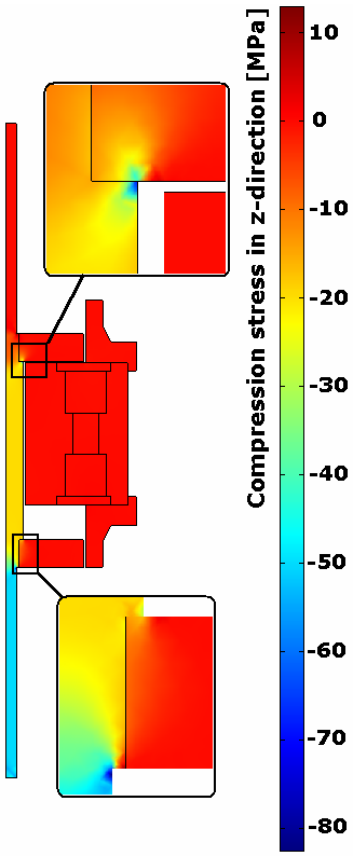

Figure 2.27 Normal stress distribution

Therefore, the actuator should withstand the main mechanical stress involved in the oscillation process.

SUMMARY

This Chapter presents three types of Finite Element Analysis: electromagnetic, thermal and mechanical. The finite element method (FEM) has proved its ability in analyzing and designing electromagnetic devices, and it is now an important tool in the electrical machine design process. Each type of FEA realized has a theoretical background were are briefly introduced, in a simple way, the main equations that govern the software utilized. The purposed configuration and it's operating principle is introduced. Experimental validation was made for electromagnetic FEA. Various dependencies have been fetched to be utilized in dynamic simulations and control strategies that will be presented later in this thesis. FEA derived core losses model was developed. In order to predict the performance of any electromechanical devices, in the design stage, a coupled simulation is recommended due to the dependency of the material characteristics on temperature. Therefore, the temperature influence on the magnets flux is analyzed and possible solutions are purposed. Static mechanical analysis was made to check if the actuator will overcame the main stresses within.

CHAPTER 2 - REFERENCES

[1] Hameyer K., Henrotte F., Vande Sande H., Deliège G., and De Gersem H., ``Finite element models in electrical machine design,'' in *Int.conference CBMag 2002*, no. invited paper (on CD Rom), Nov. 2002.

[2] Andersen, O.W., "Transformer leakage flux program based on the finite element method," *IEEE trans. onpower apparatus and systems, PAS-92*, p.p. 682-9.

[3] C. Schlensok, T. Scheermesser, D. van Riesen, G. Henneberger, "Finite-Element Models of Electrical Machines and their Calculation", 21st CAD-FEM User's Meeting, Potsdam, Germany, November 12-14, 2003

[4] Finite Element Method Magnetics Users Manual - http://femm.foster-miller.net/wiki/Documentation/

[5] LUA Scripting Language Home Page – www.lua.org

[6] Wikipedia – The Free Encyclopedia – http://en.wikipedia.org/wiki/Wiki http://en.wikipedia.org/wiki/Lua_(programming_language)

[7] C. Bernez, M. Gabsi, H. Ben Ahmed, M. Lecrivain and E. Gimet - "High-acceleration linear Drives: Dimensioning and Constraints relative to electromagnetic Valves" - Laboratoire SATIE - ENS Cachan, 61, av. du Prsident Wilson, 94235 Cachan Cedex, France

[8] F.Marignetti, J.R.Bumby, "Electromagnetic modelling of Permanent Magnet Axial Flux Motors and Generators" 16th International Conference on Electrical Machines. 5-8 September Cracow (Poland). vol. 1, pp. 588-594.

[9] S. McFee, J. P. Webb, and D. A. Lowther, "A tunable volume integration formulation for force calculation in finite-element based computational magnetostatics," IEEE Transactions on Magnetics, 24(1):439-442, January 1988.

[10] F. Henrotte, G. Deliege, and K. Hameyer, "The eggshell method for the computation of electromagnetic forces on rigid bodies in 2D and 3D," CEFC 2002, Perugia, Italy, April 16-18, 2002.

[11] I. Boldea, S. Agarlita, L. Tutelea, F. Marignetti – "Novel linear PM valve actuator: FE design and dynamic model ", Record of LDIA 2007, Lille, France

[12] I.Boldea, S. C. Agarlita, F. Marignetti and L. Tutelea – "Electromagnetic, Thermal and Mechanical design of a linear PM valve actuator laboratory model", Record of OPTIM 2008, Vol. IIA, Brosov, Romania

[13] I. Boldea, S. A. Nasar – "*Linear Motion Electromagnetic Drives* ", Taylor and Francis, 2001

[14] I. Boldea, S.A. Nasar – "*Linear Electric Actuators and Generators*", Cambridge University Press, 1997

[15] M. R. Dubois, N. Dehlinger, H. Polinder, and D. Massicotte, "Clawpole Transverse-Flux Machine with Hybrid Stator," in *International Conference on Electrical Machines* Greece, 2006.

[16] COMSOL – Heat transfer glossary - http://www.comsol.com/products/ht/glossary/

[17] Driesen J., De Gersem H., Belmans R., and Hameyer K., ``Coupled thermal-magnetic analysis of a saturated permanent magnet motor,'' in *Symposium on Power electronics electrical drives advanced machines power qualidy (Speedam 98)*, pp. P1.1-6, June 1998.

[18] Total Magnetic Solutions - http://magnetsales.com

[19] Dexter Magnetic Technologies - http://www.dextermag.com

[20] Axial Symmetry Stress-Strain Application Mode – COMSOL MultiPhysics Help

Chapter 3 Finite Element Optimal Design of the proposed configuration

3.1 Direct versus Indirect Search optimization algorithms

A good electrical machine design involves nonlinear optimization with quite complicated objective functions or constraints for which analytical solutions are not available. One of the possible solutions is the search algorithm in which, the objective function is first computed with a trial solution. This solution will be sequentially improved based on the corresponding objective function value until convergence.

The search algorithms can be classified into two types: direct search algorithm and indirect search algorithm. A direct search algorithm depends on the objective function only through ranking a countable set of function values. The method does not involve the partial derivatives of the function and hence it is called nongradient or zeroth order method. Indirect search algorithm, also called the descent method, depends on the first (first-order methods) and often second derivatives (second-order methods) of the objective function.

Direct search algorithms for solving nonlinear optimization that require objective functions, are listed below:

Random Search Method - generates trial solutions for the optimization model using random number generators for the decision variables. Random search method includes random jump method, random walk method and random walk method with direction exploitation. Random jump method generates huge number of data points for the decision variable assuming a uniform distribution for them and finds out the best solution by comparing the corresponding objective function values. Random walk method generates trial solution with sequential improvements, which is governed by a scalar step length and a unit random vector. The random walk method with direct exploitation is an improved version of random walk method, in which, first the successful direction of generating trial solutions is found out and then maximum possible steps are taken along this successful direction.

Grid Search Method - involves setting up of grids in the decision space and evaluating the values of the objective function at each grid point. The point which

corresponds to the best value of the objective function is considered to be the optimum solution. A major drawback of this methodology is that the number of grid points increases exponentially with the number of decision variables, which makes the method computationally costlier.

Univariate Method - involves generation of trial solutions for one decision variable at a time, keeping all the others fixed. Thus the best solution for a decision variable keeping others constant can be obtained. After completion of the process with all the decision variables, the algorithm is repeated till convergence.

Pattern Directions: - involves chosing the search direction along the direction of co-ordinate axis which makes the rate of convergence very slow. To overcome this drawback, the method of pattern direction is used, in which, the search is performed not along the direction of the co-ordinate axes but along the direction towards the best solution. This can be achieved with Hooke and Jeeves' method or Powell's method.

Rosen Brock's Method of Rotating Coordinates - This is a modified version of Hooke and Jeeves' method, in which, the coordinate system is rotated in such a way that the first axis always orients to the locally estimated direction of the best solution and all the axes are made mutually orthogonal and normal to the first one.

Simplex Method - Simplex method is a conventional direct search algorithm where the best solution lies on the vertices of a geometric figure in N-dimensional space made of a set of N+1 points. The method compares the objective function values at the N+1 vertices and moves towards the optimum point iteratively. The movement of the simplex algorithm is achieved by reflection, contraction and expansion.

The indirect search algorithms that are based on the derivatives or gradients of the objective function are listed below:

Steepest Descent (Cauchy) Method - the search starts from an initial trial point X1, and iteratively moves along the steepest descent directions until the optimum point is found. Although, the method is straightforward, it is not applicable to the problems having multiple local optima. In such cases the solution may get stuck at local optimum points.

Conjugate Gradient (Fletcher-Reeves) Method: The convergence technique of the steepest descent method can be greatly improved by using the concept of conjugate gradient with the use of the property of quadratic convergence.

Newton's Method: Newton's method is a very popular method which is based on Taylor's series expansion.

Marquardt Method: Marquardt method is a combination method of both the steepest descent algorithm and Newton's method, which has the advantages of

BUPT

both the methods, movement of function value towards optimum point and fast convergence rate.

Quasi-Newton Method: Quasi-Newton methods are well-known algorithms for finding maxima and minima of nonlinear functions. They are based on Newton's method, but they approximate the Hessian matrix, or its inverse, in order to reduce the amount of computation per iteration. The Hessian matrix is updated using the secant equation, a generalization of the secant method for multidimensional problems [1-7].

Figure 3.1 shows a general flowchart that illustrates how a search algorithm works.

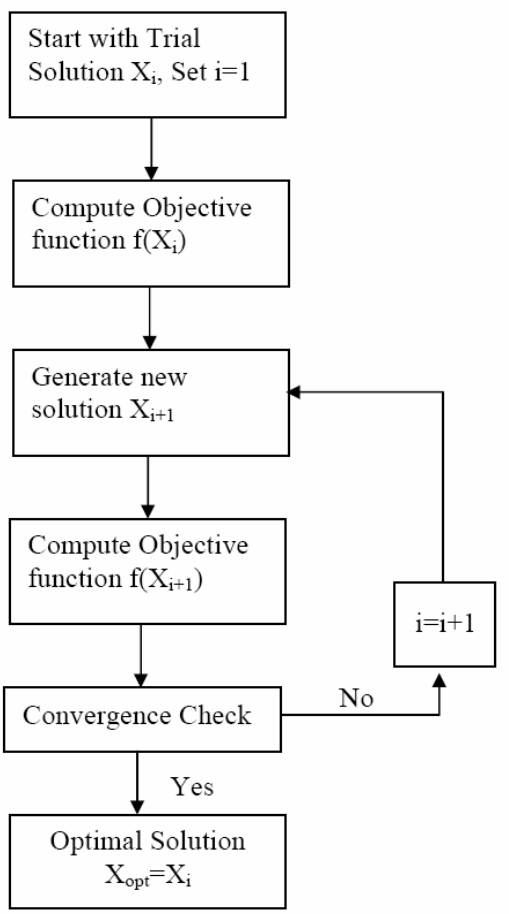

Figure 3.1 Flowchart of Search Algorithm

3.2 The grid search optimization algorithm

Grid search optimization is the most accurate way to search for the global optimum, but the main drawback is the high number of calculations of the objective function. Using LUA Script we are able to draw the geometry of the actuator and to implement the grid search algorithm.

The geometry involved in the optimization process is shown in Figure 3.2 along with the main dimensions utilized in the process.

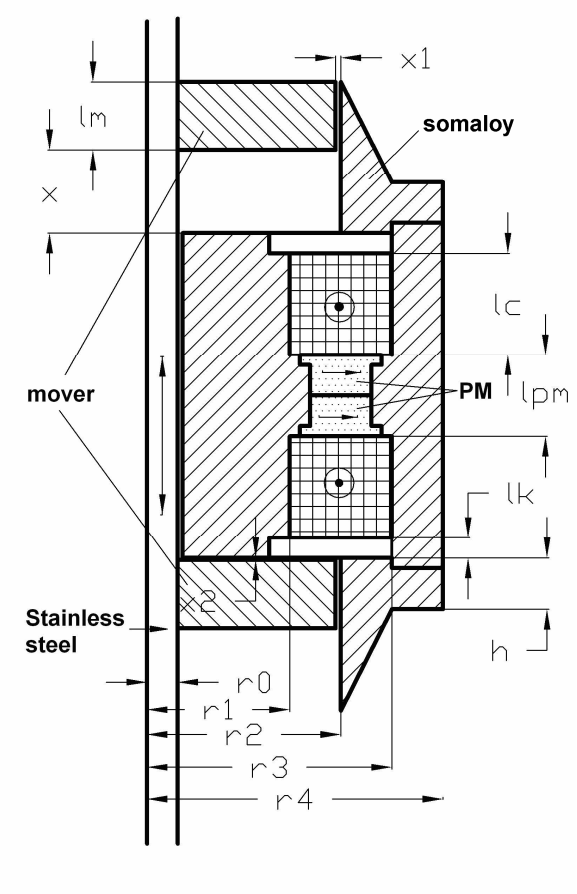

Figure 3.2 Actuator's optimized dimensions

We have chosen to modify the following geometrical parameters:

- r0 – shaft radius;
- r1 – interior stator average radius;
- r2 – intermediate stator interior radius;
- r3 – external stator interior radius;
- r4 – external stator exterior radius;
- lpm – PMs height;
- lc – coils height;
- lm – mover plate height;
- h – intermediate stator external height.

Each of these parameters has been modified in a certain range of values with a certain step. Each variable has an initial value, a final value and a fixed step value.

The objective function consists in satisfying the following conditions:

- $F_{PM} > 300$ N – the cogging force;
- $K_F = F_{max}/ F_{PMmax} > 1.8$ – force coefficient;
- $a_{max} > 5000$ [m/s2] - maximum acceleration;
- $P_{cu} < 120$ [W] – copper losses;

As a constraint, the total volume of the actuator should not exceed $V_t = 0.2$ liters.

The objective function has been FEM evaluated for 2301 situations. In Table 3.1 we have listed only the solutions that fit the conditions.

Table 3.1 – Objective functions selected values

F_{PM} [N]	F_{max} [N]	a [m/s^2]	P_{cu} [W]	V_t [dm^3]
306,38	661,24	4902,4	115,9	0,1521
343,92	**702,01**	**5204,7**	**115,89**	**0,16316**
318,47	677,44	5022,5	96,594	0,17373
370,16	700,97	5197	100,87	0,17461
315,23	698,84	5181,1	115,9	0,17461
258,11	656,22	4865,2	112,58	0,17936
233,34	648,81	4810,2	100,88	0,18041
291,31	648,52	4808,1	82,748	0,1843
340,01	670,54	4971,4	84,062	0,18592
309,63	685,25	5080,4	96,549	0,18592
365,89	659,09	4886,5	90,107	0,18644
385,38	726,05	5382,9	100,88	0,18644
359,89	756,76	4852,2	106,22	0,18959

BUPT

255,71	669,97	4967,2	112,59	0,19075
234,4	655,43	4859,3	100,87	0,19223
328,97	650,22	4820,7	72,067	0,19723
294,12	660,93	4900,1	82,764	0,19723
422,92	766,08	5679,7	112,58	0,19759
359,69	699,88	5188,9	84,078	0,19852
382,01	731,84	5425,9	100,88	0,19867

Considering that the total volume should be as small as possible, having also a good acceleration of the mover and a ratio between the maximum force and the cogging force around 2 (in order to assure lift control), from those 20 solutions we have picked the second one in Table 3.1.

The PM force should be grater than the spring force in order to lock the valve in one of the two extreme positions without power consumption. The coils should be able to "destroy" the entire PM flux in order to release the valve and let the energy stored in the springs to push it to the other end.

The actual valve acceleration after being released is given by the spring force, which should be around 0.9 * F_{PM} ≈ 300 N theoretically. Further in this thesis we will see that the manufactured actuator has suffered some changes due to the available materials used to construct it.

The values of the geometrical parameters of the optimal found topology are: r0=3 mm, r1=14 mm, r2=19 mm, r3=24 mm, r4=29 mm, x=8 mm – valve displacement, x1=0.5 mm – air gap, x2=0.2 mm – air gap, lm=6.68 mm – mover length, lc=12 mm – copper slot length, lpm=8 mm – pm length, lk=2 mm, h=5 mm.

The time necessary to perform the grid search optimization was 6 seconds per iteration, yielding to a total period of 13806 seconds, which means 3 hours, 50 minutes and 6 seconds.

BUPT

3.3 Hooke-Jeeves optimization algorithm

3.3.1 Theoretical background

In the Hooke and Jeeves' method, a sequential technique is used consisting of two moves: exploratory move and the pattern move. Exploratory move is used to explore the local behavior of the objective function, and the pattern move is used to take advantage of the pattern direction [8-12]

For a given step size, which has different values for each coordinate direction, and can change during the optimization search, the exploration proceeds from a given initial point. If the objective function has a "better" value in the new point, the step is considered successful. Otherwise, the step will be modified and the algorithm will search in the opposite direction. The displacement is considered successful depending on the evaluation of the objective function. After investigating all given coordinates the exploratory mode is completed and the resulting point is termed a base point. [2]

The pattern move consists of a single step from the present base point along the line from the previous to the current base point.

Such a point can be calculated using the formula (3.1):

$$x_{k+1} = x_k + (x_k - x_{k-1}) \tag{3.1}$$

The new point x_{k+1} is accepted only if the evaluation of the objective function is improved.

The Hooke-Jeeves algorithm consists in moving a search vector into a N-dimensional space along a direction that minimize an objective function, HJ(x).

We have to establish the following initial conditions:

- the optimized parameters high and low limitations - x_{min}, x_{max};
- the optimized parameters initial value - x_i;
- the maximum and minimum variation of the optimized parametersd - Var_{min}, $dVar_{max}$;
- parameters initial variation values $dVar_i$;
- eps – the HJ(x) lower limit that stops the optimum search;
- initial value of $V_i = HJ(x_i)$ calculated in the initial point.

The search vector has a base value and a peak value.

The algorithm can be divided in 8 basic steps.

BUPT

Step 0. We evaluate the objective function in the base and the head of the searching vector: $H=B=HJ(b_i) = HJ(h_i)$, because $b_i=h_i$;

Step 1. We pick a dimension d (d=1), that corresponds to a certain geometrical parameter that we chose to optimize. We move the head of the searching vector with an initial step (variation) that can be different for all dimensions, in the positive search direction ($h_d = h_d + dVar_d$) and we evaluate the objective function, $H'=HJ(h_d)$. If $H' \leq H$, then $H'=H$ and we move to step 4, otherwise we move to step 2.

Step 2. For the same dimension we make a left displacement of the vector's head ($h_d = h_d - dVar_d$) from the previous initial position v_i. We calculate $H'=HJ(h_d)$. If $H' \leq H$, then $H'=H$ and we move to step 4, otherwise we move to step 3.

Step 3. We reconsider the initial point, h_i.

Step 4. We take into account the next dimension of the N-dimensional space and then we check to see if the number of dimensions (d_{max}) has been exceeded. If not we move to step 1, otherwise of move to step 5.

Step 5. We check if the objective function has a lower value in the head of the searching vector than in the vector base. If not so we move to step 7, otherwise to step 6.

Step 6. If the current value of the objective function is smaller than the lower limit of the objective function then we reach the optimum established and the process stops. If not then we have to consider the new base of the vector as being the actual head and we move to step 0.

Step 7. We return to the initial vector base b_i and we calculate a new, smaller variation for the current dimension, $dVar_{d2} < dVar_d$. We check to see if we have exceed the lower variation limit ($dVar_{min}$). In not then we move to step 0, otherwise we consider that we reached the optimum and the algorithm stops [13-15].

A flowchart of the above described algorithm is shown in Figure 3.3.

BUPT

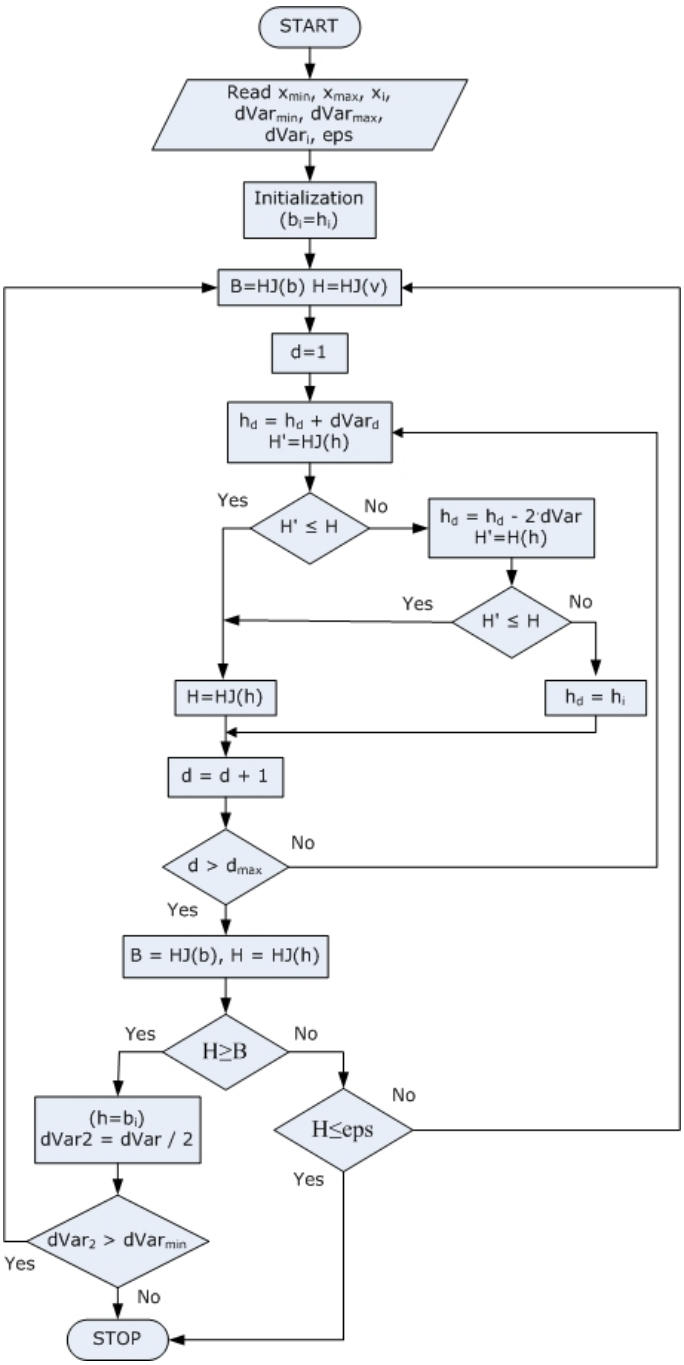

Figure 3.3 Flowchart of the basic Hooke-Jeeves algorithm

A DSP implementation of the Hooke-Jeeves algorithm can be seen in Figure 3.4, [3]. This flowchart gives us a more modular view on what this algorithm is concerning with.

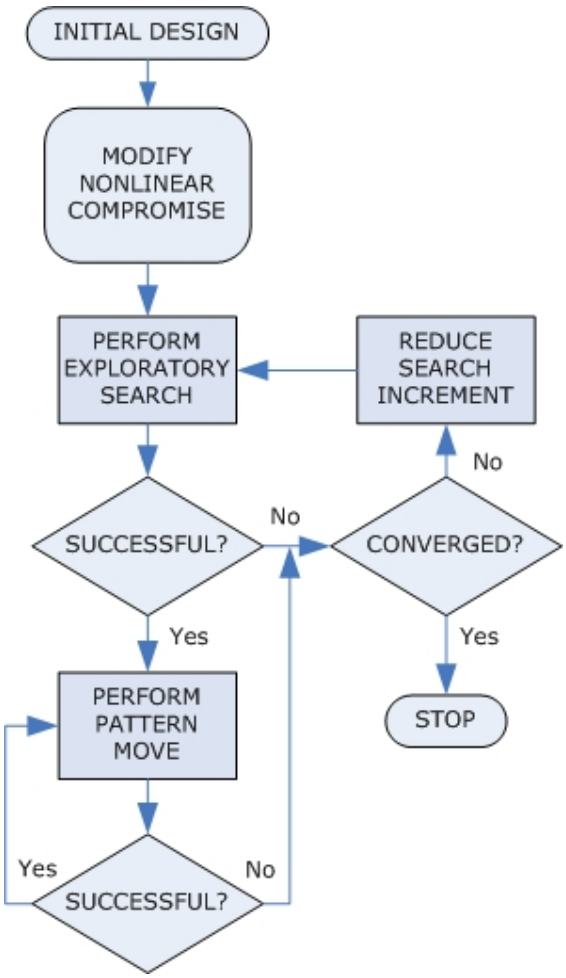

Figure 3.4 Flowchart of DSP Hooke-Jeeves implementation

3.3.2 Modified Hooke Jeeves optimization algorithm

3.3.2.1 Modified algorithm description – exploratory and pattern moves

We will use a modified Hooke-Jeeves algorithm to perform the actuator's optimal design. The algorithm is implemented in Matlab environment that can access FEMM finite element software as an ActiveX client.

This way, one can send commands to the FEMM Lua interpreter and receive the results of the command. To aid in the use of FEMM from Matlab, a toolbox called OctaveFEMM is available. This toolbox implements Matlab commands that subsume the functionality of Lua using equivalent Matlab commands.

The algorithm can be split in the following steps:

Step 1. Establishment of the geometrical variables that we want to optimize. We will group all this variables in a vector Var0 that will contain the variables initial values.

Step 2. We establish for each optimized variable the up and low limits of variation due to some technological mititations or geometrical constraints.

Step 3. We determine the objective scalar function, f_{ob_s}: $R^n \rightarrow R$. Other constraints can be added to this function by considering a penalty function f_{ob_p} : $R^{p+q} \rightarrow R_+$, where p – the number of equality constraints and q – the number of inequality constraints.

The objective function has two parts, as the formula (3.2) shows:

$$f_{ob}(\bar{x}) = f_{ob_s}(\bar{x}) + f_{ob_p}(\bar{x}) \tag{3.2}$$

Step 4. Establishment of the initial values of the optimize vector Var0, the initial step vector dVar0, the minimum allowed values of the initial step vector $dVar0_{min}$, and a ratio that will modify the current step vector r.

Step 5. Evaluate the objective function. This procedure implies calling the FEMM program, compute all LUA commands needed to establish the magnetic type of problem and to introduce the material properties, boundary conditions and circuit properties. Next, all necessary geometrical dimensions are computed and then the objective function can be evaluated.

Step 6. The exploratory move can start. The program makes research movements in the N-dimensional space in the positive and negative directions. Figure 3.5 illustrates the searching process into a bi-dimensional space.

BUPT

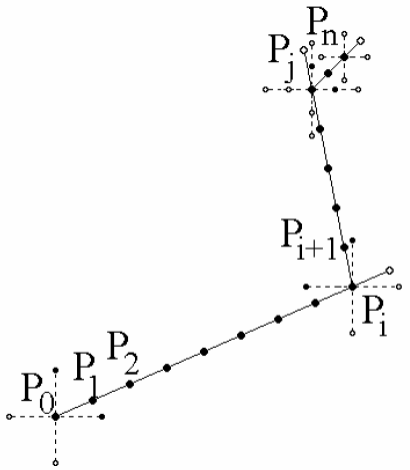

Figure 3.5 Exploratory moves and pattern moves of the Hooke-Jeeves modified algorithm

Referring to Figure 3.5, the filled points correspond to track points, where the objective function has met a local improvement and the empty points correspond to worse points, where the objective function was not successful.

Step 7. The track points become better points when performing pattern moves and the exploratory movement can start again considering the initial values for the algorithms as being the new found better point.

BUPT

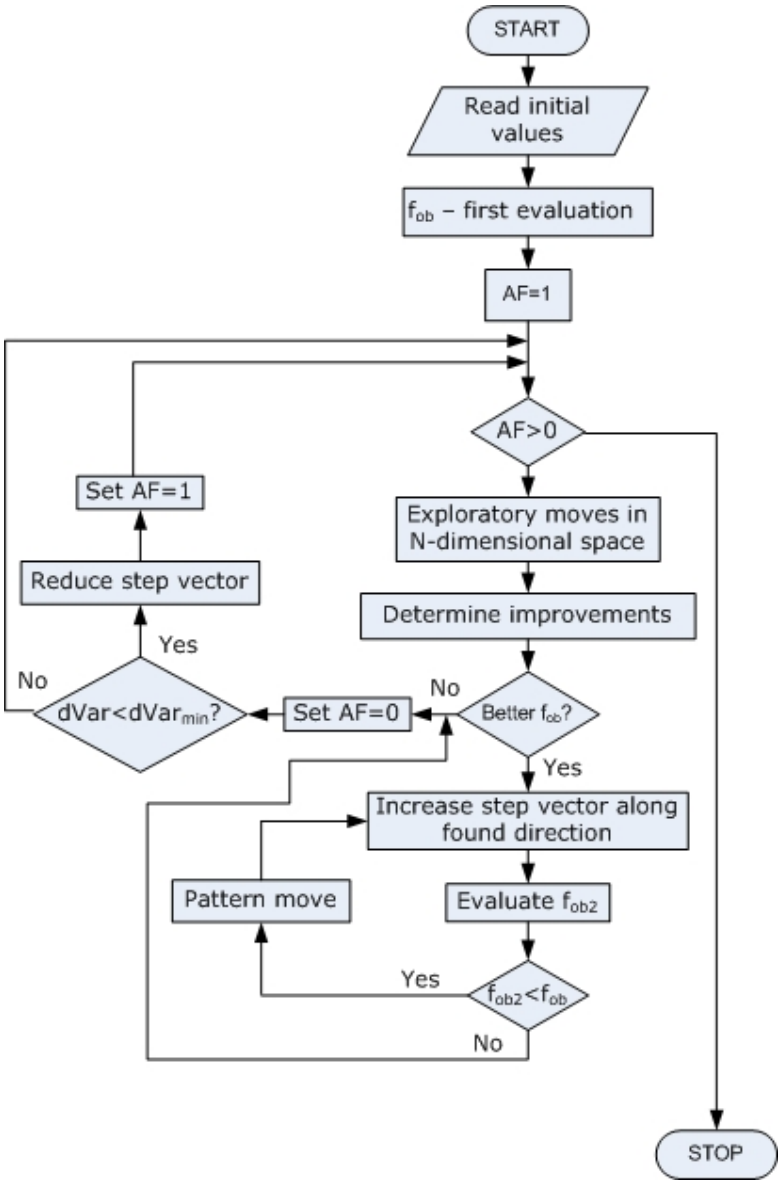

Figure 3.6 Flowchart of the modified Hooke-Jeeves algorithm

3.3.2.2 Variables and Constraints

A large number of variables influences the actuator design, some of them have a great influence and others can be maintained constant or can be expressed as a function of others.

We chose to utilize the following parameters for the optimization design:

- r0 – actuator's shaft radius;
- r10 = r1-r0, r1 – internal stator radius;
- r21 = r2-r1, r2 – interior radius of the intermediate stator, which equals the exterior mover's plate radius plus a certain airgap
- r32 = r3-r2, r3 – exterior stator interior radius;
- r43 = r4-r3, r4 – exterior stator exterior radius;
- lm – mover plate width;
- h – intermediate stator exterior width;
- lc – coil slor width;
- lp – PMs width;
- je – current density.

As one can see we use nine geometrical parameters and an electrical one. Based on the geometrical variables r1, r3 and lc and on the current density we can calculate the current injected in the twin coils. The fill factor was also introduced, Equation (3.3) :

$$I = j_e * (r_3 - r_1) * l_c * k_{fill} \tag{3.3}$$

Where k_{fill} = 0.5 and is a constant.

As we will see in the next section the objective function calculation needs information about mover acceleration and total volume. The last one is easy to calculate knowing all geometrical variables. To obtain the acceleration we need Atomet-EM1 density, Stainless steel density and the valve mass, Equation (3.4) :

$$acc = \frac{F}{\rho_{Atomet} \cdot 2 \cdot V_{mover} + \rho_{Steel} \cdot V_{shaft} + m_{valve}} \tag{3.4}$$

Where: F – developed force, ρ_{ATOMET} = 7.1 g/cm^3, ρ_{STEEL} = 7.8 g/cm^3, and the valve plus valve's stem is around 40 grams.

The Atomet-EM1's density is, however an average one, because the exact value depends on the compacting pressure exerted when manufacturing the material, Figure 3.7 .

BUPT

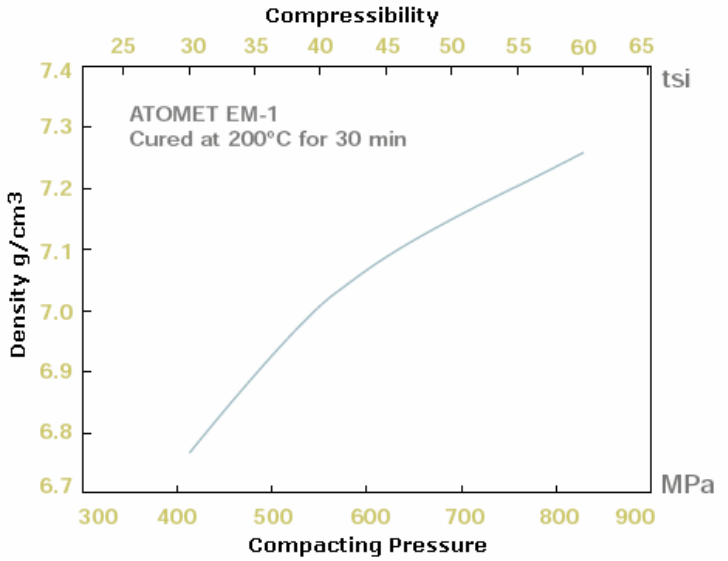

Figure 3.7 Atomet-EM1 compressibility

3.3.2.3 Objective function calculation

The implemented objective function has expression given in equation (3.5):

$$f_{ob} = P_{cu}(p_f + p_a + p_v + 1) \tag{3.5}$$

Where:

- P_{cu} – copper losses – FEMM derived
- p_f - the force penalty factor;
- pa - the acceleration penalty factor;
- p_v - the volume penalty factor

The penalty factors tend to increase the objective function if the corresponding constraints are not satisfied.

These factors are calculated as follows, formulas (3.6), (3.7) and (3.8):

$$p_f = k_f \left(\frac{F_{PM\,\min}}{F_{PM}} \right)^2 \text{, if } F_{PM} < F_{PMmin}\text{, otherwise } p_f = 0; \tag{3.6}$$

$$p_a = k_a \left(\frac{acc_{\min}}{acc} \right)^2 \text{, if } acc < acc_{min}\text{, otherwise } p_a = 0; \tag{3.7}$$

$$p_v = k_v \left(\frac{V_T}{V_{T\max}} \right)^2 \text{, if } V_T > V_{Tmax}\text{, otherwise } p_v = 0; \tag{3.8}$$

Where: $k_f = k_a = 5$ and $k_v = 1$;

The values for F_{PM}, acc and V_T – are determined by interrogating the FEMM program connected to Matlab environment.

The acceleration is calculated dividing the total force developed to the mover mass. Two FEMM interrogations per exploratory move are needed: one with no current (in order to fetch the cogging force) and one with current in order to obtain the maximum force and the copper losses.

3.3.2.4 Optimization results

Figure 3.8 illustrates the Objective function evolution as the exploratory search increase in iterations.

We chose to start the optimization process from four different initial points: the maximum values allowed for each dimension, the minimum values, a random selection of these values and the optimal point obtained from the previous grid search optimization.

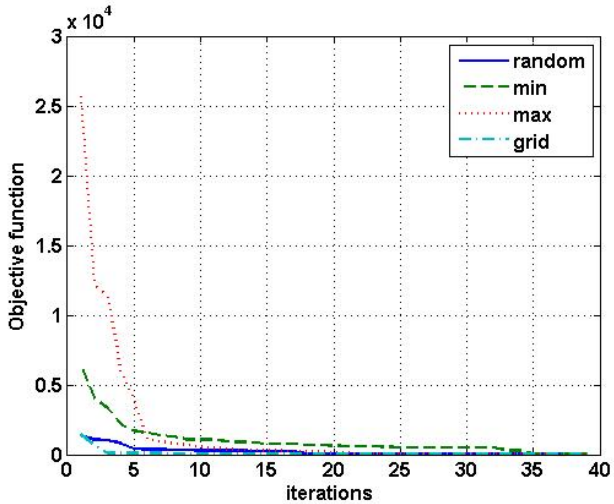

Figure 3.8 Objective function evolution versus program iterations

We can observe that the initial evaluation of the objective function is closer to the final evaluation, when starting the Hooke-Jeeves optimization process from values obtained before from grid search optimization. Furthermore, after only 6 iterations the objective function has been improved by 92%, which is the best improvement rate for all four cases.

Copper losses evolution with program exploratory and pattern iterations are shown in Figure 3.9. As can be seen the worse starting point is from the maximum values as in the objective function presented above. Here minimum value possible is needed.

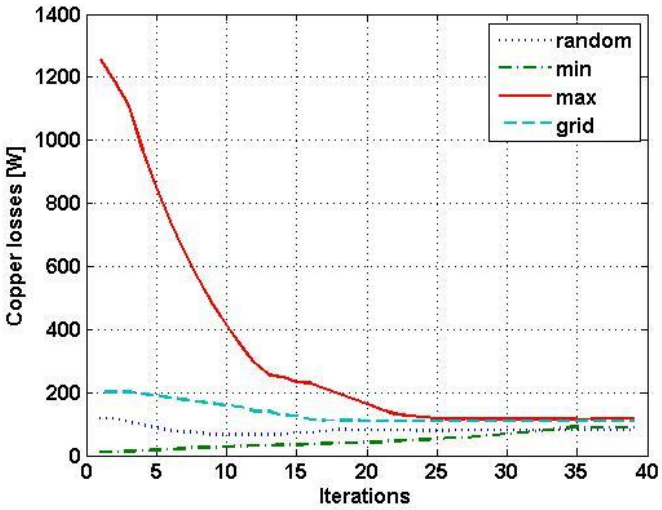

Figure 3.9 Copper losses evolution versus program iterations

The evolution of the cogging force along the iterations is illustrated in Figure 3.10. In this case the force needed is around 350 N.

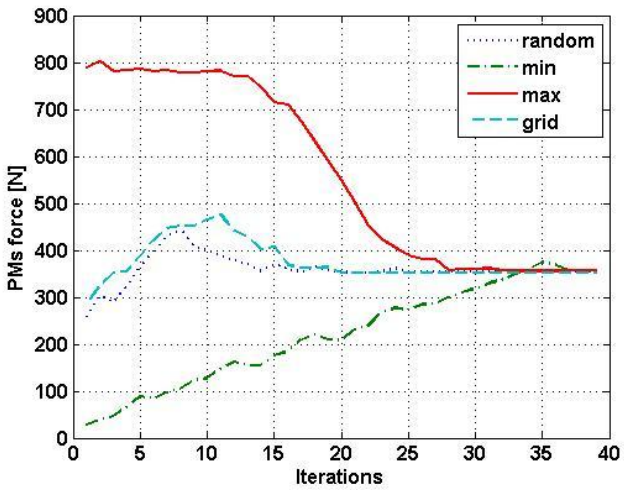

Figure 3.10 Cogging force evolution versus program iterations

The moving part acceleration to desired value convergence is illustrated in Figure 3.11

BUPT

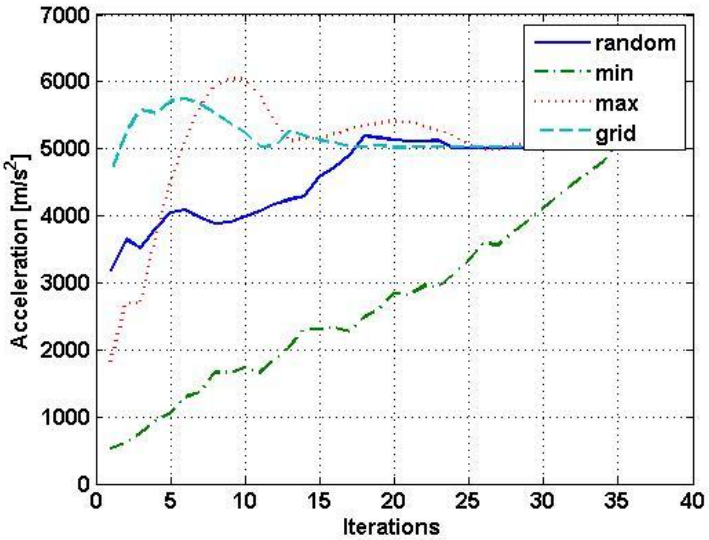

Figure 3.11 Acceleration evolution versus program iterations

The maximum acceleration needed is around 5000 m/s2.

The total volume of the actuator should be smallest as possible. In this case we can see that the program has found quite different values after performing the optimization. However all values indicate a volume lees than 0.2 liters, Figure 3.12.

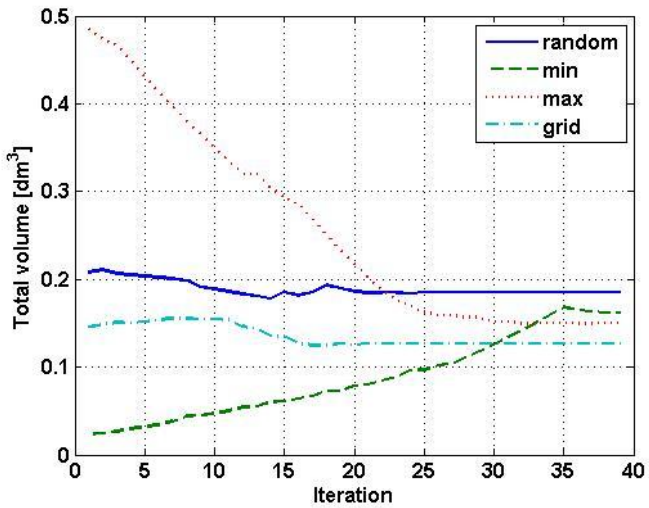

Figure 3.12 Total volume evolution versus program iterations

An important observation has to be made. In all the presented entities evolutions above the program reaches the desired value in all cases with the minimum number of iterations when starting from the previous optimal point obtained from grid search optimization.

Even if the final results after performing two different optimizations are not exactly the same, they look satisfactory.

The obtained geometrical dimensions in all four cases are presented in Table 3.1

Table 3.2 Obtained geometrical parameters

	r0	r10	r21	r32	r43	lm	h	lc	lpm
min	4.5	10	4.9	5.8	6	7.1	6.2	9.66	11
max	4.6	9.7	4.84	5.62	5.38	6.65	5.41	9.22	11.2
random	4.36	10.17	5.2	4.8	5.36	7.19	6.16	9.56	10.8
grid	5	9	5	5	5	6.7	6	10	10

The values are more or less close to the ones obtained from the grid search optimization. However, this optimization method is accurate when searching a local minimum within a relatively small domain.

In addition, if we compare the time needed to compute the two optimization algorithms, Grid Search and Hooke-Jeeves (all three cases: min, max and random), we conclude that with the last one good results emerge quickly, see Figure 3.13

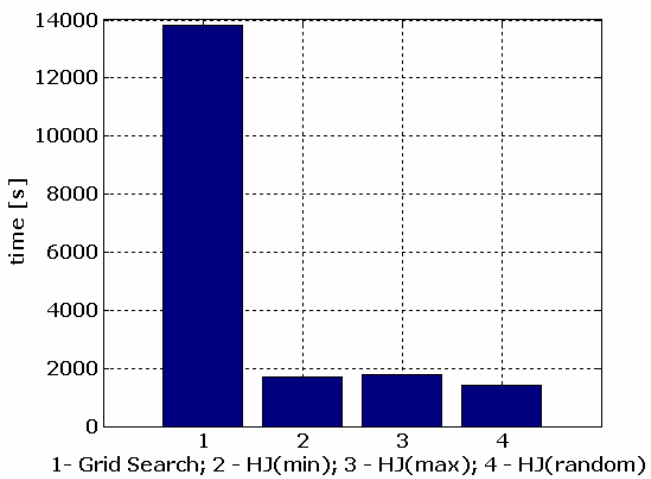

Figure 3.13 Optimization algorithm used versus time needed to realized

SUMMARY

This chapter deals with the actuator optimization process based on FEA results. Finite-Element methods allows for the development and optimization of new devices without the necessity of extensive prototyping, which is a more economical approach. Direct and indirect search algorithms with short descriptions are listed. Two algorithms are presented and utilized in out optimal design process: grid search and Hooke-Jeeves. Although the grid search technique is more reliable it becomes impractical with increasing dimensions. While computationally much less demanding than a grid search, the success of a Hooke-Jeeves algorithm is heavily dependent upon the choice of the starting point. In our case, with both algorithms, we obtain relatively the same results, but Hooke-Jeeves has proved to be more time and resources saving.

CHAPTER 3 - REFERENCES

[1] D Nagesh Kumar - „Optimization Methods: Advanced Topics in Optimization - Direct and Indirect Search Methods „, Bangalore

[2] Rao, S.S. – „Engineering Optimisation: Theory and Practice", Wiley, 1996

[3] Hamin R. Parsaei, Jian Dong – „Rapid Response Manufacturing – Contemporary methodologies, Tools and Technologies", Chapman and Hall, 1996

[4] R. Fletcher, "Function minimization without evaluating derivatives | a review", The Computer Journal, 8 (1965), pp. 33-41.

[5] R. Fletcher and M. J. D. Powell, "A rapidly convergent descent method for minimization, The Computer Journal", 6 (1963), pp. 163-168.

[6] R. Hooke and T. A. Jeeves, "Direct search solution of numerical and statistical problems", Journal of the Association for Computing Machinery, 8 (1961), pp. 212-229.

[7] R. M. Lewis, V. Torczon, and M. W. Trosset, *Why pattern search works*, Optima, (1998), pp. 1-7. Also available as ICASE Technical Report 98-57. ICASE, Mail Stop 132C, NASA Langley Research Center, Hampton, Virginia 23681-2199.

[8] J. A. Nelder and R. Mead, A simplex method for function minimization, The Computer Journal, 7 (1965), pp. 308-313.

[9] M. J. D. Powell, "An efficient method for finding the minimum of a function of several variables without calculating derivatives", The Computer Journal, 7 (1964), pp. 155-162.

[10] H. H. Rosenbrock, An automatic method for finding the greatest or least value of a function, The Computer Journal, 3 (1960), pp. 175-184.

[11] V. Torczon, "Multi-Directional Search: A Direct Search Algorithm for Parallel Machines", PhD thesis, Department of Mathematical Sciences, Rice University, Houston, Texas, 1989; available as Tech. Rep. 90-07, Department of Computational and Applied Mathematics, Rice University, Houston, Texas 77005-1892.

[12] F. H. Walters, L. R. Parker, Jr., S. L. Morgan, and S. N. Deming, "Sequential Simplex Optimization", Chemometrics Series, CRC Press, Inc., Boca Raton, Florida, 1991

[13] M. H. Wright, "Direct search methods: Once scorned, now respectable", in Numerical Analysis 1995 (Proceedings of the 1995 Dundee Biennial Conference in Numerical Analysis), D. F. Griths and G. A. Watson, eds., Pitman Research Notes in Mathematics, Addison Wesley Longman, 1996, pp. 191-208.

[14] R. M. Lewis and V. J. Torczon, "Rank ordering and positive bases in pattern search algorithms", Tech. Rep. 96-71, Institute for Computer Applications in Science and Engineering, Mail Stop 132C, NASA Langley Research Center, Hampton, Virginia 23681-2199, 1996.

[15] K. I. M. McKinnon, "Convergence of the Nelder-Mead simplex method to a non-stationary point", SIAM Journal on Optimization, 9 (1998), pp. 148-158.

Chapter 4 Open loop Control - Simulation and experimental results

4.1 Introduction – Open Loop Control Systems

A system that has its outputs changed in a prescribed way by means of intelligent manipulations of its inputs can be referred as a controlled system.

Open loop control of a system is mainly characterized by the lack of the feedback control loop. This type of control uses only the current state of the system controlled and its model to drive it. An open-loop control does not observe the output of the system that it is controlling, there by it can not compensate for any errors that may appear in the output. The only thing it compensates is the action of disturbances for which it has been designed, other disturbances will not be removed [1-5].

An open-loop control can not become unstable as long as the controlled system is stable.

This type of control is well suited for systems were the relationship between the input and the output can be modeled by a mathematical formula.

The general structure of a multivariable control system is shown in Figure 4.1, [1].

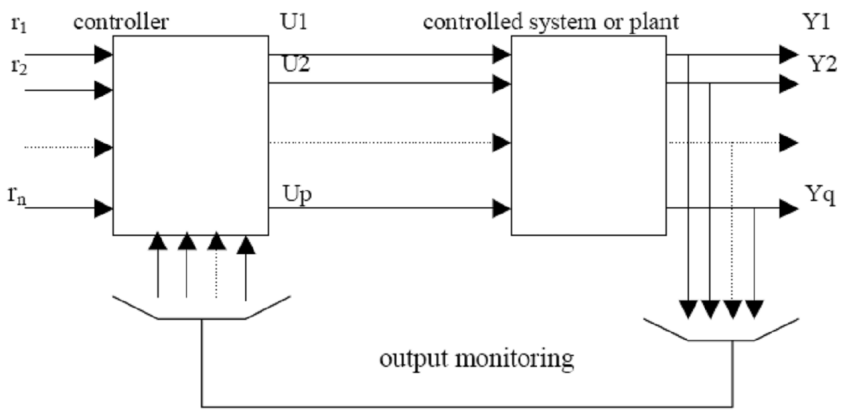

Figure 4.1 General structure of an open loop control system

The controlled system is generally a fixed component of the system whose physical characteristics are beyond control. The output of the controlled system is measured by *q* variables Y1(t), Y2(t), …,Yq(t) whose values give an indication of plant behavior. Direct control of the plant is exerted by means of controlling the quantities U1(t),…,Up(t). These quantities are applied by some controlling device, called controller which determines proper control action based upon the reference commands R1(t), …,Rq(t) and information obtained via output sensors concerning the actual output. In this type of systems, the controller operates on some pre-set pattern without taking account of the outputs [6-10].

4.2 Open-loop U/f dynamic control – simulation and experimental validation

In order to perform an open loop control, the actuators model must be first established. The model comprises the electrical part and the mechanical one. Both parts need FEM derived data to calculate inductances, motion induced voltages and forces.

The dynamic model equations are:

$$V = R \cdot I + \frac{d\varphi(I,x)}{dt} \tag{4.1}$$

$$F = m \cdot \frac{d\overset{*}{x}}{dt} = F(I,x) - k \cdot x - FC - F_{load} \tag{4.2}$$

Where:

- V – applied voltage;
- R – stator resistance;
- I – the current through the two twin coils connected in series;
- φ(I,x) – total flux, which is a function of current and position;
- m – the mover mass plus the mass of the rod and the valve;
- x – mover position;
- F(I,x) – actuator developed force;
- k – the spring constant;
- FC - Coulombian Friction force;
- F_{load} – load force implemented as a damping force.

The maximum force developed by the spring F_{spring} = - k * x_{max} should be smaller than the cogging (magnet) force in order to hold the valve in the close or

BUPT

open position without current consumption. The force created by the coils has to be almost equal to that developed by the magnets because we have to control the lift of the valve by being able "to destroy" at any moment the PM flux. The potential energy stored in the springs moves the rod. FC represents the Columbian friction that appears at low speeds [2].

The electrical part of the actuators model is illustrated in Figure 4.2.

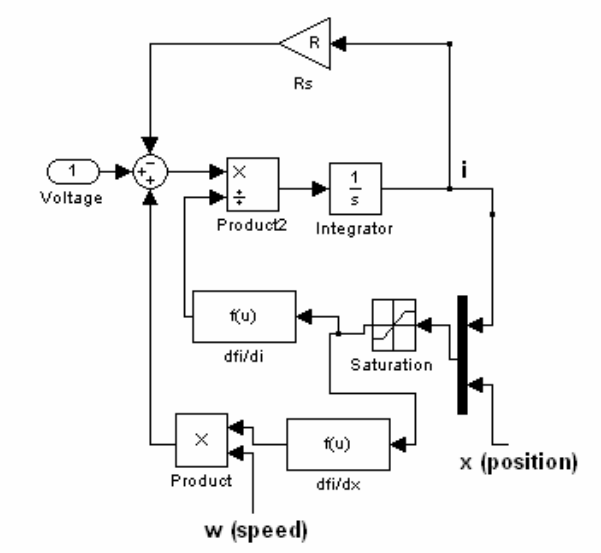

Figure 4.2 Electrical part of the actuator model

The variation of total flux with current and position is a FEM derived data and it is illustrated in 3D in Figure 4.3.

In order to utilize in the dynamic model this variation and avoid using Look-up Tables a polynomial surface fitting process was made and the results are shown in 2D in Figure 4.4.

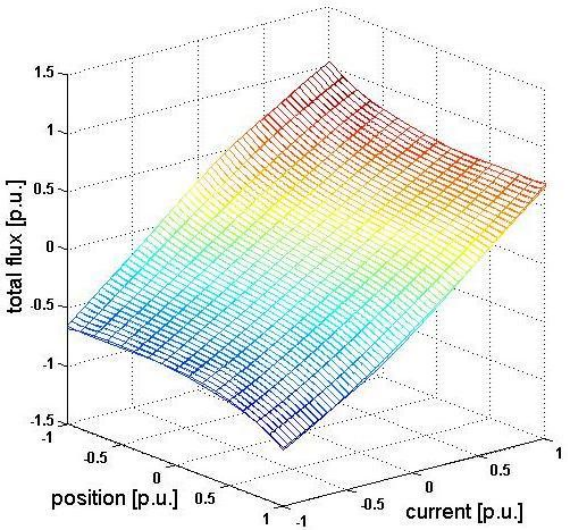

Figure 4.3 3D plot of the total flux variation with current and position

In order to obtain a well-scaled fitting process all involved variables were transformed in Per Unit. The base values are: Φb = 0,63243 mWb, xb = 4 [mm] and Ib = 25A.

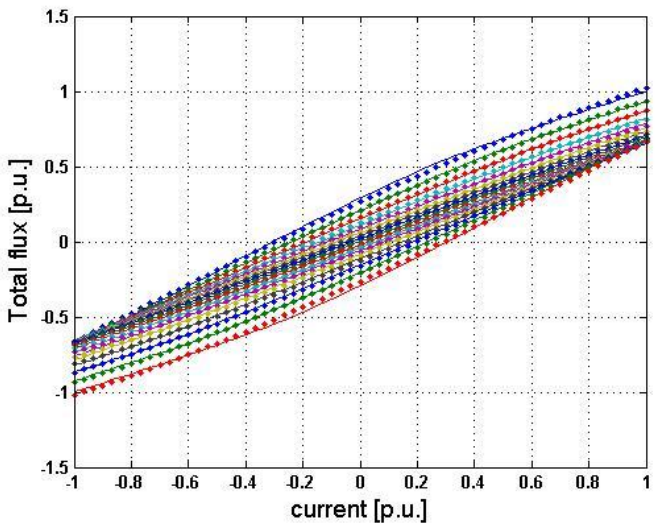

Figure 4.4 2D plot of the total flux variation with current for different position, dots correspond to surface fitting values and lines to FEM derived values

The polynomial fitting process for the actuator's total flux variation with current and position was made using formula (4.3):

$$\Phi = c_1 x^3 + c_2 x^2 y + c_3 x y^2 + c_4 y^3 + c_5 x^2 + + c_6 xy + c_7 y^2 + c_8 x + c_9 y + c_{10} \qquad (4.3)$$

The above formula is describing a third order polynomial function.

The surface fitting program is using the least squares method to determine the polynomial function coefficients.

The mechanical part of the model is illustrated in Figure 4.5. The same third order polynomial fitting process was applied to FEMM in order to obtain a function of two variables for the electromagnetic force. The mover mechanical limitation is simulated by adding to the spring force another "spring", which has a very high constant (k=5.000.000 N/m).

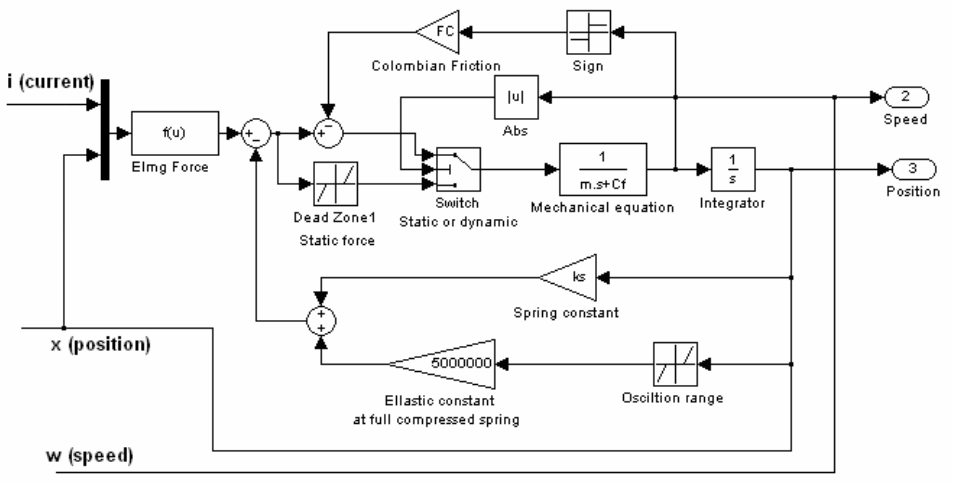

Figure 4.5 Mechanical part of the actuator model

The mechanical simulation has as an input the force developed by the actuator. In order to obtain this force we made an another surface fitting process based on it's variation with current and position.

Figure 4.6 illustrated the fitting process results obtained.

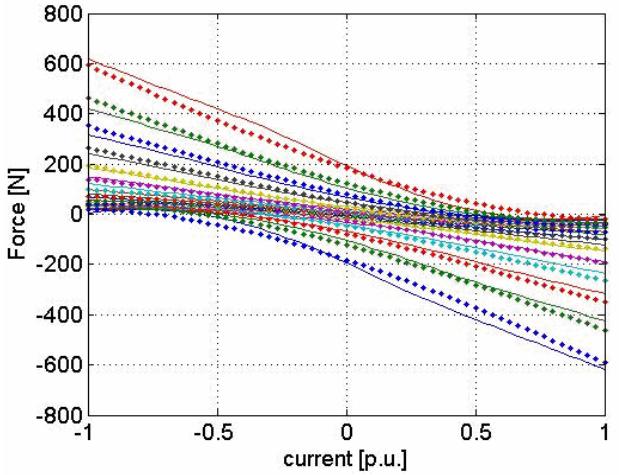

Figure 4.6 FEMM derived force (line) and fitted (dots) / current / position

The damping coefficient can be determined experimentally according to the amplitudes of the impulses response of the mechanical system using the logarithmic decrement method [11-14].

U/f open loop experiments were made for various frequencies, however we will illustrate here only the results obtained for 60 Hz and 80 Hz frequency sinusoidal voltage applied to the actuator coils (two coils connected in series).

Figure 4.7 a) and b) illustrates the current and position response in both cases: simulation and experiments, for a 60 Hz oscillatory motion.

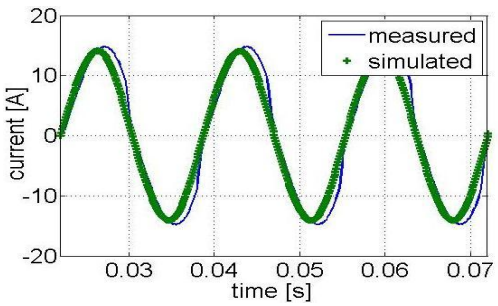

a)

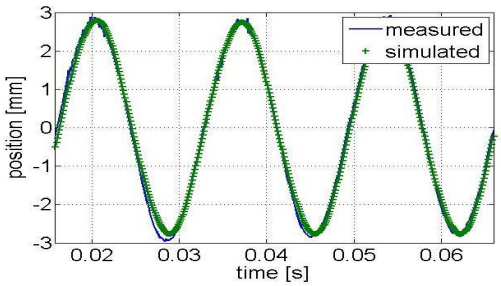

b)

Figure 4.7 Current a) and position b) response for a sinusoidal voltage having 10 V amplitude and 60 Hz frequency

Figure 4.8 a) and b) illustrates the current and position response (simulation and experiments) for a 80 Hz oscillatory motion.

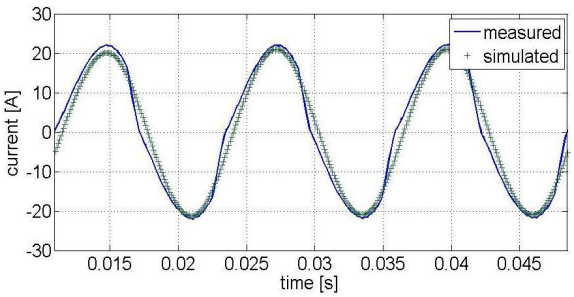

a)

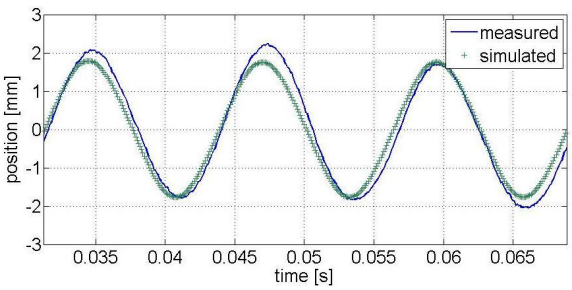

b)

Figure 4.8 Current a) and position b) response for a sinusoidal voltage having 20 V amplitude and 80 Hz frequency

The actuator model was constructed using Matlab/Simulink environment. The manufactured model was controlled using a DSpace platform.

BUPT

The dynamic model uses F(I,x), φ(I,x) and L(I,x) functions extracted from FEM analysis in order to implement the dependencies of force, flux and inductance on position and current.

Given the complexity of the machine behavior (with magnetic saturation playing a strong role) we anticipate that the agreements between the model and experiments are satisfactory.

BUPT

4.3 Open-loop I/f dynamic control – simulation and experimental validation

I/F open loop control was also implemented. Here experimental position response for 40Hz and 70Hz oscillatory motion frequency and various current amplitudes has been performed.

Figure 4.9 shows the actuator position response for a sinusoidal current having 5A (Figure 4.10) amplitude and 40 Hz frequency, for both cases: digital simulations and experiments.

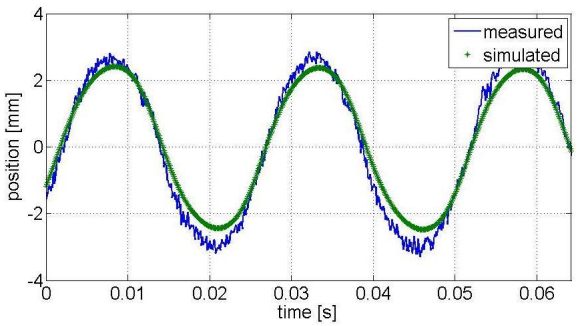

Figure 4.9 Position response for an injected sinusoidal current having 5 A amplitude and 40 Hz frequency

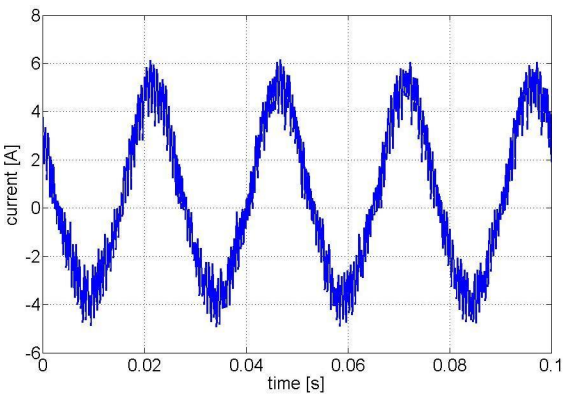

Figure 4.10 Injected current for a 40Hz oscillatory motion having 2.3 mm amplitude

The position is measured using a high speed analogue sensor which has a measuring range of 100 mm. For a 8 mm actuator stroke, in order to avoid a good part of the measured position noise we used a filter to eliminate chattering.

Figure 4.11 illustrates the position response when applying a sinusoidal current having 18A in amplitude (Figure 4.12) and 70Hz frequency. Again the agreement between theory and experiments looks satisfactory.

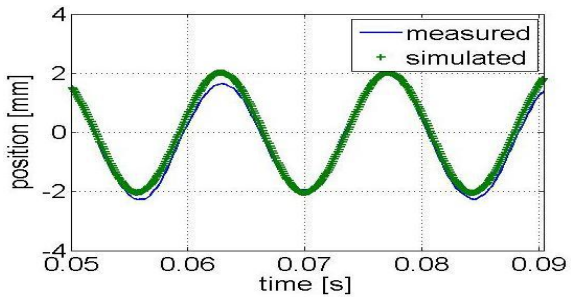

Figure 4.11 Position response for an injected sinusoidal current having 18 A amplitude and 70 Hz frequency

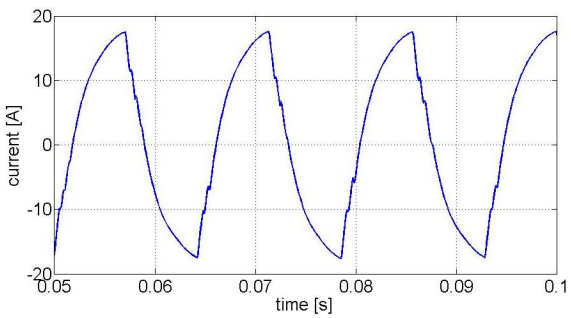

Figure 4.12 Injected current for a 70Hz oscillatory motion having 2 mm amplitude

The experiments were made using a DC source having 32 V as the maximum dc voltage and 20A the maximum supplied current. The triangular shape of the measured currents shows that the PI regulator needs more voltage to realize the desired sinusoidal shape.

BUPT

4.4 Position estimation using FEM derived dependencies

4.4.1 A FEM derived position estimation

The use of an electromagnetic actuator for valve movement poses delicate control problems. The speed of the valve near both ends of the stroke should be around 0.3 m/s in order to reduce acoustical noise and wear of the valve chair. To realize the soft touch functionality, feedback control is needed due to the instability of the system near the stroke ends.

In this section we are presenting two position estimators that may be used in future work to realize sensorless feedback control.

Both estimators use FEM derived functions that express the dependencies of position on the main flux in the motor and the current in the twin coils. Using a third order polynomial surface fitting (least square method) based on formula (4.4), we obtained the polynomial coefficients of the position function, from φ(I,x).

$$x = c_1 \quad ^3 + \quad ^2 + \quad ^2 + \quad ^3 + \quad ^2 + \quad ^2 + \quad + \quad + \quad + \quad \tag{4.4}$$

Figure 4.13 illustrates the position reconstructed using surface fitting based on FEM Analysis data.

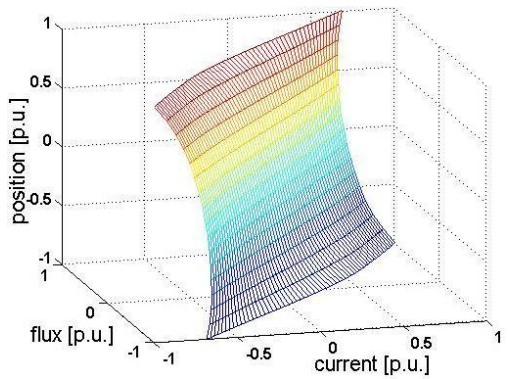

Figure 4.13 Position reconstruction using surface fitting process

In order to obtain a good scaling of matrixes of the surface fitting program we chose to transform all variables in per unit.

BUPT

Figure 4.14 illustrates the position estimator that utilize the main coils to obtain the position and Figure 4.15 shows the estimator based on extra coils.

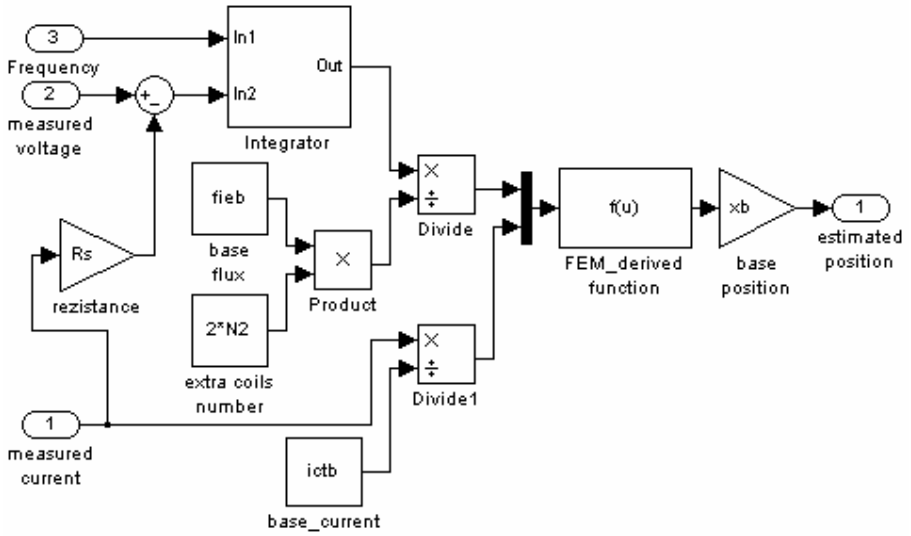

Figure 4.14 Main flux estimator Simulink scheme

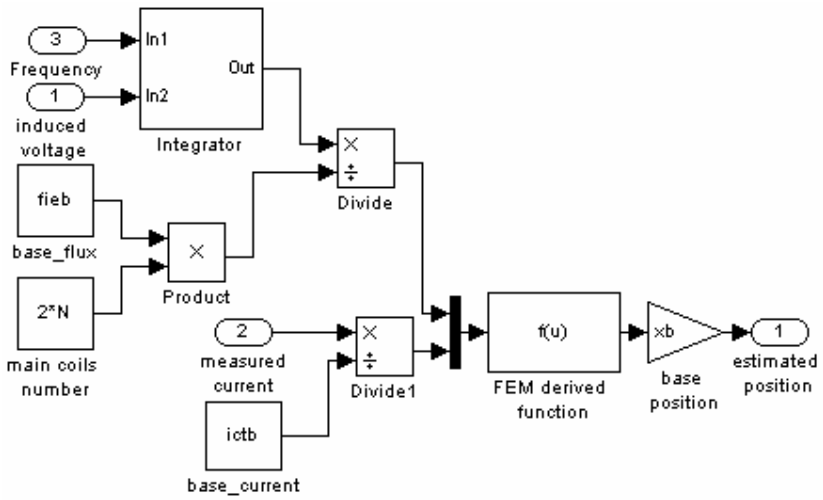

Figure 4.15 Extra flux estimator Simulink scheme

Having these dependence and introducing it in the open loop program, implemented in Simulink and converted into a real time simulation running on DSpace hardware, we were able to test the two estimators presented in what follows.

BUPT

One estimator (φ_m output) is using the main coils voltage (U) and current (I) to calculate the total flux and the other (φ_e out) is using some extra coils inserted near the main coils to calculate the same flux, formulas (4.5) and (4.6):

$$\varphi_m = \varphi_{m0} + \int (U - R \cdot I)dt \tag{4.5}$$

$$\varphi_e = \varphi_{e0} + \int U_e dt \tag{4.6}$$

Where:

- φ_m – total flux of the motor;
- U, R, I – voltage applied, resistance of the coils and current through the coils;
- φ_e – extra flux obtained from extra coils;
- φ_{e0}, φ_{m0} – the initial values for fluxes;
- U_e – induced voltage in extra coils;
- $2N_1$=100 – the number of turns per main coils;
- $2N_2$ =10 – the number of turns per extra coils.

The integrator must be periodically reset in order to compensate the effect of integration drift due to offsets and uncertainties. This reset can be made when the actuator is in a known operating condition, so that the initial condition is known. Instead we have used for integration the following transfer function, :

$$H(s) = \frac{s}{s^2 + 2 \quad _0 + \frac{2}{0}} \tag{4.7}$$

where: ω_0 = 3.14 rad/s; ς = 1;

This function acts as an integrator for high frequencies, with small phase and amplitude errors, rejecting the continuous component.

The Bode diagram of this transfer function is illustrated in Figure 4.16 . As one can see, the magnitude response is quite similar to an integrator, but the phase response is acceptable only after 125 rad/sec, which corresponds to 20 Hz frequency.

Therefore in order to utilize the expression (4.7) as an integrator for frequencies below 20 Hz we need the compensate this phase shortcoming.

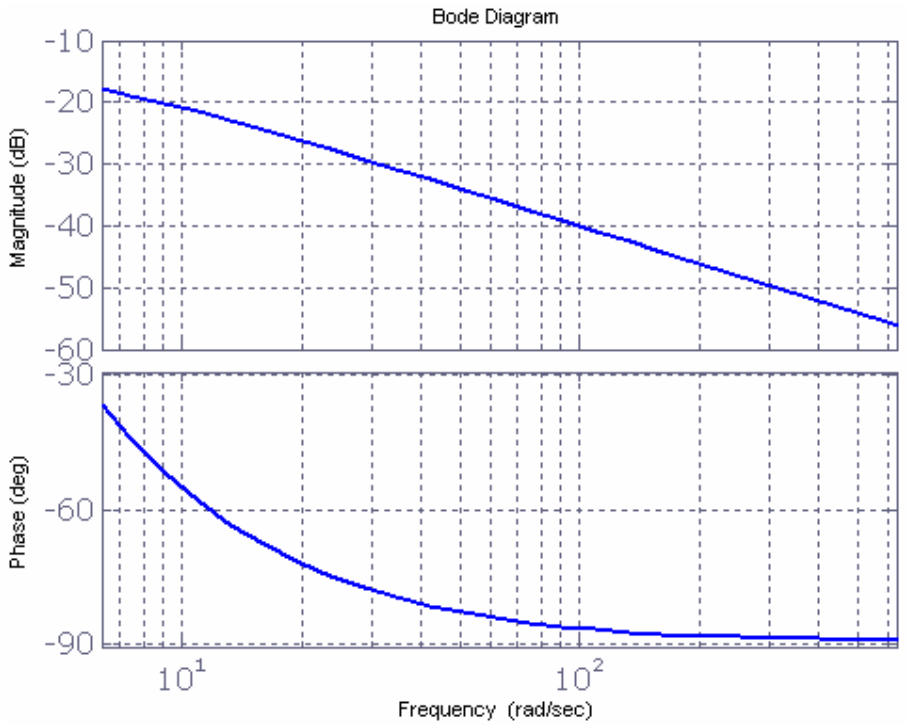

Figure 4.16 Bode diagram of the utilized transfer function

Figure 4.17 illustrates the block diagram of utilized integrator.

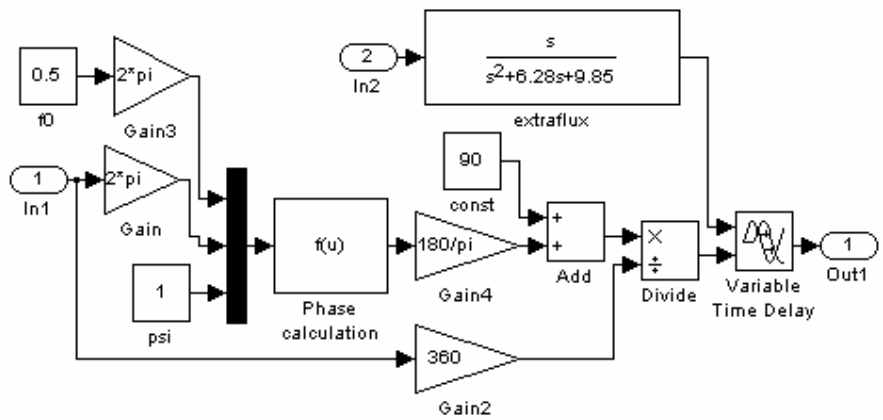

Figure 4.17 Compensated phase integrator diagram

The phase calculation function present in Figure 4.17 is based on Equation (4.8):

$$\varphi = \frac{\omega_0^2 - \omega^2}{2 \cdot \omega_0^2 \cdot \omega^2 \cdot \xi} \tag{4.8}$$

Figure 4.18 illustrates the integrator function response when a applying a sinusoidal signal at it's input having 1 Hz frequency.

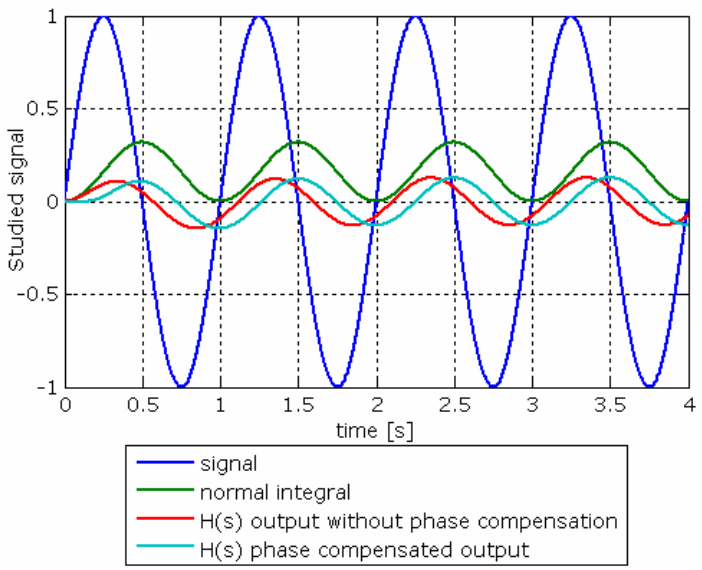

Figure 4.18 Integrator Function response when supplying a sinusoidal signal having the amplitude equal to 1 and 1 Hz frequency

The Integral function H(s) automatically corrects the phase of the output signal so that it remains exactly -90 degrees, same as a pure integrator.

4.4.2 Position estimation validation when performing U/f open loop control

Figure 4.19 show the position estimation using both fluxes (main flux) φ_m and (extra flux) φ_e when applying U/f open loop control for 30, 60, and 80 Hz frequency.

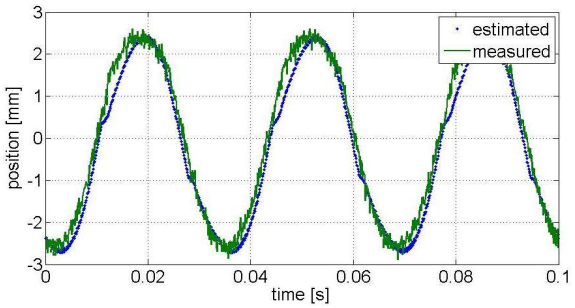

a1) extra coils φe, U/f, 30 Hz

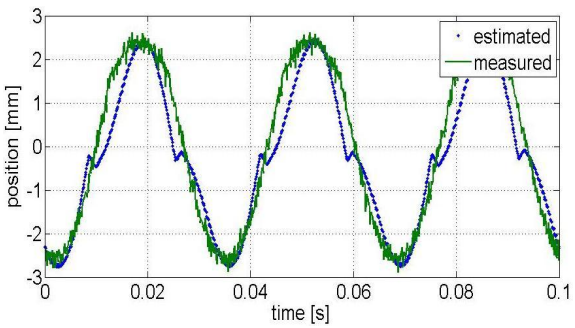

b1) main coils φm, U/f, 30 Hz

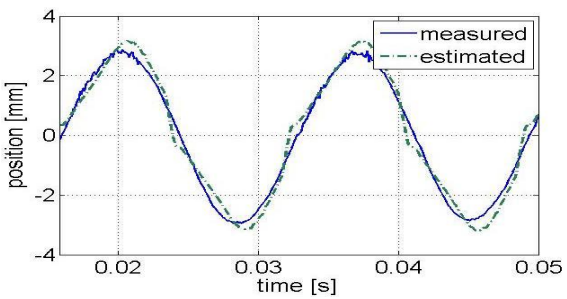

a2) extra coils φe, U/f, 60 Hz

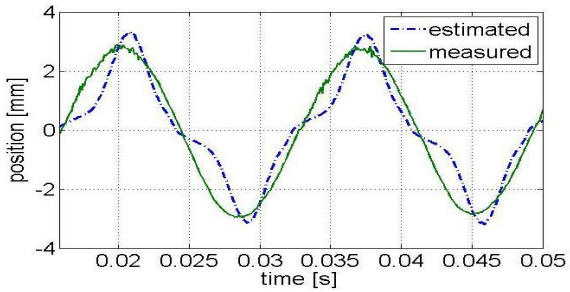

b2) main coils φm, U/f, 60Hz

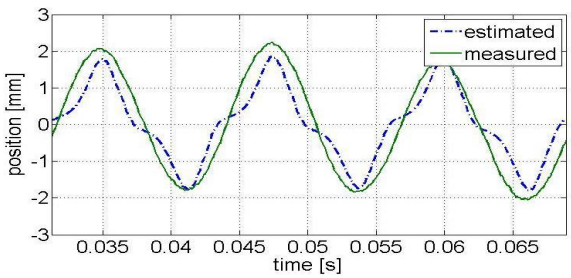

a3) extra coils φe, U/f, 80 Hz

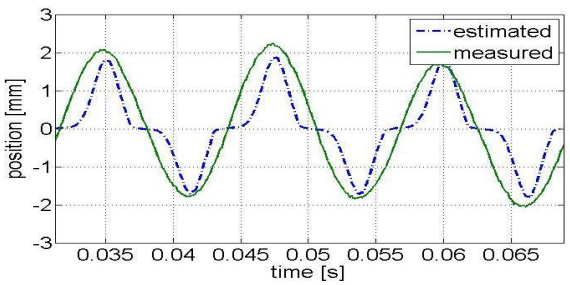

b3) main coils φm, U/f, 80 Hz

Figure 4.19 Estimated position using extra flux a) and main flux b) U/f open loop control @ 30, 60, 80 Hz sinusoidal voltage

After testing the estimators for a U/f open loop control of the actuator we observe that the position obtained using extra coils traces better the measured one for low frequencies. At high frequencies both estimated positions lose their sinusoidal form. The position estimated from the flux obtained from the main coils is subjected to resistance variations, due to high temperatures generated by high currents at high dynamics demands.

4.4.3 Position estimation validation when performing I/f open loop control

In order to realize I/f open loop control, a PI regulator implementation was needed, Figure 4.20. The Multiport Switch selects, based on the sign error, which control strategy should be applied (U>0, U=0 or U<0) in order to decrease the error. Such a control strategy selects which IGBT of the single phase inverter should be turned on or off and what is it's duty cycle. However a more detailed explanation will be presented in Chapter 6.

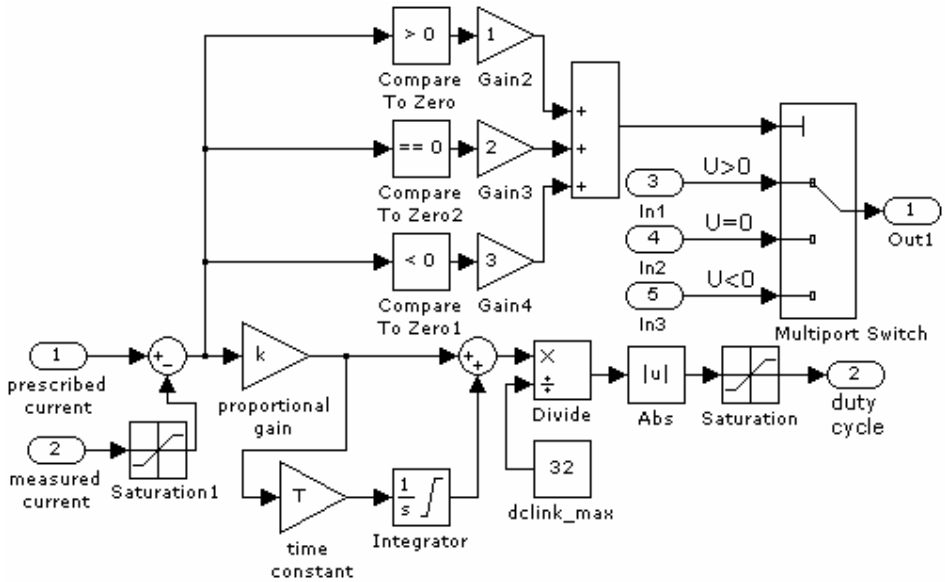

Figure 4.20 PI current regulator

I/f open loop control was also performed at 5, 10, 20, 30, 40, 50, 60, 70, 80, 90 Hz to see how the estimators work. Figure 4.21 and Figure 4.22 illustrate the measured and estimated position in both cases (with extra and main coils) for a prescribed sinusoidal position having 5 Hz frequency and 1 mm, respectively 1.5 mm amplitude.

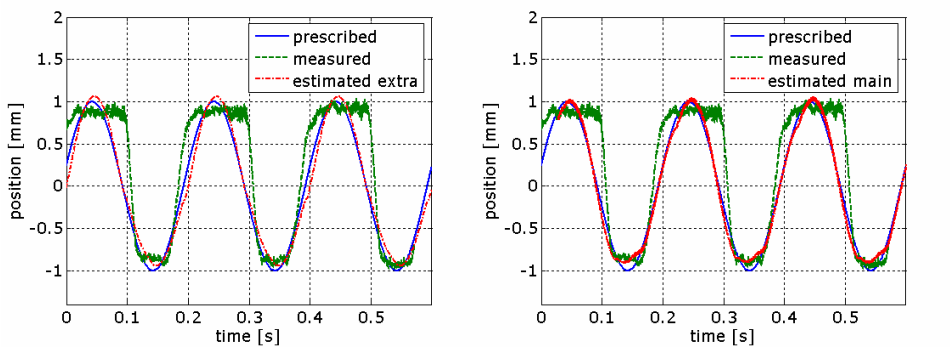

a) b)

Figure 4.21 1 mm @ 5 Hz, I/f open loop control, a) extra coils φe, b) main coils φm

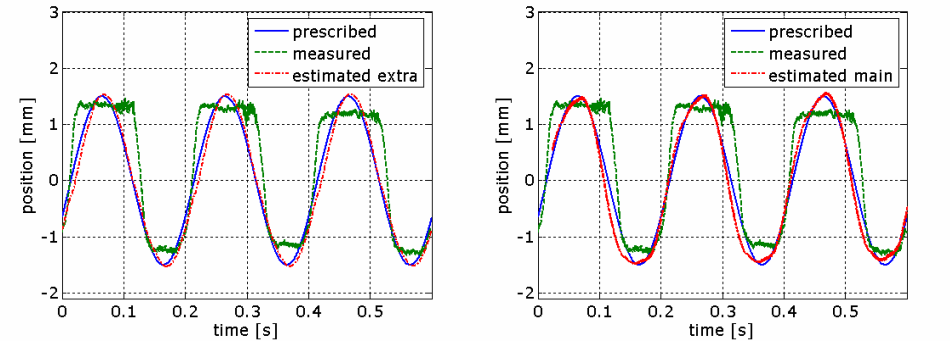

a) b)

Figure 4.22 1.5 mm @ 5 Hz, I/f open loop control, a) extra coils φe, b) main coils φm

For a desired position having 10 Hz frequency and various amplitudes (1, 1.5 mm) the results obtained experimentally are illustrated in Figure 4.23 and Figure 4.24. For 20 Hz frequency and various amplitudes (1, 1.5, 2, 2.5 mm) the results obtained experimentally are illustrated in Figure 4.25, Figure 4.26, Figure 4.27 and Figure 4.28.

For 30 Hz frequency and various amplitudes (1, 1.5, 2, 2.5 mm) the results obtained experimentally are illustrated in Figure 4.29, Figure 4.30, Figure 4.31 and Figure 4.32.

For 40 Hz frequency and various amplitudes (1, 1.5, 2, 2.5, 3 mm) the results obtained experimentally are illustrated in Figure 4.33, Figure 4.34, Figure 4.35, Figure 4.36 and Figure 4.37.

For 50 Hz frequency and various amplitudes (1, 1.5, 2, 2.5, 3, 3.5 mm) the results obtained experimentally are illustrated in Figure 4.38, Figure 4.39, Figure 4.40, Figure 4.41, Figure 4.42 and Figure 4.43.

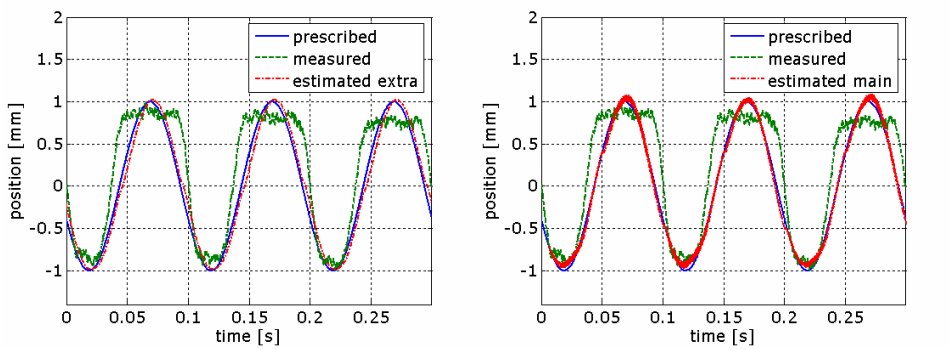

a) b)

Figure 4.23 1 mm @ 10 Hz, I/f open loop control, a) extra coils φe, b) main coils φm

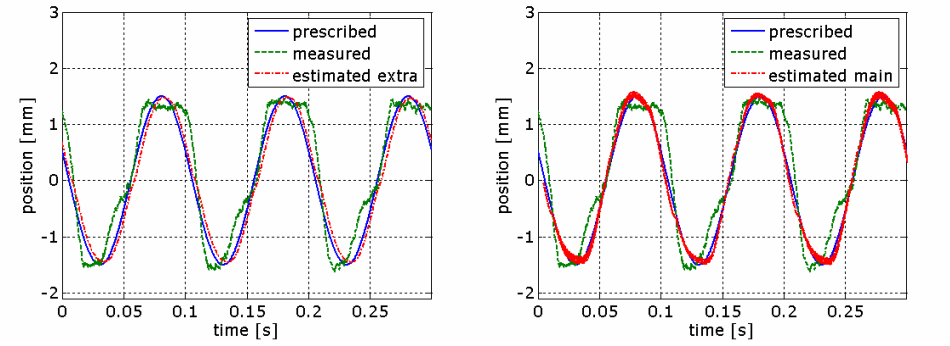

a) b)

Figure 4.24 1.5 mm @ 10 Hz, I/f open loop control, a) extra coils φe, b) main coils φm

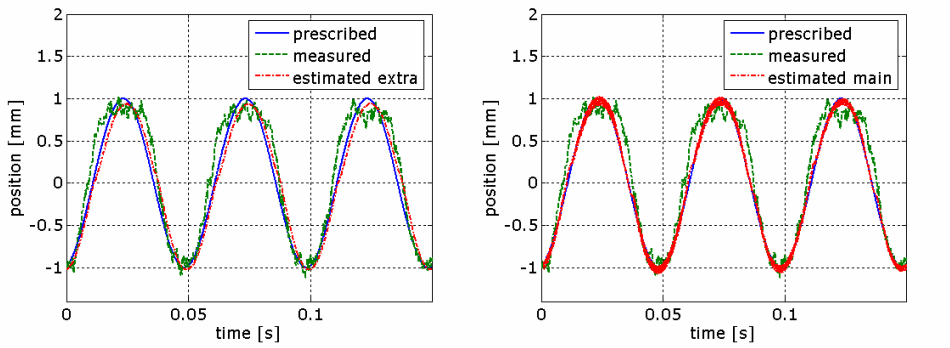

a) b)

Figure 4.25 1 mm @ 20 Hz, I/f open loop control, a) extra coils φe, b) main coils φm

BUPT

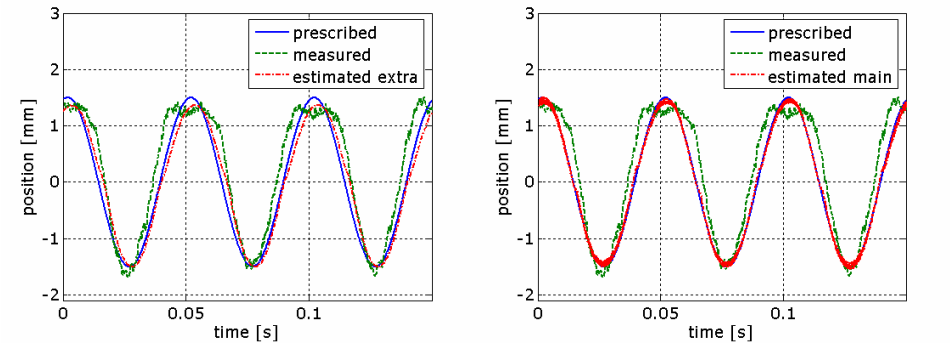

a) b)

Figure 4.26 1.5 mm @ 20 Hz, I/f open loop control, a) extra coils φe, b) main coils φm

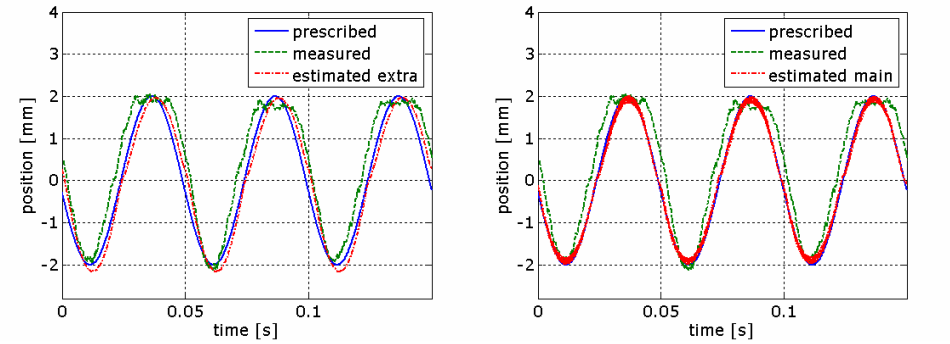

a) b)

Figure 4.27 2 mm @ 20 Hz, I/f open loop control, a) extra coils φe, b) main coils φm

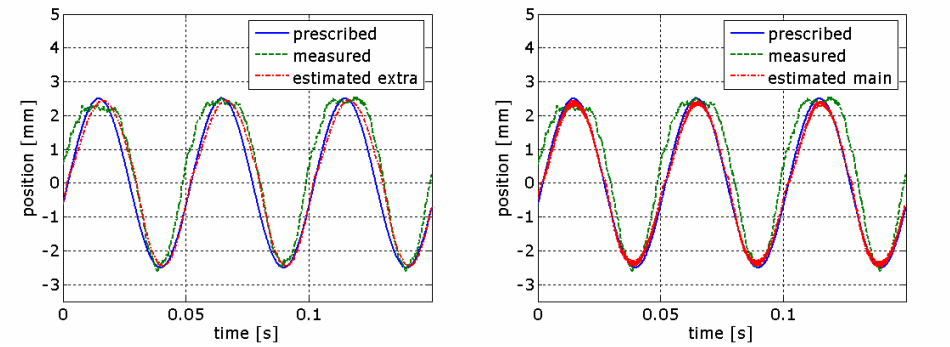

a) b)

Figure 4.28 2.5 mm @ 20 Hz, I/f open loop control, a) extra coils φe, b) main coils φm

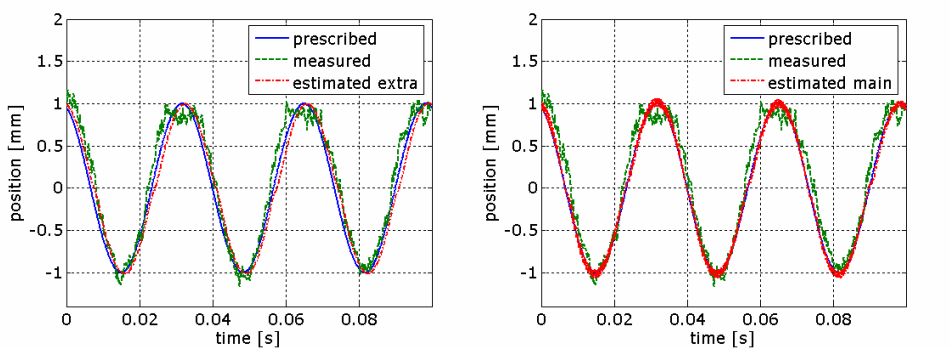

a) b)

Figure 4.29 1 mm @ 30 Hz, I/f open loop control, a) extra coils φe, b) main coils φm

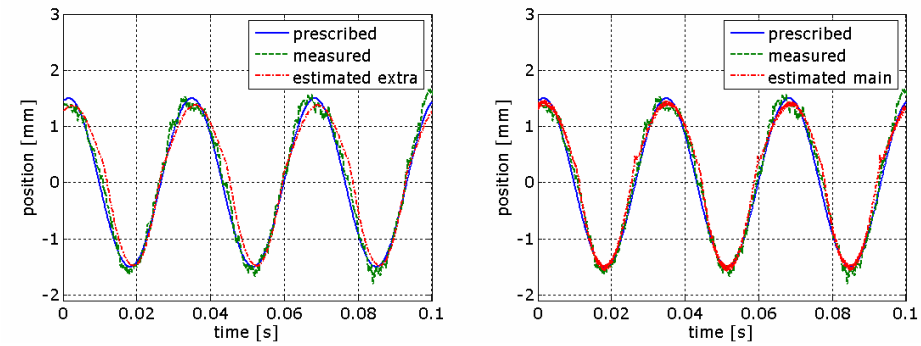

a) b)

Figure 4.30 1.5 mm @ 30 Hz, I/f open loop control, a) extra coils φe, b) main coils φm

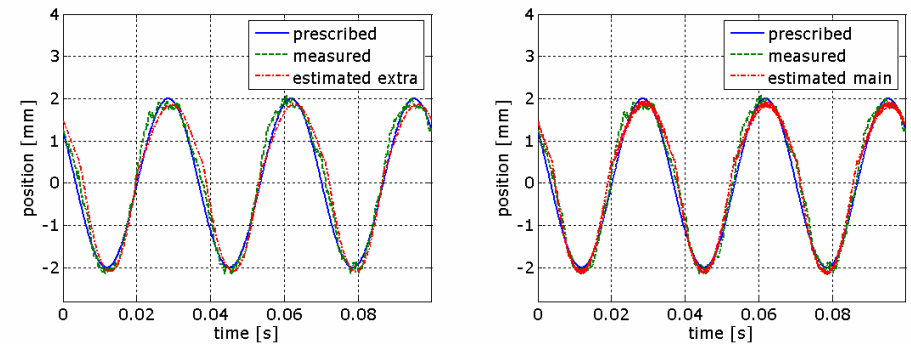

a) b)

Figure 4.31 2 mm @ 30 Hz, I/f open loop control, a) extra coils φe, b) main coils φm

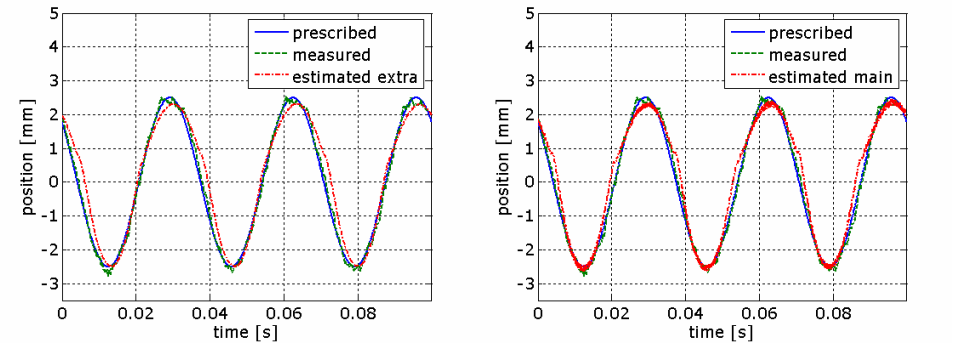

a) b)

Figure 4.32 2.5 mm @ 30 Hz, I/f open loop control, a) extra coils φe, b) main coils φm

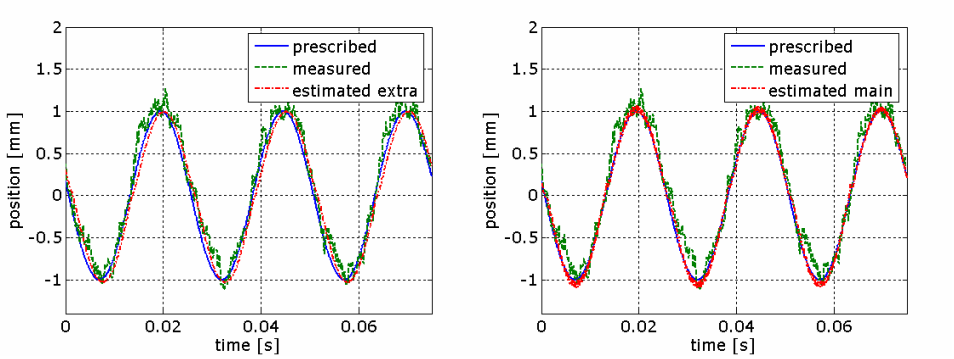

a) b)

Figure 4.33 1 mm @ 40 Hz, I/f open loop control, a) extra coils φe, b) main coils φm

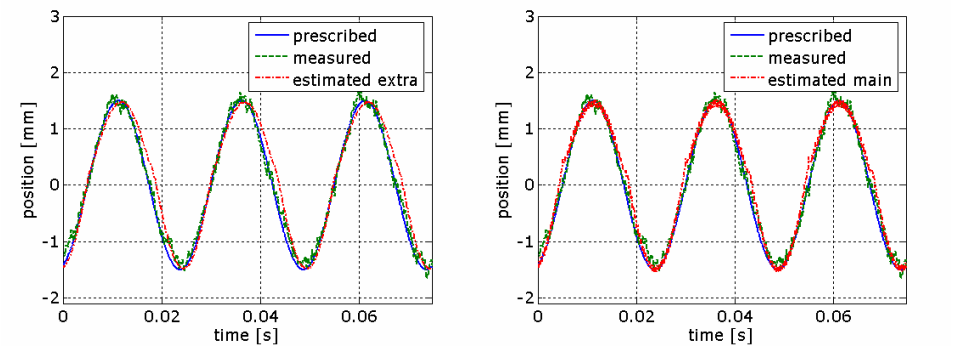

a) b)

Figure 4.34 1.5 mm @ 40 Hz, I/f open loop control, a) extra coils φe, b) main coils φm

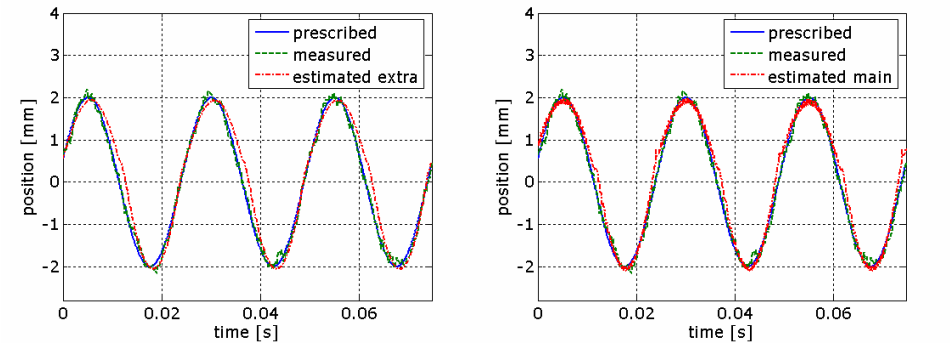

a) b)

Figure 4.35 2 mm @ 40 Hz, I/f open loop control, a) extra coils φe, b) main coils φm

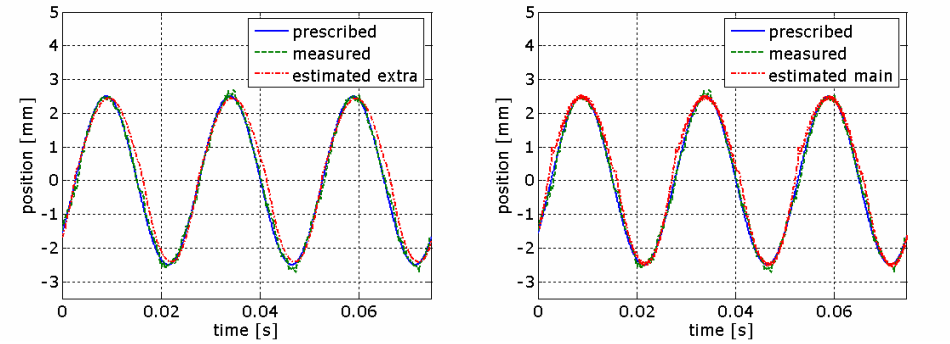

a) b)

Figure 4.36 2.5 mm @ 40 Hz, I/f open loop control, a) extra coils φe, b) main coils φm

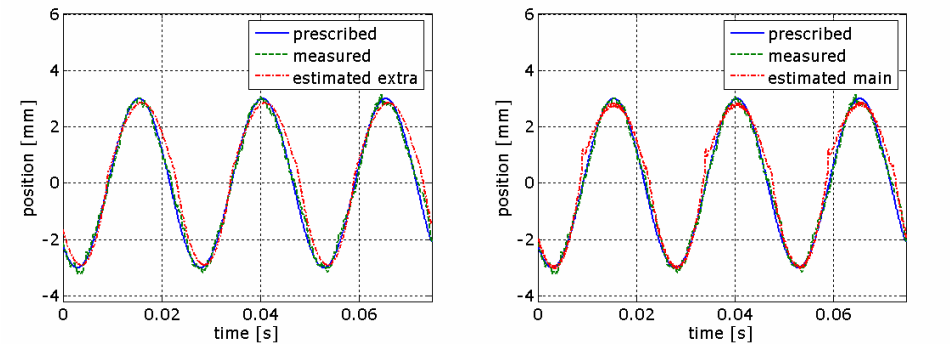

a) b)

Figure 4.37 3 mm @ 40 Hz, I/f open loop control, a) extra coils φe, b) main coils φm

BUPT

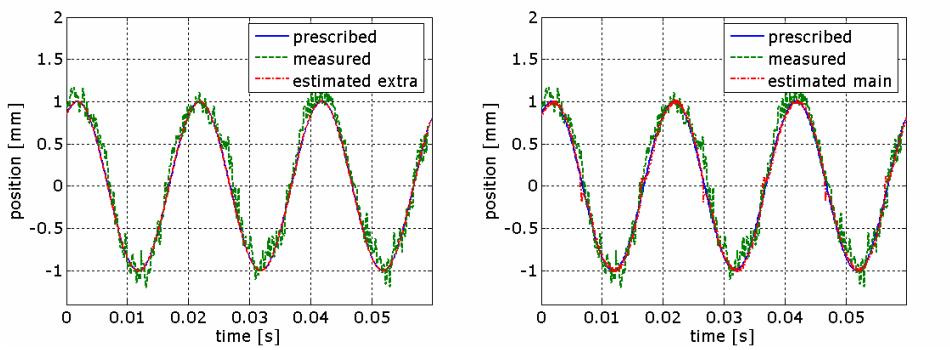

a) b)

Figure 4.38 1 mm @ 50 Hz, I/f open loop control, a) extra coils φe, b) main coils φm

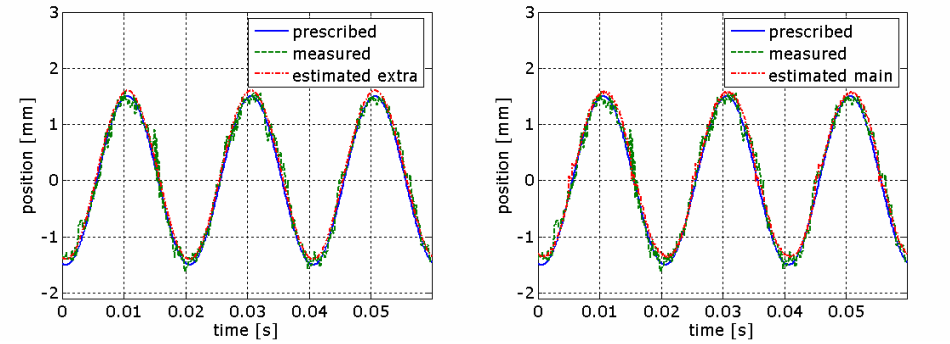

a) b)

Figure 4.39 1.5 mm @ 50 Hz, I/f open loop control, a) extra coils φe, b) main coils φm

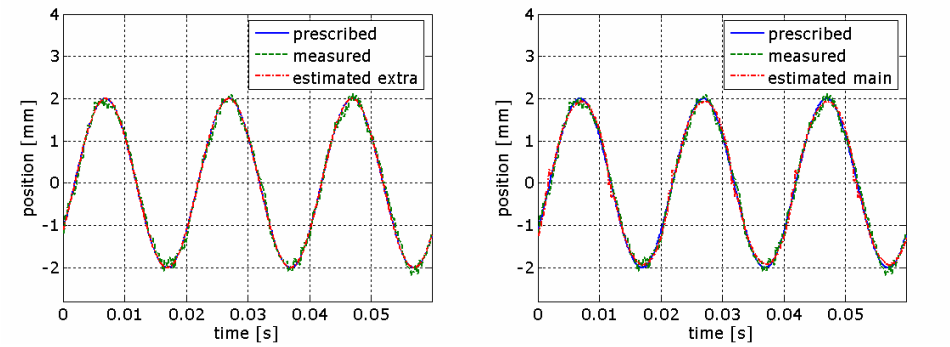

a) b)

Figure 4.40 2 mm @ 50 Hz, I/f open loop control, a) extra coils φe, b) main coils φm

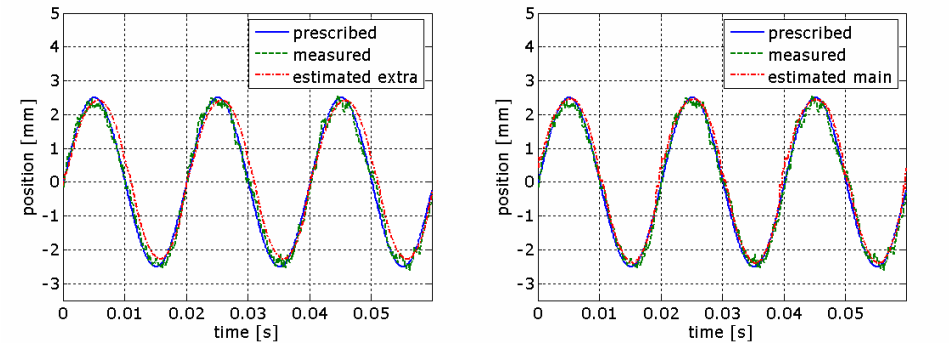

a) b)

Figure 4.41 2.5 mm @ 50 Hz, I/f open loop control, a) extra coils φe, b) main coils φm

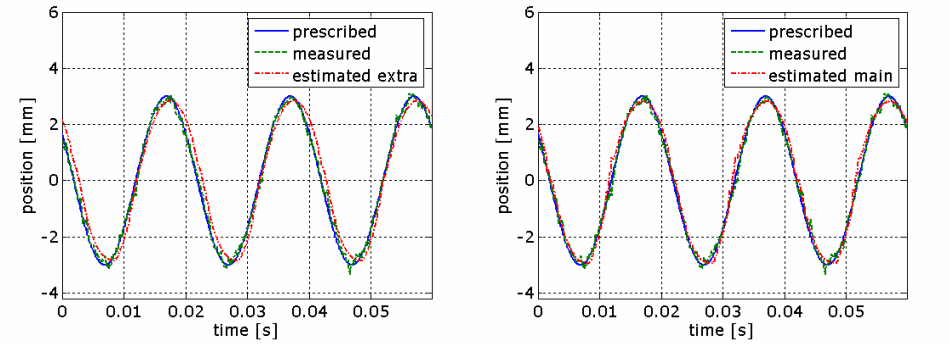

a) b)

Figure 4.42 3 mm @ 50 Hz, I/f open loop control, a) extra coils φe, b) main coils φm

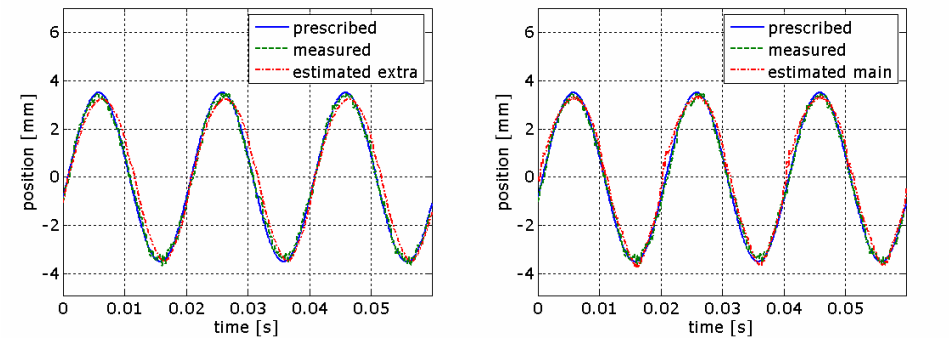

a) b)

Figure 4.43 3.5 mm @ 50 Hz, I/f open loop control, a) extra coils φe, b) main coils φm

As anyone can see the I/f open loop control is superior to U/f open loop control in what concerns the estimation of actuator position.

We introduce a prescribed position to calibrate the injected current with respect to the desired position amplitude, which varies in steps equal to 0.5 mm.

The needed current amplitude is obtained empirically after applying a trial and error method.

Let's look next to the results obtained for frequencies higher that 50 Hz.

For 60 Hz prescribed sinusoidal position and various amplitudes (1, 1.5, 2, 2.5, 3 mm) the results are shown in Figure 4.44, Figure 4.45, Figure 4.46, Figure 4.47 and Figure 4.48.

For 70 Hz prescribed sinusoidal position and various amplitudes (1, 1.5, 2 mm) the results are shown in Figure 4.49, Figure 4.50 and Figure 4.51.

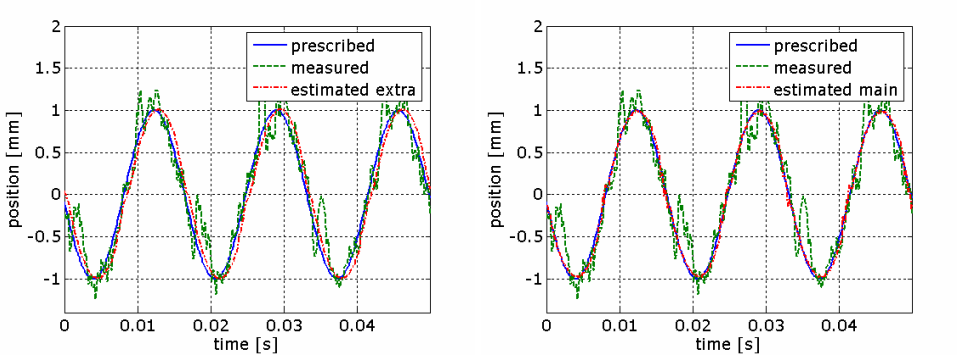

a) b)

Figure 4.44 1 mm @ 60 Hz, I/f open loop control, a) extra coils φe, b) main coils φm

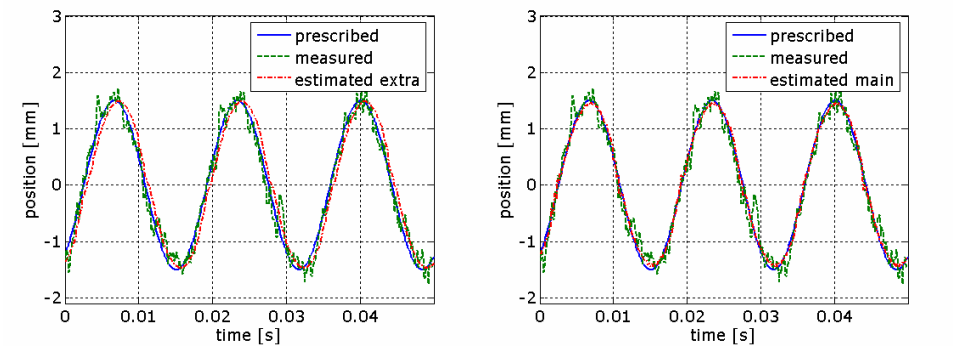

a) b)

Figure 4.45 1.5 mm @ 60 Hz, I/f open loop control, a) extra coils φe, b) main coils φm

BUPT

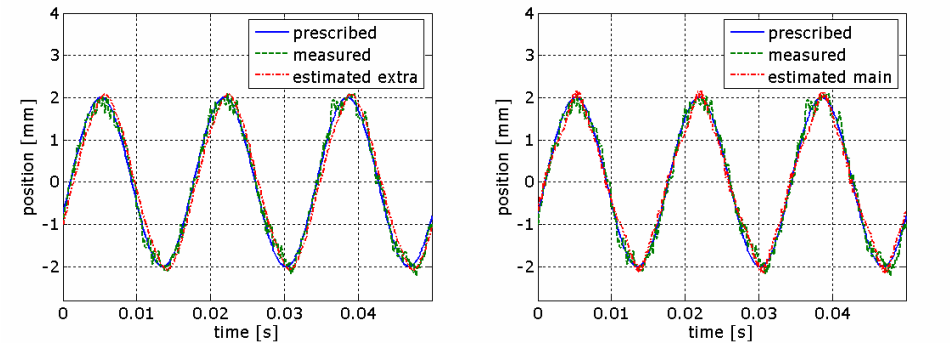

a) b)

Figure 4.46 2 mm @ 60 Hz, I/f open loop control, a) extra coils φe, b) main coils φm

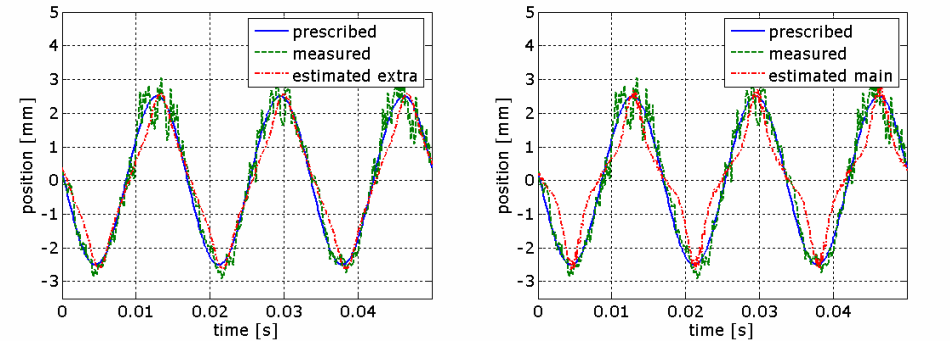

a) b)

Figure 4.47 2.5 mm @ 60 Hz, I/f open loop control, a) extra coils φe, b) main coils φm

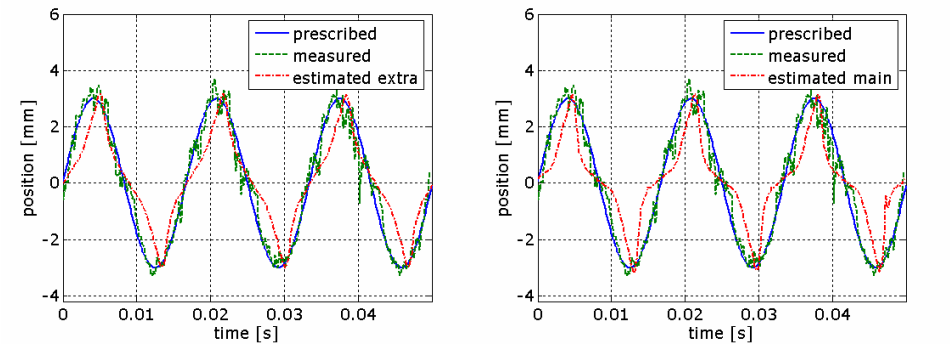

a) b)

Figure 4.48 3 mm @ 60 Hz, I/f open loop control, a) extra coils φe, b) main coils φm

BUPT

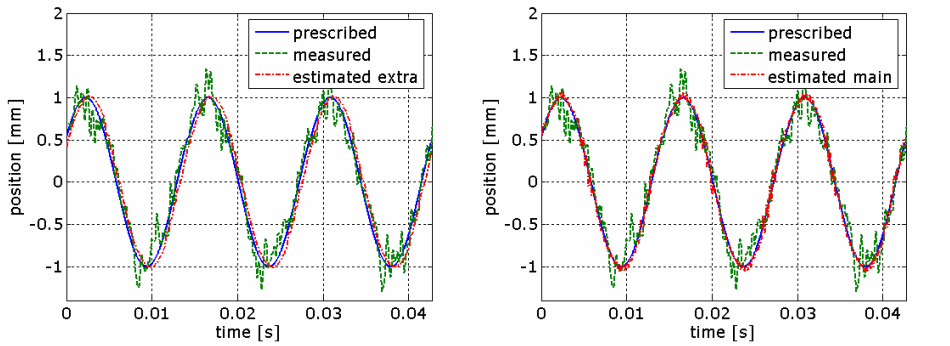

a) b)

Figure 4.49 1 mm @ 70 Hz, I/f open loop control, a) extra coils φe, b) main coils φm

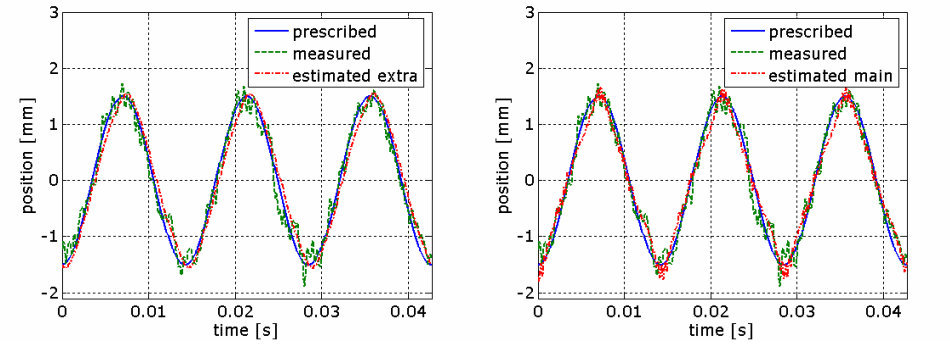

a) b)

Figure 4.50 1.5 mm @ 70 Hz, I/f open loop control, a) extra coils φe, b) main coils φm

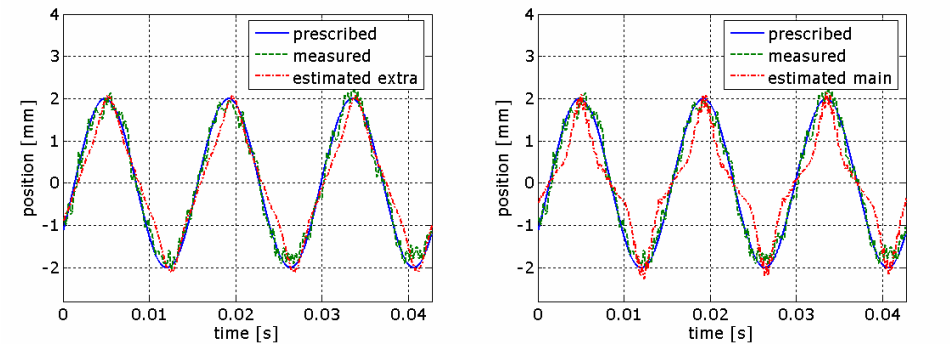

a) b)

Figure 4.51 2 mm @ 70 Hz, I/f open loop control, a) extra coils φe, b) main coils φm

In Figure 4.47 (2.5 mm @ 60 Hz) one can observe that the estimated position based on the main coils begins to loose it's sinusoidal shape earlier than the one obtained from the extra coils.

For 80 Hz prescribed sinusoidal position and various amplitudes (1, 1.5 mm) the results are shown in Figure 4.52 and Figure 4.53.

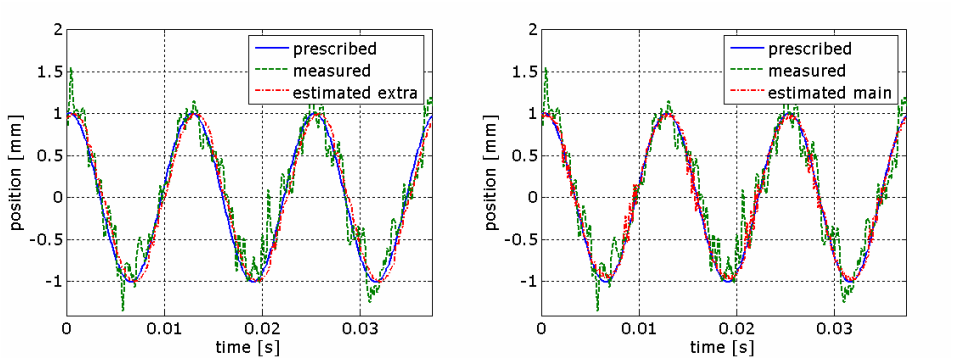

Figure 4.52 1 mm @ 80 Hz, I/f open loop control, a) extra coils φe, b) main coils φm

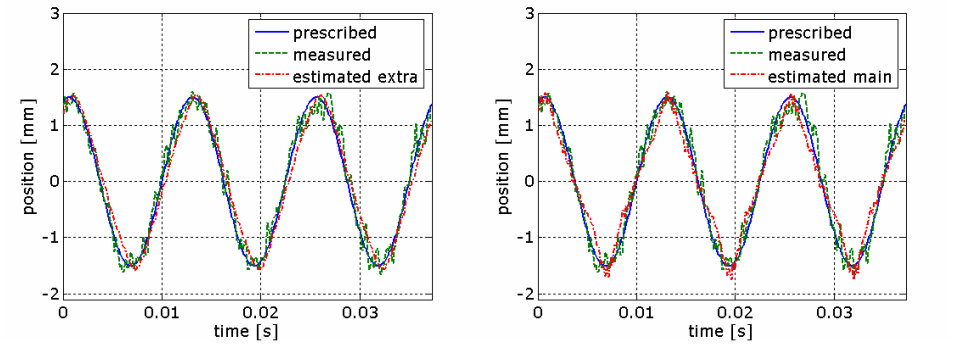

Figure 4.53 1.5 mm @ 80 Hz, I/f open loop control, a) extra coils φe, b) main coils φm

For 90 Hz prescribed sinusoidal position and various amplitudes (1, 1.5 mm) the results are shown in Figure 4.54 and Figure 4.55.

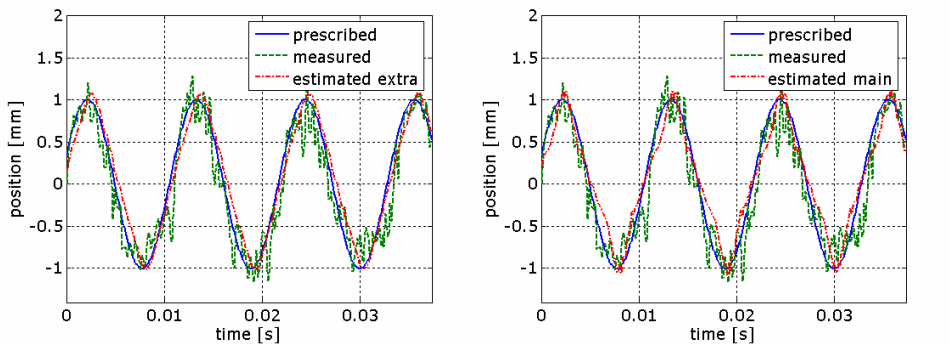

Figure 4.54 1 mm @ 90 Hz, I/f open loop control, a) extra coils φe, b) main coils φm

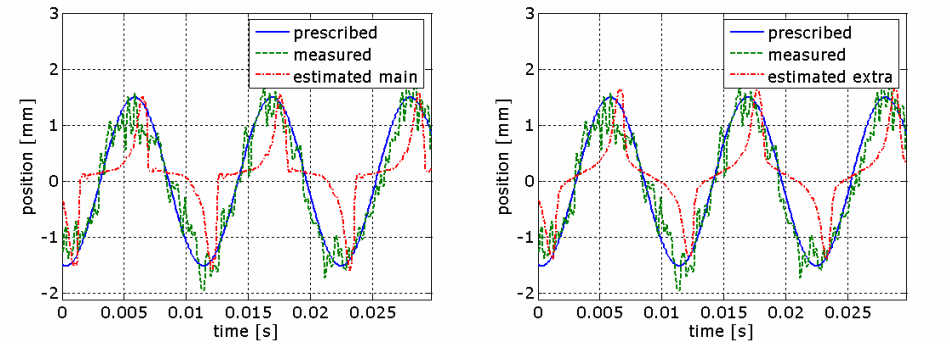

Figure 4.55 1.5 mm @ 90 Hz, I/f open loop control, a) extra coils φe, b) main coils φm

It should be noted that sinusoidal current control leads to better position estimation over a wider frequency range. It goes without saying that the interior current loop control should be kept when exterior position close loop control will be attempted, in the next Chapter.

During experiments without close loop position control (U/f and I/f) the moving part of the linear motor was made of steel which acts as a damper, due to the eddy currents and saturation within. We use this material to stabilize the movement in open loop position control, because when using Atomet-EM1 for the moving part the systems was unstable.

In both cases, simulation and experiments, the system seems to be unstable at large amplitudes (closer to +/- 4 mm).

Next, we will examine the position amplitude error obtained throughout the entire frequency domain where the experiments were made.

Figure 4.57 shows the position amplitude error variation with frequency. The errors are acceptable and they seem not to be systematic, because the fitting

between the prescribed position and the measured position was made after performing a trial and error process whose success was approximately appreciated visually by the human eye. The resulted current amplitude needed to obtain small errors is illustrated in Figure 4.56. All lines in Figure 4.57, which shows the position amplitude error, have an ascending shape, which means that the amplitude error increases with frequency in all cases due to the DC power limitation on one hand and to the losses within the mover on the other hand.

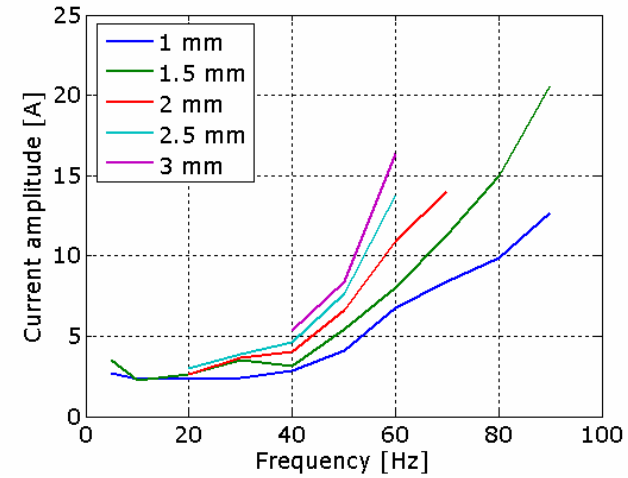

Figure 4.56 Current amplitude versus frequency, I/f open loop position control

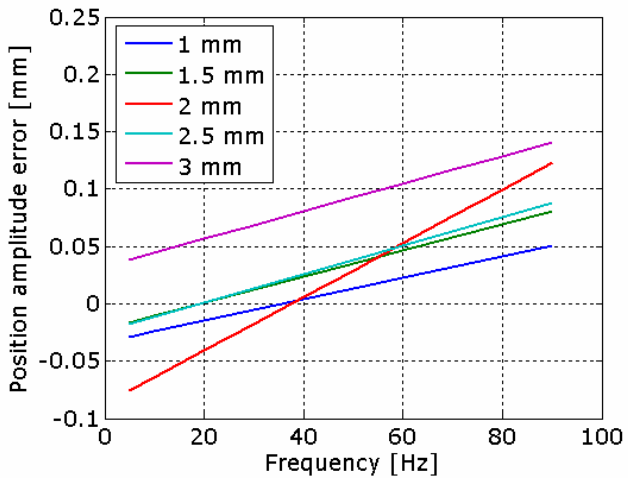

Figure 4.57 Position amplitude error versus frequency when performing I/f open loop position control

BUPT

The phase error is illustrated in Figure 4.58.

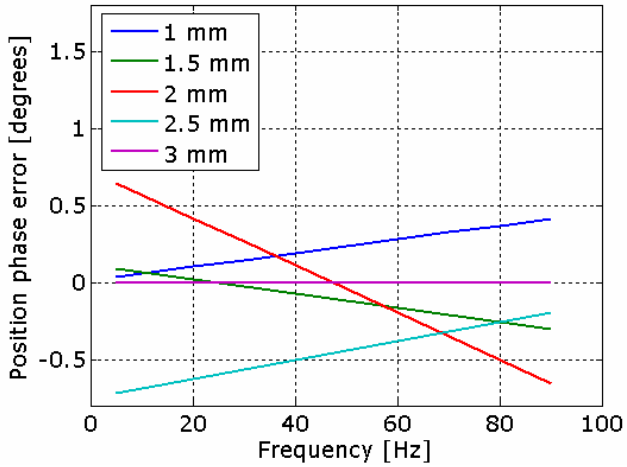

Figure 4.58 Phase error versus frequency when performing I/f open loop position control

The phase error is also acceptable. No systematic characterization can be associated with this error. The apparent power versus frequency is illustrated in Figure 4.59.

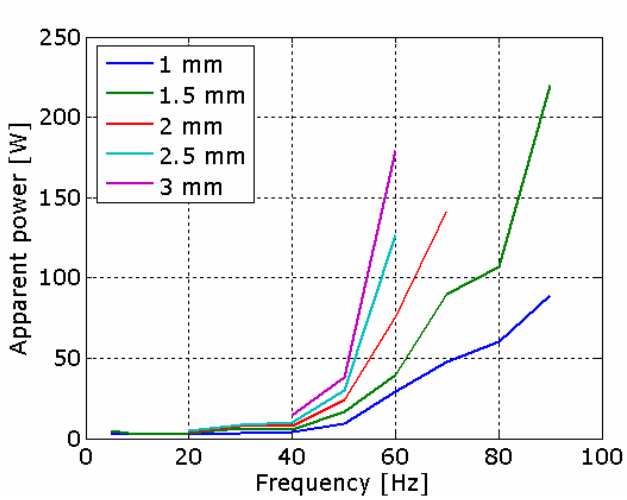

Figure 4.59 Apparent power versus frequency when performing I/f open loop position control

For 1.5 mm prescribed amplitude position at 90 Hz we have the peak value of the apparent power needed. The estimated position in this case has the worse shape of all, (see Figure 4.55) and we face here one edge of our estimator.

SUMMARY

In this chapter open loop control was made. The actuator's dynamic model, made in Matlab/Simulink environment, that utilizes FEM derived data, is introduced. Open loop simulations (U/f, I/f) validated with experiments for various position amplitudes and frequencies are presented. Two FEM derived position estimators are introduced, explained and documented. The two estimator performance are analyzed based on open loop U/f and I/f experiments. It turns up that the interior current loop control lead to better position estimation over a wider frequency range with acceptable amplitude and phase errors. Therefore, this loop will be used in the next chapter where the closed-loop position control is developed.

CHAPTER 4 - REFECENCES

[1] Rama Aravind – "Open Loop Computer Control System – Interfacing a small used guidable program operated, tram to a personal computer", Department of Computer Science and Engineering, Dr.Navalar Nedunchezhiyan College of Engineering, Tholudur, India, 2002

[2] I. Boldea, S. Agarlita, L. Tutelea, F. Marignetti – "Novel linear PM valve actuator: FE design and dynamic model ", Record of LDIA 2007, Lille, France

[3] James, H.M., Nichols, N.B., Phillips, R.S., (1947), „Theory of servomechanisms", volume 25 of MIT Radiation Laboratory Series, McGraw-Hill, New York, 1947.

[4] Blomberg, H., Ylinen, R., (1983) „Algebraic theory for multivariable linear systems". Academic Press, 1983.

[5] Bode, H.W., (1940) Feedback amplifier design, Bell Systems Technical Journal, vol.19, 1940, pp.42

[6] Fernández-Cara E., Zuazua, E**.,** Control Theory: Hystory, Mathematical Achievements and Perspectives. Notes, Universidad de Sevilla and Universidad Autónoma Madrid, Spain

[7] Hall, H.R., (1907) Governors and governing mechanisms. The Technical Publishing Co., 2nd ed., Manchester 1907.

[8] Jackson, E.A., (1994) A first look at the second metamorphosis of science. Technical Report, Santa Fe Institute, 1994.

BUPT

[9] Kalman, R.E., (1960a) Contributions to the theory of optimal control. Bol. Soc. Mat. Mexicana, vol.5, 1960, pp.102-119.

[10] Kalman, R.E., Bertram, J.E., (1960) Control system analysis and design via the "second method" of Lyapunov. I. Continuous-time systems, ASME J. Basic Eng., 1960, pp.371-393

[11] Lyapunov, A.M., (1877) Problème général de la stabilité du mouvement. Ann. Fac. Sci. Toulouse, vol.9, 1907, pp.203-474.

[12] Pontryagin, L.S., Boltyansky, V.G., Gamkrelidze, R.V., Mishchenko, E.F., (1962) The mathematical theory of optimal processes, Wiley, New York, 1962

[13] Popov, V.M., (1961) Absolute stability of nonlinear systems of automatic control. Automatic Remote Control, vol.22, 1961, pp.857-875, 1962

[14] Willems, J.C., (1991) Paradigms and puzzles in the theory of dynamic systems. IEEE Transaction on Automatic Control, vol.36, 1991, pp.259-294.

Chapter 5 - Closed loop position - sensorless control

5.1 Closed Loop Control Systems –An introduction

A closed loop system is mainly characterized by the fact that the inputs signal of the leaded process is a known defined function of the process response. This is done by using a feedback loop, Figure 5.1.

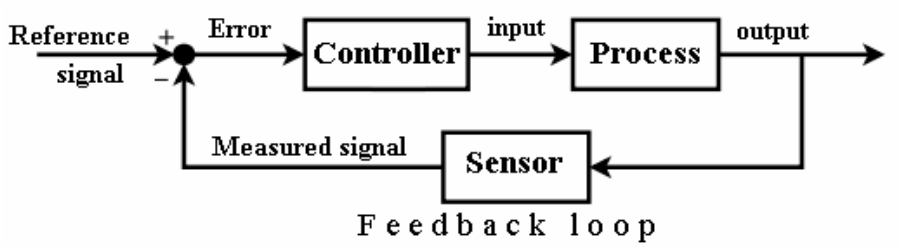

Figure 5.1 Feedback loop basic structure

In a control system we can distinguish two issues related to feedback: the feedback signal, which represents the information fetched from the process about the initial event and the feedback loop, which stands for the causal path that leads from the initial generation of the feedback signal to the subsequent modification of the event [1-5].

Our actuator's close loop control system is based on two types of control methods: PI control and a Sliding Mode control, used in a simple cascade architecture approach.

5.1.1 PID Close loop control system

The PID algorithm is the one of the most popular feedback controllers used to lead industry processes. The control itself is a robust, easily understood algorithm that can provide excellent control performance despite the varied dynamic characteristics of process plant [6-10].

The mathematical equation of a PID controller is illustrated in Equation (5.1) :

$$c(t) = Kc[e(t) + \frac{1}{T_i}\int e(t)dt + T_d \frac{de(t)}{dt}] \quad (5.1)$$

Where:

- c(t) – the controller output;
- Kc – the controller gain;
- e(t) – error signal;
- T_i – integral time;
- T_d – derivative time constant.

The P-only controller offers the advantage of faster response time, but it produces deviation from the set point. This deviation is known as the offset, and it is usually not desired in a process. The offset can be minimized by combining P-only control with another form of control, such as I- or D- control.

The integral control is often used due to its ability to remove any deviations that may exist, leading the system to both steady state and its original setting. A negative error will cause the signal to the system to decrease, while a positive error will cause the signal to increase. The main drawback of I-only controllers is that they provide a much slower response time than P-only controllers because they are dependent on more parameters.

The integral time, introduced in Equation 5.1 is defined as the amount of time needed for the controller to change its output by a value equal to the error.

Unlike P-only and I-only controls, D-control is a form of feed-forward control. D-control anticipates the process conditions by analyzing the change in error. It functions to minimize the change of error, thus keeping the system at a consistent setting. The control output is calculated based on the rate of change of the error with time [11, 12].

For practical problems, the PID designs can not assure competitive control based only on the above considerations, because we have ignored noise and nonlinear effects that may appear. Thereby, derivative filtering and integrator anti-windup must be considered.

Differentiation of a signal amplifies noise and thus the derivative term in the controller is highly sensitive to noise, and can cause a process to become unstable if the noise and the derivative gain are sufficiently large.

To deal with integrator windup phenomenon, controller parameters are designed ignoring the actuator constraints and added an anti-windup compensator in the integral part of the controller [3].

Figure 5.2 shows block diagram of a control system with an anti-windup measure.

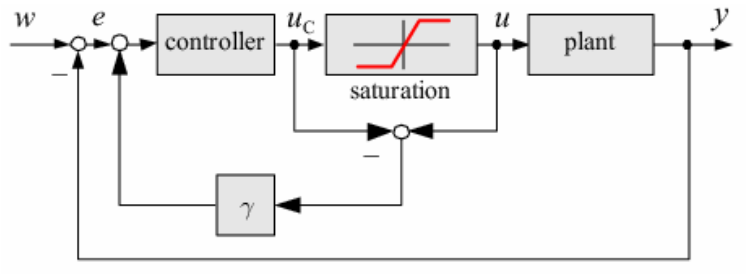

Figure 5.2 Block diagram of a control system with anti-windup

5.1.2 Sliding Mode Control

Variable structure control (VSC) with sliding mode control was first introduced by Emel'yanov and several co researchers [4, 5, 6, 7] in the early 1950's in Russia.

At that time, the plant was considered a linear second order system modelled in phase variable form. Now, VSC has become a general design method that is examined for a wide spectrum of system types including Non-linear System, Multi–Input /Multi–Output systems (MIMO), Stochastic Systems, Discrete–Time Models, Large–Scale and Infinite – Dimensional Systems.

The most important feature of VSC is that it provides a very robust control approach that proceeds with good transient performance, fast response, insensitive to parameter variations and external disturbances [8, 9, 10, 11]. Sliding mode control design is an approach whose structure is intentionally changed with a discontinuous control, which drives the phase trajectory to a stable hyper-plane. This design method is basically formulated from the time domain point of view which uses a Lyapunov function – based control law to ensure the closed–loop stability [12].

The purpose of the switching control is to drive a nonlinear plant's state trajectory onto a desired surface in the state space. The control must also maintain the plant's state trajectory on this surface for an amount of time.

The desired surface is called a switching surface. When the plant state trajectory deflects from the surface in a certain direction, the feedback path has one gain. If the plant state trajectory deflects from the surface in a different direction the feedback path will use different gain. This surface defines the rule for proper switching.

A Lyapunov approach is used to check if the switched control is able to drive the plant state to the switching surface and to maintain it on the surface.

Lyapunov method is usually used to determine the stability properties of an equilibrium point without solving the state equation.

Formula (5.2) defines a single input linear system:

$$x^{(n)} = f(\bar{x},t) + c(\bar{x},t)u(t) \tag{5.2}$$

Where:

- $\bar{x}(t)$ - the state vector, - u(t) – the control input, - x – the output state of interests, f($\bar{x}(t)$,t) and b($\bar{x}(t)$,t) are nonlinear functions of time and states.

The function f is not exactly known, but the extent of the imprecision on f is upper bounded by a known, continuous function of $\bar{x}(t)$. Similarly, the function b is not exactly known, but is of known sign and is bounded by known, continuous functions of $\bar{x}(t)$. The control problem is to get the state $\bar{x}(t)$ to track a specific time-varying state $\bar{x}_d(t)$ in the presence of model imprecision on f and b. A time varying surface s(t) is defined in the state space R^n by equating the variable $s(\bar{x}(t); t)$, defined in equation (5.3), to zero.

$$s(\bar{x},t)=\left(\frac{d}{dt}+\delta\right)^{n-1}\bar{x}_r(t) \tag{5.3}$$

Where:

- δ is a strict positive constant - the bandwidth of the system;
- $\bar{x}_d(t)$ - is the desired state;
- $x_r = x(t) - x_d(t)$ is the error in the output state.

The problem of chasing vector $\bar{x}_d(t)$ is thereby replaced by a first-order stabilization problem.

Referring to equation (5.3), we only need to differentiate $s(\bar{x},t)$ once for the input u(t) to appear. Furthermore, bounds on s can be directly translated into bounds on the tracking error vector, and therefore the scalar s represents a true measure of tracking performance.

In this way, an nth-order tracking problem can be replaced by a 1st-order stabilization problem.

5.1.3 Cascade arhitecture – basic considerations

A cascade control implementation is needed to improve disturbance rejection. Such a control comprises two ordinary controllers from the PID family.

Figure 5.3 illustrates the a schematic diagram of the cascaded control attempted.

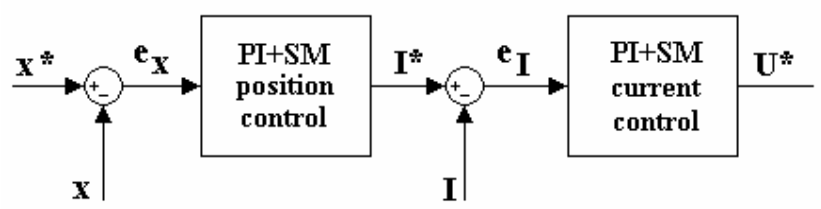

Figure 5.3 Two PI cascaded controllers

In a classical feedback loop, we need to control a so-called manipulated variable such that another measured process variable remains at a given set point.

In order to realize a cascade approach we need to identify a secondary process variable that has to meet certain criteria:

- it must me measured (the current sensor);
- both, primary (x) and secondary (i) manipulated variables must be modified only by the process control variable (U);
- both manipulated variables are affected by the same disturbances;
- the second variable must respond before the primary variable to these disturbances.

We say that the process performance is improved if the added inner loop helps to minimize the effect of disturbances more quickly and efficiently than the same control strategy without an inner loop.

To guarantee the success of a cascade architecture, the settling time of the secondary loop, in our case the current loop, has to be faster than the settling time of the position loop, which is the primary loop.

Due to the fact that the integral component of a PI controller increases settling time and offsets it is recommended to use a P-only Controller for the inner secondary current loop.

The first to be tuned in a tuning process of such a cascade architecture is the inner loop using a set point tracking criteria.

5.2 Combined sliding mode and PI controller closed loop performance with position measured

5.2.1 The controller

We choose to realize a preliminary combined PI – sliding mode control that comprises a current loop in order to obtain a more stable oscillatory motion.

The block diagram of the implemented control is shown in Figure 5.4.

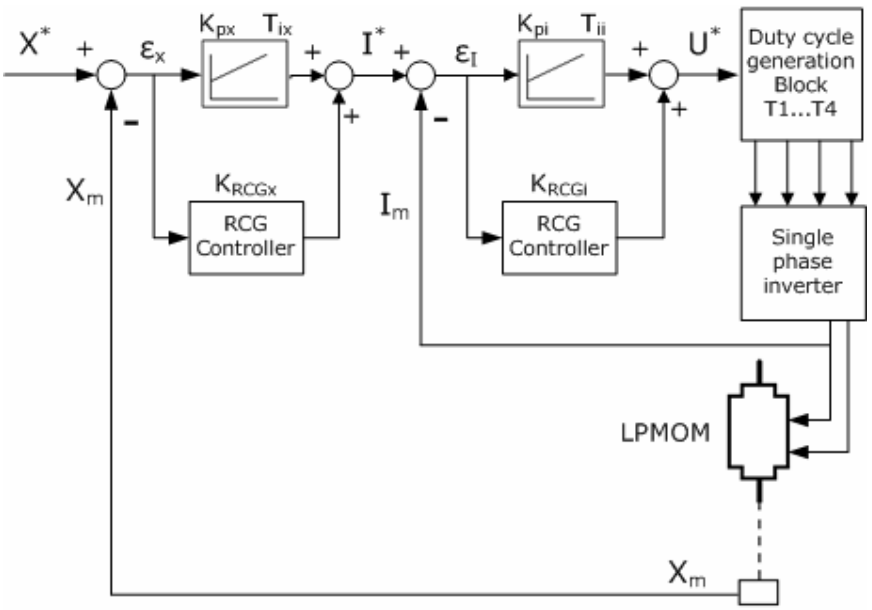

Figure 5.4 Combined PI plus SM implemented control with position measured

Referring to Figure 5.4, the position error calculated based on the information obtained from the laser sensor is feed in the position regulator, whose output is the prescribed current. Measuring the current and feeding the resulting current error into the current regulator we obtain the prescribed voltage, Equations (5.4) and (5.5).

$$I^* = {}_x[\ {}_{px}(1+\frac{1}{sT_{ix}}) + \ {}_{RCGx}] \tag{5.4}$$

BUPT

$$U^* = {}_i[\ {}_{pi}(1+\frac{1}{sT_{ii}}) + \ {}_{RCGxi}] \quad (5.5)$$

The gains are determined after performing a trial and error tuning method.

The proportional gain, as we know, is always a tradeoff between decreasing overshoot and increasing settling time. The propositional gain, K_p, contributes the bulk of the position change, and is settle experimentally to a higher value than K_{RCG}. After observing the oscillations around the setting point the integral gain is set.

The gain of the RCG controller (Relay with Constant Gain) is picked approximately half of proportional gain, or even smaller depending on the frequency at which the actuator is working.

The combined contribution of the two controllers differs upon the error's magnitude. During transients, for large errors, the PI component action is strong. In steady state, the RCG contribution is dominant and switching behavior is obtained.

In Figure 5.5 one can see the position (prescribed, measured and estimated), current (prescribed and measured) and applied voltage (measured) waveforms obtained when performing a VSC-only position control, for a prescribed sinusoidal position having 1 mm amplitude and 50 Hz frequency.

Figure 5.6 illustrates the same entities but for 2 mm prescribed position amplitude. As one can observe chattering is present in both cases, and it has a higher intensity for lower position amplitudes.

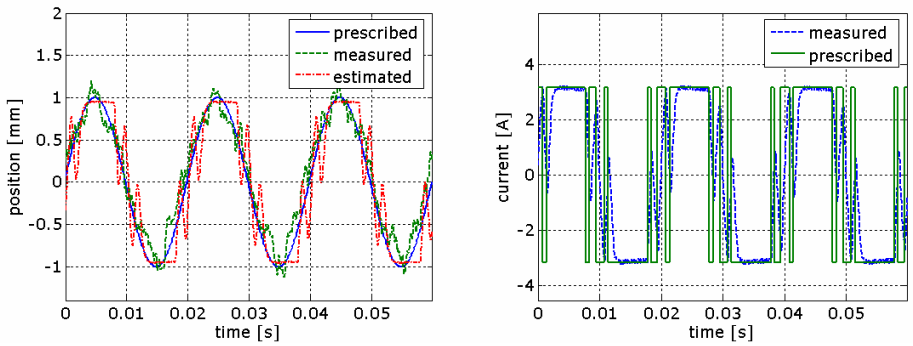

a) b)

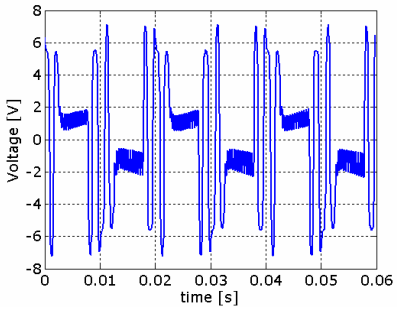

c)

Figure 5.5 a) Measured, estimated, prescribed position vs. time; b) Measured, prescribed current vs. time, c) applied voltage vs. time @ 50 Hz, 1 mm amplitude, VSC position control only

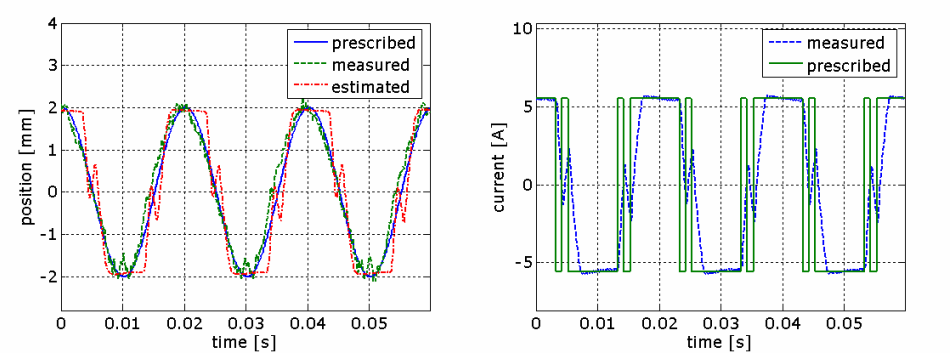

a) b)

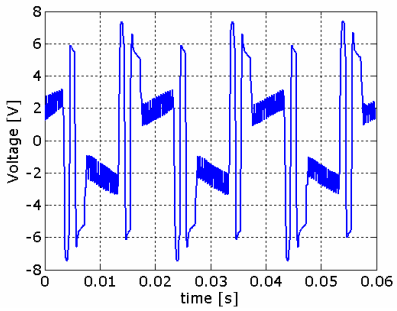

c)

Figure 5.6 a) Measured, estimated, prescribed position vs. time; b) Measured, prescribed current vs. time, c) applied voltage vs. time @ 50 Hz, 2 mm amplitude, VSC position control only

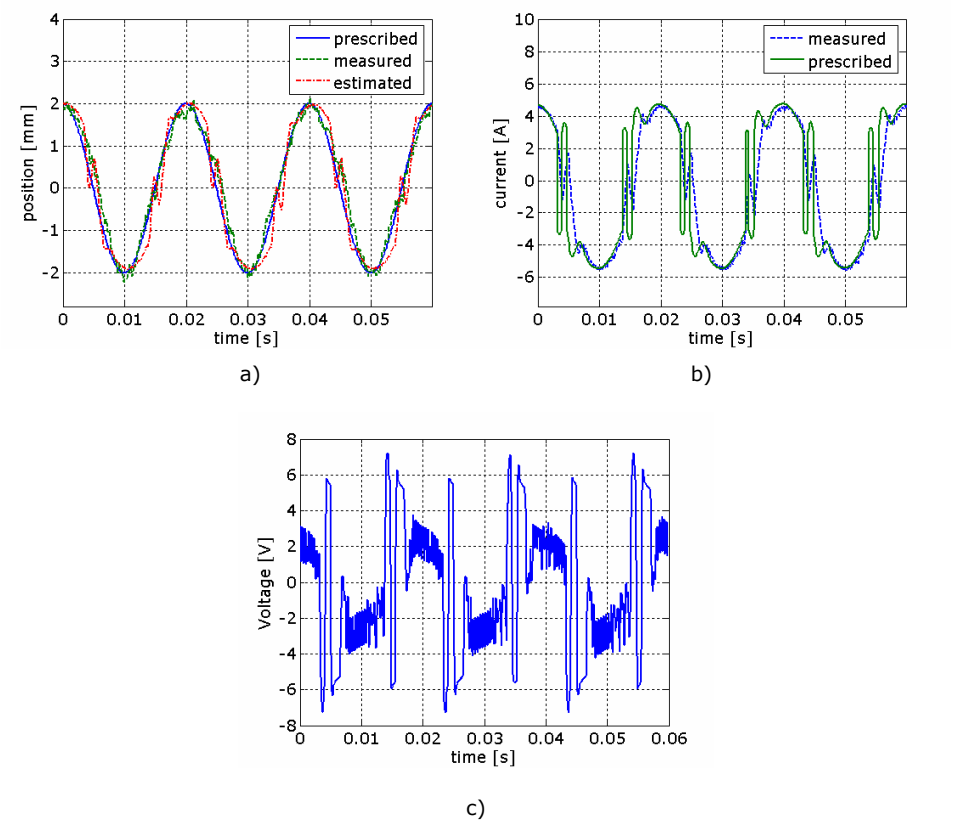

Figure 5.7 a) Measured, estimated, prescribed position vs. time; b) Measured, prescribed current vs. time, c) applied voltage vs. time @ 50 Hz, 2 mm amplitude, half VSC half PI position control

By modifying K_{RCG} one can find a good balance between linear behavior and VSC behavior.

5.2.2 Experimentally obtained results

Using the high speed analogue sensor to measure the position we were able to realize different motion amplitudes at 30, 40, 50 Hz.

Figure 5.8 illustrate how the position control response when prescribing a sinusoidal position having a 30Hz frequency and 1 mm amplitude and, respectively, the prescribed current and the measured one in the same conditions.

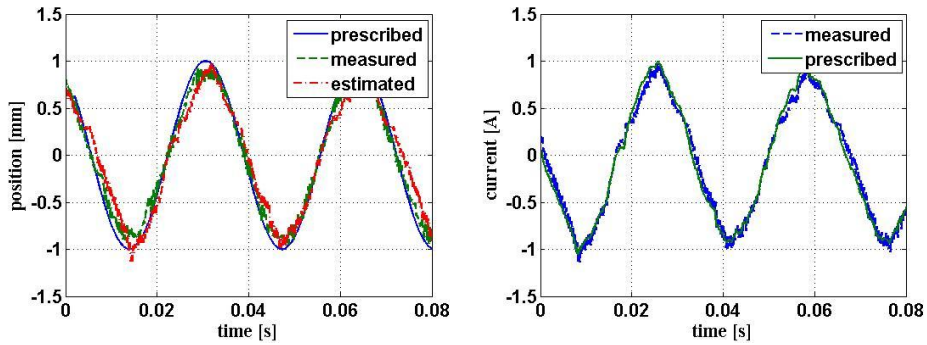

a) b)

Figure 5.8 a) Measured, estimated, prescribed position / time; b)Measured, prescribed current vs. time @ 30 Hz, 1 mm amplitude

Figure 5.9 show the prescribed (1 mm @ 40 Hz), measured and estimated position a), and respectively the prescribed resulting current and measured current.

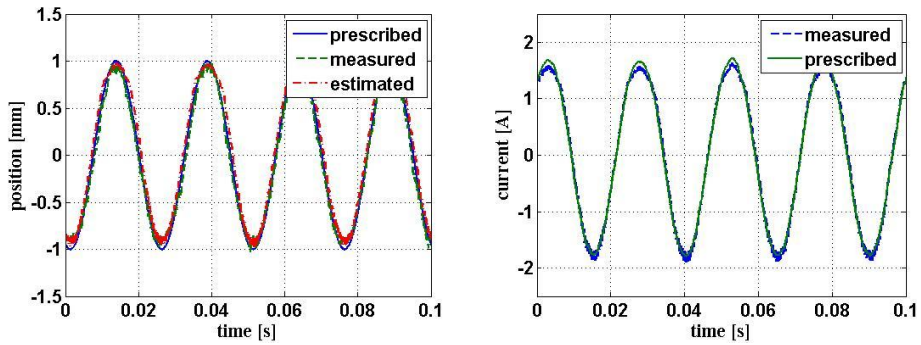

a) b)

Figure 5.9 a) Measured, estimated, prescribed position / time; b) Measured, prescribed current vs. time @ 40 Hz, 1 mm amplitude

Figure 5.10 show the prescribed (1.5 mm amplitude @ 40 Hz, sinusoidal shape), measured and estimated position a), and respectively the prescribed resulting current and measured current.

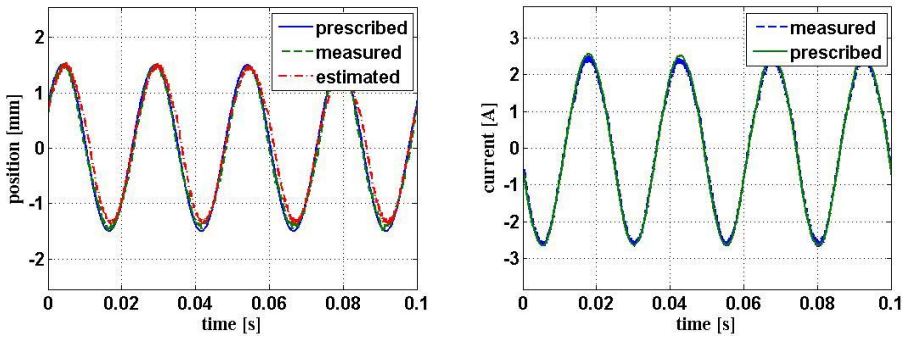

a) b)

Figure 5.10 a) Measured, estimated, prescribed position / time; b) Measured, prescribed current vs. time @ 40 Hz, 1.5 mm amplitude

Same results are shown in Figure 5.11 for a prescribed sinusoidal position of 40Hz frequency and 2 mm amplitude.

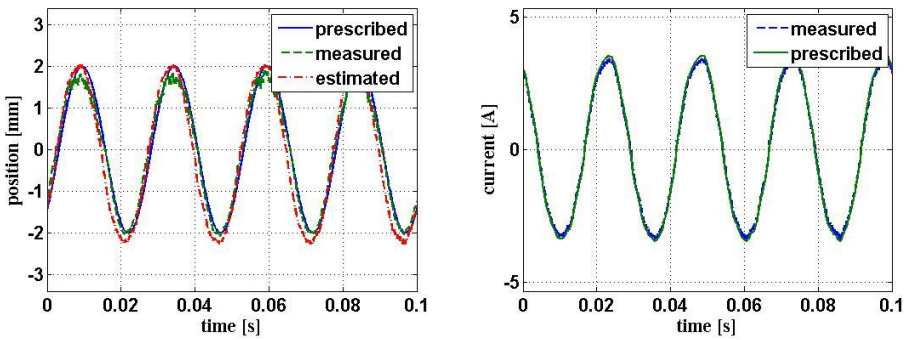

a) b)

Figure 5.11 a) Measured, estimated, prescribed position / time; b) Measured, prescribed current vs. time @ 40 Hz, 2 mm amplitude

Figure 5.12 show the results obtained for a prescribed sinusoidal position of 40Hz frequency and 2.5 mm amplitude and Figures 5.9 for a prescribed sinusoidal position of 40Hz frequency and 3 mm amplitude.

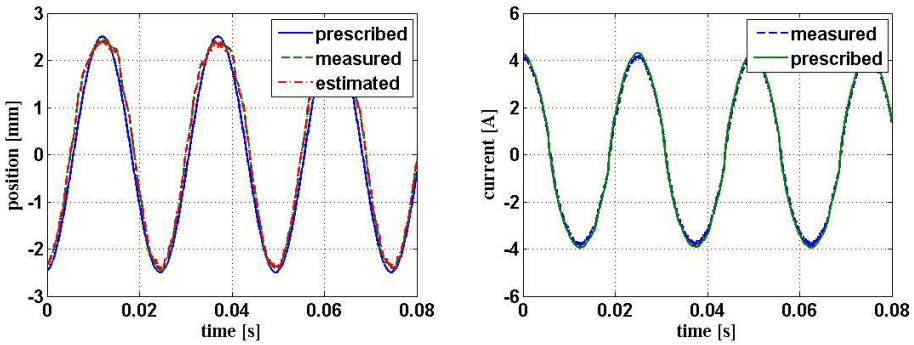

a) b)

Figure 5.12 a) Measured, estimated, prescribed position / time; b) Measured, prescribed current vs. time @ 40 Hz, 2.5 mm amplitude

Figure 5.13 illustrates the three positions (prescribed, measured and estimated) and the associated currents corresponding to a 40 Hz sinusoidal motion having 3 mm in amplitude.

Figure 5.14, 5.11, 5.12 and 5.13 show the results for a 50 Hz sinusoidal motion having 1, 1.5, 2, 2.5 mm in amplitude.

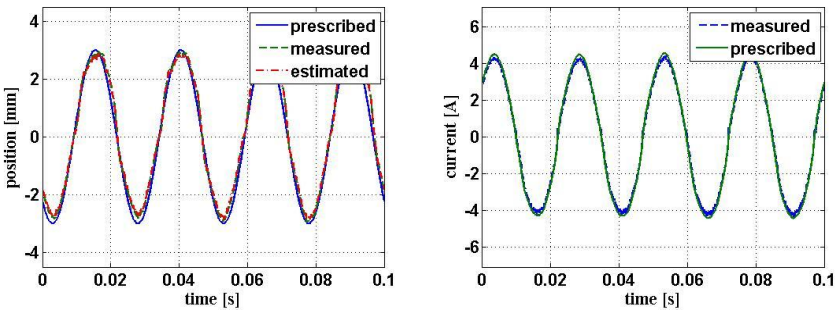

a) b)

Figure 5.13 a) Measured, estimated, prescribed position / time; b) Measured, prescribed current vs. time @ 40 Hz, 3 mm amplitude

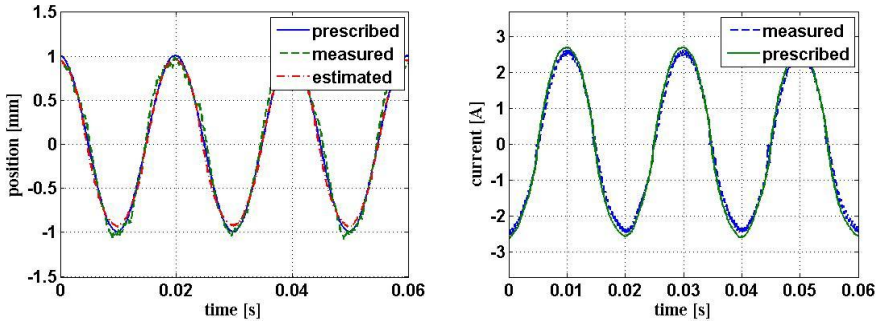

a) b)

Figure 5.14 a) Measured, estimated, prescribed position / time; b) Measured, prescribed current vs. time @ 50 Hz, 1 mm amplitude

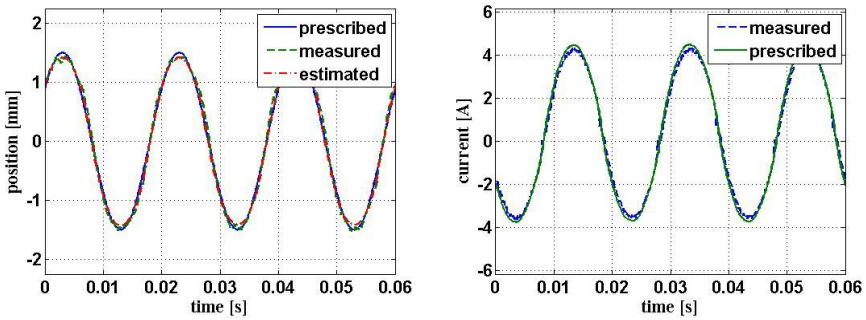

a) b)

Figure 5.15 a) Measured, estimated, prescribed position / time; b) Measured, prescribed current vs. time @ 50 Hz, 1.5 mm amplitude

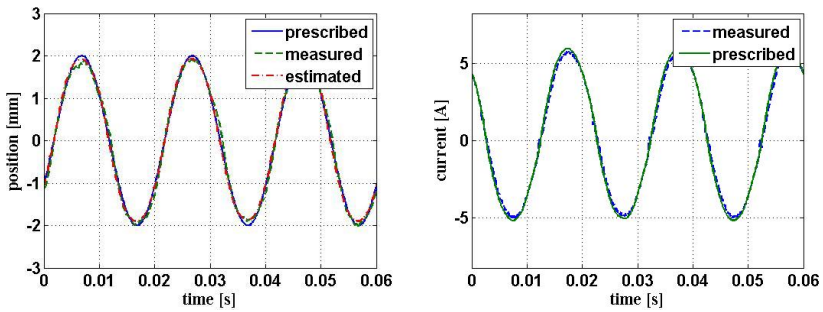

a) b)

Figure 5.16 a) Measured, estimated, prescribed position / time; b) Measured, prescribed current vs. time @ 50 Hz, 2 mm amplitude

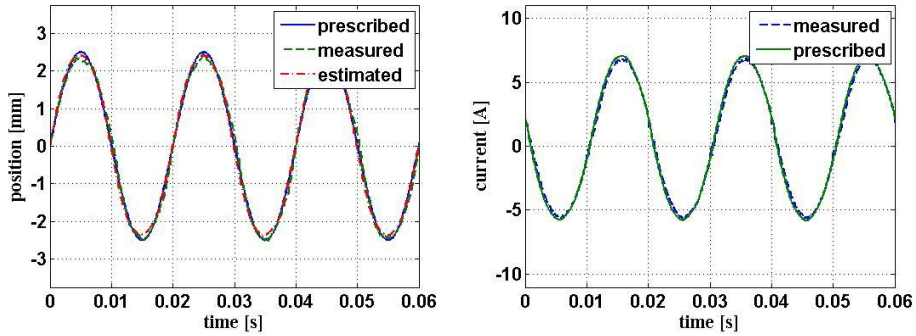

a) b)

Figure 5.17 a) Measured, estimated, prescribed position / time; b) Measured, prescribed current vs. time @ 50 Hz, 2.5 mm amplitude

5.3 Combined sliding mode and PI controller sensorless closed loop control

5.3.1 Fixed amplitude and frequency sinusoidal prescribed position performance

Using FEM derived data we estimated the position, by realizing a curve fitting process. The two estimators were presented in Chapter 4. We use the same control presented in the previous section, but here the position supplied to the controller is the one estimated by rebuilding the total flux with the aid of 2 extra coils inserted near the main coils, Figure 5.18.

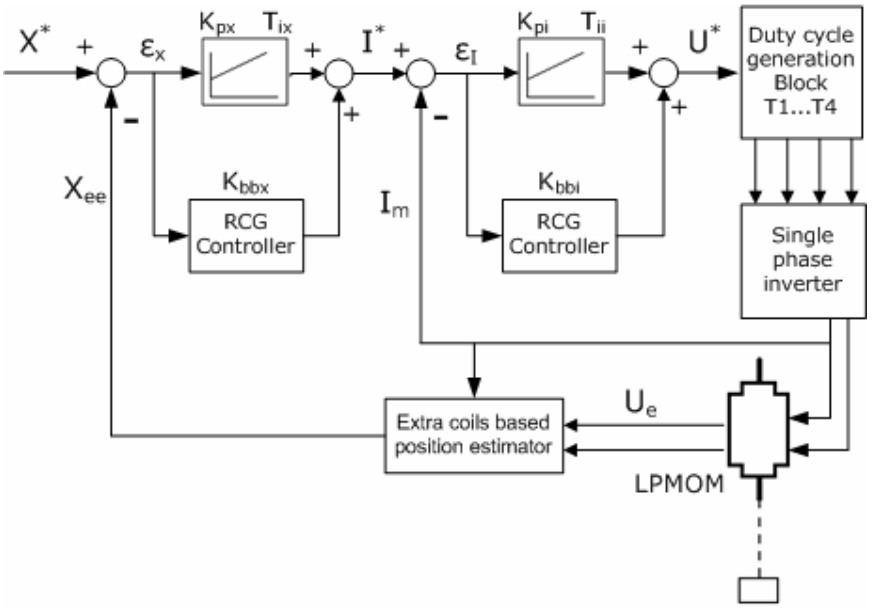

Figure 5.18 Combined PI plus SM implemented control with position estimated

When performing sensorless closed loop control the systems seems to be more stable leading to a smooth sinusoidal position shape. As anyone can notice with sensorless control we were able to realize low frequency oscillations (1, 5, 10, 20 Hz), which were not possible when using the high-speed analogue sensor. Furthermore, due to the available laser sensor, which was not the optimum solution in what concerns the position measurement instrumentation, we had to use some

BUPT

lop pass filters to cut off the undesired noise, when performing closed loop control with sensor. In sensorless operation all low pass filters can be removed. At each frequency we tried to obtain the highest amplitude possible.

Figure 5.19, Figure 5.20 and Figure 5.21 show the results obtained when prescribing a sinusoidal reference position having 1 Hz frequency and 1 mm amplitude, and respectively 1 Hz frequency and 1.5 mm amplitude.

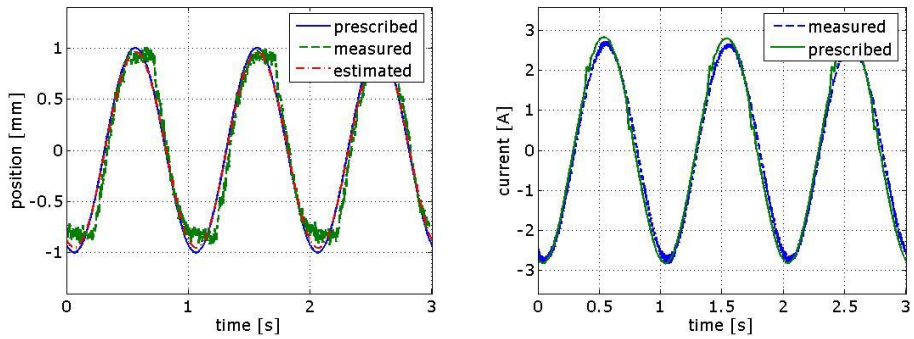

Figure 5.19 a) Measured, estimated, prescribed position / time; b) Measured, prescribed current vs. time @ 1 Hz, 1 mm amplitude

One can see that the results have a quite good accuracy, despite the fact that the forces developed at low frequencies become comparable with the friction forces which are subjected to uncertainties.

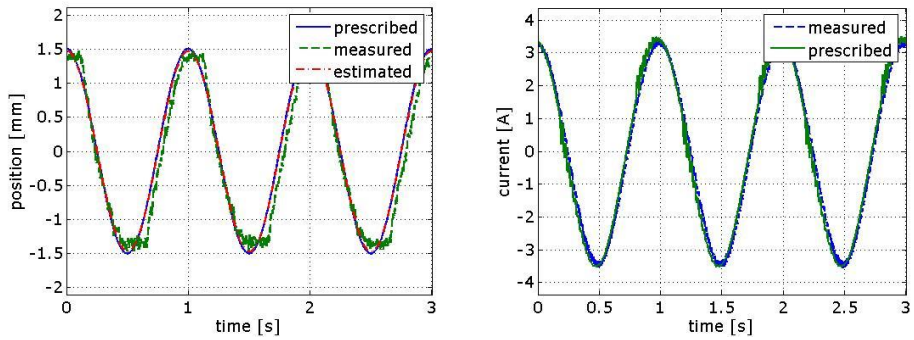

Figure 5.20 a) Measured, estimated, prescribed position / time; b) Measured, prescribed current vs. time @ 1 Hz, 1.5 mm amplitude

BUPT

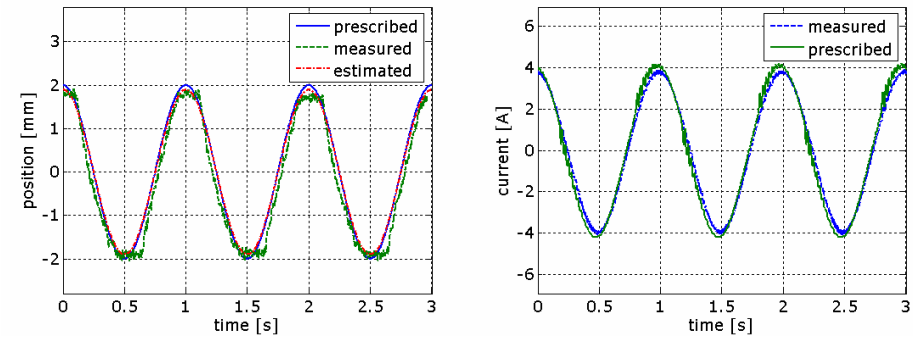

Figure 5.21 a) Measured, estimated, prescribed position / time; b) Measured, prescribed current vs. time @ 1 Hz, 2 mm amplitude

Figure 5.22, Figure 5.23 and Figure 5.24 show the results obtained when controlling the actuator in closed loop control using a PI regulator combined with sliding mode for a prescribed sinusoidal position having 1, 1.5, and 2 mm in amplitude and 5 Hz frequency.

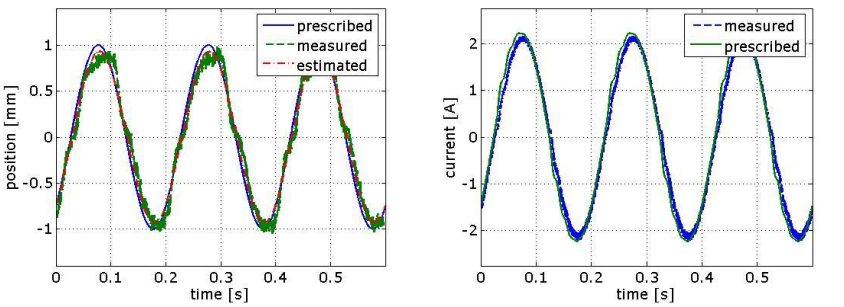

a) b)

Figure 5.22 a) Measured, estimated, prescribed position / time; b) Measured, prescribed current vs. time @ 5 Hz, 1 mm amplitude

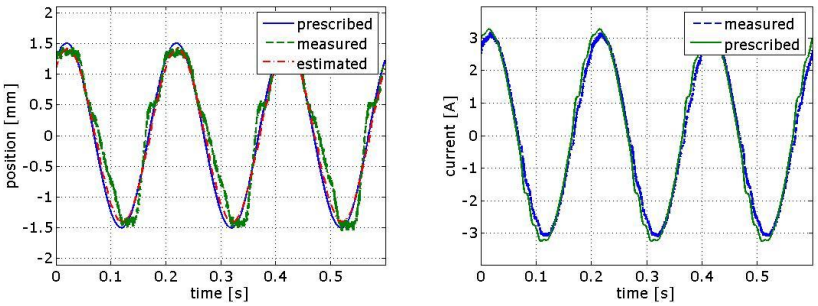

a) b)

Figure 5.23 a) Measured, estimated, prescribed position / time; b) Measured, prescribed current vs. time @ 5 Hz, 1.5 mm amplitude

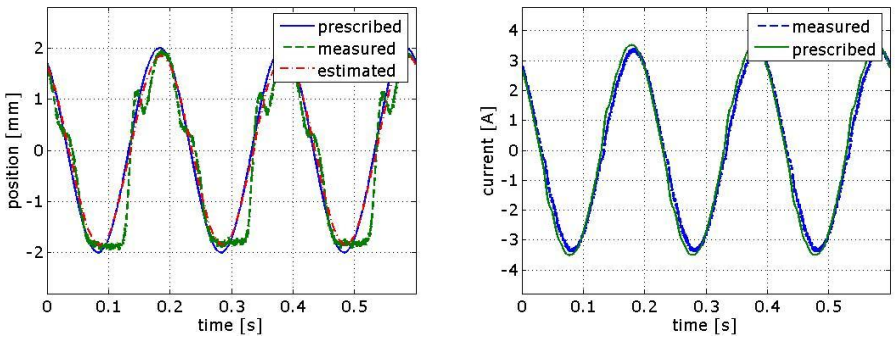

a) b)

Figure 5.24 a) Measured, estimated, prescribed position / time; b) Measured, prescribed current vs. time @ 5 Hz, 2 mm amplitude

This low frequencies will not be used however if the actuator will serve as a internal combustion engine (ICE) valve actuator for a usual family car, because this will mean that the crankshaft speed will be 150 rpms, whish is lower that the usual engine idle speed (between 600 and 1000 rpms). The idle speed represents the minimum operating speed of a ICE. At idle speed, the engine generates enough power to run reasonably smoothly and operate its ancillaries (water pump, alternator, and, if equipped, other accessories such as power steering), but usually not enough to perform useful work, such as moving an automobile.

Figure 5.25, Figure 5.26, Figure 5.27 and Figure 5.28 illustrate the results obtained for 1, 1.5, 2 and 2.5 mm sinusoidal reference position amplitude, having 10 Hz frequency.

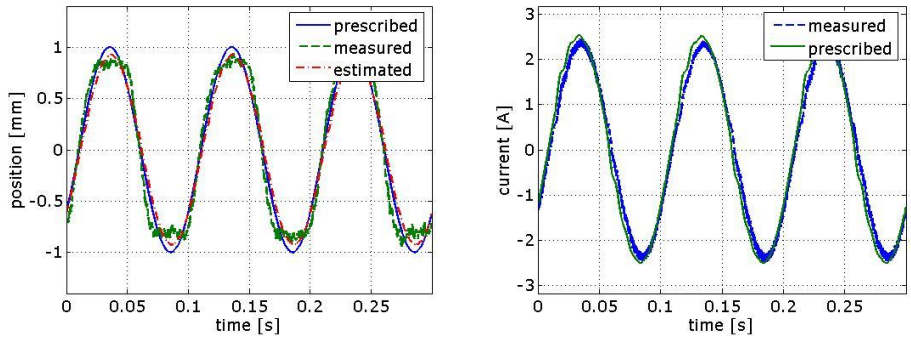

a) b)

Figure 5.25 a) Measured, estimated, prescribed position / time; b) Measured, prescribed current vs. time @ 10 Hz, 1 mm amplitude

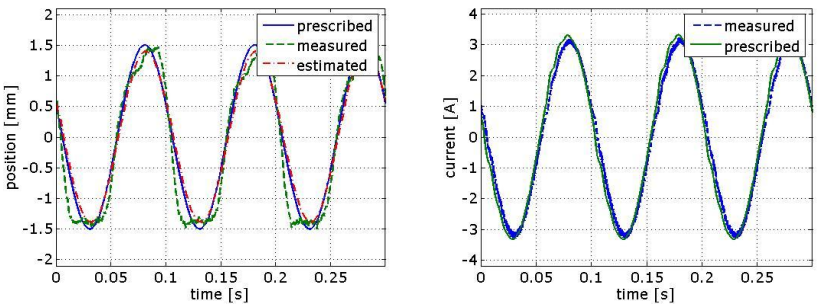

a) b)

Figure 5.26 a) Measured, estimated, prescribed position / time; b) Measured, prescribed current vs. time @ 10 Hz, 1.5 mm amplitude

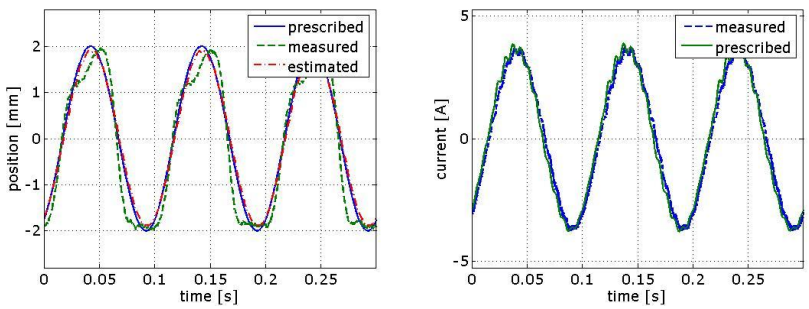

a) b)

Figure 5.27 a) Measured, estimated, prescribed position / time; b) Measured, prescribed current vs. time @ 10 Hz, 2 mm amplitude

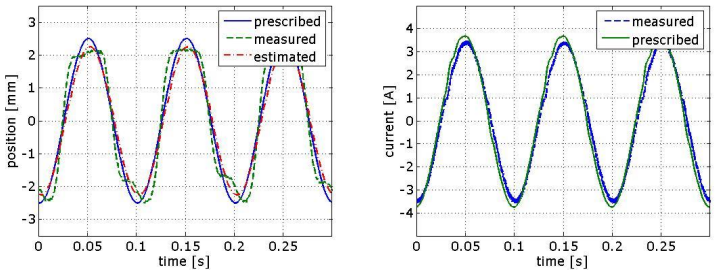

a) b)

Figure 5.28 a) Measured, estimated, prescribed position / time; b) Measured, prescribed current vs. time @ 10 Hz, 2.5 mm amplitude

Figure 5.29, Figure 5.30, Figure 5.31 and Figure 5.32 illustrate the results for 1, 1.5, 2 and 2.5 mm sinusoidal reference position amplitude, having 20 Hz frequency.

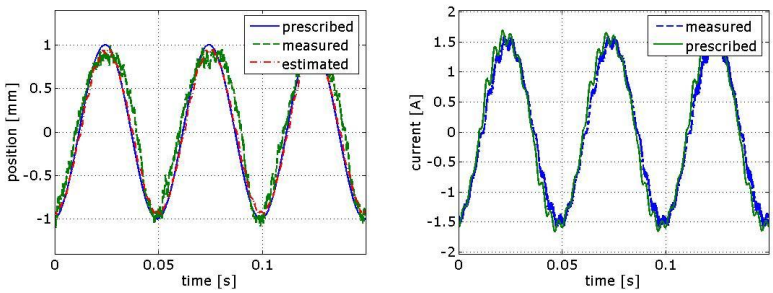

a) b)

Figure 5.29 a) Measured, estimated, prescribed position / time; b) Measured, prescribed current vs. time @ 20 Hz, 1 mm amplitude

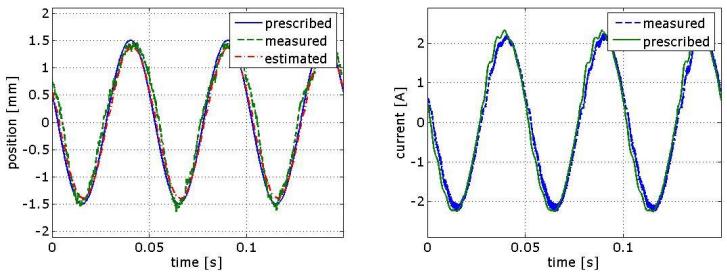

a) b)

Figure 5.30 a) Measured, estimated, prescribed position / time; b) Measured, prescribed current vs. time @ 20 Hz, 1.5 mm amplitude

BUPT

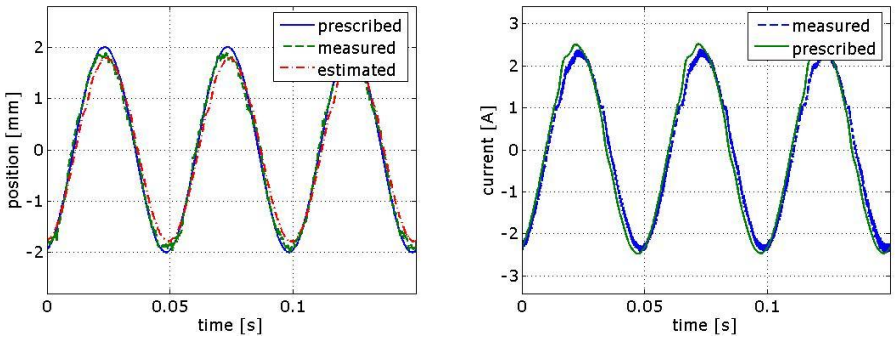

a) b)

Figure 5.31 a) Measured, estimated, prescribed position / time; b) Measured, prescribed current vs. time @ 20 Hz, 2 mm amplitude

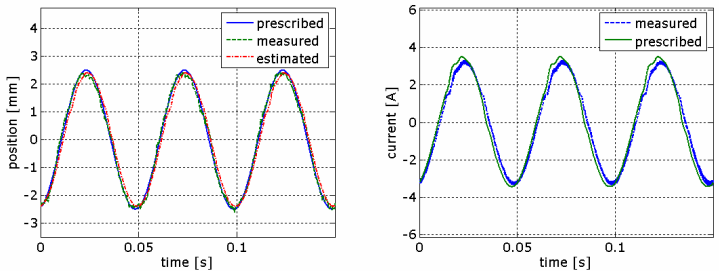

Figure 5.32 a) Measured, estimated, prescribed position / time; b) Measured, prescribed current vs. time @ 20 Hz, 2.5 mm amplitude

Figure 5.33, Figure 5.34, Figure 5.35 and Figure 5.36 illustrate the results obtained for 1, 1.5, 2 and 2.5 mm sinusoidal reference position amplitude, having 30 Hz frequency.

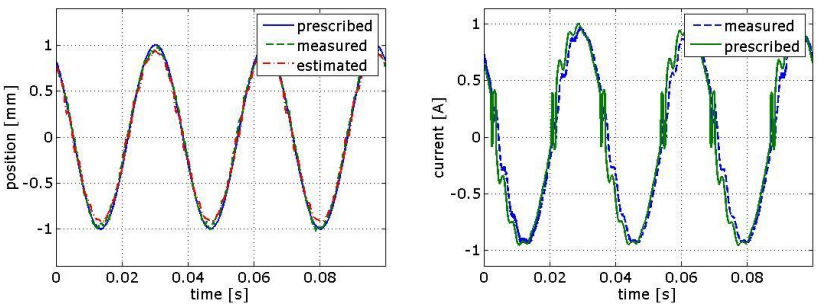

a) b)

Figure 5.33 a) Measured, estimated, prescribed position / time; b) Measured, prescribed current vs. time @ 30 Hz, 1 mm amplitude

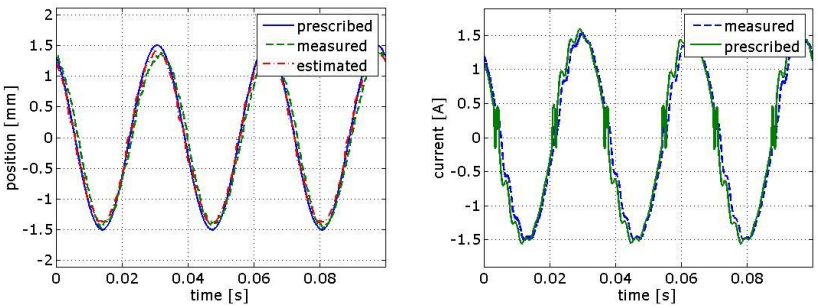

a) b)

Figure 5.34 a) Measured, estimated, prescribed position / time; b) Measured, prescribed current vs. time @ 30 Hz, 1.5 mm amplitude

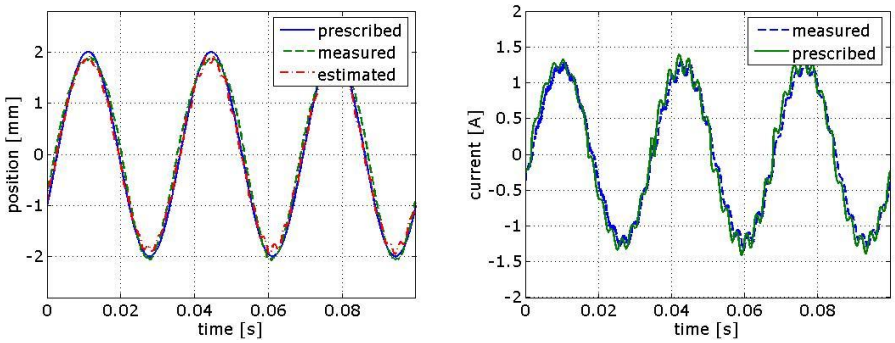

a) b)

Figure 5.35 a) Measured, estimated, prescribed position / time; b) Measured, prescribed current vs. time @ 30 Hz, 2 mm amplitude

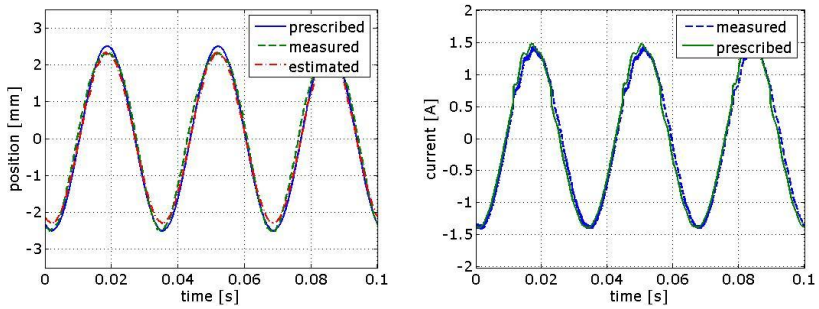

a) b)

Figure 5.36 a) Measured, estimated, prescribed position / time; b) Measured, prescribed current vs. time @ 30 Hz, 2.5 mm amplitude

Figure 5.37, Figure 5.38, Figure 5.39, Figure 5.40, Figure 5.41 and Figure 5.42 illustrate the results obtained for 1, 1.5, 2 and 2.5, 3 and 3.5 mm sinusoidal reference position amplitude, having 40 Hz frequency.

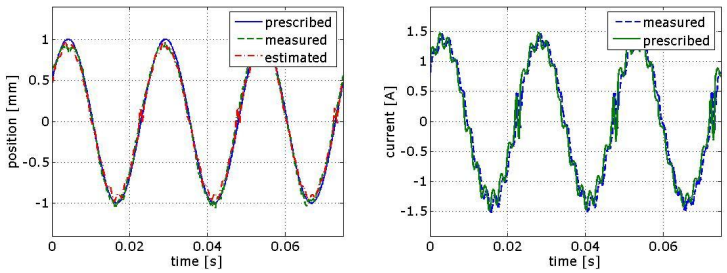

a) b)

Figure 5.37 a) Measured, estimated, prescribed position / time; b) Measured, prescribed current vs. time @ 40 Hz, 1 mm amplitude

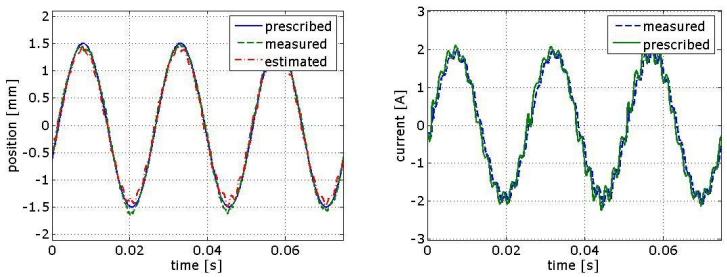

a) b)

Figure 5.38 a) Measured, estimated, prescribed position / time; b) Measured, prescribed current vs. time @ 40 Hz, 1.5 mm amplitude

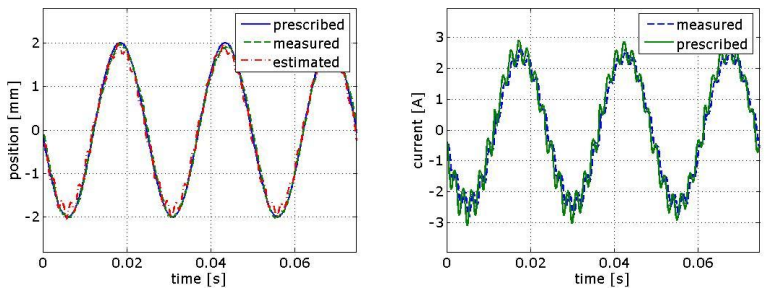

a) b)

Figure 5.39 a) Measured, estimated, prescribed position / time; b) Measured, prescribed current vs. time @ 40 Hz, 2 mm amplitude

BUPT

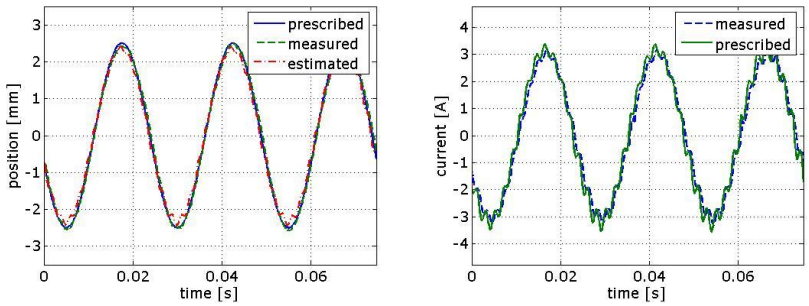

a) b)

Figure 5.40 a) Measured, estimated, prescribed position / time; b) Measured, prescribed current vs. time @ 40 Hz, 2.5 mm amplitude

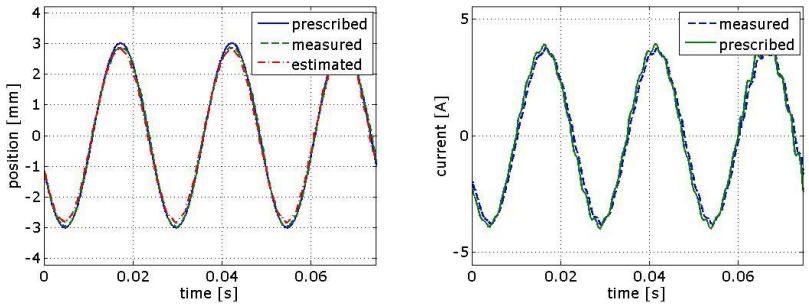

a) b)

Figure 5.41 a) Measured, estimated, prescribed position / time; b) Measured, prescribed current vs. time @ 40 Hz, 3 mm amplitude

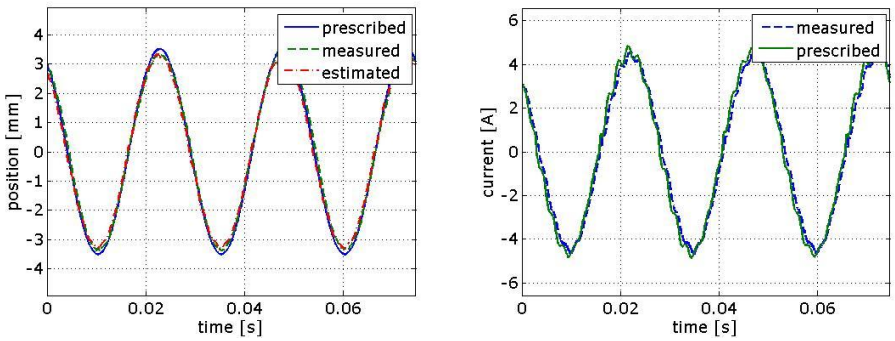

a) b)

Figure 5.42 a) Measured, estimated, prescribed position / time; b) Measured, prescribed current vs. time @ 40 Hz, 3.5 mm amplitude

Figure 5.43, Figure 5.44, Figure 5.45, Figure 5.46, Figure 5.47 and Figure 5.48 illustrate the results obtained for 1, 1.5, 2 and 2.5, 3 and 3.5 mm sinusoidal reference position amplitude, having 50 Hz frequency.

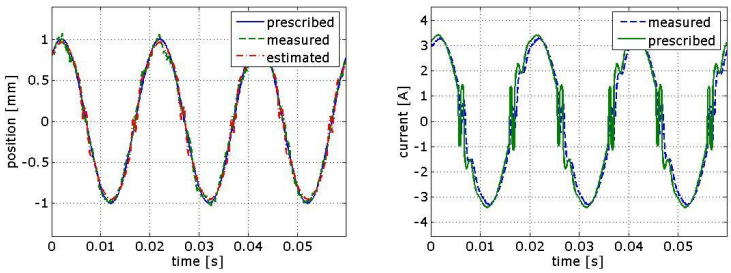

a) b)

Figure 5.43 a) Measured, estimated, prescribed position / time; b) Measured, prescribed current vs. time @ 50 Hz, 1 mm amplitude

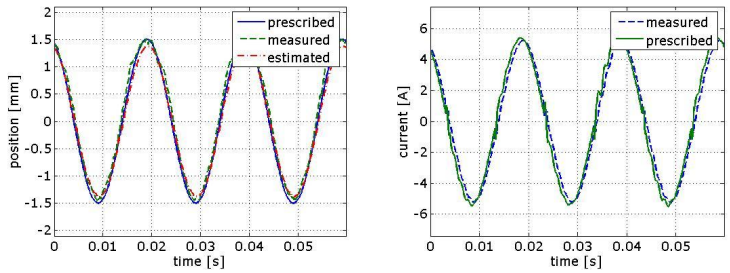

a) b)

Figure 5.44 a) Measured, estimated, prescribed position / time; b) Measured, prescribed current vs. time @ 50 Hz, 1.5 mm amplitude

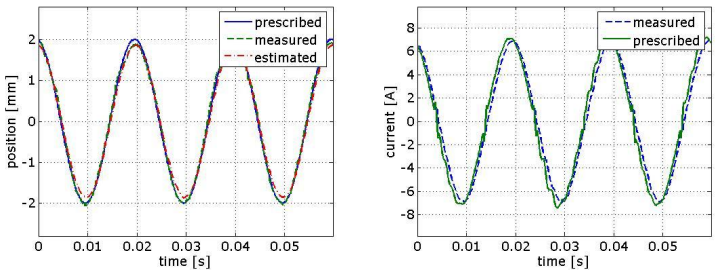

a) b)

Figure 5.45 a) Measured, estimated, prescribed position / time; b) Measured, prescribed current vs. time @ 50 Hz, 2 mm amplitude

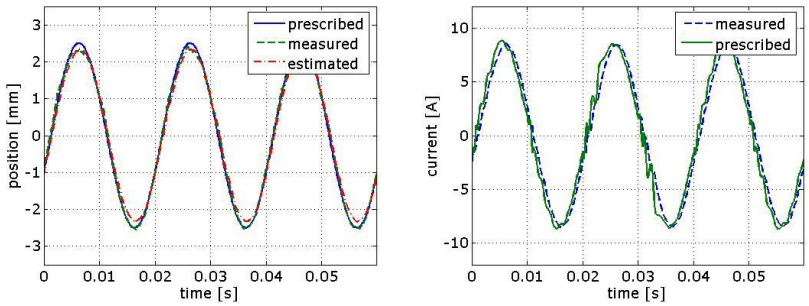

a) b)

Figure 5.46 a) Measured, estimated, prescribed position / time; b) Measured, prescribed current vs. time @ 50 Hz, 2.5 mm amplitude

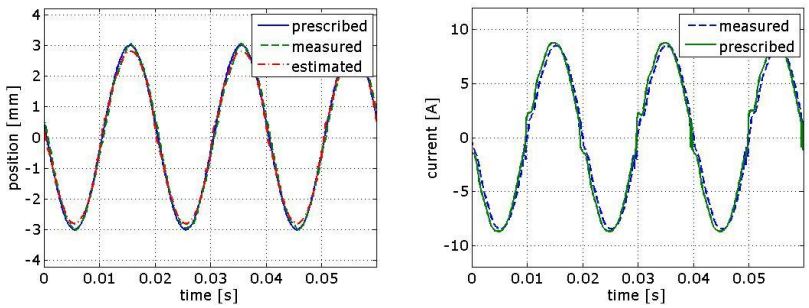

a) b)

Figure 5.47 a) Measured, estimated, prescribed position / time; b) Measured, prescribed current vs. time @ 50 Hz, 3 mm amplitude

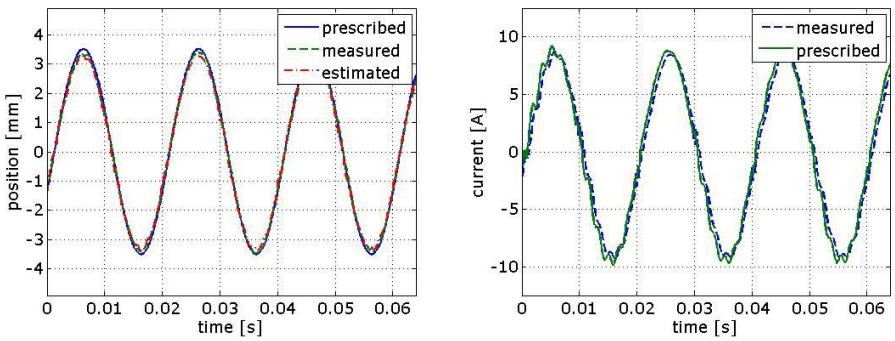

a) b)

Figure 5.48 a) Measured, estimated, prescribed position / time; b) Measured, prescribed current vs. time @ 50 Hz, 3.5 mm amplitude

BUPT

Figure 5.49, Figure 5.50, Figure 5.51, Figure 5.52, Figure 5.53 and Figure 5.54 illustrate the results obtained for 1, 1.5, 2 and 2.5, 3 and 3.5 mm sinusoidal reference position amplitude, having 60 Hz frequency.

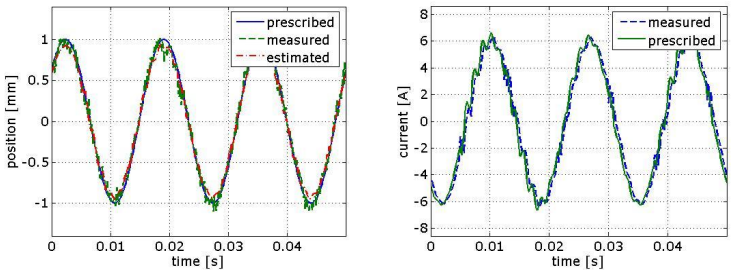

a) b)

Figure 5.49 a) Measured, estimated, prescribed position / time; b) Measured, prescribed current vs. time @ 60 Hz, 1 mm amplitude

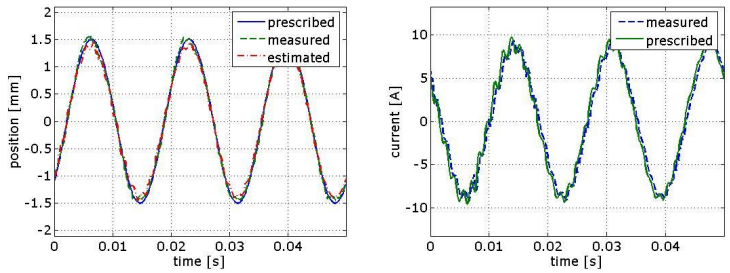

a) b)

Figure 5.50 a) Measured, estimated, prescribed position / time; b) Measured, prescribed current vs. time @ 60 Hz, 1.5 mm amplitude

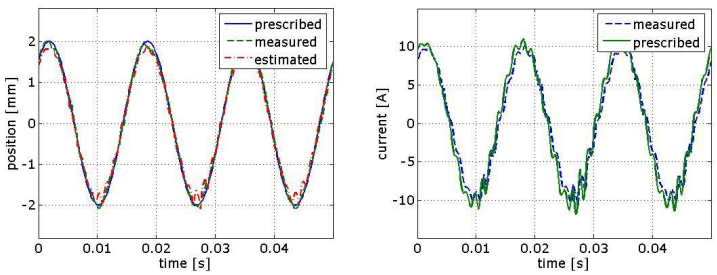

a) b)

Figure 5.51 a) Measured, estimated, prescribed position / time; b) Measured, prescribed current vs. time @ 60 Hz, 2 mm amplitude

BUPT

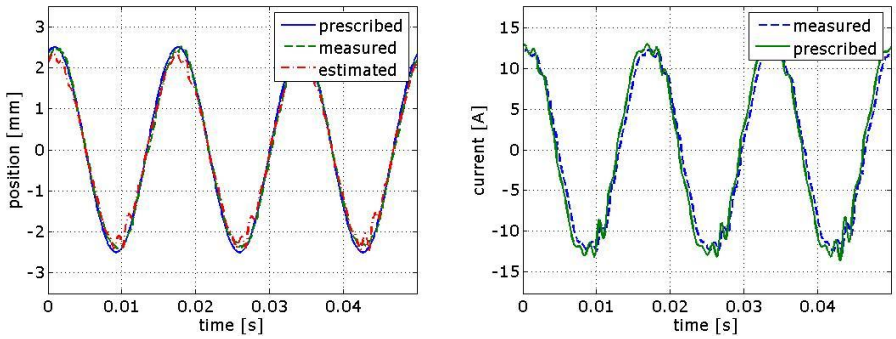

a) b)

Figure 5.52 a) Measured, estimated, prescribed position / time; b) Measured, prescribed current vs. time @ 60 Hz, 2.5 mm amplitude

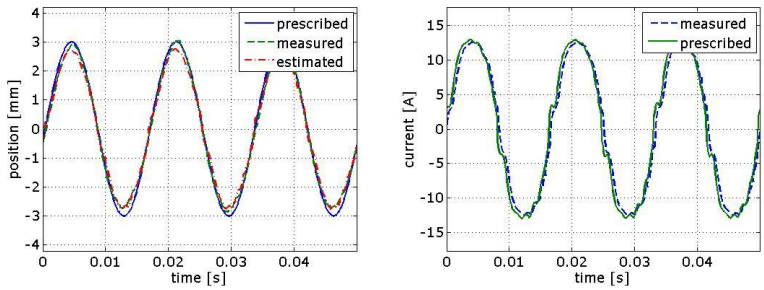

a) b)

Figure 5.53 a) Measured, estimated, prescribed position / time; b) Measured, prescribed current vs. time @ 60 Hz, 3 mm amplitude

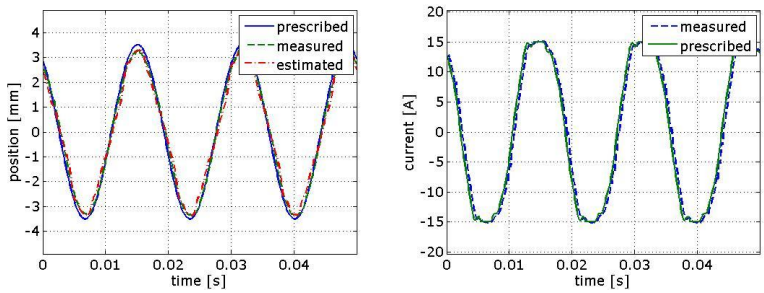

a) b)

Figure 5.54 a) Measured, estimated, prescribed position / time; b) Measured, prescribed current vs. time @ 60 Hz, 3.5 mm amplitude

BUPT

Figure 5.55, Figure 5.56 and Figure 5.57 ilustrate the results obtained for 1, 1.5 and 2 mm sinusoidal reference position amplitude, having 70 Hz frequency.

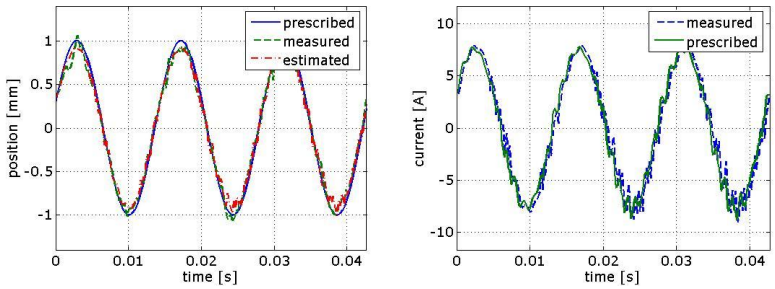

a) b)

Figure 5.55 a) Measured, estimated, prescribed position / time; b) Measured, prescribed current vs. time @ 70 Hz, 1 mm amplitude

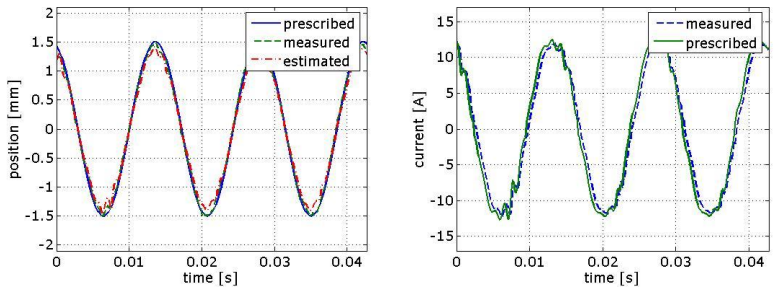

a) b)

Figure 5.56 a) Measured, estimated, prescribed position / time; b) Measured, prescribed current vs. time @ 70 Hz, 1.5 mm amplitude

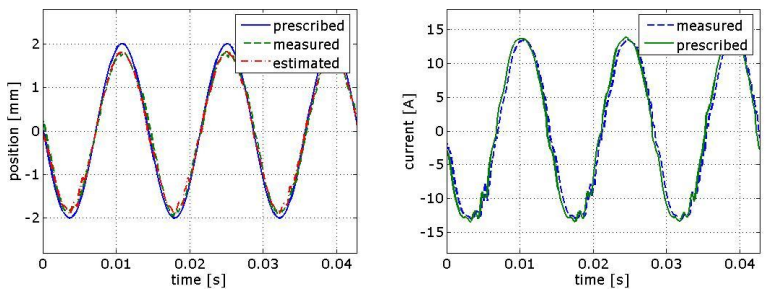

a) b)

Figure 5.57 a) Measured, estimated, prescribed position / time; b) Measured, prescribed current vs. time @ 70 Hz, 2 mm amplitude

BUPT

Figure 5.58 and Figure 5.59 illustrate the results obtained for 1 and 1.5 mm sinusoidal reference position amplitude, having 80 Hz frequency.

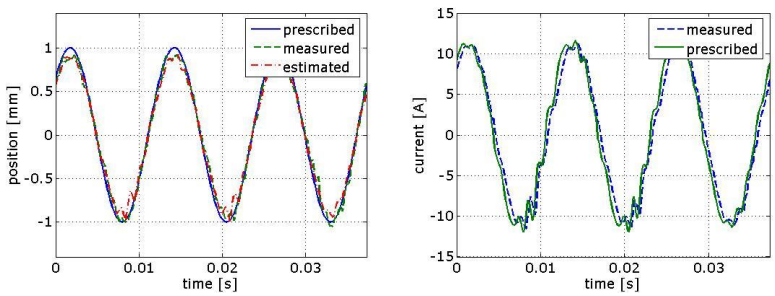

a) b)

Figure 5.58 a) Measured, estimated, prescribed position / time; b) Measured, prescribed current vs. time @ 80 Hz, 1 mm amplitude

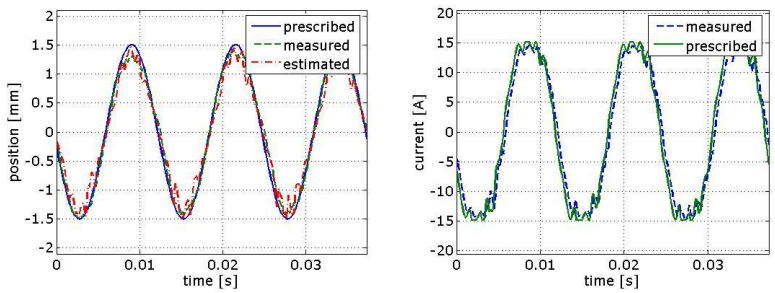

a) b)

Figure 5.59 a) Measured, estimated, prescribed position / time; b) Measured, prescribed current vs. time @ 80 Hz, 15 mm amplitude

Next we will illustrate in Figure 5.60, the results obtained when prescribing a 2 mm amplitude sinusoidal position at 80 Hz. As one can see the results are not satisfactory, so we face here the actuator's control limits.

BUPT

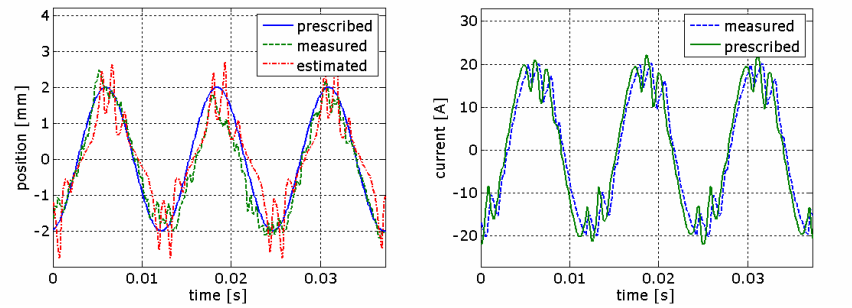

Figure 5.60 a) Measured, estimated, prescribed position / time; b) Measured, prescribed current vs. time @ 80 Hz, 2 mm amplitude

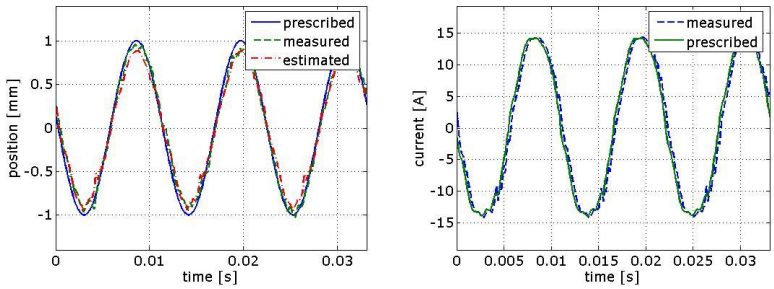

a) b)

Figure 5.61 a) Measured, estimated, prescribed position / time; b) Measured, prescribed current vs. time @ 90 Hz, 1 mm amplitude

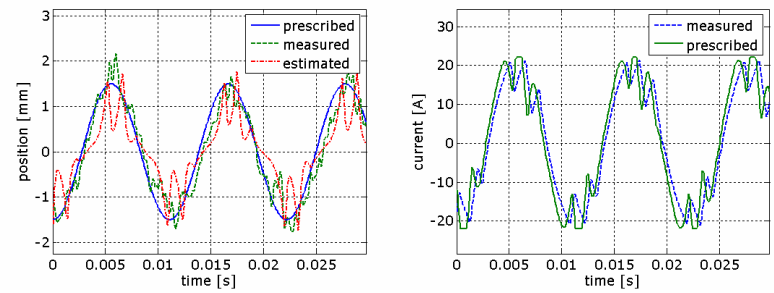

a) b)

Figure 5.62 a) Measured, estimated, prescribed position / time; b) Measured, prescribed current vs. time @ 90 Hz, 1.5 mm amplitude

Referring to Figure 5.62, the estimated position has no longer a sinusoidal shape and for higher values of the prescribed sinusoidal amplitude, the situation is

getting worse, furthermore the current needed exceeds 20 A amplitude which is the DC link limit.

5.3.2 Step amplitude change at constant frequency of prescribed position

In this section we choose to investigate the actuator response when applying, at a given frequency, successive amplitude steps. For a fixed 50 Hz sinusoidal prescribed position we modify the amplitude in 3 steps: from 1 to 1.5 mm, from 1.5 to 2 mm and from 2 to 2.5 mm.

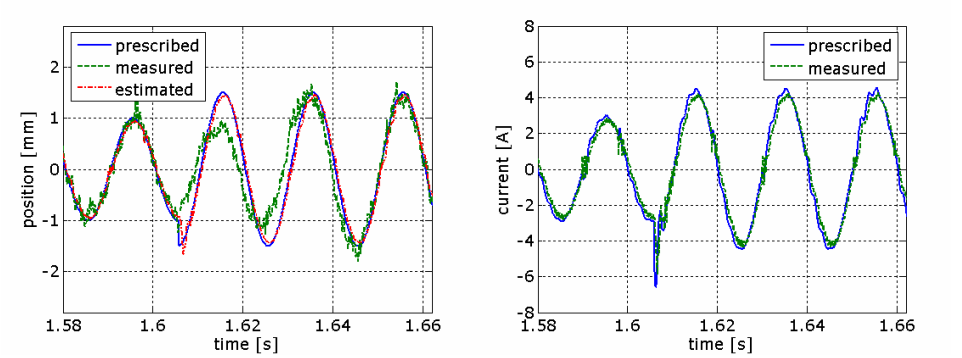

a) b)

Figure 5.63 Position a) and current b) response to a step amplitude modification from 1 to 1.5 mm of the prescribed position, at 50 Hz frequency

In Figure 5.63a one can see that at 1.606 seconds the prescribed position amplitude changes. Due to that fact that the change takes place near a maximum value of the sinusoidal wave (the negative one) the difference between the two values, after and before the switching time, is relatively large causing also a suddenly modification of the prescribed current, Figure 5.63b.

Also referring again to Figure 5.63a, one can see that the estimated positions suffers also suddenly a shape modification due to the fact that it is build based on current information. On the other hand, the measured position does not seem to be affected by the sudden modification and it smoothly rise in one and a half period to the new prescribed position.

The same observations are available for the step amplitude modification of the prescribed position from 1.5 to 2 mm, but this time the change occurs near the maximum value of the positive side, see Figure 5.64a and b.

BUPT

Another observation that has to be made is that the measured position suffers a small phase modification with respect to the prescribed one for about two signal periods.

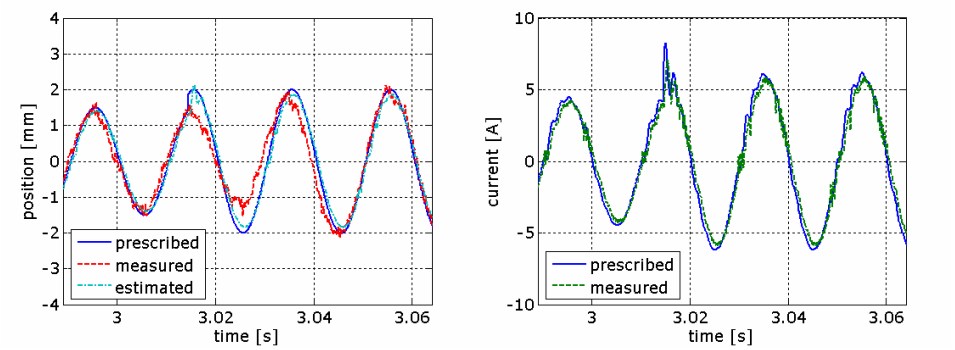

a) b)

Figure 5.64 Position response to a step amplitude modification from 1.5 to 2 mm of the prescribed position, at 50 Hz frequency

Figure 5.65a illustrates a step change in the prescribed position amplitude that occurs near zero. As expected there are no spikes in the prescribed current (see Figure 5.65b) and in the estimated position, the measured position phase suffers minor modifications and rises smoothly to the new prescribed position in one and a half period.

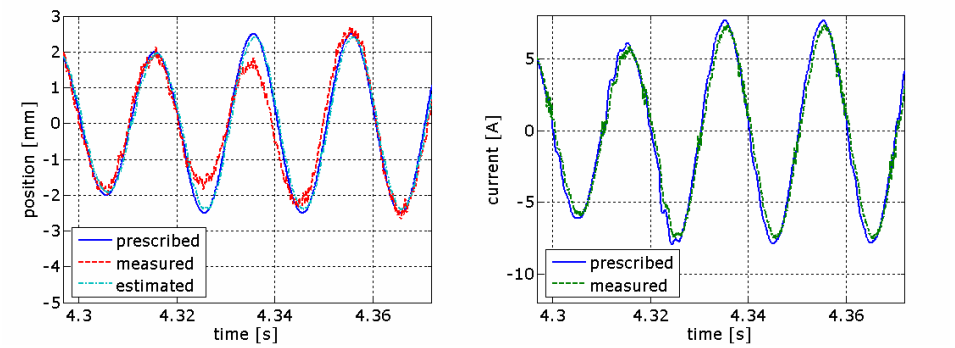

a) b)

Figure 5.65 Position response to a step amplitude modification from 2 to 2.5 mm of the prescribed position, at 50 Hz frequency

5.3.3 Step amplitude and step frequency change of the prescribed position

This section presents the actuator response when applying step changes both in amplitude and in frequency of the prescribed position.

We start first from zero to 10 Hz frequency and 1 mm amplitude of the prescribed position. After a certain time period, we switch to 40 Hz frequency and 2 mm amplitude. The next switch will be to 50 Hz frequency and 2.5 mm amplitude and finally to 70 Hz frequency and 1.5 mm amplitude.

As can be seen in Figure 5.66a the position response has no major phase delays and the actuator does not respond to short period current spikes, see Figure 5.66b.

Short current impulses have been injected in the actuator coils in some previous preliminary open loop experiments, and the results showed that these pulses need to have a minimum width in order to cause the mover oscillation. However, the green line in Figure 5.66b represents the prescribed current which at the time of the switch jumps to -4 A, the actual measured current in the actuator's coils reach just -2 A.

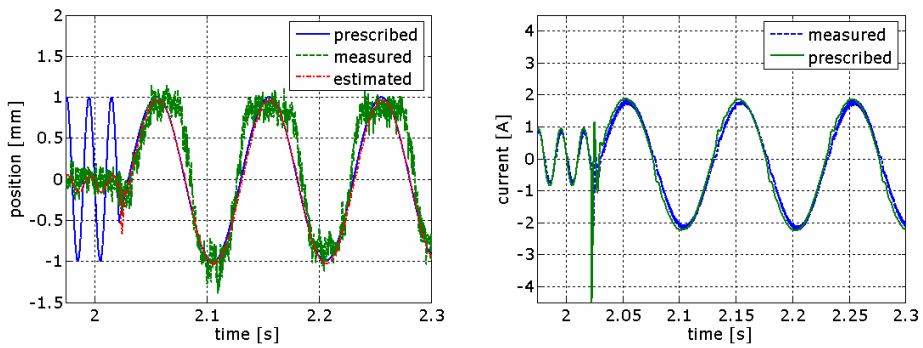

Figure 5.66 Position a) and current b) response when performing a step change of the prescribed position from zero to 10 Hz frequency and 1 mm amplitude

Next, in Figure 5.67 are shown results obtained when suddenly switching to 40 Hz and 2 mm prescribed sinusoidal position. At the switching moment the position error changes abruptly causing a sudden rise of the prescribed current. The prescribed position (blue line in Figure 5.67a) is closely followed by the estimated position, but the measured one seams to undergo a mechanical exterior disturbance. However after some oscillations the motion stabilize itself.

BUPT

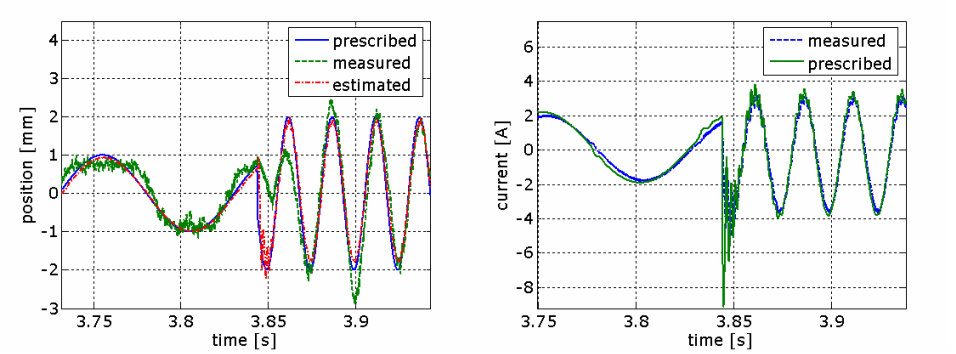

a) b)

Figure 5.67 Position a) and current b) response when performing a step change of the prescribed position from 1 mm and 10 Hz to 2 mm and 40 Hz

The next switch is to 50 Hz frequency and 2.5 mm amplitude prescribed position, see Figure 5.68. Here the leap in amplitude and in frequency is relatively small and no major switching oscillations occur.

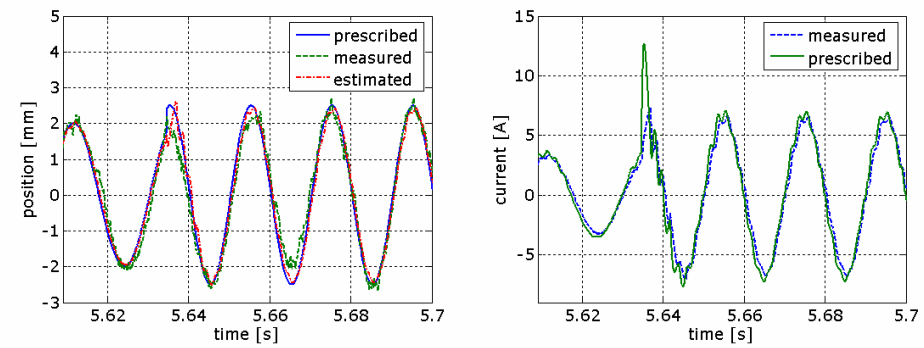

a) b)

Figure 5.68 Position a) and current b) response when performing a step change of the prescribed position from 2 mm and 40 Hz to 2.5 mm and 50 Hz

The switching to 70 Hz and 1.5 mm prescribed position is illustrated in Figure 5.69.

BUPT

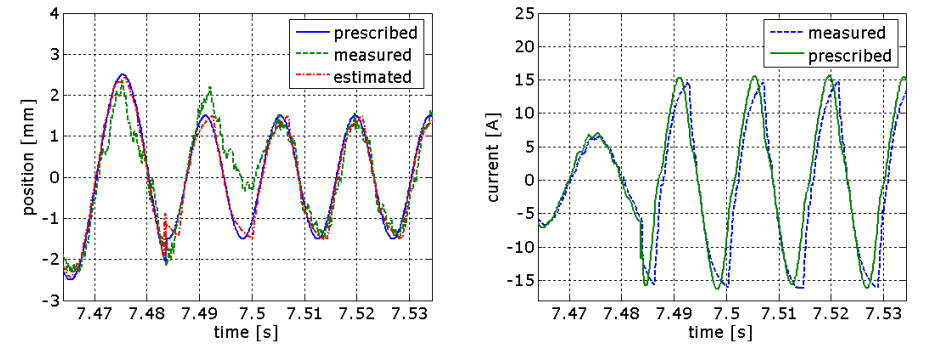

a) b)

Figure 5.69 Position a) and current b) response when performing a step change of the prescribed position from 2.5 mm and 50 Hz to 1.5 mm and 70 Hz

After viewing all the results presented in this section one should notice that the estimated position do not trace any short time period oscillation of the measured position and it's shape is mainly determined by the current profile. Sudden exterior mechanical disturbances also do not reflect themselves in the estimated position and therefore are not followed by current corrections intended to stabilize the movement.

5.3.4 Closed loop position sensorless control performance analysis

In this section will be presented the amplitude error and phase error between the prescribed and measured position. In addition, the apparent power needed to realize the demanded dynamics will be discussed and emerging conclusions will be taken.

According to Figure 5.70 for small amplitudes of the prescribed position (1 mm and 1.5 mm) the amplitude error is small, somewhere around 0.05 mm and rises with frequency. Due to losses and saturation within the actuators mover, which is made of Steel, for higher desired dynamics (amplitude and frequency) we have higher errors.

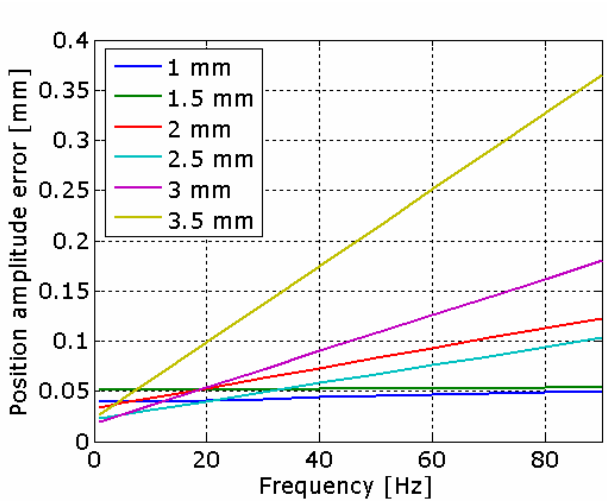

Figure 5.70 Position amplitude error versus frequency for different amplitudes of the prescribed position

The phase error is illustrated in Figure 5.71. According to this figure at low frequencies and small motion amplitude, we obtain relatively high errors. The phase error decreases when frequency increases.

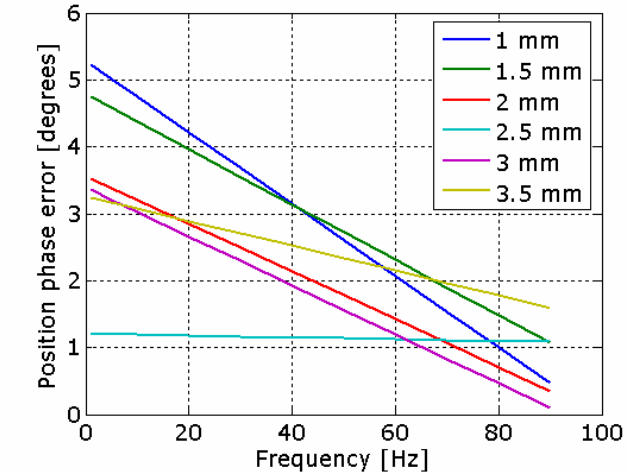

Figure 5.71 Position phase error versus frequency for different prescribed position amplitudes

The apparent power variation with frequency for different amplitudes is shown in Figure 5.71.

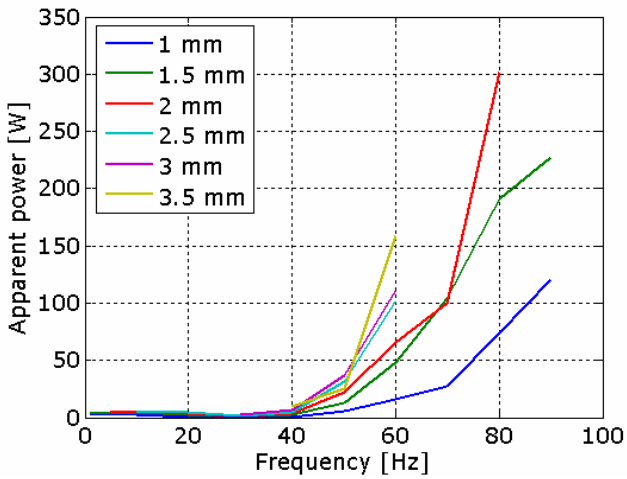

Figure 5.72 Apparent power versus frequency for different position amplitudes

If we adopt a logarithmic scale on the apparent power axis, see Figure 5.73, one can observe better that around 30 Hz the apparent power needed has a minimum for all amplitudes tested.

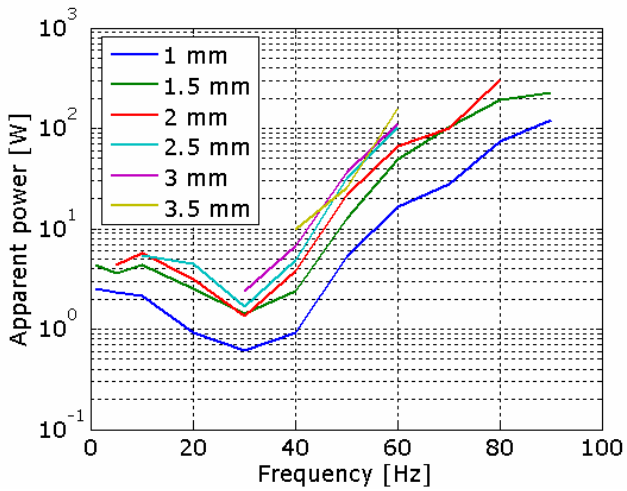

Figure 5.73 Apparent power (logarithmic scale) versus frequency for different position amplitudes

This frequency corresponds to resonant frequency of the spring-mass system formed by the actuator's moving plates, shaft and the two springs.

SUMMARY

In this chapter closed loop position control with and without sensor is presented. First, a brief introduction to PID control and (SM) sliding mode control is made. The combined PID and SM strategy utilized to control the actuator is introduced. Experiments in both cases (with position sensor and sensorless) for various frequencies are presented. Due to the poor position sensor performance the experiments with sensor are limited within a frequency domain around 50 Hz. Fixed amplitude and frequency, step amplitude at fixed frequency, step amplitude and step frequency oscillation experiments are listed when performing sensorless position control. Amplitude and phase errors are calculated yielding acceptable values.

BUPT

CHAPTER 5 - REFERENCES

[1] M.J. Willis, „Proportional-Integral-Derivative Control", Dept. of Chemical and Process Engineering University of Newcastle, October 1999

[2] Ardemis Boghossian, James Brown, Sara Zak, „PID intro", - ControlsWiki articles, October 6, 2007.

[3] Markaroglu H., Güzelkaya M., Eksin İ., Yeşil E., 2006. „Tracking Time Adjustment in Back Calculation Anti-windup Scheme", ECMS-2006,20th European Conference on Modelling and Simulation, Bonn, Germany.

[4] S. V. Emel'yanov: "Use of Non-linear Correcting Devices of Switch Type to Improve the Quality of Second Order Automatic Control System ", Automate. I Telemekh, Vol. 20, No 7, 1959, (In Russian).

[5] E. A. Barbashin and E. I. Gerashchenko. :" On Introduction to Sliding Modes in Control Systems", Differential Equations, Vol. 1, No. 1, 1965.

[6] U. ITKIS: "Control Systems of Variable Structure ", John Wiley, 1976.

[7] V. I. UTKIN: "Sliding Modes and Their Applications in Variable Structure Systems ",
MIR, Moscow, 1978.

[8] J. Y. Hung, W. Gao and J. C. Hung: "Variable Structure Control: A survey ", IEEE
Transactions on Industrial Electronics, Vol. 40, No. 1, Feb. 1993.

[9] V. I. UTKIN: "Sliding Mode Control Design Principles and Applications to Electric Drives ", IEEE Trans. Ind. Electr., Vol. 40, No. 1, PP. 23 – 36, Feb. 1993.

[10] A. A. Ahmed, H. H. TAHIR and A. A. ALI: "Digital Simulation of D. C. Motor Position Control Based on the Variable – Structure System (VSS)", 1st Specialist Conference on Control, M.P.E., Nov. 1999, Baghdad, IRAQ

[11] "Designing Digital Autopilot for SSM Based on Variable Structure Controller (VSC)", 3rd Scientific Conference for M.E.C., June 2000, Baghdad, IRAQ.

[12] Tahir, H.H.; Al-Rawi, A.A.A. – „Variable Structure Control Design of Process Plant Based on Sliding Mode Approach", Control Conference, 2006. CCC 2006. Chinese,
7-11 Aug. 2006

[13] Scientific and technical Research Report – CEEX – AMTRANS, No. X2C33/2006, Aditional note no. 2, „New electrical actuators technologies for automotive ", Stage III, 2008, University Politehnica of Timisoara, Romania

[14] A. Sabanovici, K. Abidi, M. A. Elitas, „Study on high accuracy discrete-time sliding mode control", in Proc. EPE-PEMC 2006, Portoroz, Slovenia, pp. 355-360, 2006.

BUPT

[15] T.L. Dragomir, Elemente de teoria sistemelor, Ed. Politehnica, Timisoara, Romania, 2004

BUPT

Chapter 6 The Experimental test platform

6.1 The hardware platform components

As one can observe from Figure 6.1 the main components are:

- The Linear PM Oscillatory Machine;
- The DSpace platform;
- High speed analogue laser sensor;
- A single phase inverter;
- A Load Cell.

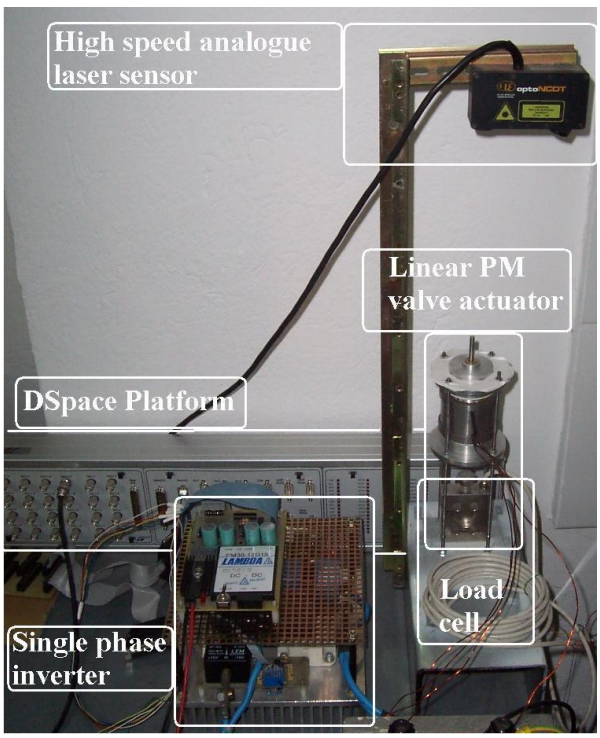

Figure 6.1 The experimental platform

6.1.1 The Linear PM Oscillatory Machine

The oscillatory machine is actually a linear actuator that will be described in this section.

The actuator was manufactured in Italy at the University of Cassino. The actuators cross-section is illustrated in Figure 6.2.

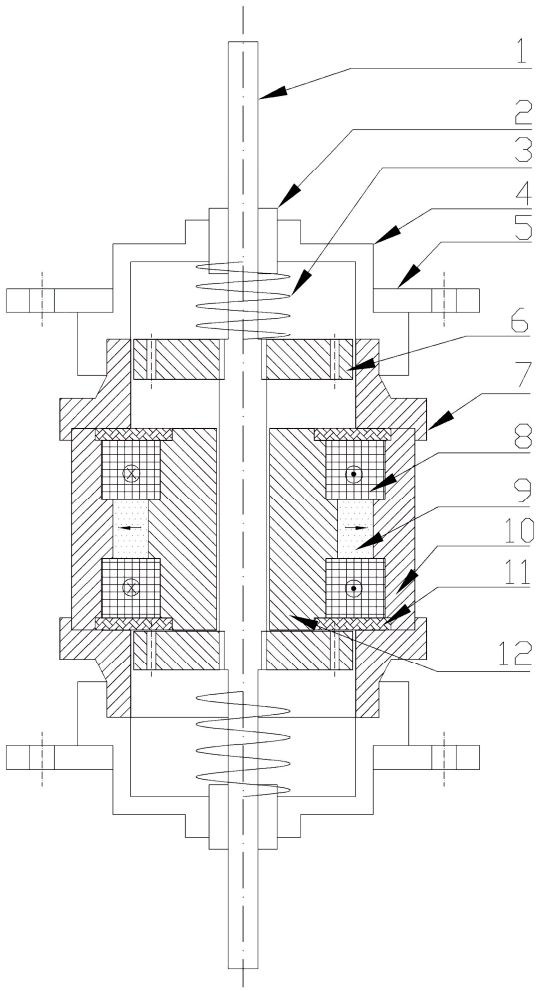

Figure 6.2 The actuator cross section view [1]

Table 6.1 lists the actuator components as they appear in Figure 6.2, and the materials used to manufacture them.

Table 6.1 – Actuator components

Sketch number	Piece name	Material	Number of pieces to manufacture	Observations
1	Shaft	Stainless steel	1	
2	Linear bearing	-	2	
3	Mechanical Spring	-	2	
4	Actuator cover	Stainless steel	2	
5	Actuator mount ring	Stainless steel	2	
6	Mover	Atomet	2	
7	Intermediate stator	Atomet	2	
8	Coils	Copper	2	Identical, series connection
9	Permanent Magnets	NeFeB [2,3]	8	
10	External stator	Atomet	1	
11	Ring Resin	Kevlar	2	
12	Internal stator	Atomet	1	

Figure 6.3 illustrates all manufactured actuator components.

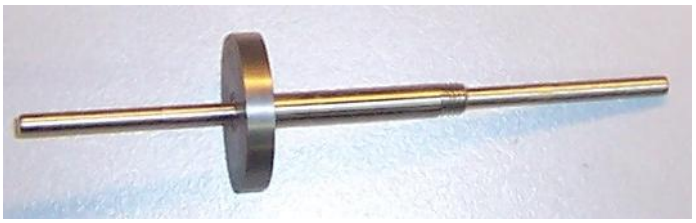

a) The shaft with a moving plate mounted

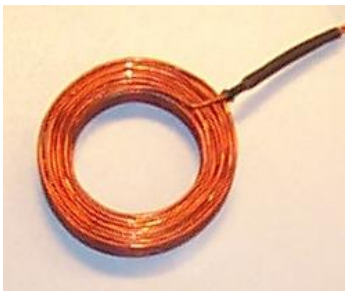

b) actuator coil – there are actually 2 twin coils

c) intermediate stator

d) interior stator with PMs mounted

e) mounting ring

f) exterior stator

g) mounting ring

h) exterior stator

Figure 6.3 Actuator manufactured components

6.1.2 The DSpace platform

Dspace 1103 platform is a flexible and powerful tool, featuring high computational capability and comprehensive I/O periphery. This platform is built for real-time control system based on one controller board (Figure 6.4). Dspace 1103 has been used in all experiments presented in this thesis.

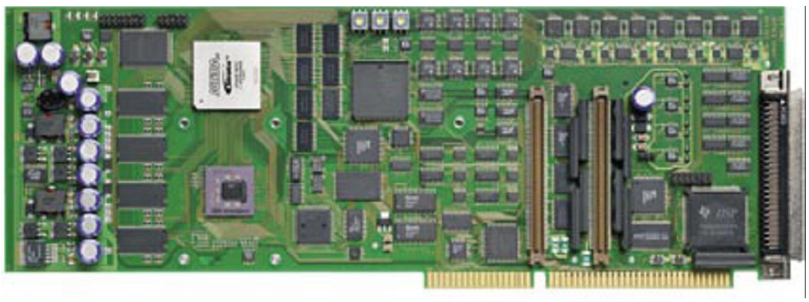

Figure 6.4 DS1103 PPC Controller Board [4]

The controller board can be fully programmable by using the Simulink block diagram environment. One can configure all I/O graphically by dragging RTI blocks from Matlab® libraries, providing this way a quick and easy way to implement control functions on the board and reduces the implementation time.

Additional I/O tasks are addressed based on a DSP controller unit built around Texas Instruments TM320F240 DSP that is used as a subsystem (Figure 6.5).

Figure 6.5 DS1104 R&D Controller Board

BUPT

An overview of the functional units of Dspace 1103 is shown in Figure 6.6.

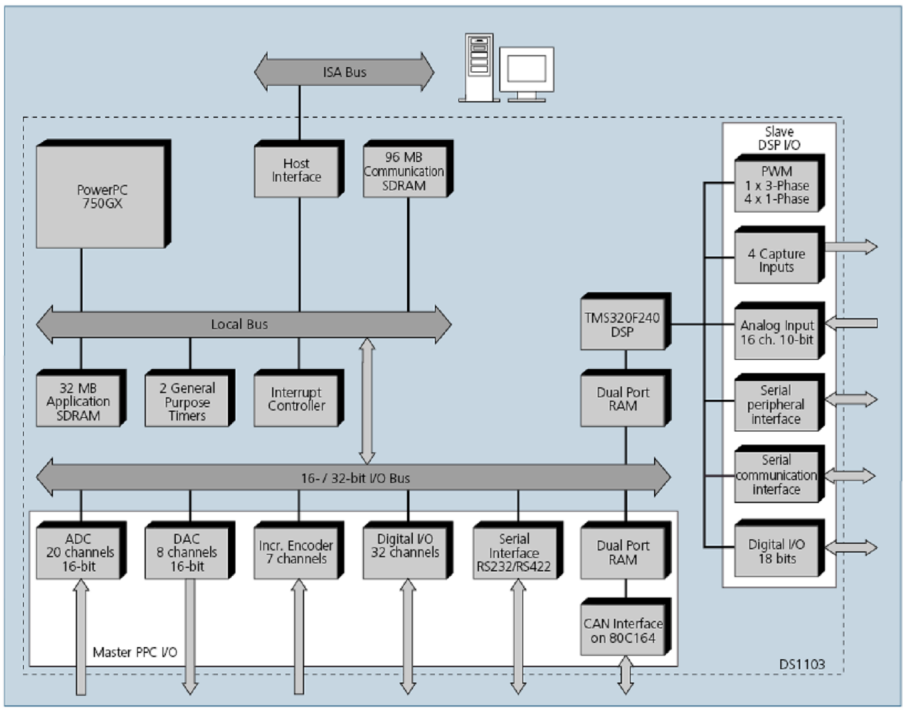

Figure 6.6 Block diagram of Dspace 1103 [3]

This bord meets the requirements of a rapid control prototyping, being suitable for applications such as:

- Automotive controllers;
- Induction motor control;
- Robotics;
- Positioning systems and stepper motors;
- Active vibration control.

6.1.3 The high speed analogue sensor laser

The sensor is based on the triangulation method to determine the changes in position.

A laser beam is emitted from the sensor and creates a visible spot on the surface of the measured object. Depending on the distance measured, a CMOS line scan camera besides the laser ”views” this spot under varying angles. Using this angle and the known distance of laser and camera, the Digital Signal Processor computes the distance between the sensor and the measured object, Figure 6.7.

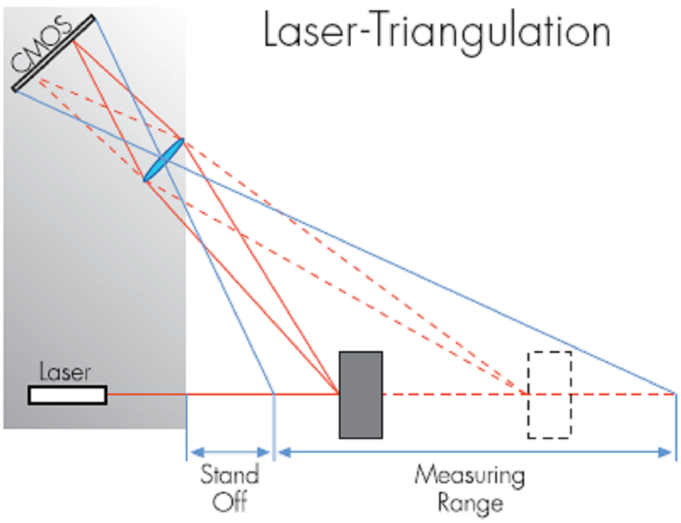

Figure 6.7 The laser-triangulation method [5]

The vast majority of such sensors combine a high resolution CMOS line scan camera with a DSP to provide pure digital acquisition and processing of measured values. This combination provides for a very stable output signal, regardless of surface conditions.

The sensor code is optoNCDT 1607 and is manufactured by Micro-Epsilon.

The optoNCDT16x7 consists of a laser-optical sensor and a signal conditioning electronics. The sensor uses the principle of optical triangulation, i.e. a visible, modulated point of light is projected onto the target surface. The diffuse element of the reflection of the light spot is imaged by a receiver optical element positioned at a certain angle to the optical axis of the laser beam onto a high-sensitivity resolution element (PSD element), in dependency on distance. From the output signal of the PSD element the controller calculates the distance between the

light spot on the object being measured and the sensor. The distance is linearized and then issued via an analog or digital interface [6].

Figure 6.8 shows a schematic view of how such a sensor works and the resulting output electrical parameters.

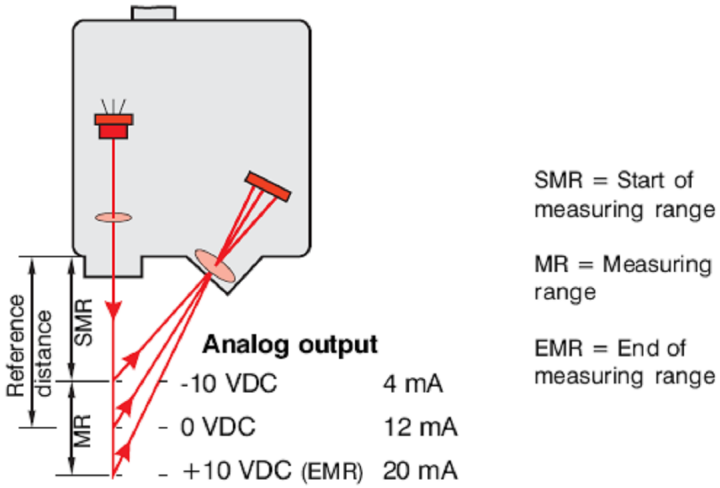

Figure 6.8 Definition of terms, output signals

6.1.4 The single phase inverter

The single phase inverter is based on two Super-fast NPT-IGBT modules SKM100GB063D modules, Figure 6.9.

Figure 6.9 SKM100GB063D module, outside view [7]

The schematic of the internal structure of such a module is shown in Figure 6.10.

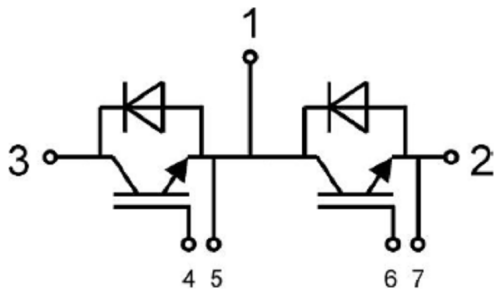

Figure 6.10 Internal structure of SKM 100 GB063D module

The features of the module are:

- N channel, homogeneous Silicon structure (NPT – Non punch through IGBT);
- Low tail current with low temperature dependence;
- High short circuit capability, self limiting if terminal G is clamped to E;
- Positive temperature coefficient of VCEsat;
- Latch-up free;
- Fast and soft inverse CAL diodes;
- Isolated copper Bonding Technology without hard mould;
- Large clearance and creepage distances.

The DC link capacity is 6000 μF obtained with electrolytic capacitors plus 80μF from double metallized polypropylene film capacitors.

We made a circuit board to interface the IGBT drivers with the Dspace output digital signals. This board comprises an octal thi-state line buffers, four optocouplers, and the additional DC supply circuit to power the onboard components.

We choose to utilize for all four IGBTs the drivers supplied by the manufacture, Semikron SKHI 22A [8], see Figure 6.11.

BUPT

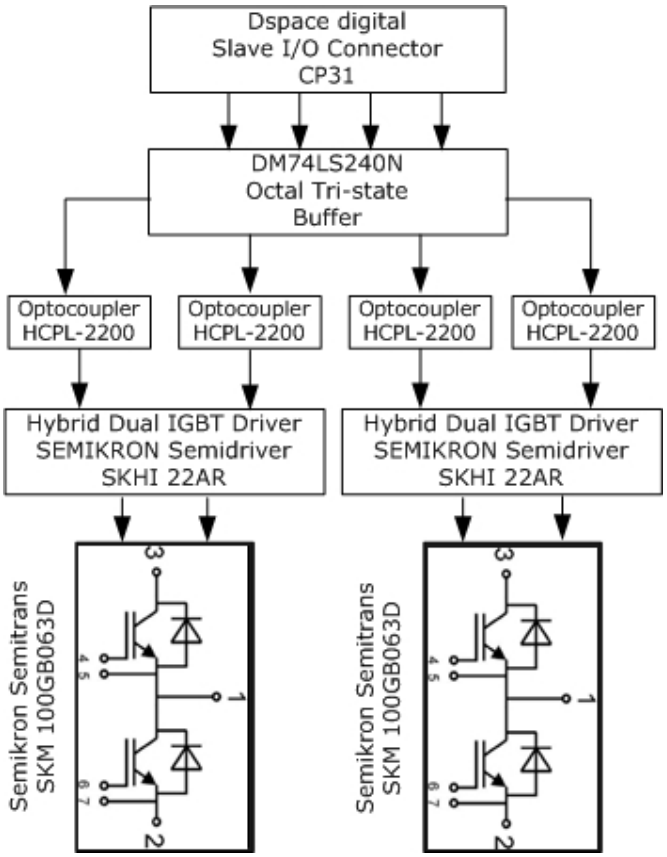

Figure 6.11 Single phase inverter block scheme

6.1.5 The bi-directional load cell

The measured forced presented in this thesis were measured based on a load cell. The majority of today's designs use strain gauges as the sensing element, whether foil or semiconductor.

Strain gauge patterns offer measurement of tension, compression and shear forces. Semiconductor strain gauges come in a smaller range of patterns than the foil gauges, but are extremely small and have large gauge factors, providing larger outputs for the same given stress, [9].

The TCA series load cells are ideal for measuring both tensile and compressive forces. The standard metric threads at each end of the load cell are designed to accept standard spherical seating rod-end bearing. There is great flexibility in the TCA design, allowing manufactures to offer different special sizes, to meet specific application requirements, or different end thread sizes/combinations. There are versions available with male threads at each end, or male threads one end, female the other.

The TCA series can be supplied as with standard shapes or can be modified to meet a particular application requirement [10].

Figure 6.11 shows the outside view of the used load cell.

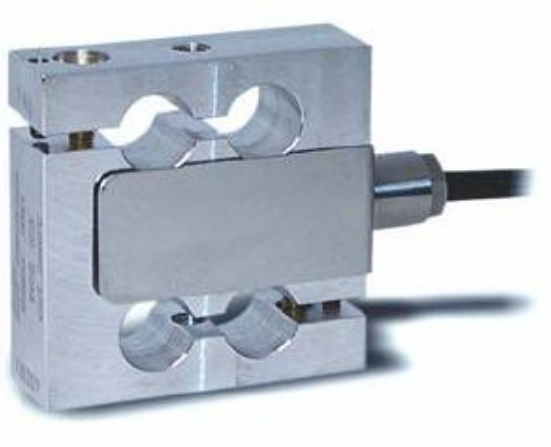

Figure 6.12 Bi-directional load cell

We used the load cell to measure the forces developed by the actuator. Due to some mounting problems, we subjected the cell only to compression forces, thereby to measure the negative forces we have to capsize the actuator.

6.2 The Software

The control algorithms were implemented in Simulink environment, compiled automatically using Microtec C compiler for Motorola Power PC and Texas Instruments C compiler and built/downloaded automatically using the dSpace system specialized MLIB/MTRACE mechanism (Figure 6.13).

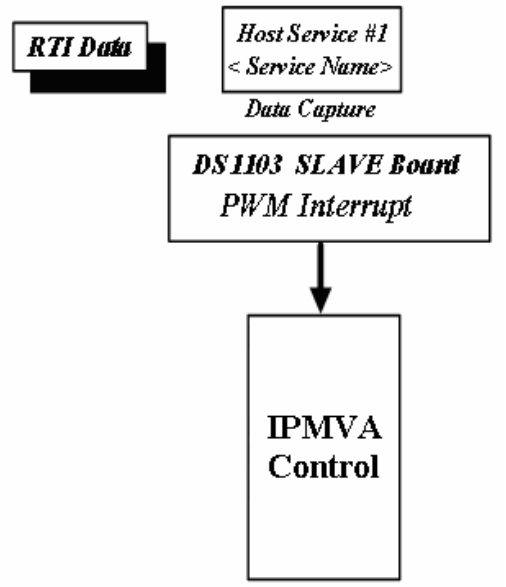

Figure 6.13 Schematic of the Simulink software

An preview of the software is shown in Figure 6.14. For simplicity reasons some blocks were removed. The figure was elaborated on a computer that has not installed the DSpace Real Time Interface and therefore the messenge "Bad Link" appears in some blocks.

BUPT

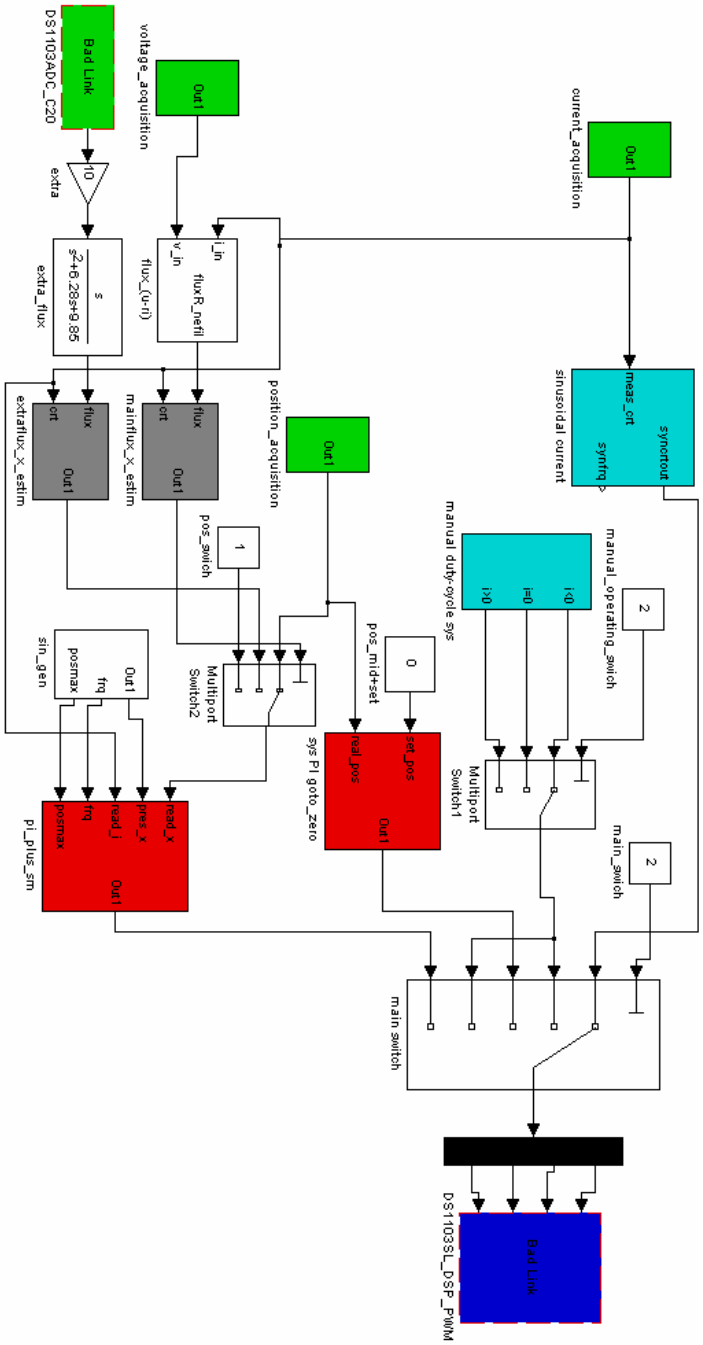

Figure 6.14 Simulink blocks of the implemented model

The electrical part of the actuator's dynamic model presented in Chapter 4 is illustrated in Figure 6.15 and the mechanical one in Figure 6.16.

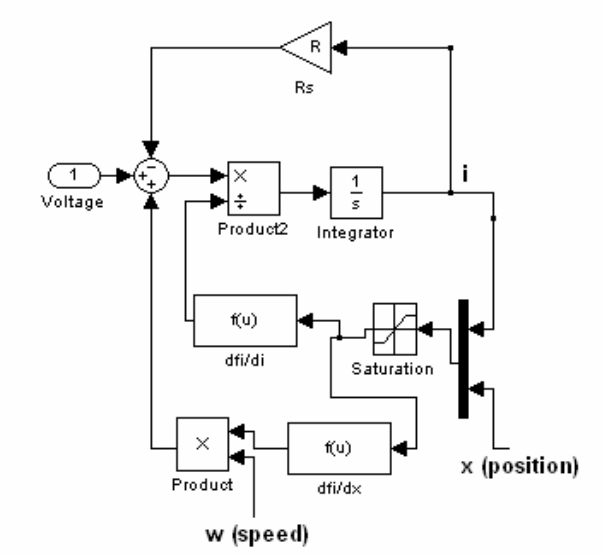

Figure 6.15 Electrical part of the dynamic simulation

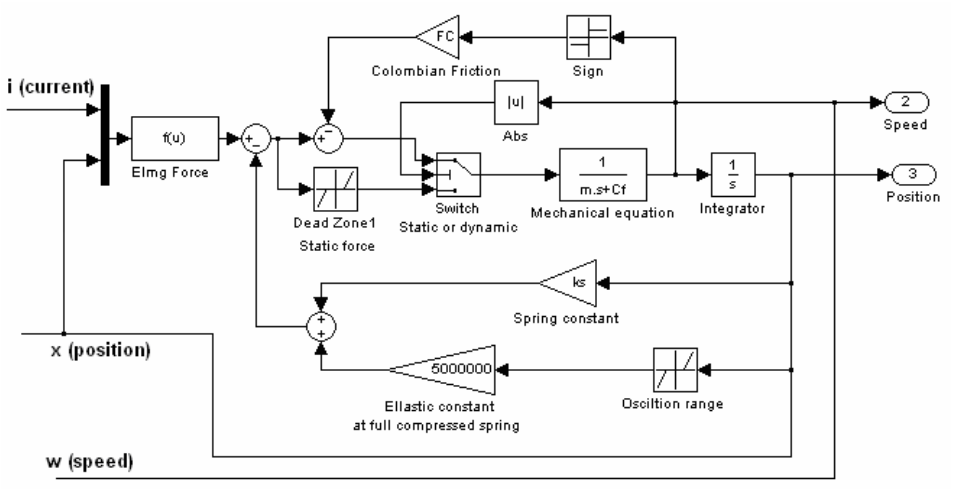

Figure 6.16 Mechanical part of the dynamic simulation

As one can observe both dynamic model parts are based on FEM derived data.

Figure 6.17 and Figure 6.18 illustrate the schemes of the two estimators made in Matlab / Simulink environment.

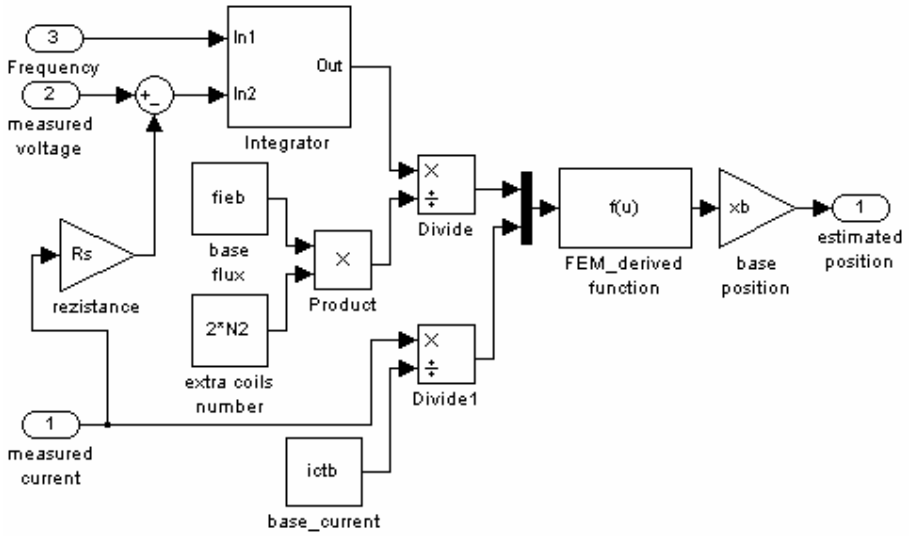

Figure 6.17 Position estimation scheme based on the main flux

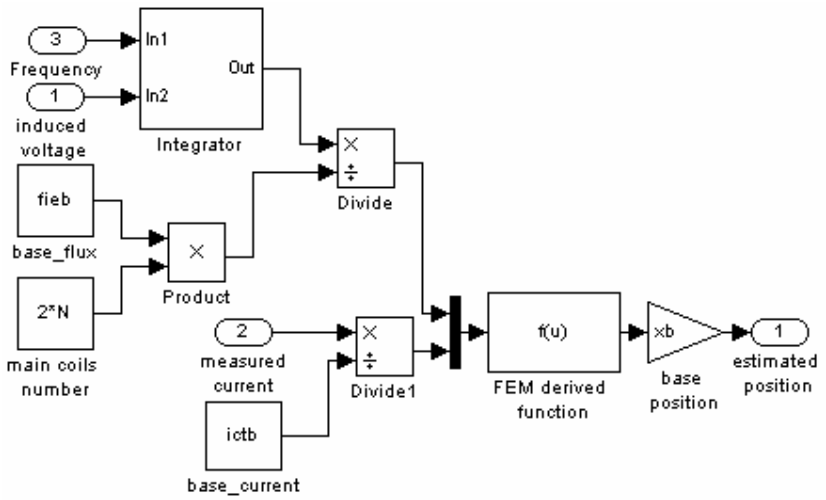

Figure 6.18 Position estimation scheme based on the extra flux

The function used as an integrator is shown in Figure 6.19.

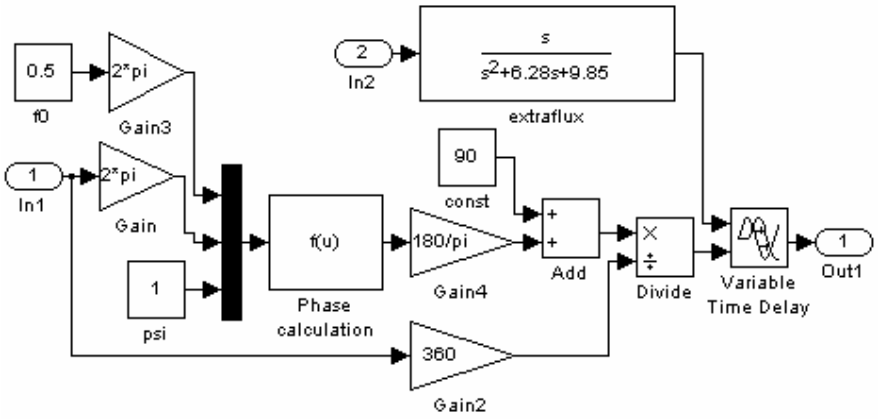

Figure 6.19 Compensated phase integrator block diagram

Figure 6.20 illustrates the PI current regulator used to perform open loop I/f control.

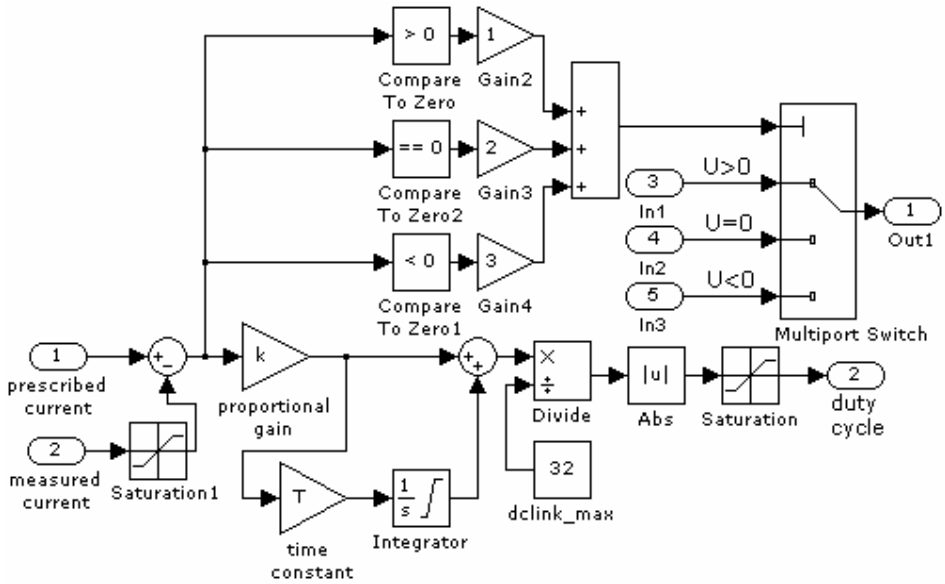

Figure 6.20 The PI current regulator

SUMMARY

The experimental platform utilized is described in this chapter. The actuator manufactured components are presented separately. All other hardware components such as: the single phase inverter, the position laser based sensor, the bi-directional load cell were presented. The software was implemented in Matlab / Simulink. A real-time interface, linked to the Simulink variables, has been used to control the machine.

CHAPTER 6 - REFERENCES

[1] I. Boldea, S. Agarlita, L. Tutelea, F. Marignetti – "Novel linear PM valve actuator: FE design and dynamic model", Record of LDIA 2007, Lille, France
[2] Total Magnetic Solutions - http://magnetsales.com
[3] Dexter Magnetic Technologies - http://www.dextermag.com
[4] Dspace web site - www.dspace.com
[5] Atlas Digital Laser Sensors web site – www.lap-laser.com
[6] Micro-Epsilon Sensors and Systems Instructuion Manual – www.micro-epsilon.com
[7] Semitrans IGBT Datasheet – www.semikron.com
[8] Semidriver Semikron Driver Electronics Datasheet – www.semikron.com
[9] The World of Sensors and Data System – www.sensorland.com
[10] Measurement and Sensors Technology – Althen site - www.althensensors.com

Chapter 7 – Conclusion and Contributions

7.1 Conclusion

The present work is dedicated to linear interior permanent magnet actuator design, control and applications.

The thesis focused on the following topics:

- automotive electrification applications;
- linear actuator industry applications;
- Electromagnetic, Thermal and Mechanical Finite Element Analysis;
- Optimization methods for electrical machines based on FEA derived data;
- U/f versus I/f open loop performance of the linear actuators;
- Position estimation of linear motors based on FEA derived data;
- Closed loop position sensorless control performance of linear actuators.

Based on the above listed topics the main conclusions are:

- Automotive industry tends to replace mechanical actuators by electrical ones, improving this way electrical system efficiency, finding alternatives to the present DC voltage system, and improving safety and comfort by introducing new functions that are best controlled electrically. Packing flexibility is the main motivation of the electrifying process of the car. The flexibility feature needed by automotive designers can be provided this way.
- Variable Valve Timing is an automotive technology that needs linear actuator. By developing a way to change valve timing between high and low rpm's, car manufactures can now tune valve operation for optimum performance and efficiency throughout the entire speed range.
- The finite element method (FEM) has proved its ability in analyzing and designing electromagnetic devices, and it is now an important tool in the electrical machine design process. A coupled simulation is

recommended due to the dependency of the material characteristics on various electrical and non-electrical parameters.

- Finite-Element methods allows for the development and optimization of new devices without the necessity of extensive prototyping, which is a more economical approach.
- Two optimization techniques have been implemented: grid search and Hooke-Jeekes. The grid search technique is more reliable but it becomes impractical with increasing dimensions. While computationally much less demanding than a grid search, the success of a Hooke-Jeeves algorithm is heavily dependent upon the choice of the starting point.
- When performing open loop control, an internal current loop leads to more stable operation of the purposed linear actuator over la wide range of frequencies. Also, position estimation attempted based on FEM derived data offers better results when current control is utilized.
- For sensorless position control, fixed amplitude and frequency, step amplitude at fixed frequency, step amplitude and step frequency oscillation experiments have been made, yielding acceptable amplitude and phase errors.

7.2 Original contributions

The presents thesis, from the author's perspective, the following original contributions:

- A comprehensive literature survey of rotary and linear actuators for achieving VVT;
- The interior permanent magnet linear actuator topology;
- Development of three Finite Element Analysis : electromagnetic, thermal and mechanical;
- Actuator's optimal design realization based on two optimization methods: Direct Search and Hooke-Jeeves.
- Open loop U/f and I/f control implementation on the purposed actuator;
- 2 Position estimators development based on FEM derived data;
- Closed loop position sensorless control implementation of the purposed actuator;

BUPT

- Single phase inverter design and manufacture with voltage and current sensors;
- Implementation of all necessary setup using DSpace 1103 system to perform all presented experiments.

Author's papers related to the Ph.D. Thesis

1. I. Boldea, S. C. Agarlita, L. Tutelea, F. Marignetti – "Novel linear PM valve actuator: FE design and dynamic model ", Record of LDIA 2007, Lille, France (Inspec).

2. I.Boldea, S. C. Agarlita, F. Marignetti and L. Tutelea – "Electromagnetic, Thermal and Mechanical design of a linear PM valve actuator laboratory model", Record of OPTIM 2008, Vol. II-A, Brosov, Romania (ISI, Inspec, Compendex)

3. S. C. Agarlita, I. Boldea, F. Marignetti and L. Tutelea – "Linear PM valve actuator: dynamic model digital simulations, open loop U/f, I/f validation and position estimation performance with experiments", accepted at Electromotion 2009, July 1-3 2009, Lille, France (Inspec)

BUPT

Author's CV

Sorin-Cristian AGARLIŢĂ

Home Address: Kiseleff Street, No. 66
220190, Drobeta Turnu Severin, Romania
Mobile: +40 0745 581 489
E-mail: agasoryn@yahoo.com

Education

2005 – 2009	PhD student at "Politehnica" University of Timisoara, Romania, Department of Electrical Engineering
2005	Dipl. degree in Electrical Engineering
2000-2005	Student at "Politehnica" University of Timisoara, Faculty of Electrical Engineering
1996-2000	National College "TRAIAN", Drobeta Turnu Severin, Romania

Professional Experience

3 months in 2007	Guest Researcher at University of Cassino, Frosinone, Italy

Personal Information

Born: March 16th, 1982
Family: Unmaried